COMPUTATIONAL MODELING OF LEFT VENTRICLE-VALVE DYNAMICS USING A FLUID-STRUCTURE INTERACTION FRAMEWORK

A Dissertation
Presented to
The Academic Faculty

by

Andres D. Caballero

In Partial Fulfillment
of the Requirements for the Degree
Doctor of Philosophy in the
Department of Biomedical Engineering

Georgia Institute of Technology & Emory University
December 2019

COMPUTATIONAL MODELING OF LEFT VENTRICLE-VALVE DYNAMICS USING A FLUID-STRUCTURE INTERACTION FRAMEWORK

Approved by:

Dr. Wei Sun, Advisor
School of Biomedical Engineering
Georgia Institute of Technology and Emory University

Dr. John Oshinski
School of Biomedical Engineering
Georgia Institute of Technology and Emory University

Dr. Cyrus Aidun
School of Mechanical Engineering
Georgia Institute of Technology

Dr. Rudolph Gleason
School of Biomedical Engineering
Georgia Institute of Technology

Dr. Stamatios Lerakis
School of Medicine
The Mount Sinai Hospital

Date Approved: October 28, 2019

Dedicated to my parents, Betty Gaviria and Julio Caballero

ACKNOWLEDGEMENTS

I would first like to thank my advisor, Dr. Wei Sun, for allowing me the opportunity to be a part of such a special group and for the trust you put in me. My time in the Tissue Mechanics Laboratory has included some of the most difficult and enjoyable periods of my life. Dr. Sun introduced me to the field, its pioneers, and an unlimited frontier of possibilities. He always provided me with just the mix of knowledge, experience, and freedom that I needed to succeed. I am beyond thankful for your mentorship throughout. To my thesis committee: Drs. Cyrus Aidun, Stamatios Lerakis, John Oshinski and Rudolph Gleason, you each helped shape my thesis work, providing me with engineering and clinical guidance and experience. I owe a huge debt of gratitude to all of you.

Next, I would like to thank the members of the Tissue Mechanics Laboratory at Georgia Tech, past and present, not only for their critical feedback to this work, but also for their friendship and perspective: Dr. Wenbin Mao, Dr. Caitlin Martin, Dr. Qian Wang, Dr. Thuy Pham, Fatiesa Sulejmani, Dr. Liang Liang, Dr. Tongran Qin, Dr. Anastassia Pokutta, Minliang Liu, Kyle Murdock, Dr. Haofei Liu and Dr. Hai Dong. You all made this work fun and rewarding, I would never have reached this point without you. Among so many of you, I must acknowledge in particular Dr. Wenbin Mao for his guidance, time and effort. I would also like to thank my undergraduate researchers, especially Brian Barrett, Michael Moon, Samantha Kodikara and Eric Beer. You each contributed meaningfully to the completion of this thesis. It was a pleasure working alongside you, struggling, learning, and achieving together.

I am grateful to our collaborators Drs. Raymond McKay M.D. and Charles Primiano M.D. from the Hartford Hospital, CT for their invaluable clinical insights and their unwavering support of my research. I would like to specially acknowledge my pre-doctoral fellowship from Fulbright Colombia and the Colombian Department of Science, Technology and Innovation (COLCIENCIAS). The financial support has meant a great deal to me and I appreciate its faith in my research vision.

To my all my Colombian, Latino, Italian, American and non-Latino friends near and far that stood by me for so long, this work and my time in Georgia Tech would not have been as successful and fun without you. Thanks for making Atlanta such an enjoyable place to live. You kept me sane and continued to show me there was light at the end of the tunnel.

To my family: I would not be who I am today without the unconditional support, guidance and love of my mother and father, sister, and all my family members. Leaning on you during these years has meant more than you know. I am beyond blessed to have my family, I love you.

To Karol: You have been the steady force behind my every academic success. The love, generosity and patience you have provided through so many challenges are immeasurable, and I cannot thank you enough. I truly couldn't have done any of this without your love, support and encouragement each step of the way. I love you.

TABLE OF CONTENTS

LIST OF TABLES

LIST OF FIGURES

LIST OF SYMBOLS AND ABBREVIATIONS

AML Anterior Mitral Leaflet

AL-NC Anterolateral Neochordae

APM Anterolateral Papillary Muscle

AS Aortic Stenosis

AV Aortic Valve

BAV Bicuspid Aortic Valve

BEV Balloon-Expandable Valve

BHV Bioprosthetic Heart Valve

CFD Computational Fluid Dynamics

CVD Cardiovascular Diseases

FE Finite Element

FSI Fluid-Structure Interaction

LA Left Atrium

LH Left Heart

LV Left Ventricle

LVOT Left Ventricular Outflow Tract

LVEF Left Ventricular Ejection Fraction

MA Mitral Annulus

MR Mitral Regurgitation

MS Mitral Stenosis

MV Mitral Valve

NC Neochordae

PL-NC Posterolateral Neochordae

PM Papillary Muscle

PML Posterior Mitral Leaflet

PPM Posteromedial Papillary Muscle

SEV Self-Expandable Valve

SPH Smoothed Particle Hydrodynamics

SV Stroke Volume

TAV Transcatheter Aortic Valve

TAVR Transcatheter Aortic Valve Replacement

TEE Transesophageal Echocardiography

TTE Transthoracic Echocardiography

TMVR Transcatheter Mitral Valve Repair

MSCT Multi-Slice Computed Tomography

RF Regurgitant Fraction

RV Regurgitant Volume

SUMMARY

The left heart (LH) is a key player of the cardiovascular system. Diseases of and associated with the left ventricle (LV)-valve complex account for a large share of cardiovascular disease (CVD)-related deaths. As accurate and detailed interrogation of cardiac function has been actively pursued clinically in recent years, computational modeling has emerged as a viable approach to study the LH dynamics in healthy and diseased states. Yet, most of the previous computational investigations have either solved the fluid or structural physics alone, have been limited to idealized or 2D geometries, have adopted linear elastic material models, have focused on a short time frame of the cardiac cycle, or have not incorporated all LH structures. Proper LV-valve dynamics require a balanced interplay between the LV, the left atrium (LA), the aortic valve (AV), the mitral valve (MV) and the blood flow. Thus, blood-leaflet interaction, leaflet coaptation, and flow dynamics into, within and outward of the LV are all critical parameters to investigate, an area where fluid-structure interaction (FSI) computational modeling is required.

The main objective of this dissertation is to model the FSI between the blood flow, the heart valves and the cardiac wall during the entire cardiac cycle in order to improve our understanding of the biomechanics of the LH complex under baseline, diseased and repaired states. First, a novel FSI framework for modeling the 3D LV-valve dynamics will be developed and validated. Aim 1 will involve the creation of physiologic and pathological LH models that incorporate imaged-based cardiac wall motion, anatomically accurate valve geometries, anisotropic nonlinear hyperelastic constitutive models, and human cardiac tissue material properties. Next, these holistic LH models will be used to

better understand the biomechanical challenges facing transcatheter valve technologies that cannot be fully evaluated by finite element (FE) or computational fluid dynamics (CFD) models, or by in vitro studies or medical imaging alone. Thus, Aim 2 will investigate the LH dynamics under various transcatheter MV repair (TMVR) and transcatheter AV replacement (TAVR) procedures. The findings from this study may unfold new perspectives for an improved understanding of cardiovascular pathophysiology, device-host biomechanical interaction, inform treatment strategies, support better device design, and ultimately support improved clinical outcomes.

CHAPTER 1. INTRODUCTION

The LH is a key structure of the cardiovascular system and, when diseased, is associated with a large share of CVD-related deaths (1). After a few decades of research, the clear anatomic, functional and hemodynamic interdependency of the LV-valve complex and the use of various tools to analyze such interactions are well recognized and documented (2). While impressive advances in medical imaging techniques such as magnetic resonance imaging (MRI) and echocardiography now allow the extraction of anatomical details, valve and cardiac motion characteristics, and even time-resolved blood flow data, these imaging modalities on their own are not a predictive tool, only provide an incomplete picture of the LV-valve biomechanical environment, and do not yield detailed information on the loads applied to the valves that arise from the coupled fluid and structure interaction of the cardiac tissues and the blood flow (3). In order to better understand the biomechanics of the LH and significantly impact the diagnosis as well as the treatment of CVD, it is required to supplement clinical observations with computer technologies that allow for a detailed quantitative examination of the dynamics of the LH under physiologic, pathologic and repaired states.

Investigation of cardiac function using computational models is an active research area that encompasses several numerical approaches, which can be broadly categorized into structural-only (FE), fluid-only (CFD), and FSI methods. LV-valve computational studies have provided insights into normal cardiac dynamics (2, 4), the biomechanics underlying LV and valvular diseases (5, 6), and treatment interventions (7, 8). However, previous studies have been limited to idealized geometries, have adopted linear elastic

material models, have been focused only on a short time frame of the cardiac cycle, have not included the complete LH apparatus, and particularly, have either solved the fluid or structural physics alone. FE models, mostly developed to study valve function, assume the hemodynamic pressure load is uniform over the surface of the valve, a factor which has been previously shown to affect full dynamic/transient valve dynamics (3). CFD models on the other hand, yield the non-uniform pressure field across the valve, yet do not account for its deformation, which in turn regulates the complex blood flow patterns into, within and outwards of the LV. FSI allows to accurately model the LH dynamics because the fluid and structural domains are coupled together, and the corresponding dynamics are solved simultaneously (changes in the structural domain affect the fluid domain and vice versa). The pressure load applied to the valve is calculated from the coupling applied to both domains, not from the boundary conditions applied to the model, and is non-uniform. Thus, FSI models can capture the 3D time-dependent intraventricular flow and the transient deformation of the valvular tissue.

FSI modeling of LH dynamics, however, is made challenging by the complexity of the heart morphology, the large deformation experienced by the valve leaflets and the cardiac wall, the nonlinear elastic behavior of the valvular tissue, and the pulsatile hemodynamic loads during the cardiac cycle. Significant progress is still required in the modeling procedures before patient-specific LH models can support professionals in clinical decision-making and device design. Thus, the overall objective of the present research was to develop and implement a LV-valve FSI framework that took into account the coupled interactions between blood flow, the heart valves and the cardiac wall during the entire cardiac cycle, such that LH dynamics in normal, diseased and repaired states can

be accurately modeled. In this context, FSI simulations can provide highly controlled and quantitative analyses of the distinct effects of various working conditions and implantable devices on the coupled LH dynamics, and are thus advantageous over FE or CFD computational models, and complementary to imaging techniques and in vitro models alone. This proposed research will greatly advance the state of the art of cardiac modeling and will lead to more powerful large-scale simulation tools for future managing heart valve diseases of individuals, such as patient-specific modeling for valve design and placement.

CHAPTER 2. BACKGROUND

2.1 Heart anatomy and physiology

The human heart is a muscular organ that generates the force necessary to circulate blood through the entire body. The heart consists of four chambers: the left and right atria (LA and RA), and the left and right ventricles (LV and RV). The right side of the heart pumps blood to the pulmonary circuit, while the left side pumps blood to the systemic circuit. Two valves are located on each ventricle to guarantee the unidirectional blood flow through the heart. The inlet valves are the tricuspid and the mitral (TV and MV), while the outlet valves are the pulmonary and the aortic (PV and AV). This study will focus on the left heart (LH), which refers to the LV, LA, MV, AV and the LV outflow tract (LVOT).

As seen in Figure 1, the events during a normal cardiac cycle can be divided into seven phases. During atrial systole (1), the atria contract ejecting blood into the ventricles resulting in a rise in ventricular pressure. At the onset of systole, which is typically 1/3 of the cardiac cycle, ventricular isovolumic contraction (2) occurs with the closing of the inlet or atrioventricular valves first followed by the outlet or semilunar valves. As the name suggests, the ventricular volume remains constant. In the rapid ejection phase (3), as soon as the pressure in the LV exceeds the pressure in the aorta, the AV opens and blood flows rapidly from the LV into the aorta. Following rapid ejection, the rate of outflow from the ventricle decreases, and the ventricular and aortic pressures start to decrease in the reduced ejection phase (4). At the end of systole, during the isovolumic relaxation phase (5), the ventricular ejection decreases to zero. The ventricular pressure falls below the pressures in the aorta and pulmonary artery, which causes the aortic and pulmonary valves to close

(beginning of diastolic phase). Once the ventricular pressure falls below the atrial pressure the atrioventricular valves open and rapid ventricular filling begins (6). During this period, the flow of blood from the aorta to the peripheral arteries continues, and the aortic pressure slowly decreases. This rapid ventricular filling phase is followed by the reduced ventricular filling phase (7) in which a large portion of filling occurs. The timing of the events can be seen in Figure 1. The diagram show the pressure variations in the LA, LV and the aorta, the LV volume change and the LVOT flow rate throughout one cardiac cycle. The opening and closing events of the valves are indicated with a star.

The AV and MV are more susceptible to diseases and are subjected to a harsher environment than the valves in the right side of the heart, withstanding a pressure gradient of about 80 mmHg and 120 mmHg during closure, respectively. The amount of blood remaining in the LV when the AV closes is defined as the end-systolic volume (ESV), while the volume of blood inside the LV when the MV closes is called the end-diastolic volume (EDV). The total volume of blood ejected during systole is called the stroke volume (SV), and is defined as $SV = EDV - ESV$. In a normal resting adult heart at 75 bpm, systole lasts approximately 270 ms (1/3) and diastole lasts about 430 ms (2/3), having a SV ~ 70-80 ml (9).

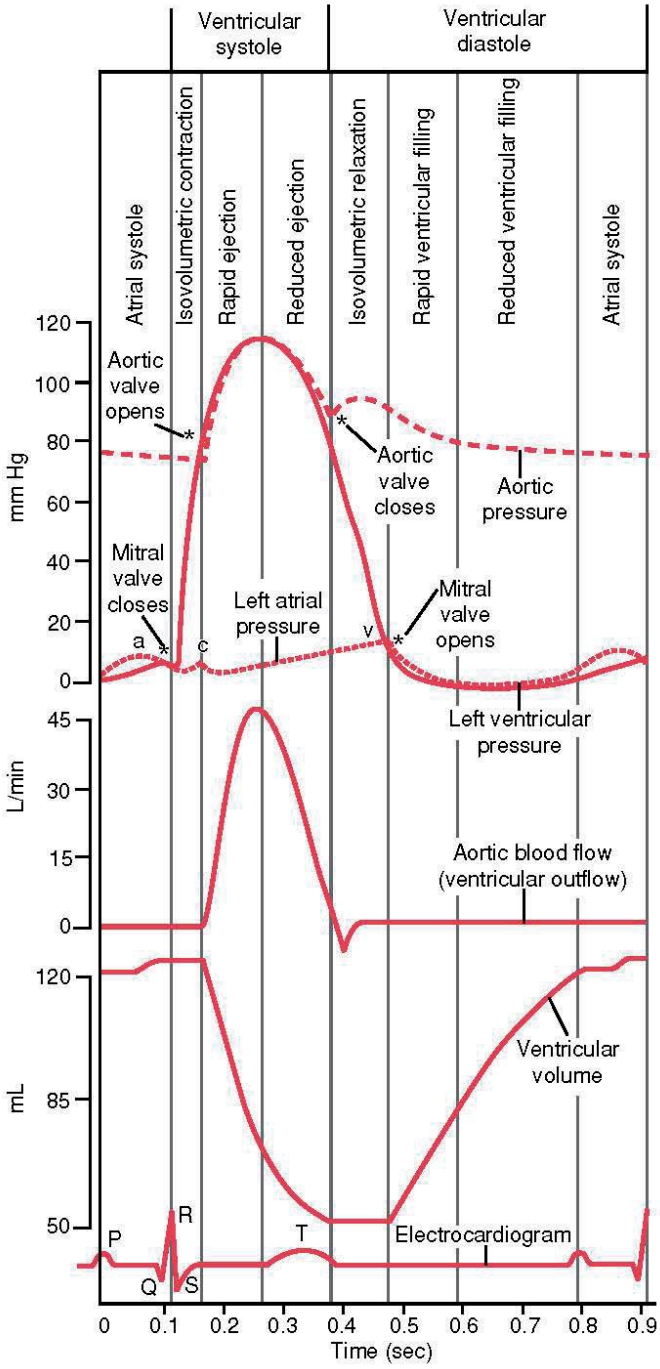

Figure 1. Diagram showing the events occurring in the LH during one cardiac cycle (10).

2.2 Left ventricular blood flow

The LV is not a simple positive displacement pump. The efficiency of such a pumping function is dependent on the interactions between the blood flow, the motion of the cardiac wall, and the proper mechanical function of the heart valves. During diastole, the LV flow is primarily characterized by a strong compact jet that enters the chamber through the mitral orifice. The jet has two distinct pulses: the early-filling wave (E-wave) during ventricular relaxation, followed by the A-wave produced by the atrial contraction. The entering jet has an almost irrotational core surrounded by a shear layer that rolls up and immediately arranges into a compact ring-shaped vortex structure that enters the LV. Moreover, the MV acts as a flow-diverter, creating blood flow patterns characterized mainly by an asymmetric vortex. This asymmetric structure is considered to act as a reservoir that stores kinetic energy as it redirects blood towards the lateral LV wall and initiates MV closure and pre-ejection filling of the LVOT in early systole (11, 12) (Figure 2). The loss of this vortical circulation has been associated with loss of energy, higher risk of thrombogenesis, and less efficient overall work (13, 14).

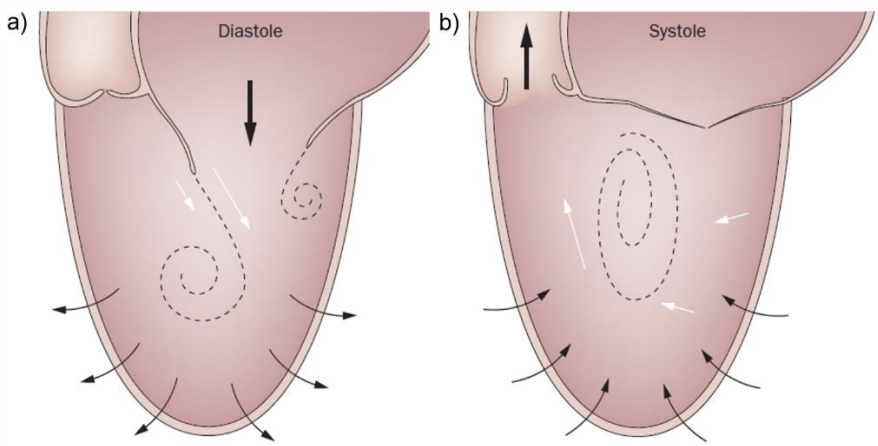

Figure 2. Blood flow patterns during a) diastole and b) systole (12).

2.3 The mitral apparatus

The MV, a key player in cardiac function, requires all of its components in order to work properly: the mitral annulus (MA), the two mitral leaflets, the papillary muscles (PM) and the chordae tendineae (abbreviated chordae); together they are called the mitral apparatus (Figure 3a). The MA is a ring of fibrous tissue which surrounds and supports the mitral orifice and anchors the two leaflets. The shape of the annulus approximates a hyperbolic paraboloid, often described as a 3D saddle shape. Studies indicate that the saddle shape of the annulus plays an important role in optimizing chordal force distribution (15) and reducing leaflet stresses (16). The MV and AV share a common fibrous boundary, as shown in Figure 3b. The anterior MA is flanked by the right and left fibrous trigones separated by a rigid span of fibrous tissue, the intertrigonal region. The anterior MA is anatomically coupled to the aortic annulus. This confluence is usually referred to as

the aortic-mitral curtain or intervalvular fibrosa (17). Normal physiological function of either of these two valves involves the complementary function of the other.

The MV consists of two leaflets: the anterior (AML) and posterior (PML) mitral leaflets. They are indented at two points and these indentations are known as commissures. The AML is adjacent to the LVOT and occupies 1/3 of the annular circumference, whereas the PML occupies the rest. During valve closure, the leaflets will fold towards each other, forming a closed seal called the coaptation zone. Most commonly, surgeons adopt the suggestion of Carpentier (18), who labeled the functional components of the valve in alphanumeric fashion with the posterior scallops named P1 to P3, and opposing anterior segments named A1 to A3 (Figure 4). The anterior commissure is located where both leaflets free edges join in the A1 and P1 area, while the posterior commissure is located where both leaflet's free edges join in the A3 and P3 area.

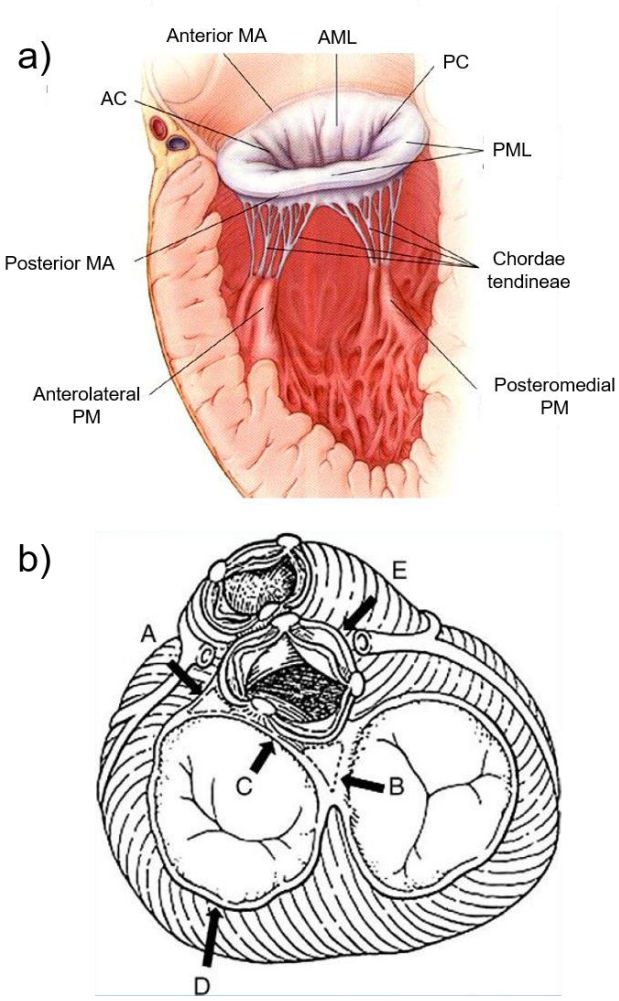

Figure 3. a) Mitral apparatus (adapted from (19)), b) the anterior MA is flanked by the left (A) and right (B) fibrous trigones. The confluence of the MA (C) and the aortic annulus (E) is called the aortic-mitral curtain (adapted from (20)).

The subvalvular apparatus lies completely in the LV and is composed by the PM and the chordae (Figure 3a). The PM are cone-shaped muscles extending upward from the ventricular free wall and into the LV cavity. There are two PM: the anterolateral PM (APM) and the posteromedial PM (PPM). The chordae are string-like fibrous structures that extend from the tips of the PM and insert into the ventricular surface of the mitral leaflets. The

chordae divide into branches, with 15-32 major chordae trunks arising from the PM (21). The main function of the subvalvular apparatus is to prevent the valve leaflets from being everted into the LA when the ventricle contracts. During systole, the PM contract to tighten the chordae tendineae. The forces exerted by the leaflets on the chordae are transferred to the PM, hence they have an essential load-bearing role.

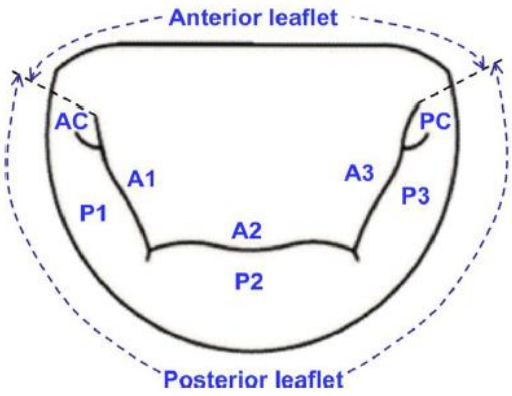

Figure 4. Labeling convention for the various regions of the mitral leaflets (adapted from (22)).

2.4 Mitral regurgitation

MV disease is the most common valvular disease(23). Mitral regurgitation (MR) occurs when the MV does not close completely during systole. The current prevalence of moderate to severe MR in the U.S. is estimated to be 2 to 2.5 million(24). Additionally, a significant portion of the patient population that experiences MR is elderly: The AHA reports that of all patients aged 75 and above, 9% present with some form of MR (25). Causes of MR are divided into two different categories: primary (degenerative) and secondary (functional). Primary MR includes malformations or abnormal tissue properties of valve components.

Morphologic changes may include connective tissue deficiency or excess. Rupture or elongation of one or more chordae is usually observed (26). Consequently, primary MR almost always exhibits one or more locations of leaflet flail or prolapse into the LA (Figure 5).

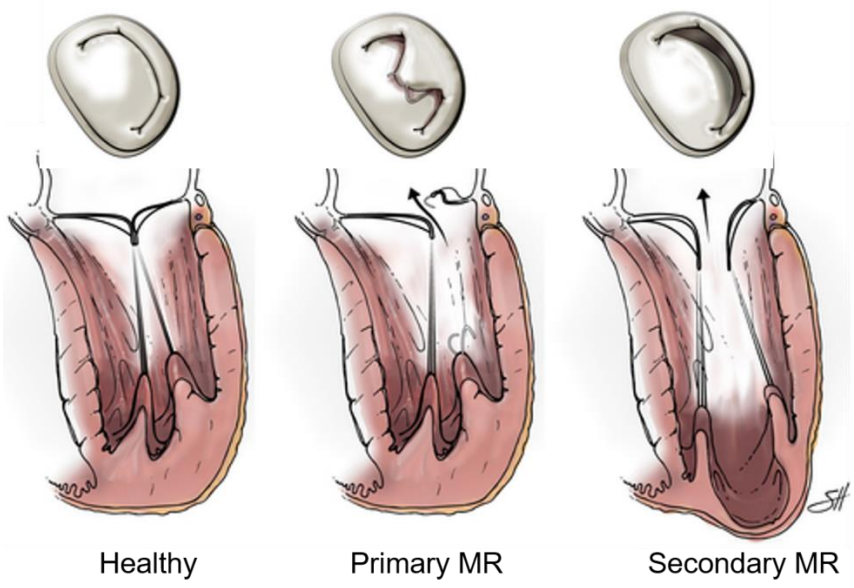

Figure 5. Normal, prolapsed and leaking MV (adapted from (27)).

Secondary MR, on the other hand, occurs when regurgitation is secondary to a disease of the LV. Secondary MR is typically caused either by ischemia or other disease-related dilation of the LV, and is associated with a doubling in mortality among patients with mild or greater degrees of MR following a heart attack (28). In ischemic MR, LV remodeling after myocardial infarction results in PM displacement, causing systolic tenting of the MV (Figure 5). Global LV ejection fraction (LVEF) may or not be reduced; as regional wall motion abnormalities with remodeling may result in sufficient MV tethering to cause severe MR, despite preserved LVEF (29). Symmetric or asymmetric leaflet

tethering may occur. Symmetric tethering is usually associated with global systolic dysfunction with a central regurgitant jet. Asymmetric tethering most frequently results from tethering of the PML which is associated with an akinetic or hypokinetic posterolateral segment of the LV myocardium, resulting in a posteriorly directed asymmetric regurgitant jet into the LA (30). MA dilation typically occurs late in the pathophysiology of secondary MR, and is often asymmetric with greater involvement of the posterior MA (31). Significant MR eventually leads to volume overload and enlargement of the LV, in order to accommodate both the SV and the regurgitant volume with each heartbeat. There can also be an enlargement of the atrial chamber and an increase in the pressure. The increased atrial pressure can lead to pulmonary congestion and edema. Over time, further LV enlargement may not adequately address these demands, leading to reduced LVEF. If left untreated, moderate to severe MR can lead to heart failure (26).

Table 1 shows the quantitative parameters recommended by the American College of Cardiology/American Heart Association (ACC/AHA) to evaluate MR and its severity (1). Echocardiography with Doppler is currently the method of choice for the detection and evaluation of the severity and etiology of valvular regurgitation (32). 2D echocardiography allows an evaluation of the valvular structure as well as the impact of the volume overload on the cardiac chambers. Structural parameters including LA and LV size, MV leaflet and support apparatus are examined through 2D echo and signs such as leaflet calcification, tethering, flail motion or vegetation, enlarged LA or LV and ruptured PM can give indirect clues as to the severity of regurgitation. Color flow Doppler provides three methods of quantifying MR severity including regurgitation jet area, vena contracta and flow convergence or proximal isovelocity surface area (PISA). Continous wave Doppler signal

provides information on the velocity profile and density which is a qualitative index of MR severity. Pulsed Doppler tracings at the mitral leaflet tips are commonly used to evaluate LV diastolic function while Pulsed Doppler evaluation of pulmonary venous flow is a useful adjunct to evaluating the hemodynamic consequences of MR (32). While the quantitative and qualitative information described above can be measured by both transthoracic echocardiography (TTE) and transesophageal echocardiography (TEE), TEE has higher resolution, multiplane capabilities, and proximity to the MV which makes vena contracta imaging and PISA easier and more accurate.

Table 1. Classification of MR severity in adults from ACC/AHA guidelines (1).

Degree of MR	Regurgitant fraction	Regurgitant Orifice area
Mild	< 20%	
Moderate	20 – 40%	
Moderate to severe	40 – 60%	
Severe	> 60%	> 0.4 cm^2

2.5 Corrections for mitral regurgitation

Surgical MV repair or replacement is indicated in patients with severe MR and symptoms, or LV dysfunction (LVEF < 60% or LV end-systolic diameter > 40 mm) (26). There are different surgical repair options for the MV including, but not limited to: annuloplasty ring implantation, edge-to-edge repair, leaflet resection and neo-chordae implant. An annuloplasty ring is a prosthetic ring designed to restore normal MA shape and prevent future dilation (33). A ring is typically sutured in combination with another repair technique, as it reduces the tension on sutures used in leaflet and chordae repairs (33). There are many different ring designs that vary in shape (flat vs. saddle), stiffness (rigid

vs. semi-rigid vs. flexible), and length (closed vs. partial ring). Moreover, since the MA size varies between patients, the rings come in multiple sizes. The edge-to-edge repair technique, on the other hand, involves suturing the free margin of the prolapsing or flail leaflet with the corresponding edge of the normal opposing leaflet. As seen in Figure 6, there are two types of repairs: double-orifice stitch (central leaflet correction) and single orifice stitch (paracommissural leaflet correction) (34). The non-physiological dual-orifice geometry of the central leaflet correction remains a concern in regards to long-term durability, and is a topic of active investigation.

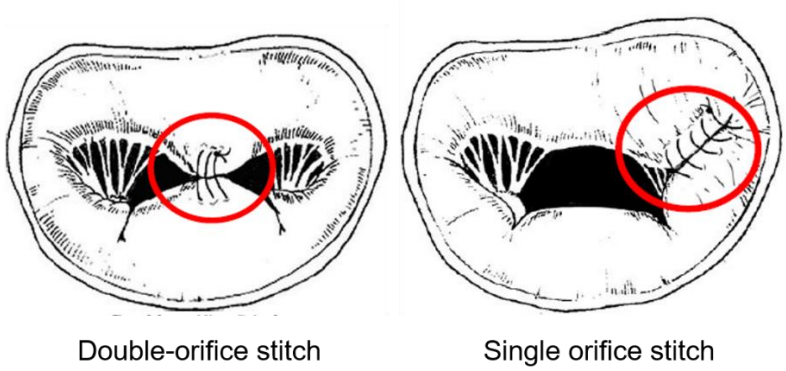

Figure 6. Edge-to edge MV repair (adapted from (35)).

There also exist several options for surgical MV replacement, although there is some debate as to which method of treatment is superior (36). Yet, cardiac surgeons are more likely to perform surgical MV replacement with the primary reason that many physicians do not have the experience and specialized skills to consistently repair the MV in complex MR cases (37, 38). Additionally, many patients – especially these elderly patients previously mentioned – present with significant comorbidities or LV dysfunction

that is severe enough such that they are not referred for conventional surgical treatment (39). It is therefore becoming increasingly relevant to develop minimally invasive repair and replacement devices to treat MR. The approaches for transcatheter MV repair (TMVR) are diverse and include indirect or direct annuloplasty, neochordae implantation and the MitraClip device (Abbott Vascular, Santa Clara, CA), which mimics the surgical edge-to-edge technique. In current clinical practice, TMVR is mainly limited to the MitraClip device, as other techniques are currently at the experimental or first-in-human stages. In the U.S. and Europe, the MitraClip is approved for use in patients with primary and functional MR who have severe symptoms and are at high or prohibitive risk of surgery.

2.6 Transcatheter aortic valve replacement and concomitant mitral regurgitation

Aortic stenosis (AS) is the most prevalent valvular heart disease referred for treatment. First reserved for inoperable and patients at high surgical risk, transcatheter AV replacement (TAVR) has been expanded to patients with symptomatic intermediate- and low-risk (40), with the advantages of less trauma and shorter recovery time, and thus it is fundamentally changing the current paradigm of AV replacement. Since the first-in-human implantation in 2002, there has been explosive growth in its use throughout the world.

Significant MR is common in patients with severe AS (41). In these cases, MV repair or replacement is generally performed at the time of surgical aortic valve replacement (SAVR) (42, 43). However, concomitant MR in TAVR patients is typically left untreated (44). The hallmark TAVR PARTNER trial reported incidences of moderate to severe MR of 19.8% and 22.2% in cohort A (comparison of TAVR to surgical replacement) and B (comparison of TAVR to standard therapy) patients, respectively. The

persistence of moderate-to-severe MR following TAVR is therefore a relatively new and important entity. The management of patients with severe AS and concomitant MR is challenging, mainly because the AV and MV share a common fibrous boundary and the two valves function in a reciprocal interdependent fashion. Thus, MV function could be altered after TAVR by displacing the aortic-mitral curtain (Figure 3b). Some studies have shown that MR severity improved in about 50% of patients who received TAVR (45, 46). On the other hand, MR severity remained unchanged or even worsened in a significant number of TAVR patients (47-52). Moreover, different degrees of MR improvement with the use of the self-expandable Medtronic CoreValve system compared to the balloon-expandable Edwards SAPIEN valve have been suggested (49, 53). These confounding results indicate a pressing need to develop engineering methods to improve our understanding of the coupling TAVR-MR biomechanics and predict MR changes following TAVR.

2.7 Bicuspid aortic valve disease

Bicuspid AV disease (BAV), a malformation of the AV in which only two leaflets form instead of the normal three, is the most common congenital cardiac anomaly, occurring in 0.5% to 2% of the general population (54). In the U.S. alone, approximately 4 million people are afflicted with BAV (55). BAV is characterized by a marked phenotypic heterogeneity of valve morphology. It is not simply the fusion of 2 leaflets, but a more complex process involving the leaflets, sinuses, commissures, and position of the coronary orifices(56). The fusion of two leaflets forms a ridge, called a raphe, the presence and position of which contributes to the variability of morphology. Several classifications of BAV morphology exist. As seen in Figure 7, Sievers and Schmidtke (56) proposed a

system based on 3 characteristics: the number of raphes, the spatial position of the leaflets or raphes, and the functional status of the valve. Briefly, type 0 was assigned to morphologies characterized by the presence of two symmetric leaflets and 1 commissure without evidence of a raphe. Type 1 was assigned to valve morphologies with one raphe, and type 2 when two raphes were present.

BAV is recognized as a risk factor underlying many significant clinical consequences including: valvular calcification and stenosis, regurgitation, infective endocarditis, aortic dilation, and dissection (54). Most prominently, BAV patients account for nearly 50% of all AS cases (57). Despite the extensive experience with TAVR technology, BAV stenosis has been considered a relative contraindication for TAVR due to the numerous technical challenges related to bicuspid anatomy, including extreme and asymmetric calcification, heterogeneity of leaflet morphology, the presence of a densely calcified raphe, and aortopathy. The asymmetrical and heavy calcification of the BAV leaflets may prevent uniform or adequate expansion of the valve frame and affect valve hemodynamics and long-term durability, leading to higher transvalvular gradients and paravalvular leak (PVL). The risk of aortic dissection or rupture during TAVR is theoretically increased in the presence of aortic disease. BAV stenosis has therefore been an exclusion criterion in the randomized clinical trials of TAVR. Indeed, the Instructions for Use issued by the FDA for TAVR specify that the safety and effectiveness of TAVR in bicuspid AS is not yet established. Despite these concerns, BAV stenosis is increasingly being treated with TAVR under “off-label-use”, and there is a fundamental need for the understanding of the biomechanics involved in TAVR-in-BAV.

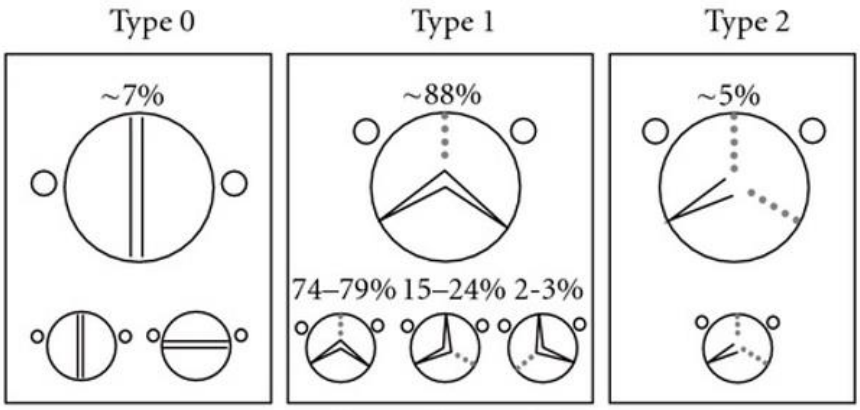

Figure 7. BAV classification. Dotted line shows the raphe position (adapted from (58)).

2.8 Left ventricle-valve computational modelling

Blood flow-leaflet interaction, leaflet coaptation, and flow dynamics into, within and outward of the LV are critical parameters to investigate in the study of LH dynamics. Yet, few modeling studies have integrated either the AV or the MV with the LV into a single model (59-61), particularly with FSI (62, 63). Reasons for this include: 1) the complex LV-valve geometries, especially the connection between the mitral subvalvular apparatus and the LV, and the aortic-mitral curtain, 2) the strong coupling between the large deformation of the nonlinear elastic structure of the leaflets and the blood flow, 3) challenges when modeling complete valve closure, where the flow domain is separated into two unconnected regions, 4) difficult choices of boundary conditions, 5) limited human tissue material properties, and 6) large computational resources required by these simulations.

From the few LV-valve FSI models that have been developed, the earliest is credited to Peskin and McQueen's pioneering work in the 1970s (64-66) using the classical

immersed boundary (IB) approach (67). Using this same method, Yin et al. (68) investigated fluid vortices associated with the LV motion as a prescribed moving boundary. Chandran and Kim (8) also reported the MV dynamics in a simplified LV chamber model during diastolic filling using an immersed interface-like approach. Recently, Gao et al. (69) presented an integrated LV-MV model using an IB-FE approach with myocardial active contraction. Some of the key limitations of these coupled models were the idealized representation of the LV and the mitral apparatus, and the complete omission of the AV geometry, which can add uncertainties in the simulation results.

2.8.1 Mitral valve computational modelling

Computational models of the MV have been developed for several decades, starting from the simplified 2D approximation to 3D models, and to multi-physics/scale models (60, 70-75). Most of the previous studies were based on structural-only and quasi-static analyses applicable to a closed valve (6). However, complete MV function during the cardiac cycle cannot be fully assessed without modeling the FSI between the valve, the proximal cardiac wall and the blood flow (6, 76). From the MV studies that have included the LV but not FSI, Wenk et al. (59) developed a FE model using MRI images from a sheep with moderate MR after myocardial infarction. This model was later extended to study MV stress distributions using a saddle shaped and asymmetric mitral annuloplasty ring (77). A more complete whole-heart model was later developed in the Dassault Systèmes' Living Heart project (78) to simulate MR caused by infarction of the posterior PM. The model included four ventricular chambers, cardiac valves, electrophysiology, and detailed myofibre and collagen architecture. Using the same model, the effects of different annuloplasty rings were studied by Rausch et al. (79). However, these investigations did not account for FSI.

Because of the complex interactions between the MV leaflets, the sub-mitral apparatus, the cardiac wall, and the associated blood flow, most MV FSI studies to date have been carried out without the integration of the LV. Kunzelman, Einstein and co-workers first simulated normal and pathological MV function by positioning the valve into a straight tube (80-82). Using a similar modeling approach, Lau et al. (3) compared MV dynamics with and without FSI, finding that valve closure configuration differed when using the FSI model. Over the last few years, a number of FSI models using the IB method have studied the flow across the MV (83-85). In a series of studies, Toma et al. (86-88) developed a SPH-based FSI MV model based on an in vitro experimental system to study the function of the chordae structure under normal and ruptured states. However, none of the aforementioned FSI models accounted for the MV interaction with the LV complex. Indeed, Lau et al. (3) found that even with a fixed U-shaped ventricle, the flow patterns are substantially different from those estimated using a tubular geometry. Despite the advancements in computational modeling techniques when modeling isolated MV (6, 75) or LV dynamics (89-91), it has remained a challenge to develop an integrated LV-valve FSI modeling framework that can handle the complex valve geometry, large leaflet deformation, and nonlinear and anisotropic material of the tissue.

2.8.2 Mitral valve repair computational modelling

In relation to computational modeling of MV repair procedures, to the best of our knowledge, the only LV-valve FSI model developed to study MV repair (edge-to-edge technique) had important simplifications regarding the geometry and the dynamics of the boundaries, including a rigid U-shaped LV geometry and the complete omission of the AV (92). On the other hand, several MV repair techniques have been simulated using FE

analysis in order to better understand the biomechanics of the valve in such states. The first FE analysis of the edge-to-edge intervention was by Votta et al. (93), where the effects of varying the suture length in MV models with different levels of annular dilation were studied. It was found that the principal stresses at systole did not differ significantly between the pre- and post-repaired models. However, during diastole the stresses in the repaired MV model were found to be similar in magnitude to the diseased model in systole. The combined effects of lateral suture positioning, length of the suture and severity of annular dilation have also been examined. Dal Pan et al. (94) created a MV model with the leaflets in a semi–closed configuration, with the free margin of the leaflet constrained simulating the effect of a suture. Suture position ranged from the center, forming two orifices, to adjacent to a commissure, forming one orifice. The different annulus sizes varied from larger than normal, as in a diseased state, to a contracted annulus, as if an annuloplasty ring had been implanted. The MV model by Avanzini et al. (95) used a similar initial configuration as the study by Dal Pan and colleagues, but suture positions included central, commissural and half-way. More recently, Mansi et al. (96) developed an integrated FE framework for edge-to-edge simulation on 25 patient-specific anatomical models. Comparisons between the simulated closed valve and 3D TEE images showed encouraging results. These studies provided useful analyses for technique improvement and optimization, and paved the way to quantitative and systematic evaluation of computational models of MV repair.

As MV prolapse following rupture of the chordae is a major cause of MR, artificial chordae implantation by ePTFE sutures has become an established conservative surgical technique to treat this disease. Kunzelman and colleagues (97, 98) were the first to study

the effect of chordae rupture and their replacement (variations in number, size, and length) on MV function. FE results showed that in the diseased state, the principal stresses in the mitral leaflets are comparable to the normal state. Although replacement of the chordae with stiffer neo-chordae restores the magnitude of the principal stress to the normal state, stress concentrations are induced at the location of the chordae due to a mismatch in stiffness. These localized peaks, however, can be minimized by increasing the number of artificial chordae.

More recently, by developing a MV model using 3D TEE data in a patient with posterior chordae rupture, Kim and colleagues (99-101) studied the effect of chordae replacement on restoring MV function. Large stresses were found in the neighboring intact posterior leaflet tissue and chordae of the MV model with ruptured chordae, and these large stresses were markedly reduced when chordae replacement was performed. Similarly, Sturla et al. (102, 103) created a MV FE model to investigate the biomechanical effect of five different neo-chordae implantation techniques for the repair of isolated posterior mitral leaflet prolapse. Four patient-specific MV models were created based on cardiac MRI and integrated with intraoperative surgical details to assess the location and extent of the prolapsing region. Leaflet geometry, coaptation area, and stresses across native chordae, ePTFE sutures and regions of the posterior leaflet were compared between models. Simulation results demonstrated that all repair types corrected MR by restoring leaflet coaptation, and redistributed stress across the valve leaflets and prosthetic chordae, relieving excessive mechanical stress on the mitral leaflets. The models with more than one neo-chordae resulted in the greatest redistribution of stress across the repaired area of posterior leaflet. It was determined that suboptimal suture length can alter the chordae

forces and leaflet stresses, which may be key parameters in determining the long-term outcome of the MV repair.

Although many different types of MV annuloplasty rings are commercially available, most clinical experts agree that proper ring selection and sizing present substantial challenges, and if performed incorrectly – can lead to a suboptimal clinical outcome. Early studies by Kunzelman et al. (104) developed FE models of the normal and dilated MV to simulate the effects of flexible and rigid annuloplasty rings. Although it was found that both rings improved leaflet coaptation, the flexible ring further reduced leaflet and chordal stresses. Subsequently, Maisano et al. (105) showed that the dog bone–shaped ring with selective reduction in the septolateral dimension is more effective than a standard D-shaped ring for treating leaflet tethering in functional MR. Votta et al. (106) also reported a comparative study between the commercial Physio and the Geoform annuloplasty rings. However, these studies were conducted on a generalized MV model and excluded or simplified the LV geometry. Recent advances were made, for example, by Wong et al. (77), who used a MRI-based ovine MV-LV model to investigate the effects of saddle-shaped vs. asymmetric annuloplasty rings. It found that all rings were capable of restoring normal valvular geometry and eliminating MR when properly implanted.

By using 3D echo images, Xu et al. (107) reconstructed MV models to examine how leaflet coaptation area, noncoapted leaflet area, and interleaflet coefficient of friction affect leaflet and chordal stress distribution. The results indicated that MV repair techniques that increase or preserve noncoapted leaflet area might decrease stresses, and thereby enhance repair durability. Morrel et al. (108) also developed human MV models, and investigated on leaflet coaptation as well as on valvular, annular and suture stress

distributions for three different ring shapes. It was shown that all rings increased leaflet coaptation and reduced stress across the MV leaflets, however, saddle-shaped prostheses were the most effective, as were smaller sizes across all ring shapes. Stevanella et al. (74) created a patients-specific MV model using cardiac MRI, while Choi et al. 22 (109) used 3D TEE. In both FE studies, restoration of leaflet coaptation was achieved. In general, the ring itself is not physically modeled, but approximated by fitting the mitral annulus to the shape of the ring. Measurements of the effectiveness of the ring implantation include: overall post-ring-implantation MV morphology, length of leaflet coaptation, regurgitant area, and stress distribution across the mitral leaflets.

2.8.3 Transcatheter aortic valve replacement computational modelling

In the last decade, computational models have been increasingly and extensively used for the simulation of TAVR. Capelli et al. (110) and Wang et al. (111) were among the first groups to perform patient-specific FE analyses of TAV deployment. These analyses showed that patient-specific geometries induce asymmetric stress distributions on the device and tissue, and impact a particular patient's risk of PVL, coronary occlusion, and rupture (112). Auricchio et al. (113), Gunning et al. (114), and Morganti et al. (113) have since shown that TAV leaflets may become distorted when the device is deployed within a realistic rather than an idealized and circular aortic root geometry. Thus, patient-specific analyses are important for predicting device function in addition to device-tissue interactions. Device positioning to align the TAV commissures with the native AV commissures may also be important for reducing TAV leaflet stresses and consequently achieving a durable result (114). More sophisticated FE models which included the calcification along with the aortic root and valve leaflets have demonstrated that the extent

and location of calcium deposits significantly affect the stent expansion process and a patient's risk of aortic root rupture during deployment (112, 115-117). Sturla et al. (118) investigated the impact of different calcification patterns on TAVR outcome. High stresses acting on calcium deposits may be a risk factor for embolization of calcific material.

More recent FE models have been applied to new-generation TAVR devices with improvements on the modeling accuracy, including precise 3D geometry of TAV through micro CT scanning (119, 120), crimping (121, 122), delivery apparatus (123), comparison against post-procedural clinical data (124, 125), and population-specific response (124-126). Bosi et al. (124) studied TAVR with the SAPIEN XT in 14 patients. Implantation site material parameters were adjusted and optimized using an experimental approach. Bailey et al. (123) simulated SAPIEN XT deployment into a patient-specific aortic root model with different orientations. It was found that the preferred orientation of the TAV leaflets is the one aligned with the native AV leaflets. Hopf et al. (126) quantified the contact forces between the implanted Nitinol stent and the host for 46 patients with the Medtronic CoreValve. Comparison of systolic and diastolic data revealed slightly higher contact forces during diastole. By analyzing clinical outcomes, an increase in mean force was associated with higher incidents of PVL and the need for a permanent pacemaker. Bianchi et al. (127) evaluated the effect of various TAV deployment locations on procedural outcome by assessing the risk for valve migration. Proximal deployment led to lower contact area, which poses an increased risk for valve migration. It was also demonstrated by Bailey et al. (122) that including the TAV leaflets in the simulation has only a marginal impact on the results. Regarding TAVR CFD simulations, PVL was numerically evaluated under steady-state (128) and transient (129-132) conditions. Flow

patterns variations in the aortic root-induced by TAVR (133) and the relation between valve thrombosis and reduced leaflet motion has also been investigated (134).

In the first TAVR FSI studies, only the coupling between blood and the aorta, or blood and the AV was considered. In the first study, TAV design was evaluated, neglecting the native valve leaflets and calcification (135). On the second study, a comparison between FE and FSI results on an idealized TAV was performed, confirming a more realistic representation of the valve when applying the FSI method (136). TAVR was also compared to the conventional surgical AV replacement in terms of leaflet stresses and thrombogenic profile (137). Up to now, only two FSI investigations have modeled the complete TAVR procedure (138, 139). In both studies, the deployment of the complete device, frame, leaflets, and skirt was performed. However, the patient-specific domain was simplified by considering the aorta as a rigid part or with a linear elastic material law. In both cases, the native AV and calcification were neglected, and the boundary conditions applied to the fluid domain were not patient-specific. Although a significant portion of AS patients referred for TAVR have concomitant MR, the biomechanical effects of TAVR on aortic-mitral coupling and MR severity are largely unknown. To the best of our knowledge, there is no computational (or experimental) study that has investigated the impact of TAVR on MR. Thus, development and application of the LV-valve FSI modeling framework to investigate the effect of TAVR deployment on MR severity as proposed in this study would represent a significant advancement in the field.

CHAPTER 3. OBJECTIVE AND SPECIFIC AIMS

CVD are the leading global cause of death, accounting for >17.9 million or 31% of all deaths per year (1). As a key structure of the cardiovascular system, the LH constitutes one of the most important and challenging domains to study, due to its significance in the initiation and propagation of numerous CVD (1). In particular, the balanced interplay between the LV, LA, MV, AV and the blood flow plays a fundamental role in the structural and functional integrity of the heart. In the U.S. alone, the prevalence of moderate-to-severe AS in patients ≥75 years old is 2.8%, while the prevalence of at least moderate MR is 9.3% (140). When the functioning of a heart valve is sufficiently impaired, surgical or transcatheter valve repair/replacement is required. As valve diseases remain a major medical problem due to their close link to cardiac dysfunction leading to morbidity and premature mortality (140), an improved understanding of physiological and pathological LV-valve biomechanics is critical to unfold new perspectives on LH function, as well as for the evaluation, selection and optimization of next-generation transcatheter technologies aimed at restoring baseline LV-valve functioning.

Investigation of patient-specific cardiac dynamics using computational models is an active research field that holds promise for the improved understanding of cardiac function in healthy and diseased states. A comprehensive computational assessment of LV-valve dynamics, however, is challenging and requires a FSI modeling approach in order to capture the complex coupling between the large deformation experienced by the heart valves and the cardiac wall, the anisotropic nonlinear elastic behavior of the valvular tissue, the pulsatile hemodynamic loads throughout the cardiac cycle, and the large inter-subject

variability in the cardiac anatomy. A number of computational studies have seek to shed some light on the LV-valve biomechanics (2, 4, 8, 76), yet, most of these studies have either solved the fluid or structural physics alone, have been limited to idealized or 2D geometries, have adopted linear elastic material models, have focused on a short period of the cardiac cycle, or have not included the complete LH complex. With these challenges in mind, the main objective of this dissertation is to model the FSI between the heart valves, the blood flow, and the cardiac wall during the entire cardiac cycle in order to improve our understanding of the LH dynamics under healthy, diseased and repaired states. This will be achieved through the following specific aims:

Specific Aim 1: Develop a novel FSI computational framework for modeling LV-valve dynamics. A FSI framework that combines smoothed particle hydrodynamics (SPH) and nonlinear FE method will be developed to describe the coupled bulk blood flow phenomena and the heart valves structural response of the LH complex throughout the cardiac cycle. This aim will involve the development of healthy and pathological LV-valve models that incorporate imaged-based cardiac wall motion, anatomically accurate valve geometries, nonlinear hyperelastic constitutive models, and human age- and gender-matched material properties. The LH models will be validated against in vivo phase contrast magnetic resonance (PCMR) imaging and echocardiography data, as well as to a traditional CFD numerical method. The validated LH FSI models will be used in Aim 2 to better understand the biomechanical challenges facing minimally-invasive AV replacement and MV repair procedures that cannot be fully evaluated by structural-only or fluid-only computational models, or by in vitro studies or medical imaging alone.

Specific Aim 2: Investigate the LV-valve dynamics under transcatheter MV repair (TMVR) and transcatheter AV replacement (TAVR) procedures. As TAVR is now the standard-of-care treatment for inoperable patients and the preferred treatment option for high-, intermediate- and low-risk patients with severe AS, there is a pressing need to improve our understanding of TAV-host interactions in more challenging scenarios, such as in patients with concomitant significant MR and BAV stenosis. Moreover, encouraged by the success of TAVR, cardiology is shifting focus toward the next major frontier in structural heart intervention: TMVR. This aim will: 1) Investigate the biomechanical effect of various TMVR technologies such as neochordae implantation, MitraClip edge-to-edge repair, and annuloplasty ring implantation on restoring baseline LH dynamics, and 2) Evaluate the biomechanical impact of TAVR on MR severity. More specifically, we will examine the effect of TAV type and implantation height on aortic-mitral coupling, and the potential to improve or worsen MR severity immediately after TAVR. Altogether, a quantitative mechanistic evaluation of LV-valve dynamics in the setting of MR and AV stenosis is not only expected to unfold new perspectives for the improved understanding of cardiac pathophysiology, but may eventually inform the therapeutic decision-making process and provide insight into patient-specific surgical planning and better device design, ultimately supporting improved clinical outcomes.

CHAPTER 4. SPECIFIC AIM 1A – PART 1, PHYSIOLOGIC LV BLOOD DYNAMICS

4.1 Introduction

Investigation of cardiac flow using CFD is an active research area that encompasses several numerical approaches, which can be broadly categorized into mesh-based methods and mesh-free methods. Most numerical LV studies to-date are based on mesh-based methods such as the arbitrary Lagrangian–Eulerian (ALE) approach (141) or the IB method (64). In general, complex geometries, boundaries with large deformations, and moving interfaces involved in the study of LV blood flow remain a major challenge for mesh-based methods (142).

To overcome these limitations, a new generation of numerical methods called mesh-free methods have been developed and adapted in recent years. Mesh-free methods are based on a Lagrangian approach instead of the Eulerian approach, therefore the continuum medium, such as blood, is discretized as a set of particles distributed over the solution domain without the need of a spatial mesh (143). In particular, the SPH method, created originally to simulate compressible flows in astrophysics (144), is a versatile fully Lagrangian approach that has been applied extensively to study a variety of physical phenomena (145-149).

While SPH or other mesh-free methods have been successfully used for blood flow simulations before, the majority of these studies have focused on vascular hemodynamics (150-152), which are far simpler than that of the heart. To date, a limited number of studies

have used SPH to study cardiac blood flow (86, 153-155). Shahriari et al. (156) presented the first work demonstrating the capability of SPH to simulate the intraventricular blood flow in a simplified LV model. In this study, the SPH code and methodology were validated against two benchmark cases, and then combined to simulate pulsatile flow in a rigid LV model. Although this study clearly demonstrated the ability of SPH to simulate the LV flow dynamics, the main limitations associated with this study were the assumption of a 2D geometry and a rigid LV model.

Although SPH is a relatively new tool in the study of cardiac flow, this method is attractive for simulating the FSI phenomenon involved in the LV blood flow. Due to its capability to handle complex geometric motion, SPH is particularly useful to model the complex LV-valve dynamics that involves nonlinear large deformations during the entire cardiac cycle with flow fragmentation during valve closure. However, there are some inherent limitations associated with SPH. For example, modeling of wall boundary conditions is non-trivial for SPH, requiring some special treatments such as placement of fixed ghost particles outside the computational domain (157, 158). Additionally, turbulence modeling has not been well developed in SPH and is currently an area of great interest (159, 160). These limitations are likely to affect the flow solution in the boundary layers and limit the study of the small-scale flow features seen in the intraventricular blood flow. Recently, SPH has been implemented in Abaqus (SIMULIA, Providence, RI), a widely used commercial nonlinear FE solver. In our recent study (155) using Abaqus/SPH coupled with nonlinear hyperelastic FE valve models, we compared SPH-FSI and FE-only simulations of a bioprosthetic valve. It was found that SPH-FSI was able to generate more realistic leaflet spatial and temporal dynamics, as well as stress and strain fields.

The ultimate goal of this dissertation is to develop a comprehensive SPH-FE FSI framework to model subject- and patient-specific LH dynamics throughout the cardiac cycle. As a first towards this goal, Specific Aim 1a – Part 1 will investigate the capability of the SPH flow solver to model the large-scale blood flow dynamics in two realistic human LV models (LV-SPH), since the bulk flow ultimately drives the deformation of the heart valves. Part 1 will also involve the validation of the LV-SPH flow results with a traditional finite volume-based CFD method (LV-CFD), and to in vivo subject-specific hemodynamic data, specifically PCMR (LV-MRI) and echo data, in terms of clinically significant large-scale blood flow measurements. Results will be analyzed to identify and discuss the key challenges, limitations, and practical implications when using SPH to study the 3D LV bulk flow.

In Part 2 of Specific Aim 1a, we will test the SPH-FE FSI method's capability to model the coupled valves structural response and the intraventricular hemodynamics in a subject-specific LV-valve model (LV-FSI). LV-FSI flow and structural results will be validated against subject-specific echo data and MSCT images, clinical observations, and in vivo and in vitro studies of healthy LV-valve dynamics. Successful completion of Specific Aim 1a will yield a novel FSI framework for the study of healthy LH dynamics, which will serve as a basis for the investigation of pathological and post-procedural LH dynamics in Specific Aim 1b and Specific Aim 2, respectively.

4.2 Materials and Methods

One healthy human volunteer with no underlying cardiac diseases and one pre-operative TAVR patient with normal LV function were selected for Specific Aim 1 – Part 1, herein

denoted as Subject 1 and Subject 2, respectively. Institutional Review Board (IRB) approval was obtained for this study. Figure 8 shows the schematic of our study design. 3D LV geometries and wall motion were obtained from medical images. In silico LV-SPH and LV-CFD models were then developed for each subject, and simulation results were compared to clinical in vivo hemodynamic data in terms of bulk blood flow features.

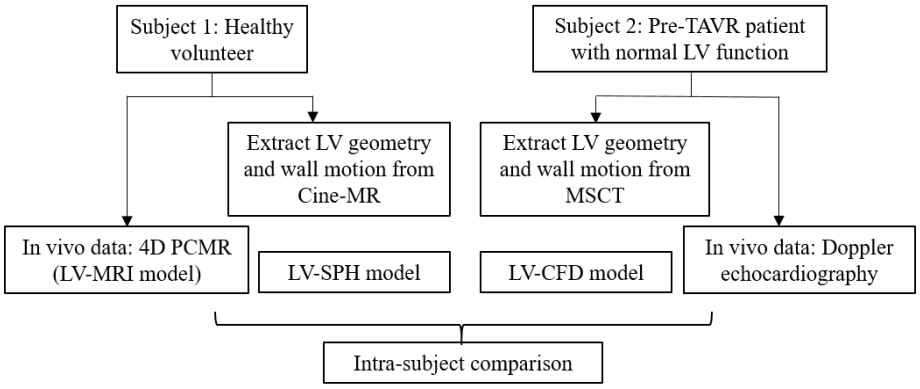

Figure 8. Schematic of Specific Aim1a – Part 1.

4.2.1 Patient information

4.2.1.1 Subject 1

Cine magnetic resonance (Cine-MR) imaging was performed in a 31-year-old healthy male volunteer on a 3T scanner (Magnetom TRIO, Siemens Medical Systems, Erlangen, Germany) using a six-element body array coil. Retrospectively ECG-gated, short axis images covering the entire LV, proximal LA and aortic root were acquired using a balanced steady-state free precession (SSFP) cine sequence, as shown in Figure 9a. An acceleration factor of 2 was used using the GRAPPA technique. The SSFP cine images were acquired

with an in-plane resolution of 1.3 x 1.3 mm, a slice thickness of 4.8 mm, and 19 phases. 23 short-axis slices were acquired to cover the entire volume of interest. Slices were acquired during and end-expiration breath-hold to minimize alignment errors caused by changes in breath-hold position.

4.2.1.2 Subject 2

From our full phase MSCT database from patients at Hartford Hospital (Hartford, CT), a 72-year-old female pre-TAVR patient with normal LV function was selected for this thesis. The MSCT examination was performed on a GE LightSpeed 64-channel volume CT scanner. A total of 2540 slices of images with an in-plane resolution of 0.82 x 0.82 mm and a slice thickness of 0.625 mm were collected for the whole cardiac cycle (Figure 9c). A collimation of 25–30 x 0.625 mm and a rotation time of 375 ms were used, resulting in 10 phases through the cardiac cycle.

4.2.2 In vivo hemodynamic data

Following acquisition of cine-MR images, LV flow was acquired for Subject 1 using a 4D phase-contrast MR sequence (4D PCMR) with the same orientation and anatomical position as the cine images. The 4D PCMR sequence provides time resolved 3D data, where each frame in time and space has 3D velocity components. The 4D PCMR sequence was an ECG-gated, gradient echo sequence with a slice thickness of 4 mm and in-plane resolution 1.8 x 1.8 mm. Other imaging parameters were as follows: repetition time (TR) 51.2 ms, echo time (TE) 3.475 ms, flip angle 15°, velocity encoding 150 cm/s. The volume of interest was resolved into 28 slices, and 17 phases were acquired through the cardiac cycle. 4D PCMR imaging provided four sets of images per time-point, i.e., magnitude

image and flow-velocity encoded images at x-, y-, z-directions. Figure 9b shows a representative PCMR phase image with the velocity encoded along the vertical axis of the slice. PCMR data was processed using an in-house Matlab code (The Mathworks, Inc., Natick, MA) following the approach in Uribe *et al.* (161).

4D PCMR magnitude images had relatively low spatial resolution and therefore were only used for manual registration and localization of imaging planes between the cine-MR and the PCMR anatomical data. Getting clear flow data during the entire cardiac cycle was challenging due to various factors, such as artifact generation due to respiratory motion, high temporal-spatial averaging, and limited signal-to-noise ratio (SNR) (162). Hence, the results obtained from PCMR are only used in this dissertation for a qualitative comparison.

For Subject 2, pre-operative transthoracic echocardiogram Doppler examination with complete 2D, M-Mode, and Doppler data was obtained from Hartford Hospital (Hartford, CT). From this data, the pulsed-waved Doppler velocity recording at the LVOT plane seen in Figure 9d was digitized and compared to the numerical results.

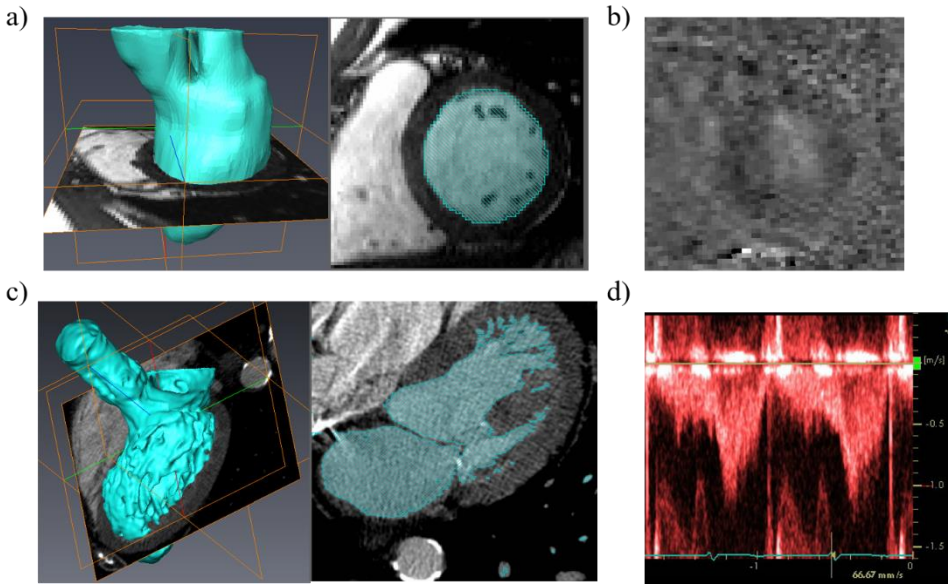

Figure 9. a) Cine images of the LV for Subject 1, b) PCMR velocity image of the LV for Subject 1, c) MSCT images of the LV for Subject 2, and d) Doppler echo velocity recordings at LVOT plane for Subject 2.

4.2.3 Model reconstruction

Cine-MR and MSCT images were imported into Amira-Avizo (Thermo Fisher Scientific, MA) and 3D Slicer (www.slicer.org) software for image segmentation, while HyperMesh (Altair Engineering, Inc., MI) software was used for mesh generation. The reconstructed geometries captured the LV internal structure and motion in detail, including the MA and proximal LA dynamics during the entire cardiac cycle. Figure 10a,b shows the successfully reconstructed subject-specific LV models at end-diastole and end-systole for Subjects 1 and 2, respectively. Although the AV and MV were not included in this first part of Specific Aim 1, we approximated valve function numerically by changing the boundary conditions for the corresponding systolic and diastolic phases (163), and geometrically by image-

based anatomically-driven dynamic annular structures. The reference planes and lines where the velocity measurements will be analyzed are indicated in Figure 10c.

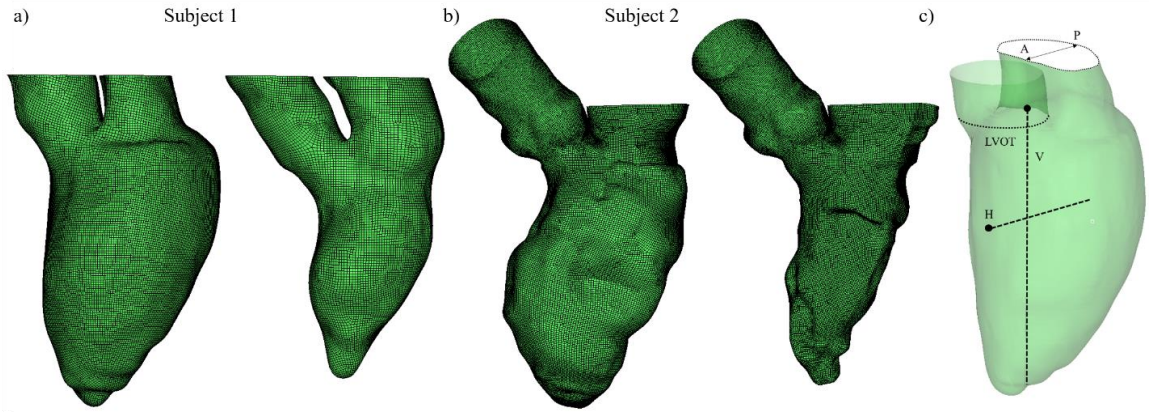

Figure 10. LV models at end-diastole and end-systole for a) Subject 1, b) Subject 2, and c) reference planes and lines. A and P represent anterior and posterior directions. H and V represent the horizontal and vertical lines, with the black circles indicating the origin of the lines.

4.2.4 Numerical methods

4.2.4.1 SPH

SPH is a fully Lagrangian particle solver where the particle connectivity evolves with time and needs to be determined by a particle search. As illustrated by a 2D example in Figure 11, each SPH particle has its own physical properties, *A*, which are interpolated by a kernel function, *W*, using the properties of its neighboring particles. This concept is interpreted numerically using a summation

$$A(\mathbf{r}_\mathrm{a}) = \sum_\mathrm{b} m_\mathrm{b} \frac{A_\mathrm{b}}{\rho_\mathrm{b}} W(\mathbf{r}_\mathrm{a} - \mathbf{r}_\mathrm{b}, h) \tag{1}$$

where A_b denotes any physical property at particle 'b' within the neighboring domain (limited by the influence length h of the kernel) of particle 'a' at position $\mathbf{r}_\mathrm{a}$. Particle 'b' has mass m_b, position $\mathbf{r}_\mathrm{b}$, and density ρ_b. In this work, a cubic spline kernel function *W* was adopted. Using this equation and its derivatives, the governing equations of fluid flow can be rewritten under the form of SPH formulation. The time derivative form of the conservation of mass gives

$$\frac{\mathrm{d}\rho_\mathrm{a}}{\mathrm{d}t} = \sum\nolimits_\mathrm{b} m_\mathrm{b} \boldsymbol{v}_\mathrm{ab} \cdot \nabla_\mathrm{a} W_\mathrm{ab}. \tag{2}$$

Here $\nabla_\mathrm{a} W_\mathrm{ab}$ is the gradient of the kernel function regarding the coordinates of given particle 'a' and $\boldsymbol{v}_\mathrm{ab} = \boldsymbol{v}_\mathrm{a} - \boldsymbol{v}_\mathrm{b}$ denotes the relative velocity vector between particles 'a' and 'b'. Similarly, the conservation of momentum under the SPH scheme can be written as

$$\frac{\mathrm{d}\boldsymbol{v}_\mathrm{a}}{\mathrm{dt}} = -\sum\nolimits_\mathrm{b} m_\mathrm{b} \left(\frac{P_\mathrm{a} + P_\mathrm{b}}{\rho_\mathrm{a}\rho_\mathrm{b}}\right) \nabla_\mathrm{a} W_\mathrm{ab} + \sum\nolimits_\mathrm{b} m_\mathrm{b} \frac{(\mu_\mathrm{a} + \mu_\mathrm{b})\boldsymbol{v}_\mathrm{ab}}{\rho_\mathrm{a}\rho_\mathrm{b}\mathbf{r}_\mathrm{ab}^2} \mathbf{r}_\mathrm{ab} \cdot \nabla_\mathrm{a} W_\mathrm{ab} \tag{3}$$

where *P* is pressure and μ is the dynamic viscosity of the fluid. The movement of the particles is governed by

$$\frac{\mathrm{d}\mathbf{r}_a}{\mathrm{d}t} = \boldsymbol{v}_\mathrm{a} \tag{4}$$

In Abaqus, the pressure is related to the density by the Mie-Grüneisen equation of state (164). In this work, the linear $U_s - U_p$ Hugoniot form is used, given by

$$p = \frac{\rho_0 c_0^2 \eta}{(1 - s\eta)^2}\left(1 - \frac{\Gamma_0 \eta}{2}\right) + \Gamma_0 \rho_0 E_m \tag{5}$$

where Γ_0 is a material constant, c_0 is the artificial speed of sound, $\eta = 1 - \rho_0/\rho$ is the nominal volumetric compressive strain, ρ is the current density, and E_m is internal energy per unit mass. A detailed description of SPH fundamentals can be found in Monaghan *et al.* (144) and Morris *et al.* (146).

In this thesis, blood was assumed as an incompressible, isothermal, Newtonian fluid with a reference density of $\rho = 1056\ kg/m^3$ and a dynamic viscosity of $\mu = 0.0035$ Pa $\cdot$ s. For the blood flow in the heart and large arteries, the speed of sound is high compared to the bulk velocity of the blood, therefore an artificial sound speed of $c_0 = 145$ m/s was employed to avoid very small computational time steps while keeping density fluctuations within a small range to maintain incompressible flow behavior. Other material parameters were chosen as $s = 0$ and $\Gamma_0 = 0$. The stable time increment was between 10^{-6} and 10^{-7} s. This small time-step size ensured numerical stability and temporal accuracy.

SPH particles were initially uniformly distributed in the domain with a spatial resolution of 0.8 mm. This led to approximately 594,000 PC3D elements in the domain for the LV-SPH model of Subject 1, and 497,400 PC3D elements for Subject 2. The mesh sensitivity of SPH particles was checked previously (155), thus a similar particle density was adopted here. Two cardiac cycles were conducted and the results from the second cycle

were analyzed. It was found that the difference in the velocity results between the first and second cycle was within 5%.

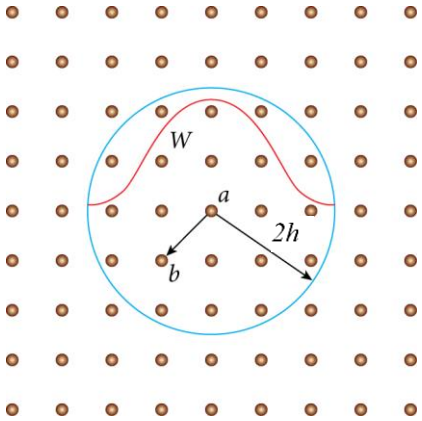

Figure 11. 2D illustration of the basic principle of SPH. Property A of particle 'a' is determined by properties of its neighboring particles (e.g., 'b'), based on an interpolating kernel function (W) which is a function of the smoothing length, h, and the distance between particle 'a' and its neighboring particle 'b'.

4.2.4.2 CFD

The Navier-Stokes equations for 3D unsteady flow with moving walls are solved using the finite volume-based CFD solver Star-CCM+ (CD-adapco, Melville, NY). For a control volume V with surface S moving with local surface velocity $\boldsymbol{v}_b$, the integral form of the continuity equation is

$$\frac{\partial}{\partial t}\int_V \rho \mathrm{d}V + \int_S \rho(\vec{\boldsymbol{v}} - \vec{\boldsymbol{v}}_b)\cdot\vec{\boldsymbol{n}}\,\mathrm{d}S = 0 \tag{6}$$

where $\vec{\boldsymbol{n}}$ is the outward unit normal vector to the differential area $\mathrm{d}S$, ρ is the density of the fluid, $\vec{\boldsymbol{v}} = (u, v)$ is the velocity vector of the fluid in the fixed coordinate system,

and $\vec{\boldsymbol{v}}_b = (u_b, v_b)$ is the velocity vector of the moving boundary S of control volume V. The momentum equation in integral form is given by

$$\frac{\partial}{\partial t}\int_V \rho\vec{\boldsymbol{v}}\mathrm{d}V + \int_S \rho\vec{\boldsymbol{v}}(\vec{\boldsymbol{v}} - \vec{\boldsymbol{v}}_b)\cdot\vec{\boldsymbol{n}}\,\mathrm{d}S = -\int_S P\vec{\boldsymbol{n}}\,\mathrm{dS} + \int_S \bar{\boldsymbol{\tau}}\cdot\vec{\boldsymbol{n}}\,\mathrm{dS} \tag{7}$$

where P is the pressure and $\bar{\boldsymbol{\tau}}$ is the viscous stress tensor. In the above equation, the body forces are ignored. For an incompressible Newtonian fluid, $\bar{\boldsymbol{\tau}}$ is expressed as

$$\tau_{ij} = \mu\left(\frac{\partial u_i}{\partial x_j} + \frac{\partial u_j}{\partial x_i}\right) \tag{8}$$

For this type of problem where the mesh is moving, an additional equation called the space conservation law is solved for the moving coordinate velocity components

$$\frac{\partial}{\partial t}\int_V \mathrm{d}V - \int_S \vec{\boldsymbol{v}}_b\cdot\vec{\boldsymbol{n}}\,\mathrm{d}S = 0 \tag{9}$$

This relates the change in cell volume to the cell-face velocity. The simultaneous satisfaction of the space conservation law and all other equations of fluid motion facilitates the general moving mesh operations performed. The development and solution of the discretized forms of these equations is straightforward within the finite volume CFD framework, provided that appropriate measures are taken to ensure obedience to the space conservation law (165). The Navier-Stokes equations for 3D flow with moving walls are solved by a second order segregated iterative method (SIMPLE algorithm). A detailed description of the numerical method can be found in (165, 166).

The final volume mesh consisted of five prism layers near the wall and hexahedral cells at the core region. Convergence criteria for all the flow parameters were set to 10^{-6}. To reach a periodic solution, the CFD simulations were run for four cardiac cycles using a time-step size of 1 ms. As shown in Figure 12, tests on mesh sensitivity were performed on the LV-CFD models by comparing results obtained with three different mesh densities: coarse (100,000 elements, 150,000 elements), medium (200,000 elements, 270,000 elements), and fine (500,000 elements, 640,000 elements), for Subject 1 and Subject 2, respectively. The L_1- relative error norm (E_{L1}) of the instantaneous velocity profile along the LVOT plane center line at peak systole for Subject 1 was 8.6 % between the coarse and fine meshes, and 4.8 % between the medium and fine meshes. For Subject 2, E_{L1} was 5.2 % between the coarse and fine meshes, and 3.9 % between the medium and fine meshes. Similarly, E_{L1} of the instantaneous velocity profile along the MA plane centerline at the E-wave for Subject 1 was 10.3 % between the coarse and fine meshes, and about 4.4 % between the medium and fine meshes. For Subject 2, E_{L1} was 9.8 % between the coarse and fine meshes, and 4.9 % between the medium and fine meshes. A reasonable convergence was therefore achieved on the medium grid resolution in terms of the intraventricular flow field. Therefore, the CFD results presented in this study employed the medium mesh density.

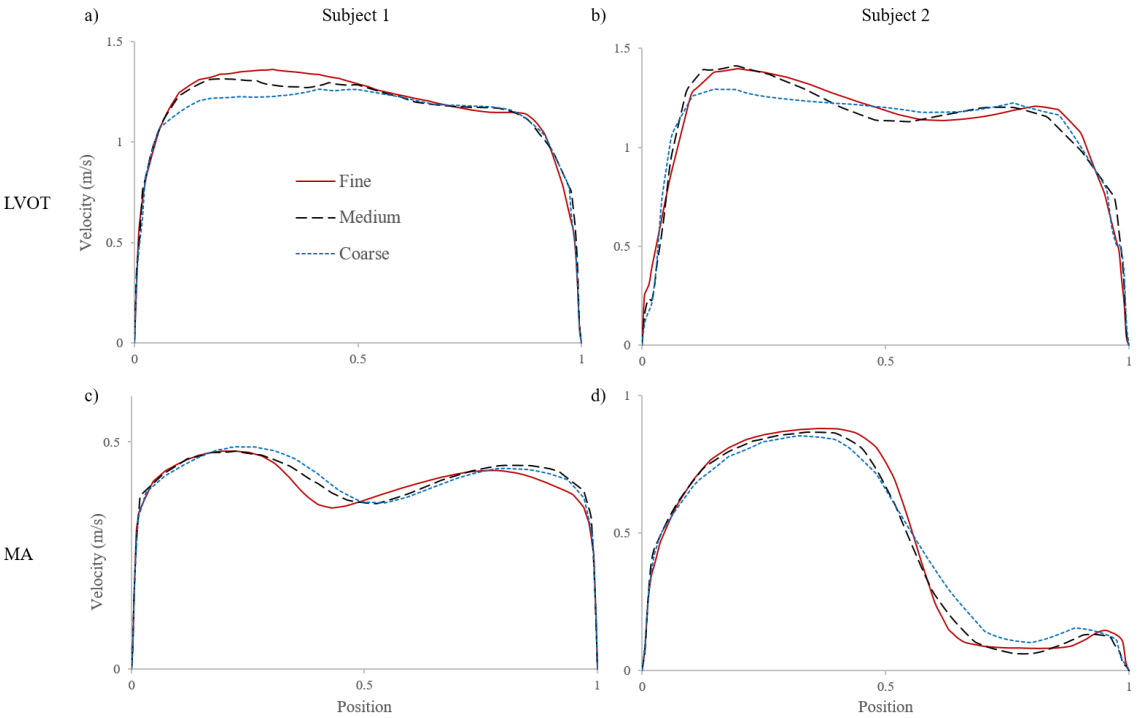

Figure 12. Results of LV-CFD mesh sensitivity for Subject 1 (a,c), and Subject 2 (b,d) models.

4.2.5 Boundary conditions

4.2.5.1 LV wall motion

Cardiac wall motion was applied to the LV-SPH and LV-CFD models as a time-dependent nodal displacement boundary condition from the cine-MR and MSCT medical images. This approach keeps the correspondence of the surface nodes of the computational domain by creating a unique mesh for all time steps, thus the movement of each node can be tracked over time. For Subject 1, a total of 8 phases from the original cine-MR images were used to prescribe the LV wall motion for one cardiac cycle, while 10 MSCT phases were used for Subject 2. First, from the segmented mesh in end-systole, a high quality template mesh

was created in Hypermesh (Altair Engineering, Inc., MI), and divided in subdomains (LV, aortic root, MA, proximal LA). Second, a preprocessing inflation simulation in Abaqus/Explicit was implemented, in which the template mesh was inflated to match the mesh from the next cine-MR or MSCT phase. Third, for some complex regions such as the aortic-mitral curtain, the morphing toolkit available in Hypermesh software was used to deform and map the template mesh to the target mesh from the next MSCT frame. In this fashion, the LV wall mesh maintained the same number of nodes across all phases, thus ensuring one-to-one connectivity.

As numerical simulations typically involve time steps smaller than the time interval between two cine-MR or MSCT phases, displacements were interpolated in time. Previous studies with linear interpolation of the LV wall showed high discontinuities in the flow and pressure solution due to the resulting discontinuities in mesh acceleration (167), thus, cubic spline was used to interpolate the displacement of each node in time. No-slip boundary condition was applied to the LV-CFD models. For the LV-SPH models, the interaction between SPH particles and the LV wall was based on node-to-surface contact. The node-to-surface contact interaction in SPH is directly related to the no penetration boundary condition. Thus, the combined effect of the smoothing kernel interpolation function near the wall and the node-to-surface contact interaction partially enforces the no-slip boundary condition.

4.2.5.2 Inlet and outlet

As blood was considered incompressible, reasoning based on mass conservation can be made to overcome the lack of detailed inflow and outflow information. The volume flow

rates into and out of the model are thus driven by the expansion and contraction of the LV and proximal LA. For the inlet boundary condition, the CFD and SPH models employed the diastolic flow rate waveform derived from the LV volume change (including the proximal LA), with its value set to zero during systole (61, 168-171) (Figure 13a). For the outlet boundary condition, a physiological aortic pressure waveform (172), as seen in Figure 13b, was applied. In order to avoid the boundary effects on the region of interest, the inlet and outlet boundaries of the models were moved away from the position of the mitral and aortic orifices by extending the proximal LA and LVOT with tubes (173, 174) (not shown in Figure 10). Since the SPH formulation in Abaqus lacks periodic boundary conditions, the tubes were extended long enough to accommodate the inflow and outflow of particles for two full cardiac cycles. Rigid plates at the extensions were used to apply the boundary conditions in the LV-SPH models (155). Similarly to the LV-CFD models, the diastolic flow rate waveform was applied on the inlet plate, while the aortic pressure curve was applied on the outlet plate of the LV-SPH models.

Note that differences in the diastolic flow rate between our results and physiological LV curves refer to 1) the fact that our flow curves included the volume change of not only the LV but also the volume change of the proximal LA, 2) imaging and segmentation uncertainties, as well as to the reduced number of imaging phases, since minor fluctuations in the volume curve lead to considerable changes in the flow rate waveform. Nonetheless, as explained in the following section, global flow parameters matched with *in vivo* clinical data and were within physiological range. The heart rate for both subjects was approximately 75 bpm, corresponding to a cardiac cycle of 0.8 s.

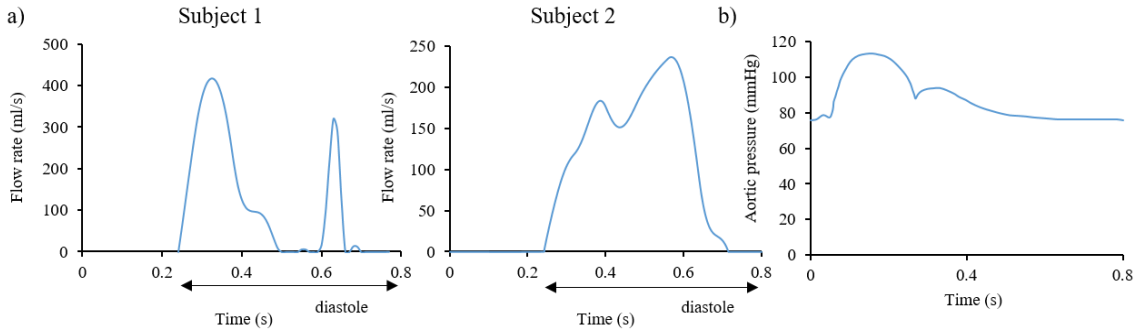

Figure 13. a) Inlet flow rate for Subject 1 (left) and Subject 2 (right), and b) Outlet pressure.

4.2.6 Data analysis

Blood flow velocity vector fields and contours at different long-axis and short-axis planes, and at different time instances of the cardiac cycle will be quantitatively compared between the LV-SPH, LV-CFD and LV-MRI models for Subject 1, and between the LV-SPH and LV-CFD models for Subject 2. An analysis and visualization of the 3D vortical structures of the intraventricular flow for the LV-CFD models was also performed. Another quantitative metric to be used for comparison between the in silico and in vivo flow data will be the velocity profile at different time instants and at different horizontal (H) and vertical (V) lines inside the LV models for Subject 1 (Figure 10c). Because of the Lagrangian nature of the SPH method, the velocity magnitude was calculated by averaging particle velocities enclosed from evenly space spheres of radius 1.5 mm along the lines. The error in the velocity measurements will be quantified by the L_1- relative error norm (E_{L1}), defined as

$$E_{L1} = \frac{\left\| v_{SPH} - v_{CFD/MRI} \right\|}{\left\| v_{CFD/MRI} \right\|} \tag{10}$$

For a more clinically relevant quantitative evaluation, we will also compare the maximum flow velocity at the LVOT plane during systole, and at the MA plane during diastole between the LV-SPH, LV-CFD and LV-MRI models for Subject 1, and between the LV-SPH model, the LV-CFD model, and the subject-specific Doppler velocity recordings for Subject 2.

4.3 Results

4.3.1 Global LV flow parameters

Figure 14 shows the time-varying LV volume change waveform for both subjects, where the points indicate the cine-MR or MSCT phases and the lines represent the cubic spline interpolation. For Subject 1, the end-diastolic (EDV) and end-systolic (ESV) volumes were 140 ml and 58 ml, respectively, which are within the physiological range typically measured in males (175). The stroke volume (SV) and the ejection fraction (EF) were 82 ml and 58%, respectively. For Subject 2, the EDV and ESV were 112 ml and 47 ml, giving a SV of 65 ml and EF of 58%, values that closely match the patient-specific data obtained from Doppler Echo of 64 ml and 57%, respectively.

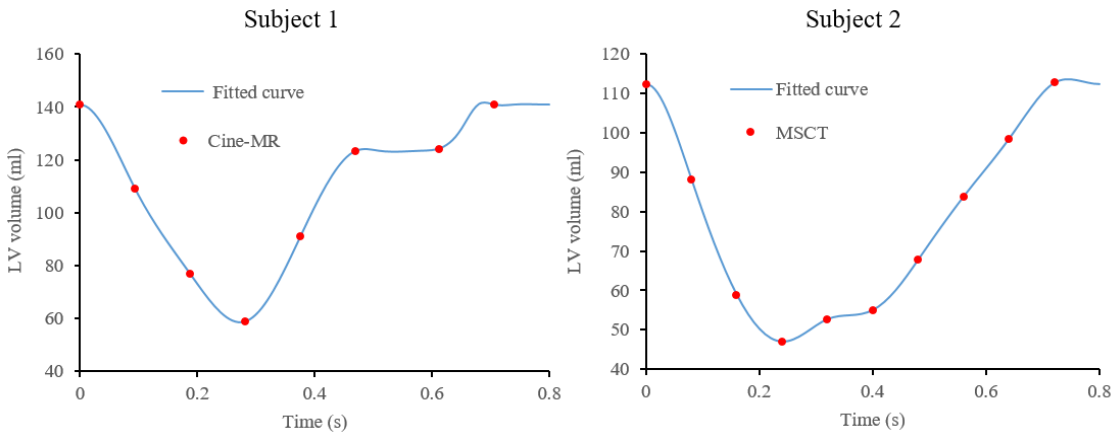

Figure 14. Time variation of LV volume for Subject 1 and Subject 2.

4.3.2 Large-scale intraventricular flow patterns

Figure 15 and Figure 16 show the velocity vectors in the anterior–posterior plane (Figure 10c) for the LV-MRI (a), LV-SPH (b,d), and LV-CFD (c,e) models during peak systole (t=0.09 s) and early diastole (t=0.37 s), respectively. From the figures it can be seen that the intra-subject LV hemodynamics generated by the LV-SPH models had a similar overall topology as those measured in the LV-MRI and simulated in the LV-CFD models. At peak systole (Figure 15), a strong outward jet was developed at the LVOT, with an almost equal maximum velocity of 1.4 m/s. The LV-SPH models gave a good representation of the ejection phase, with the flow converging towards the outflow tract. As shown in Figure 15a, the LV-MRI maximum velocity for Subject 1 was localized in the central outflow region, as compared to the CFD and SPH results. Since the MV is not included in the numerical models, some minor backflow of blood into the LA can be observed, especially in the LV-CFD for Subject 1 (Figure 15c).

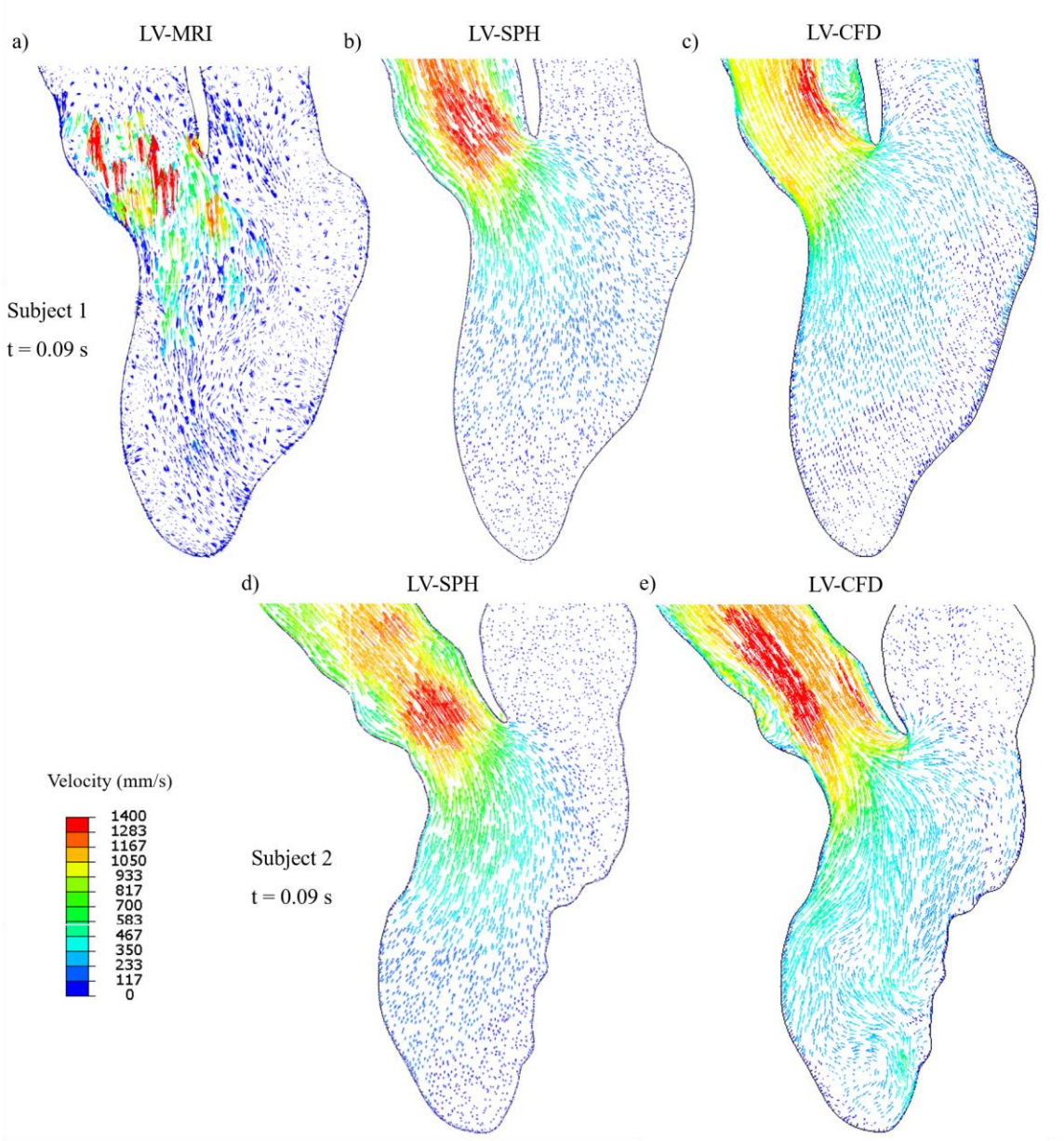

Figure 15. Velocity vectors in the anterior-posterior plane for Subject 1 (a,b,c) and Subject 2 (d,e) during peak systole at t=0.09 s.

Once diastole begins and the LV wall and MA start to expand, the blood enters from the LA to the LV, forming a jet through the mitral orifice. During early diastole (Figure 16), the intra-subject flow patterns of the LV-SPH models were similar to the CFD

results and PCMR measurements. For Subject 1, the LV-MRI maximum velocity magnitude at the level of the MA was approximately 0.68 m/s (Figure 16a), compared to the 0.45 m/s of the numerical models (Figure 16b,c).

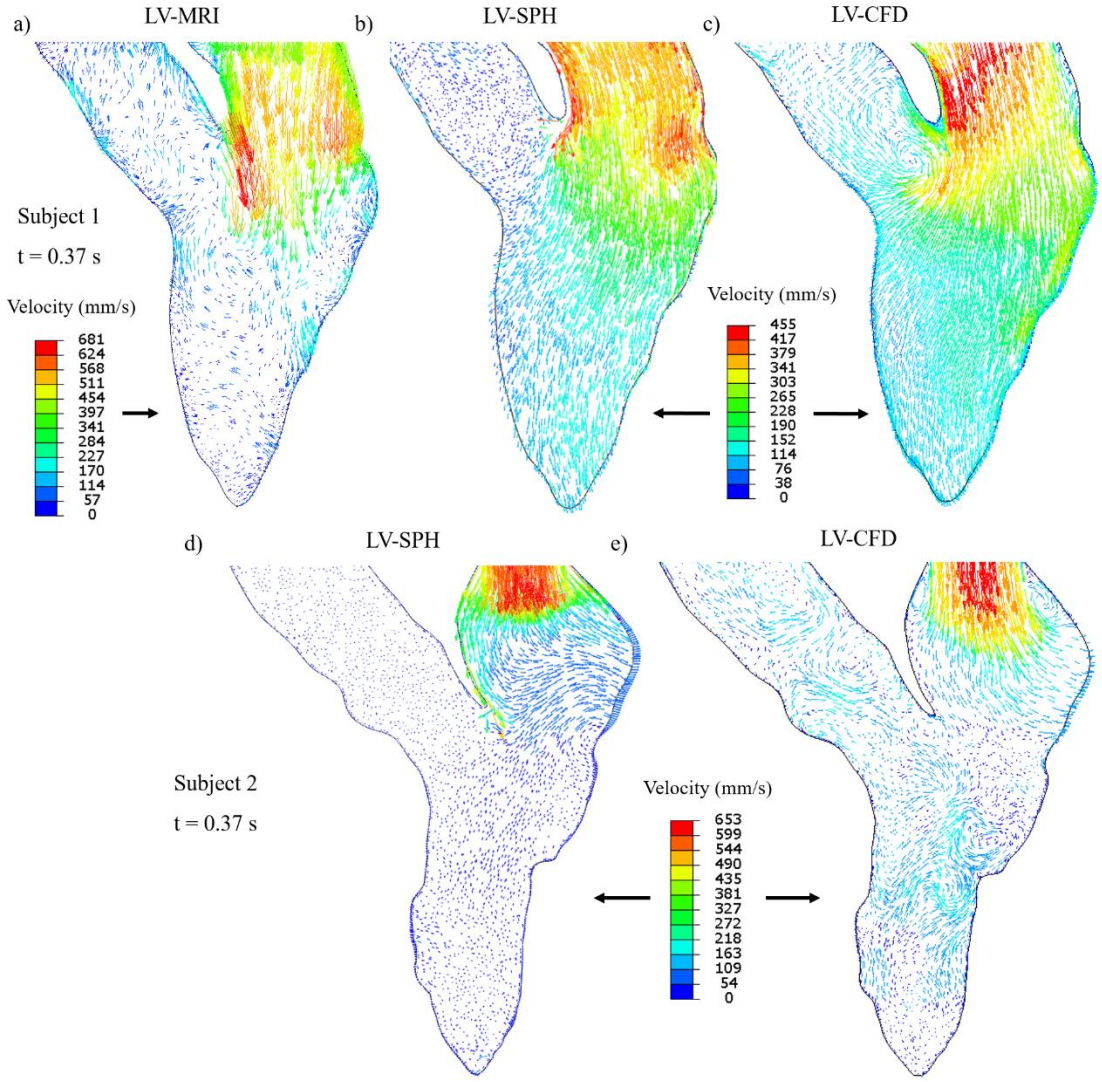

Figure 16. Velocity vectors in the anterior-posterior plane for Subject 1 (a,b,c) and Subject 2 (d,e) during early diastole at t=0.37 s. For clarity, for Subject 1, the scale of the velocity vectors is the same for the SPH and CFD models, while is different for the MRI model. For Subject 2, the velocity scale is the same for both SPH and CFD models.

In mid-diastole, due to the high velocity differences of the inflow blood and the retaining blood inside the LV, a vortex ring is developed in the LVOT region, as shown in a representative image for Subject 1 (Figure 17). The vortex seen in the SPH and CFD models is generated from the jet shear layer that is rolled up by viscous forces exerted from the resting fluid onto the jet core (12). As shown in Figure 17a and further explained below, during this phase and late-diastole the velocities in the LV are low and the LV-MRI measurements do not show a clear distinction between the small-scale vortices and the background noise.

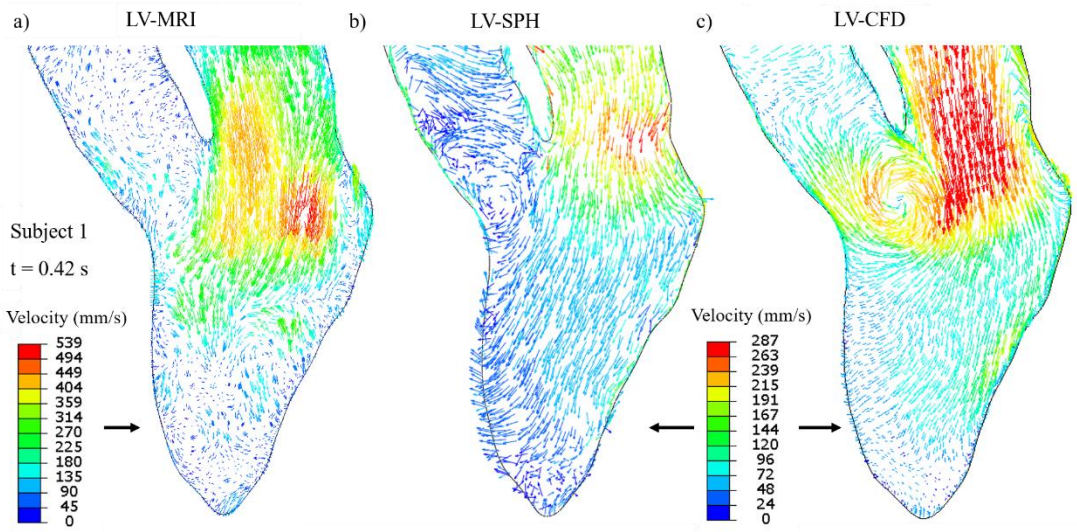

Figure 17. Velocity vectors in the anterior-posterior plane for Subject 1 during E-wave deceleration at t=0.42 s. For clarity, the scale of the velocity vectors is the same for the SPH and CFD models, while is different for the MRI model.

4.3.3 Quantitative comparison of velocity profiles

From Figure 18 it is clear that, in general, the SPH results were in good agreement with those extracted based on the CFD method. However, there was a discrepancy in the

velocity magnitudes, and this difference was mostly concentrated in the regions near the LV wall. For E_{L1}, shown in Figure 18, it is found that the velocity difference between the two models was around 11%. The highest discrepancy was 12.5%, and this occurred for line V at t = 0.32 s.

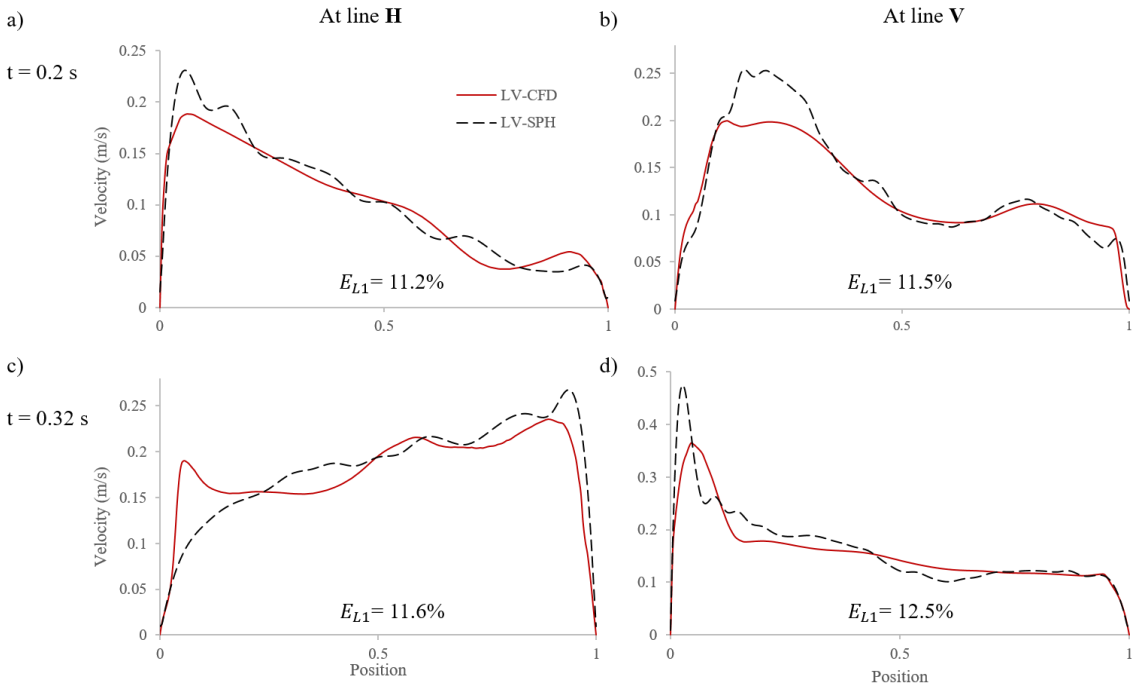

Figure 18. Velocity profiles and errors at different time instants at mid-horizontal (H) and mid-vertical (V) lines for Subject 1.

For a more clinically relevant quantitative evaluation, we compared the maximum flow velocity magnitude at the LVOT plane (Figure 10c) during the systolic phase between the LV-SPH (dotted line) and the LV-CFD (solid line) models for both Subjects. Figure 19a shows that for both numerical models of Subject 1, the LVOT velocities reached a close agreement in regards to magnitude and velocity waveform with nearly identical value around t = 0.09 s. As discussed in the next section, inaccuracies, limited resolution, and

multiple-beat ensemble averaging of the 4D PCMR data prevented a direct comparison of the LV-MRI velocity waveform with the SPH and CFD models at the LVOT plane for Subject 1.

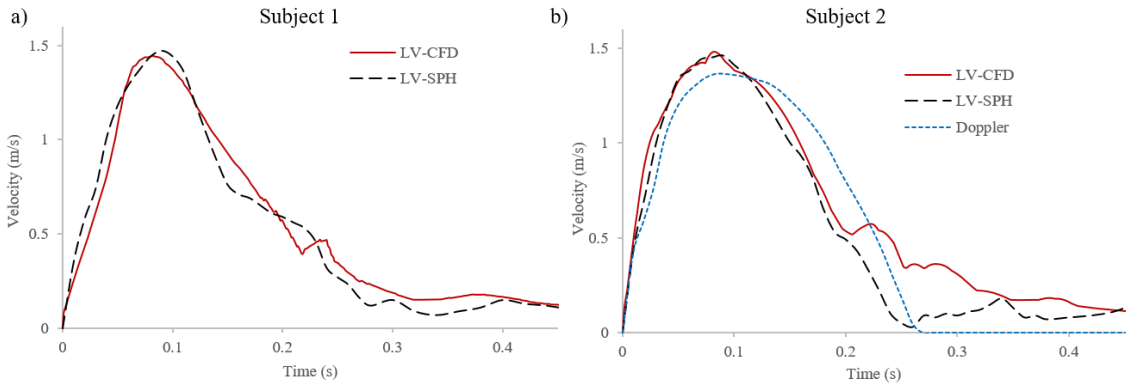

Figure 19. Maximum LVOT velocity from different data sets during systole for a) Subject 1, and b) Subject 2.

Similarly, for Subject 2, the maximum flow velocity magnitude at the LVOT during systole was compared between the LV-SPH model, the LV-CFD model, and the patient-specific Doppler velocity recordings. Figure 19b shows that for both computational models, the LVOT velocity reached a nearly identical maximum value at 0.09 s, with a close agreement in the velocity waveforms. For the Doppler waveform, however, a 6.5% lower peak velocity was observed compared to the numerical models. Overall, the LV-SPH models quantitatively matched to a good degree with the LV-CFD models and to a reasonable degree with the patient-specific *in vivo* data. Despite the fact that the near wall flow features were not modeled accurately using Abaqus SPH formulation, we obtained similar bulk flow information as the traditional mesh-based CFD models.

4.3.4 Vortex dynamics

Figure 20 illustrates the vortex structures of the LV-CFD models by plotting the λ2 vortex criterion at the indicated time instants. The λ2-method is an objective method that identifies 3D vortex cores based on their physical fluid dynamics properties, and is considered one of the most accepted vortex detection techniques (176). Vortex structures are identified by extreme negative values of λ2, roughly corresponding to local pressure minima due to vortical motion. The isosurfaces of this criterion are color-coded by the longitudinal component of the velocity, and the corresponding time instants during the cardiac cycle are highlighted on the flow-rate curve. First, during the flow acceleration associated with the E-wave (Figure 20a,e), a weak vortex ring is observed to start to pinch off from the mitral orifice and propagates and impinges on the lateral wall. At the same time, the LA is filled with a vortex ring ejected from the inlet extension (Figure 20e). For Subject 1, the vortex-induced boundary layer at the mitral inlet wall is a shear layer still not organized in a complete ring-like vortex (Figure 20a). Subsequently, due to the interaction with the wall the vortex ring becomes unstable and starts to breakdown.

During the flow acceleration phase of the A-wave, there is formation of a second vortex ring just downstream of the mitral orifice for Subject 1 (Figure 20b), while for Subject 2 the incoming flow of the A-wave goes primarily to the wall due to the interaction with the clockwise circulation, and there is no clear distinction of a well-defined vortex ring (Figure 20f). However, for Subject 2, the primary weaker vortex ring continuously moves toward the apex (Figure 20f) and starts to dissipate. The stronger A-wave vortex ring found in Subject 1 compared to Subject 2 could be because the more pronounced deceleration and diastasis phases found in Subject 1 helped to dissipate the vortices formed

during the E-wave phase. At the end of diastole and as seen in Figure 20c,g, the asymmetric vortex ring impinges on the LV wall and begins to breakdown into small-scale structures. However, as evident in Figure 20c, the vortex structure for Subject 1 exhibited a larger spread across the ventricular cavity as well as a reduced penetration compared to Subject 2. This is because two possible reasons: first, the end-diastolic vortical structure for Subject 2 was closer to the apex of the ventricle, and second, the LV model for Subject 2 had a more dynamic MA motion, which caused a larger reduction of the effective orifice area and thus a stronger inflow jet.

During systole (Figure 20d,h), blood gets ejected into the aorta and the small vortical structures that remain at the end of the diastole get stretched and aligned with this outwardly directed flow. These elongated structures are circulated within the LV by the clockwise rotational flow during early systole and subsequently pushed rapidly toward the LVOT. The overall intraventricular vortex configuration in this study is consistent with results of previous computational and experimental studies (169, 177-179). It should be noted, however, that the orientation and penetration depth of these vortex rings could be different from some studies, and this might be due to the differences in the boundary conditions, geometry, and the movement of the ventricle wall.

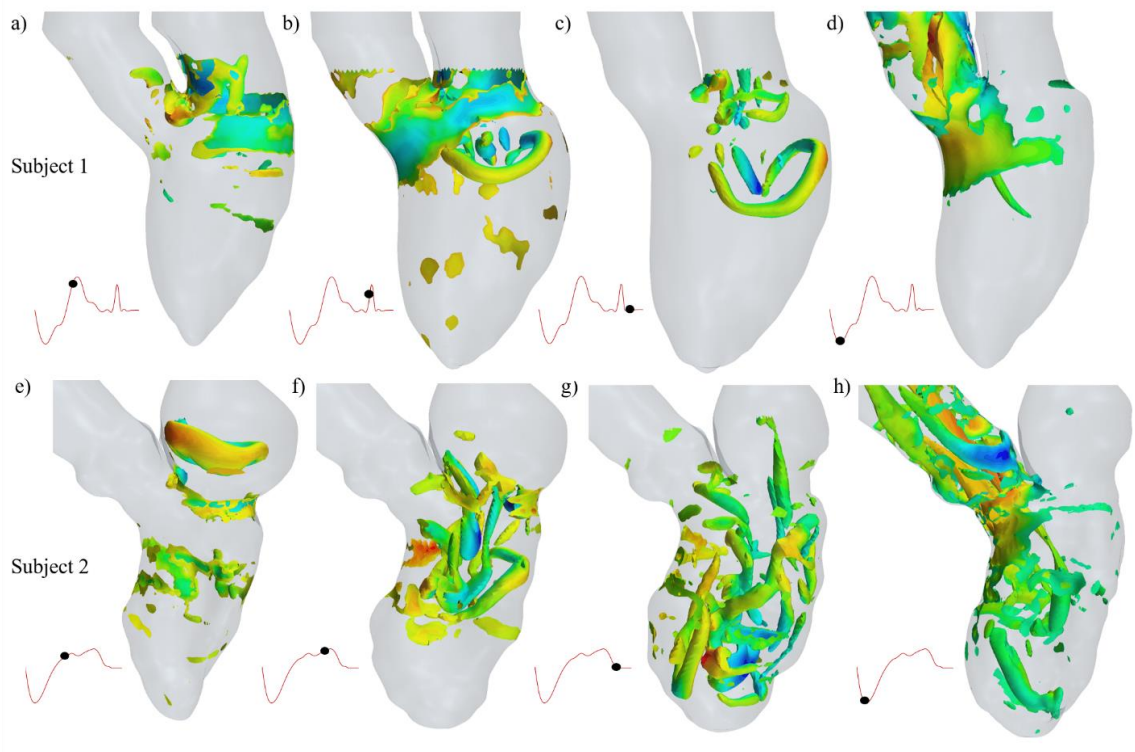

Figure 20. 3D vortical structures visualized by isosurfaces of λ2 (-2000) and colored by longitudinal component of the velocity (along the centerline of the mitral inlet). Negative velocity (colored blue) indicates towards apex.

4.4 Discussion

Specific Aim 1 – Part 1 investigated the capability of the SPH framework to simulate the bulk blood flow dynamics in two realistic 3D LV models. Quantitative and qualitative comparisons of SPH simulation results with those of in vivo clinical flow measurements and a CFD approach have been presented. The comparison between the three data sets is encouraging, showing that the SPH method can capture the large-scale flow dynamics with a similar level of accuracy as a traditional mesh-based CFD method. The study by Shahriari and colleagues (156) was essential to validate the SPH approach when applied to the study

of 2D cardiovascular flows. The main limitation of this study was, however, the assumption of a 2D rigid LV geometry. Cardiac flow with moving LV wall has also been investigated by Kulp et al (154). Nevertheless, the model analyzed in this study lacked verification of simulation results.

The SPH results of this study indicate the capability of SPH as a promising tool for predicting clinically relevant large-scale LV flow information. First, there was generally a good match between the simulated and measured velocity fields at different time points of the cardiac cycle. During systole, the intra-subject flow patterns were qualitatively similar for the three data sets of Subject 1 (Figure 15a-c), and for the two data sets of Subject 2 (Figure 15d-e). However, as shown in Figure 15a, the highly localized velocity vectors at the LVOT for the LV-MRI measurements probably originate from the level of uncertainty in the acquisition and interpolation of the PCMR data, as well as from the stronger jet flow due to the AV dynamics, which was not incorporated in this study.

During early diastole, the intra-subject flow patterns were also similar but the velocity magnitude of the LV-MRI measurement for Subject 1 (Figure 16a) was higher than that from the *in silico* models (Figure 16b,c). The absence of MV leaflets in the computational models affected the accuracy of the velocity calculations, as a bigger orifice area, and thus a smaller flow jet, was obtained for the *in silico* models. In PCMR measurements of the velocity through the MV during diastole, Kim *et al.* (180) and Fujimoto *et al.* (181) noted velocity magnitudes at the leaflet tips between 15%–20% greater than that at the MA. During mid- to late-diastole, the LV-MRI results did not show a clear presence of the vortices as the simulation results did (Figure 17). A possible reason of this phenomenon is that the velocity encoding factor used in the PCMR imaging was

constant over the entire cardiac cycle, and was selected to exceed the expected peak systolic velocities in the LVOT to avoid velocity aliasing. As a consequence, small-scale vortical features and regions with low flow suffered from low signal in the PCMR data and thus lead to impaired depiction.

When the intra-subject systolic velocity waveforms at the LVOT were quantitatively compared between the different models (Figure 19), a good agreement in regards to magnitude and velocity waveform was obtained. Moreover, the level of discrepancy between the computational and Doppler velocity measurements for Subject 2 (Figure 19b) were in-line with the inherent uncertainties in the pulsed-waved Doppler flow recordings. Doppler velocity measurements are dependent on the ultrasound beam orientation, maximum velocity information should be obtained with the ultrasound beam aligned as parallel as possible to the flow, otherwise the maximum velocity will be underestimated (182).

It is also noted that along the centerlines in Figure 18, the shape of the velocity profiles was similar, but there was a discrepancy in the velocity magnitudes near the LV wall. This may be because the no-slip condition was not fully constrained in the Abaqus SPH formulation. This situation caused differences between the LV-SPH and LV-CFD velocity profiles for Subject 1 of approximately 11%. However, the SPH method was able to capture the bulk LV flow with reasonably accuracy, and the large-scale intraventricular hemodynamic features obtained were similar to what have been reported in previous mesh-based LV studies (61, 183, 184).

PCMR is currently considered the gold standard for non-invasive quantification of cardiac blood flow, as this technique has been validated extensively (185, 186). Nevertheless, there are some known limitations associated with PCMR flow measurements (187, 188). Blurring or ghosting artifacts are common due to breathing motion (189). Particularly for 4D PCMR data acquisition, large amounts of data require measurement durations that often exceed normal human breath-holding capabilities. To achieve a high SNR, the patient needs to be scanned for multiple cardiac cycles, and the velocity fields from different cardiac cycles are combined to form a single 4D velocity field (190). To achieve a high spatial resolution, a long imaging time is also required, which will lead to more artifacts induced by respiratory movement. Therefore, there is a trade-off among SNR, time-resolution and spatial-resolution. Our comparison of the *in vivo* measured and *in silico* simulated velocity results should be interpreted with the consideration of these PCMR recording limitations.

4.5 Limitations

In comparison with conventional CFD methods, implementation of boundary conditions, especially the no-slip condition, is not straightforward with SPH (157, 158). The default interaction between SPH particles and Lagrangian boundaries in Abaqus is based on node-to-surface contact. The SPH discretization relies on a kernel interpolation that requires full support to obtain an accurate approximation of the field quantities and derivatives. When particles are close to the boundary, part of the supporting domain of the smoothing kernel will not be filled with SPH particles. Therefore, the integration accuracy for those SPH particles close to the boundary may be affected (191). To improve the SPH solution near the wall, it is possible to specify in Abaqus the so-called ghost particle method (192). Ghost

particles fill the boundary by mirroring real particles and their attributes are extrapolated such that the no-slip condition is satisfied. The two main drawbacks of this method are 1) the need of recreation of ghost particles at every time step, and 2) direct mirroring only works for simple geometries (193), thus, this boundary method could not be applied to our LV-SPH models.

Another intrinsic modeling limitation of this study was ignoring the native heart valve structures. Past studies have shown that by choosing appropriate inlet information together with global geometric and flow parameters that are within physiological range, computational models with simplified valve structures can reproduce the flow features associated with LV function with reasonably accuracy (163, 169, 172, 194, 195). It is well known that for a computational heart model to become a clinically relevant simulation tool it must be able to capture the FSI between the blood flow and the heart valves (196). Conventionally, many of the FSI approaches used to study LV function have been based on conventional CFD mesh-based methods, however, complex LV dynamics can lead to computational challenges. A fully-coupled modeling approach that combines the transparent meshless character of SPH together with a nonlinear FE formulation can be implemented in a natural and simple way to simulate the intraventricular hemodynamics and valves structural response. This is the objective of Specific Aim 1a – Part 2.

The final modeling simplification was the topology of the endocardium, by assuming a smooth-walled endocardium without PM and trabeculae. The influence of these structures on the LV flow field may be significant (177, 197), and should be explore in a future study. Given that the model simplifications were kept the same for the numerical models, it is expected that a comparison of these data sets provided useful insights into the

capability of SPH to model the large-scale LV blood flow dynamics. The LV-SPH framework presented here is an initial step towards a versatile and simple mesh-free methodology to study the global 3D LH flow phenomena.

CHAPTER 5. SPECIFIC AIM 1A – PART 2, PHYSIOLOGIC LV-VALVE DYNAMICS

5.1 Introduction

The structure and kinematics of the hearts valves are expected to have a significant impact on the LV flow field (198). Seo et al. (199) found that the MV promote the formation of a circulatory flow pattern in the LV, increasing the strength of the apical flow and enhancing washout of ventricular blood. Results by Dahl et al. (60) also suggested that a physiological representation of the LA can influence the dynamics of the mitral leaflets and the intraventricular flow patterns. Additionally, recent studies have suggested that patient-specific flow patterns in the LVOT are greatly affected by the dynamically deforming LV during diastole (200). These findings underscore the importance of comprehensive FSI models of the LV coupled with the mitral and aortic valves for reproducing many of the key features of cardiac function.

Most of the LV FSI studies to date, however, have modeled either the AV (168, 201) or the MV only(60), have been limited to idealized geometries (63), or have focused only on a short time frame of the cardiac cycle - mainly the diastolic phase (60, 61). In general, previous LV FSI models have incorporated extensive simplifying assumptions regarding the geometry, tissue mechanical properties and boundary conditions, which can add uncertainties in the simulation results. Current FSI approaches employed to study LV dynamics are mainly based on conventional mesh-based methods such as the ALE formulation (141) or the IB method (64). The most significant challenge of mesh-based

FSI studies is dealing with the coaptation between the leaflets during valve closure, where the flow domain is separated into two unconnected regions, an issue that has been circumvented but not yet solved (202). Recently, there has been an increased interest in mesh-free methods, such as the SPH method (203). The fully Lagrangian nature of SPH offers several advantages, such as handling small material-to-void ratios, solving solid and fluid dynamic equations in the same algorithm (204), and modeling large deformations with domain fragmentation.

SPH has been successfully applied in different fields of fluid and solid mechanics over the past two decades (203). More recently, some researches have used SPH in FSI problems and validated the SPH-FE coupling approach by benchmark cases such as beam impact and elastic gate (205, 206). To date, most of the mesh-free cardiovascular studies have mainly focused on the blood flow through vessels or idealized LV geometries (151, 154, 155). Shahriari et al. (156) studied and validated the capability of SPH to simulate the blood flow in a rigid 2D LV model. The FSI capability of the SPH-FE approach has also been used to simulate blood flow in a transcatheter AV model (155). In Part 1 of Specific Aim1a, we extended the application of SPH to simulate the large-scale intraventricular hemodynamics in two realistic 3D LV models with simplified valve structures. The comparison between SPH results, a traditional CFD method, and in vivo PCMR and echocardiography data showed a good quantitative agreement.

In Part 2 of Specific Aim 1a, we will test the SPH-FE FSI method's capability to model the coupled complex AV and MV structural response and the intraventricular hemodynamics in one subject-specific LV-valve model (LV-FSI). In Specific Aim 1a, we

will focus on the LV-valve dynamics occurring under baseline healthy conditions. We therefore use the term “subject-specific” instead of “patient-specific”.

Although some model simplifications are made, this work is considered the first attempt to simulate the coupled 3D AV and MV nonlinear soft tissue dynamics and the intraventricular hemodynamics in a realistic LH model throughout the entire cardiac cycle. The cardiac wall motion will be prescribed based on full phase MSCT scans, while leaflet dynamics will be simulated using a fully-coupled FSI method. The LV structure used in this study takes into account various degrees of sophistication, including detailed MA and proximal LA motion, imaged-based asymmetric leaflet geometries, anisotropic hyperelastic constitutive models, and human material properties. Leaflet kinematics, valves structural response, and large-scale intraventricular hemodynamics will be studied in detail, and compare to subject-specific echocardiography measurements. Finally, in order to investigate the coupling effects of the valves in the ventricular hemodynamics, the LV flow obtained from the FSI model will be compared with the one obtained with a LV model without valves (Specific Aim 1a – Part 1, Subject 2 model).

5.2 Materials and Methods

5.2.1 Subject-specific LH model

Part 2 of Specific Aim 1a will build upon the validated Subject’s 2 LV-SPH model developed in Part 1 to increase the model complexity by adding the 3D native heart valve structures, creating a comprehensive subject-specific LH FSI model. The valve models include various degrees of sophistication, including imaged-based asymmetric leaflet

geometries, leaflet thickness and chordae tendineae with distinguishable chordal insertion points in the mitral leaflets.

A semi-automated segmentation method previously developed was used to extract the main cardiac structures of interest (207, 208). Briefly, cardiac wall and valvular geometries were identified and manually segmented from the rest of the heart structures using Hounsfield intensity thresholding and region growing techniques for the cardiac wall, combined with the brush tool and manual pixel editing for the valve leaflets and subvalvular components, making sure to digitally dissect and clearly differentiate individual mitral chordae. Next, smoothing and wrapping operations such as islands editing, removing extrusions, filling small holes and specific automatic smoothing modules were used to fix inconsistencies in the model due to image noise and improve the mesh quality. Altogether, approximately 30 hours of work were required to segment the MSCT data, including segmentation of the 10 cardiac frames for the cardiac wall.

The AV geometry was reconstructed at the mid-systolic phase (stress-free state) from this patient, however, valve calcification was not incorporated in order to mimic a healthy state. In addition, since the complete MV geometry was not clearly detected from the MSCT scans for this particular patient due to artifacts in the valve location, the MV was adapted from a previous study from our group that validated healthy MV dynamics by quantitatively comparing the closed valve shape from FE simulation with the MSCT images during systole (73). Special care was taken to ensure that the adapted MV resembled the same positioning of the subject-specific valve. The adapted MV geometry, reconstructed from the mid-diastolic phase (stress-free state), was scaled, translated and rotated until its boundary matched the MV boundary that was delineated from the subject-

specific MSCT scans. Chordae were classified into five groups according to the respective insertion zone on the leaflets: anterior strut, anterior marginal, posterior marginal, posterior intermediate, and posterior basal (22).

The reconstructed LH model with both valves can be seen in Figure 21a. The anterior-posterior long axis plane where the velocity measurements will be analyzed is indicated as a red line in Figure 21b. The red spheres denote the probe locations for velocity measurements through the valves. In Figure 21c, the blue rectangles represent the regions of interest for stress and strain calculations, while the red dots in the leaflets represent the location for leaflet kinematic measurements. In order to investigate the coupling effects of the valves in the flow dynamics, the LV-SPH model of that did not incorporated the AV and MV was used for comparison purposes. In the text, “LV-Valve” refers to the model with the valves, while “LV-NoValve” refers to the model without valves.

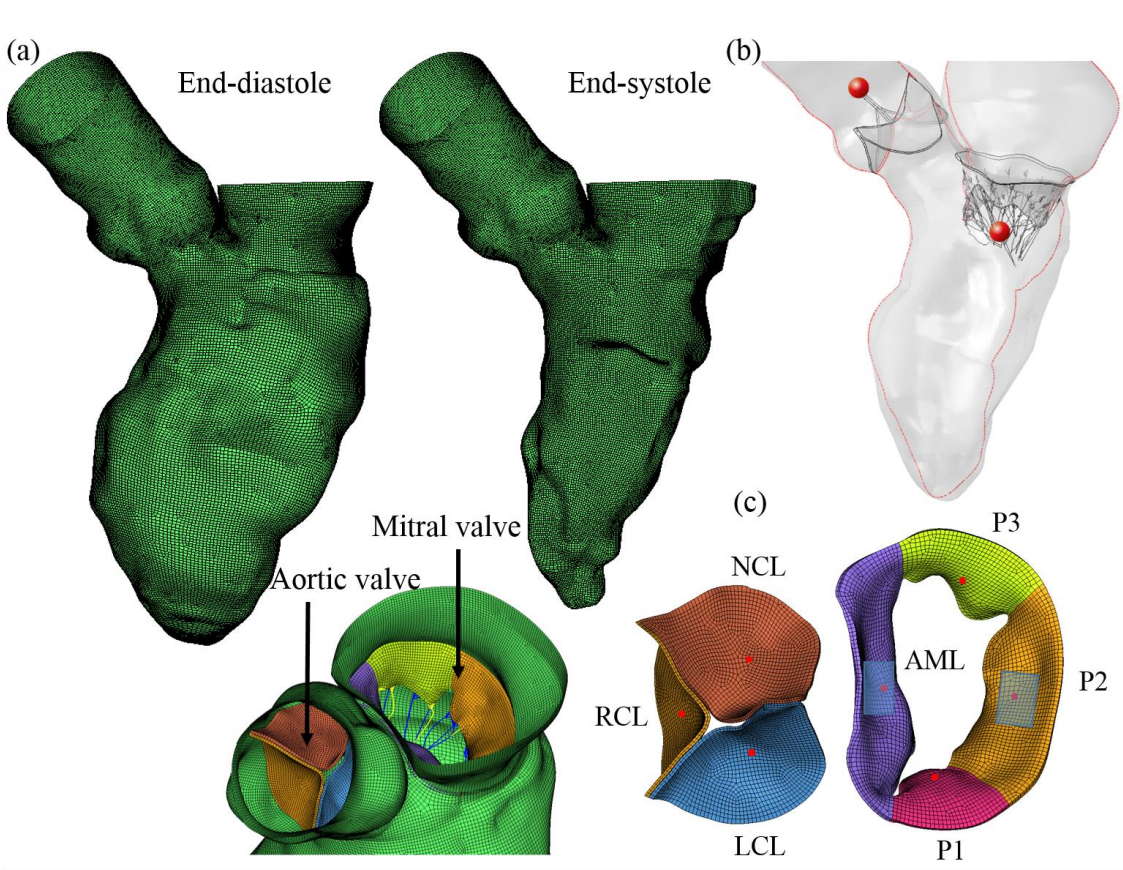

Figure 21. Schematic of LV-Valve model. (a) LV model at different phases, (b) The anterior-posterior long axis plane is shown by the red line. The red spheres denote the probe locations for velocity measurements, (c) Initial stress-free state for AV and MV. RCL: right coronary leaflet, LCL: left coronary leaflet, NCL: non-coronary leaflet, AML: anterior mitral leaflet. Posterior mitral leaflet (PML) is divided into lateral P1 scallop, central P2 scallop and medial P3 scallop.

5.2.2 FE modelling

FE meshes were generated for the LH model using Hypermesh (Altair Engineering, MI). 3D solid elements (eight-node hexahedral C3D8R elements) were used to capture the thickness of the AV and MV, 3D stress/displacement truss elements (two-node linear T3D2 elements) were used to model the MV chordae, and shell elements (four-node reduced

quadrilateral S4R elements) were used to represent the cardiac wall (i.e. LV, LA and LVOT). A constant thickness of 0.5 mm was given to the AV leaflets, while the MV leaflets had locally varying thickness with average values of 1 mm and 1.2 mm for the leaflet belly and edge regions, respectively. Two layers of elements were used across the leaflet thickness. The leaflet-chordae transition zone was modeled by creating fork-shaped truss elements at the chordal insertion points to mimic the native geometry and avoid stress concentration in the mitral leaflets (73).

Two different constitutive models were used to model the mechanical response of valve tissues. First, the modified anisotropic hyperelastic Holzapfel–Gasser–Ogden material (MHGO) model (209) was adopted to characterize the mechanical behavior of human AV and MV leaflets. The strain energy function was expressed as

$$\begin{aligned} W = {} & C_{10}\{\exp[C_{01}(\bar{I}_1 - 3)] - 1\} \\ & + \frac{k_1}{2k_2}\sum_{i=1}^{2}\left[\exp k_2\left[\kappa\bar{I}_1 + (1-3\kappa)\bar{I}_{4_i} - 1\right]^2 - 1\right] \\ & + \frac{1}{D}(J-1)^2, i = 1{,}2 \end{aligned} \tag{11}$$

where C_{10}, C_{01}, k_1, k_2, κ and D are material constants, and $\bar{I}_1$ and $\bar{I}_{4i}$ are the deviatoric strain invariants. C_{10} and C_{01} describe the matrix material, D is a material constant to impose incompressibility, and J is the determinant of the deformation gradient. k_1 is a positive constant with the dimension of stress to describe the fiber material and k_2 is a dimensionless parameter. In addition, κ describes the distribution of fiber orientation. Local coordinate systems were defined for each leaflet to include local fiber orientation. The anisotropic MHGO material model was implemented into Abaqus/Explicit with a user

sub-routine VMAT. The second material model used was the isotropic hyperelastic Ogden model (210), which was implemented to characterize the mechanical properties of human MV chordae. The Ogden strain energy function is given by

$$W = \sum_{i=1}^{N} \frac{2\mu_i}{a_i^2}(\bar{\lambda}_1^{a_i} + \bar{\lambda}_2^{a_i} + \bar{\lambda}_3^{a_i} - 3) \tag{12}$$

where μ_i and a_i are material constants, and $\bar{\lambda}_i$ are the modified principal stretches. Tissue material properties, obtained from in-house multiprotocol biaxial and uniaxial testing devices, were defined from a similar patient (age-, gender- and phenotype-matched) selected from an existing human cardiac tissue database established in our lab. Details of the determination of material parameters and FE implementation of these models have been described in our previous publications (211, 212). The material parameters used for valve tissues are listed in Table 2.

Table 2. Valve tissue material parameters.

MHGO model	C_{10} (kPa)	C_{01}	k_1 (kPa)	k_2	θ (°)	κ	D (kPa^{-1})
AV leaflets	1.738	11.368	2159.4	1158.9	4.59	0.2359	1.0e-5
AML	0.1245	13.665	11.007	84.84	13.09	0.0800	1.0e-5
PML	0.0502	15.004	3.021	144.48	25.51	0.0534	1.0e-5
Ogden model	μ_1 (kPa)	a_1	μ_2 (kPa)	a_2	μ_3 (kPa)	a_3	
Basal and intermediate chordae	10256.1	16.579	10653.8	16.554	10671.3	16.554	
Strut chordae	24341.7	11.338	10331.9	11.167	14913.6	11.188	
Marginal chordae	12995.5	15.651	13082.9	15.683	12869.7	15.662	

5.2.3 Boundary conditions

Two plate pistons located at the extensions were used to apply the boundary conditions on the LH model. As seen in Figure 22a, the LV-Valve model employed a constant LA pressure of 20 mmHg at the inlet, while a physiological aortic pressure waveform was applied at the outlet. This realistic setting allows the transvalvular pressure gradients and the LV pressure to be computed from the coupling of the fluid and structural physics. The shape of the aortic pressure waveform was carefully adjusted to be in phase with the subject-specific LV volume change waveform. Note that the atrial pressure slightly exceeds the normal physiological value in order to compensate for the long inlet extension used in the LV model. The LV-NoValve model, on the other hand, employed at the inlet the diastolic flow rate waveform derived from the LV volume change, with its value set to zero during systole (Figure 13b). For the outlet, the same aortic pressure waveform as in the LV-Valve model was applied. The patient's heart rate was approximately 75 bpm, corresponding to a cardiac cycle of 0.8 s. Note that in our models, the cardiac cycle begins at early systole, resembling the isovolumetric contraction phase. SPH particle sensitivity (155, 207) and valve mesh sensitivity (73) studies were previously performed. Simulations were run on an Intel Xeon E5-2670 cluster with 64 cores and required approximately 240 hours to run two cardiac cycles.

Cardiac wall motion was prescribed as previously explained in Part 1. The aortic and mitral leaflet boundaries were prescribed the same motion as the cardiac wall in the aortic and mitral annuli to move accordingly. Additionally, chordae origins were not directly attached to the PM tips in the LV-Valve model (see Figure 21b), but were tracked and displaced between two spatial locations representing PM tips location at mid-diastole

and mid-systole phases. The coupling between SPH and FE was handled by the node-to-surface contact algorithm since both methods are based on the Lagrangian description. Briefly, the contact force at the interface was calculated by finding the best penalty force to prevent interface penetration and satisfy conservation of momentum. The combined effect of the smoothing kernel interpolation function near the boundary and the node-to-surface contact interaction approximates the no-slip and no-penetration boundary conditions.

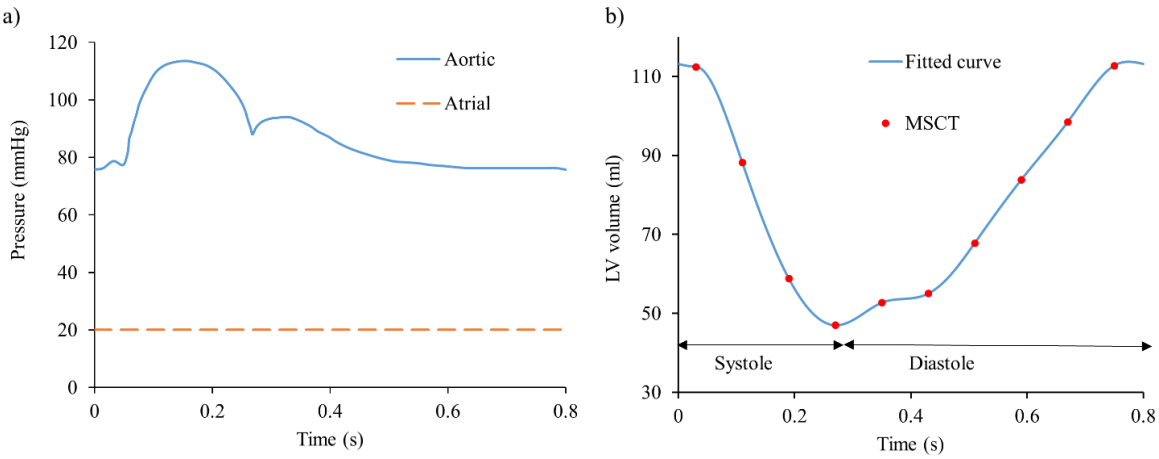

Figure 22. a) Aortic and atrial pressure boundary conditions, b) LV volume change waveform.

5.2.4 Data analysis

5.2.4.1 Structural analysis

Valve kinematics will be evaluated in terms of rapid valve opening (RVOT) and closure (RVCT) times, ejection time (ET), and MV leaflet opening and closing angles through the cardiac cycle. Subject-specific valve opening and closing times will be obtained from the

M-mode echo images, while MV leaflets angles will be measured from the Doppler recordings along the apical long-axis view. Maximum principal, radial and circumferential stress and strain distributions for the MV and AV will be quantified as well.

5.2.4.2 Fluid analysis

Global cardiac hemodynamics will be compared to subject-specific echo data in terms of mean and peak systolic pressure drops in the AV, mean and peak diastolic pressure drops in the MV, effective orifice area (EOA), E wave velocity, A wave velocity, E/A ratio, regurgitant volume (RV) and regurgitant fraction (RF). Hydrodynamic valve (drag) forces, that evaluate the contact forces exerted on the leaflets due to the blood flow. From the simulation, EOA was calculated for the AV (EOA_{AV}) (213) according to the equation $EOA_{AV}(\text{cm}^2) = \frac{MSF}{51.6\sqrt{\Delta P}}$, where MSF is the root mean square systolic flow rate (ml/s), and ΔP is the mean systolic pressure gradient (mmHg). Likewise, the EOA for the MV (214) was derived as $EOA_{MV}(\text{cm}^2) = \frac{MDF}{31\sqrt{\Delta P}}$, where MDF is the root mean square diastolic flow, and ΔP is the mean diastolic pressure gradient. The competency of the valves was quantified via the regurgitant volume (RV) and the regurgitation fraction, $RF = RV/SV$, where RV is the sum of the closing volume and leakage volume. Similarly as in Part 1, velocity vectors and contours at different long-axis and short-axis planes and at different time instances of the cardiac cycle will be evaluated. Maximum velocity waveforms at the MV and AV planes during the cardiac cycle will also be compared between the LV-valve FSI model and the subject-specific Doppler measurements.

5.3 Results

5.3.1 Valve kinematics

Valve kinematics were analyzed in terms of opening and closure dynamics during the entire cardiac cycle, and monitored through the time-dependent radial velocity of the midpoint (belly) of each leaflet (see red dots in Figure 21c). Figure 23a shows the computed RVOT and RVCT, defined as the duration tracts of the radial velocity curve with a high positive and high negative slope (215). Additionally, ET was calculated as the time from the initial opening to complete closure of the valve. The results reported in Figure 23a are also summarized in Table 3.

In Figure 23b, the opening and closing angles of the MV leaflets (dotted lines) are plotted against the angles measured from echo (solid lines) along the apical long axis view (Figure 23c). During early-diastole, the onset of rapid valve opening occurs after the LV pressure falls below the LA pressure. During this phase, the simulated leaflets followed a similar opening timing pattern as the echo measurements. During mid- to end-diastole, which represent some partial leaflet closing after the E-wave followed by a second opening due to atrial contraction (A-wave), the simulated leaflets followed a similar pattern as in the echo data, but with higher opening angles. Note that for both numerical and *in vivo* measurements, the AML maintained a higher opening angle than the PML during the diastolic phase.

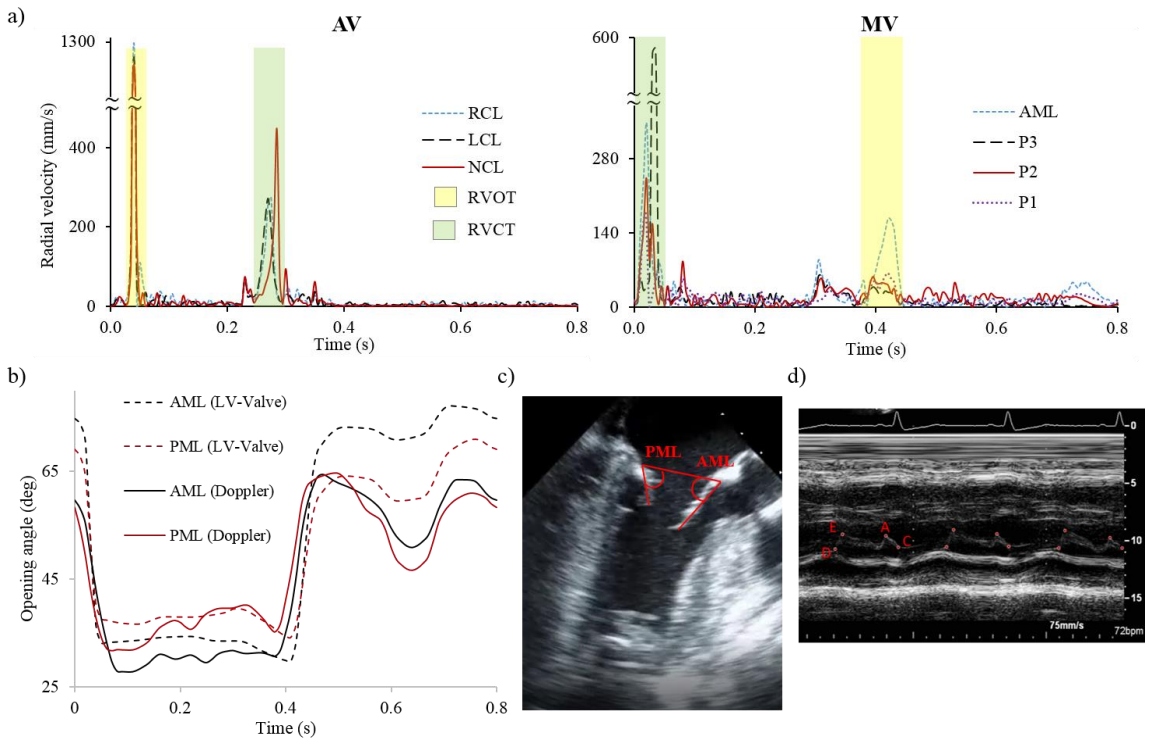

Figure 23. a) Time-dependent radial velocity of the belly (midpoint) of AV and MV leaflets. The measured RVOT and RVCT are highlighted in pale yellow and green, respectively, b) Opening angle of MV leaflets for LV-Valve model and echo data, c) schematic of angle measurements from echo video, d) M-mode echo recording at the MV.

Additionally, Figure 23d shows the subject-specific M-mode echo recording at the MV position. Letters D, E, A and C represent end-systole before MV opening, peak of early opening, peak of late opening at atrial contraction, and MV closure, respectively. Therefore, RVOT can be calculated as the time interval between D and E, and RVCT as the time interval between A and C. As seen in Table 3, simulation results were consistent with measurements from *in vivo* and *in vitro* experiments (216-218), and with the subject-specific M-mode echo data. The largest quantitative mismatch between the simulation and *in vivo* data was for the MV RVCT.

Table 3. Comparison of ET, RVOT, and RVCT between LV-Valve model, subject-specific echo data and literature.

	AV		MV		
time (ms)	**LV-Valve**	**Literature (216)**	**LV-Valve**	**Literature (217, 218)**	**M-mode echo**
ET	270	329 ± 63	470	N/A	473
RVOT	30	57.5 ± 11.1	75	75-100	50
RVCT	50	39.5 ± 5	55	100-150	94

5.3.2 Stress and strain distributions

Maximum principal logarithmic strain (LE) contours of the aortic and mitral leaflets at representative time points of the opening and closing phases are shown in Figure 24. For the AV, the peak strain during the ejection phase was observed along the leaflet attachment line, with a peak value around 16% (Figure 24a). During the valve closing phase, large strains were concentrated in the middle region of the leaflet attachment line, followed by the commissure regions. Some high strain areas were also observed in the ventricular layer near the central region, extending upwards towards the leaflet free edge during the closing and opening phases.

For the MV, Figure 24b shows that during the closing phase a heterogeneous strain distribution was found in the mitral leaflets, with high values located in the belly to annular P2 region, in the AML close to the right and left fibrous trigone annular regions, and at the insertion points of the chordae tendineae. During the opening phase, much lower strain values were obtained, with the maximum strain occurring along the MA. In general, significant heterogeneity was observed in the strain distribution for both valves due to tissue anisotropy and geometric asymmetry.

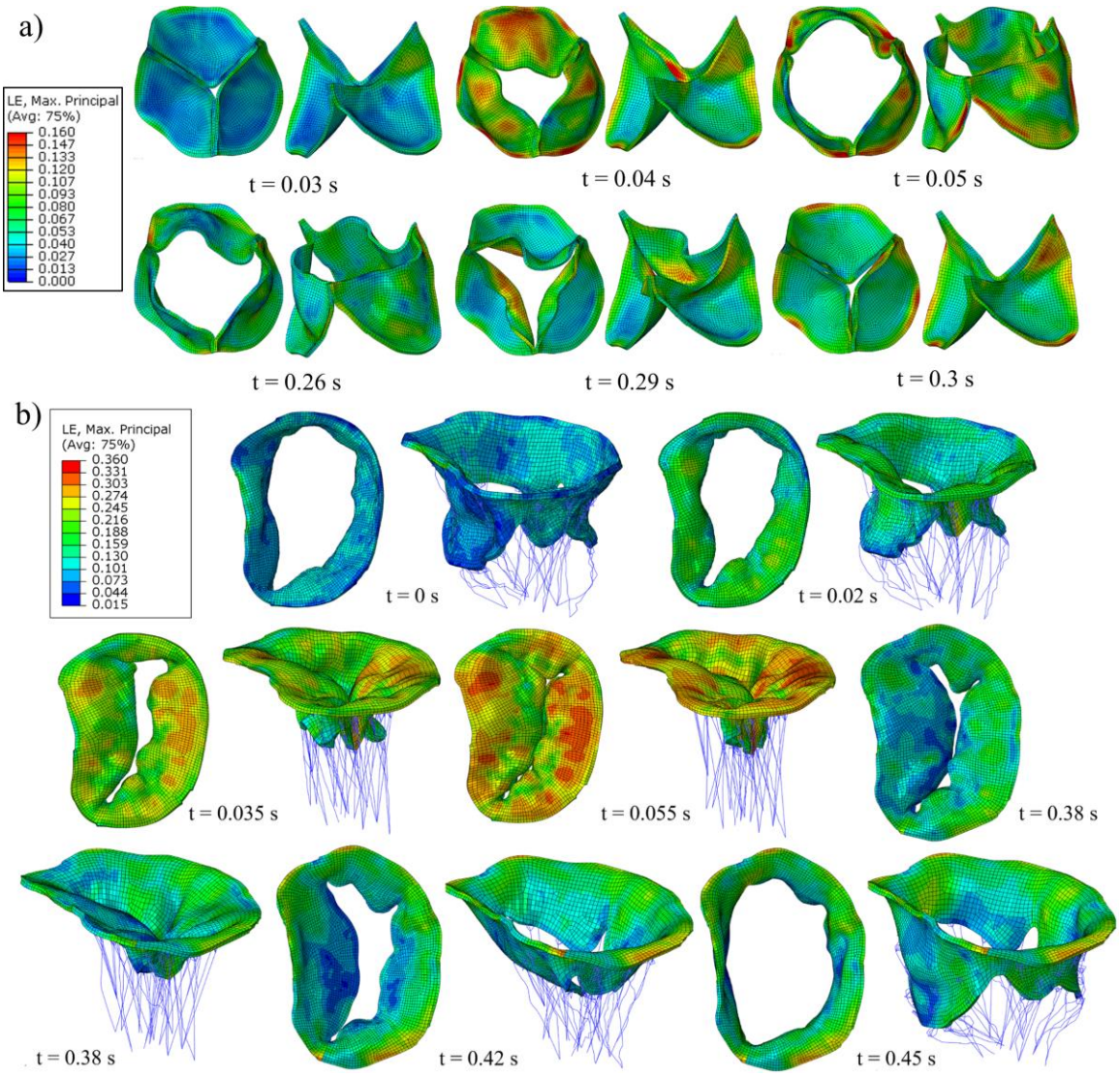

Figure 24. Opening and closing of a) AV and b) MV leaflets colored by the maximum principal strain. Strain in chordae tendineae not plotted.

In addition, Figure 25 shows the radial and circumferential averaged (over the measuring region) stresses and strains for AML and PML belly regions, as marked in the rectangles of Figure 21c. From Figure 25a and b it can be seen that, in general, higher radial and circumferential stresses were observed in the AML than in the PML. Note that the spike values enclosed by the red circles during MV closure are due to numerical artifacts,

which will be discussed later. In the diastolic phase, the stress values for both leaflets were negligible when the MV was open, with the PML circumferential stress being slightly higher at some time intervals.

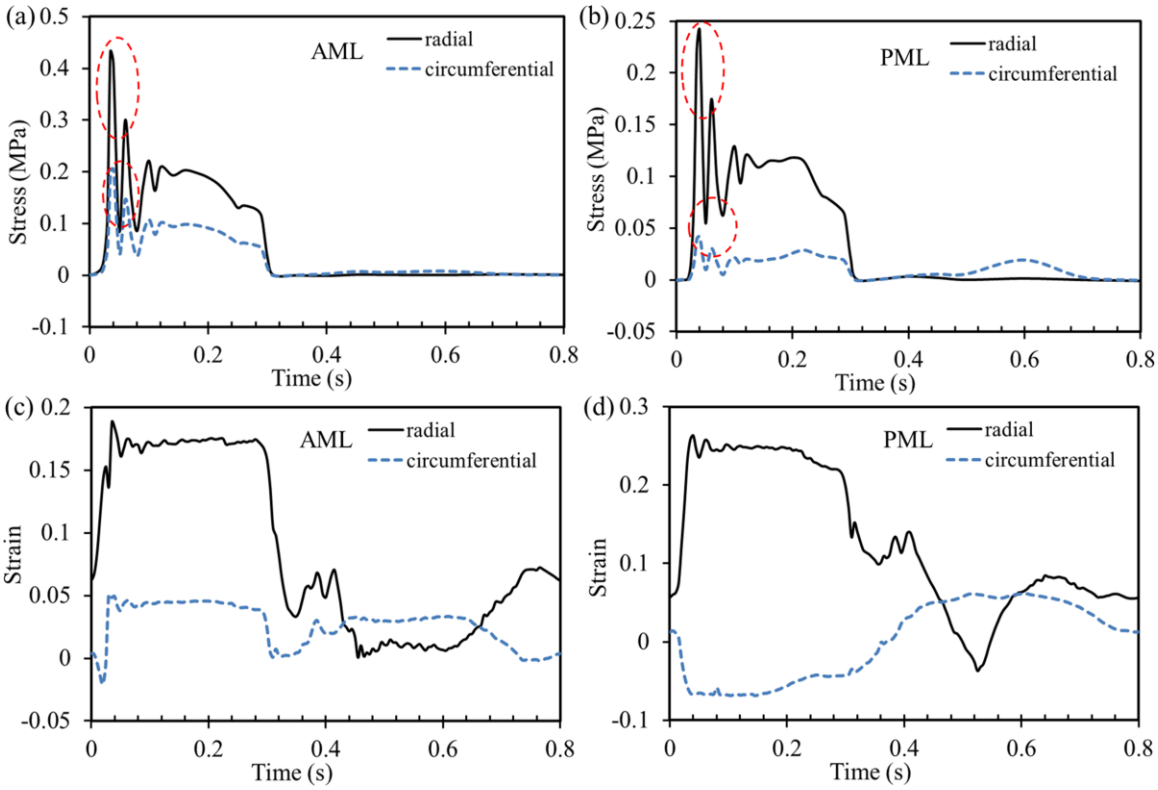

Figure 25. Averaged circumferential and radial stresses of (a) AML and (b) PML, and circumferential and radial strains of (c) AML and (d) PML, within the region of interest, as marked in Figure 21c. Note the spike values marked by the circles are due to numerical artifacts.

5.3.3 LV hemodynamics

Table 4 compares global hemodynamic parameters calculated from the LV-Valve model and obtained from the subject-specific echo data. In general, the comparison between the numerical results and the *in vivo* measurements showed a reasonable agreement. However,

it is noted that the difference between these values is significant during the diastolic phase. This is mainly due to the absence of calcifications at the MA in our adapted MV model compared to clinical observations. Additionally, Figure 26a shows the transvalvular pressure drop waveforms, measured one diameter upstream and three diameters downstream from the valve annuli. The shape and values of the pressure waveforms agree with well-known physiological measurements, except for the spike values enclosed by the circles during the early systolic phase, which will be discussed later.

Table 4. Comparison of hemodynamic parameters calculated from the LV-Valve model and the subject-specific echo data.

Parameters	LV-Valve	Echo Doppler
MSPD (mmHg)	11.1	10.1
PSPD (mmHg)	23.3	18.2
MDPD (mmHg)	2.0	3.6
PDPD (mmHg)	5.2	8.2
E/A	1.02	0.88
EOA_{AV} (cm^2)	1.6	1.3
EOA_{MV} (cm^2)	3.8	2.8
RV_{AV} (ml)	4.8	N/A
RF_{AV} (%)	7.4	N/A
RV_{MV} (ml)	9.8	N/A
RF_{MV} (%)	15	N/A

5.3.4 Hydrodynamic forces

Figure 26b shows the axial hydrodynamic forces acting on the AV and MV, calculated by vector addition of the axial contact forces exerted on the leaflets surface due to the blood flow. Positive values represent the opening force, while negative values correspond to the closing force. During systole, peak values were 2.17 N and -14.6 N for the AV and MV, respectively. In diastole, peak forces reached up to -8.28 N and 0.54 N for the AV and MV,

respectively. The MV opening force was found to be much lower than the value of the AV, which is due to the smaller mitral transvalvular pressure drop. During the closing phase, the hydrodynamic force on the MV was much higher than that on the AV.

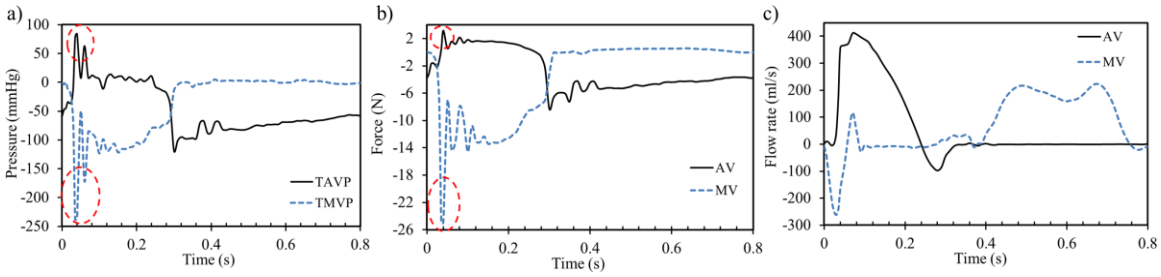

Figure 26. a) Transvalvular pressure drop, b) hydrodynamic forces acting on the valves, and c) flow rate through the valves. Note the spike values marked by the circles are due to numerical artifacts.

Table 5 summarizes the average chordae tendineae tension at peak systolic pressure. These forces were found to be well within the range of *in vitro* experimental results (219). Additionally, PM forces for the LV-Valve model were determined as the sum of the reaction forces on the chordal origin nodes that represent the tips of the PMs. At the systolic peak, the forces for the anterolateral and posteromedial PMs were 5.18 N and 4.7 N, respectively. These values agree with to the ones measured *in vitro* by Jensen et al. (15) and simulated by Wang et al. (73).

Table 5. Chordae peak systolic tension.

Chordae force (N)	LV-Valve	Jimenez et al. (219)
Marginal	0.221	0.23 ± 0.06
Strut	0.607	0.65 ± 0.13
Basal	0.235	0.22 ± 0.07

5.3.5 Blood flow velocity

Figure 26c shows the calculated flow rate through the valves during the entire cardiac cycle. The retrograde flow can clearly be seen during valve closing. By integrating the negative flow rate in time, the RV of the AV and MV was calculated as 4.8 ml and 9.8 ml, respectively, representing a healthy valvular state. Note that RV is an important clinical hydrodynamic metric that can only be calculated from a fully-coupled FSI approach, which several previously published models (220, 221) were not able to quantify. In Figure 27a, the maximum flow velocity downstream of the AV (Figure 21b) was monitored throughout systole and compared to the subject-specific Doppler recordings (Figure 27c). A quantitative comparison indicates that the AV velocity reached a similar peak value in both the LV-Valve model and the Doppler measurement. Furthermore, when compared to the LV-NoValve model, a much lower peak velocity of 1.16 m/s was observed. During the AV closing phase, a retrograde velocity is clearly seen for the LV-Valve model. In the LV-NoValve model, however, the retrograde velocity cannot be calculated. It is also important to be aware of the considerable limitations associated with Doppler velocity measurements. Since CW Doppler examination cannot pinpoint where along the ultrasound beam the measured velocity comes from (222), retrograde flow measurements are challenging to obtain.

Similarly, the comparison of the flow velocity through the MV is shown in Figure 27b. The flow velocity was calculated at the midpoint between the tips of the opened MV leaflets (Figure 21b), which corresponds to the probe location usually used in PW Doppler measurements. It is noted that although the LV-Valve model had a similar MV waveform pattern as the echo data (Figure 27d), the peak value was not accurately predicted (0.74

m/s vs. 1.17 m/s). Moreover, it is observed that for the LV-NoValve model the velocity was much lower (0.28 m/s) than the echo data.

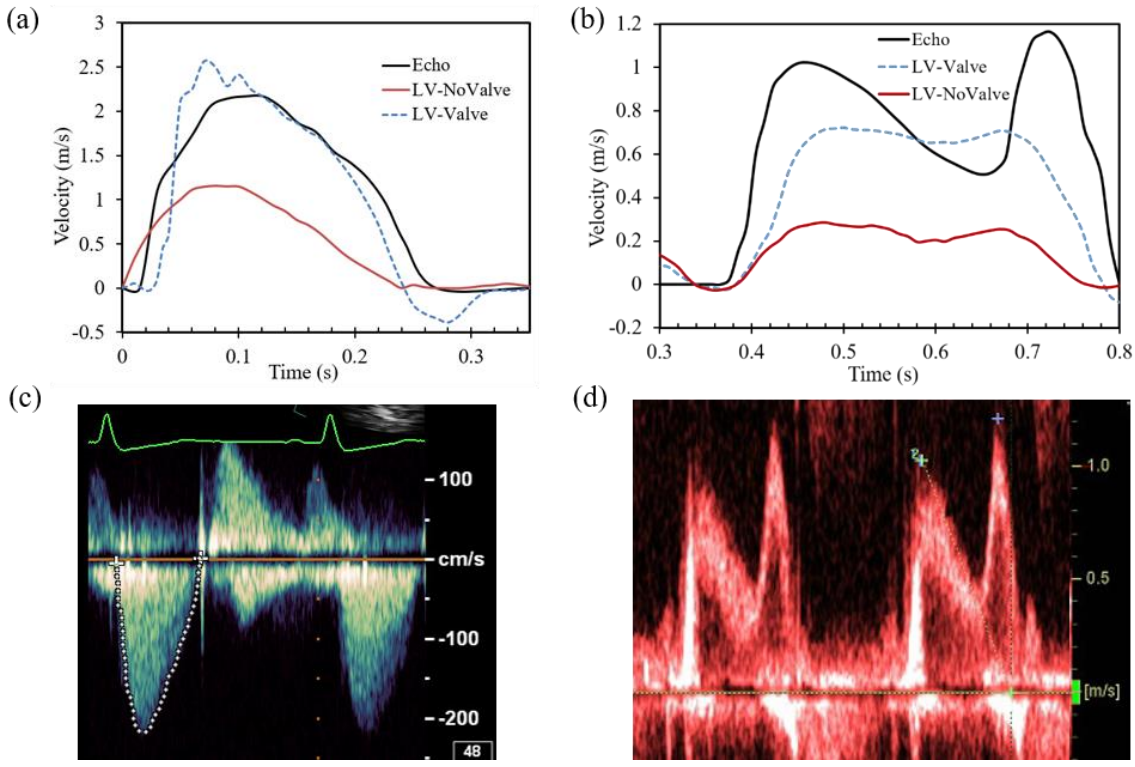

Figure 27. Flow velocity through the (a) AV and (b) MV. Doppler echo velocity recordings at c) AV and d) MV.

5.3.6 Large-scale intraventricular flow patterns

Flow velocity vector fields in the anterior-posterior long axis plane (Figure 21b) for the LV-Valve and LV-NoValve models at two different time points are shown in Figure 28a. At peak systole (~80 ms), a constricted and symmetric central jet was observed immediately downstream of the AV in the LV-Valve model, whereas a relatively uniform velocity profile from the LVOT to the ascending aorta was observed in the LV-NoValve

model. As expected, without the constriction of the AV, the central jet velocity in the LV-NoValve model is much lower. Similarly, during the E-wave (~490 ms), the flow jet through the MV cannot be observed in the LV-NoValve model. Additionally, a vortex adjacent to the AML that is developed in the LV-Valve model is not present in the LV-NoValve model.

Finally, flow velocity vector fields from the LV-Valve model at additional time points are shown in Figure 28b. During MV (~25 ms) and AV (~285 ms) closing, a large retrograde flow through the valve is observed, while the opposite valve remained fully closed. A large asymmetric vortex that has been shown to initiate MV closure and pre-ejection filling of the LVOT (12) can be seen at late diastole (~740 ms).

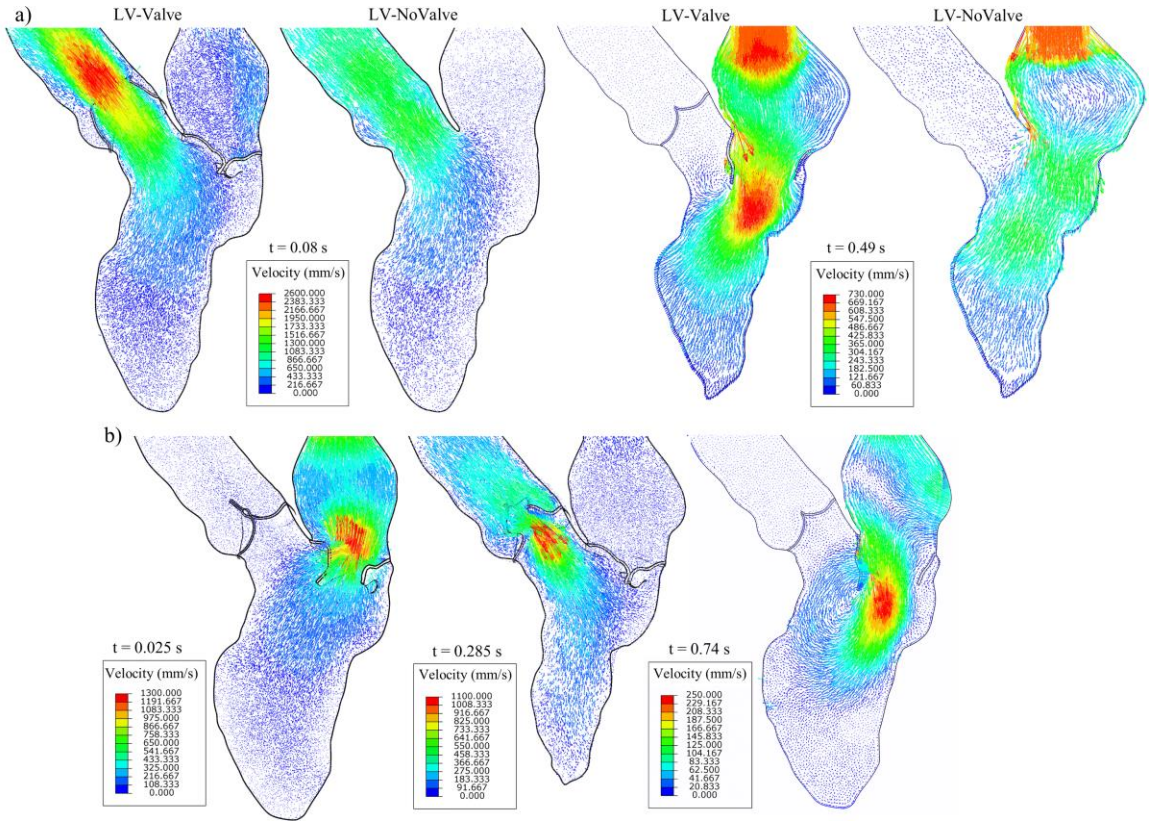

Figure 28. a) Velocity vector fields in the anterior-posterior plane for the LV-Valve and LV-NoValve models at peak systole and E wave, and b) for the LV-Valve model during MV closing, AV closing and late diastole.

5.4 Discussion

5.4.1 Structural analysis

Understanding the coupled interaction between the valves and the LV is important for the assessment of cardiac function in healthy and diseased states, as well as for the evaluation and design of clinical procedures and medical devices for valve repair and replacement. In Part 2 of Specific Aim 1a, we quantified the valves maximum principal strain, and the circumferential and radial stress and strain of the AML and PML throughout the entire

cardiac cycle. In particular, it was found that the leaflets experienced a highly anisotropic mechanical response. Note that during systole, Figure 258c,d shows that the radial strain was higher in the PML than in the AML. This feature was previously observed by Lee et al. (223) and Watton et al. (83). In the circumferential direction, however, the PML showed negative strain values during the entire aortic ejection phase. The PML compressive strain is likely caused by the strong mechanical coupling between the circumferential and radial directions at systole. Indeed, in vivo and in vitro studies (217, 224) have shown that the coupling of the stretches in two directions can generate compressive stretches in the circumferential direction of the PML at the beginning of MV closure, when there is a large stretch in the radial direction.

Additionally, MV strains shown in Figure 25c,d were qualitatively similar to previous *in vivo* and *in vitro* studies (224-227), with a rapid strain increase to the point of full coaptation, followed by a stable plateau in both radial and circumferential directions during systolic ejection. In Table 6, the strains obtained numerically at the fully loaded state are quantitatively compared to those measured *in vivo* and *in vitro* in ovine and porcine MVs. Our numerical results show a close agreement with the *in vivo* and experimental results.

Table 6. Comparison of the MV strain values between the current study and the literature.

Study	Model	Strain (%)
AML		
LV-Valve	FSI	Circumferential: 4.5 Radial: 17.2
Sacks et al. (225)	*In vivo*	Circumferential: 3.2 ± 0.4 Radial: 16 ± 3
Amini et al. (226)	*In vivo*	Circumferential: 8 Radial: 21
Sacks et al. (227)	*In vitro*	Circumferential: 11 ± 3 Radial: 30 ± 8
Jimenez et al. (228)	*In vitro*	Circumferential: 11 ± 5 Radial: 22 ± 7
PML		
LV-Valve	FSI	Circumferential: -6.8 Radial: 25.1
He et al. (217)	*In vitro*	Circumferential: 3 Radial: 23
Padala et al. (229)	*In vitro*	Circumferential: 10 ± 8 Radial: 29 ± 8

5.4.2 Fluid analysis

A quantitative flow field comparison between the LV-Valve model and the LV-NoValve models is presented in Figure 28a. The presence of the AV resulted in a decreased orifice area of 2.24 cm^2 at the tip of the leaflets during peak systole. Meanwhile, without the valve, the geometric orifice area at the annulus was about 4.55 cm^2. The large-scale flow patterns were quite different as well. Figure 28a shows that for the LV-Valve model, the maximum velocity occurred just downstream of the AV, where the flow jet is highly concentrated but the flow velocity inside the sinus region is less than 0.1 m/s. However, in the LV-NoValve model, the maximum flow velocity occurred at the annulus with an unrealistically high flow velocity of 0.5 m/s in the sinus region. Similarly, the MV flow velocity was much

higher in the LV-Valve model than that in the LV-NoValve model. Due to the strong flow jet and the closure of the AV, a vortex adjacent to the AML was developed in the LV-Valve model, which was not seen in the LV-NoValve model. This vortex is considered to act as a reservoir that stores kinetic energy as it redirects blood towards the lateral LV wall and initiates MV closure and pre-ejection filling of the LVOT in late-diastole (12). It is also noted that since complete closure of the MV and AV was achieved in the FSI simulation, several interesting characteristics such as regurgitant flow have been observed (Figure 28b) and quantified (Table 4).

The spike values enclosed by the red circles in the leaflets stresses (Figure 25a,b), transvalvular pressures (Figure 26a) and hydrodynamic forces (Figure 26b) are thought to be caused by numerical artifacts in the FSI simulation. During early systole, there is a short time period when both valves are nearly closed, forming a nearly closed system. Due to the assumption of incompressible fluid, a small compression in volume for a closed system can cause a large change in pressure. In our FSI model, the motion of the cardiac wall was prescribed according to the MSCT data, thus, a small decrease in LV volume, which is very likely to occur during early systole, could lead to a large fluctuation in pressure. This fluctuation, however, damped out rapidly due to the viscous effect of the fluid. This numerical artifact could be resolved by modeling the interaction between the myocardium and the blood flow by considering the active contraction of the myocardium.

Flow velocity passing through the MV from our models was compared to the Doppler echo data in Figure 27b. Even with the inclusion of the valves, our simulated flow velocity is lower than that of the subject-specific data. Two possible reasons may cause this discrepancy: 1) the MV geometry used in the LV-Valve model is not subject-specific but

was adapted from a previous study from our group (73). Specifically, MA calcification was detected in the subject-specific Doppler examination (see Figure 23c) but was not included in our model in order to mimic a healthy state. MA calcification could potentially restrict normal leaflet motion and cause a smaller opening area during diastole. Indeed, as shown in Figure 23b and Table 4, relatively larger mitral leaflets opening angle and EOA, as well as lower MDPD and PDPD values were obtained from the FSI simulation compared to the *in vivo* measurements; 2) only proximal LA wall motion was included in our model due to the limited imaging window of the MSCT images. The incomplete LA dynamics could affect the mitral flow during atrial passive filling and contraction (60, 230). Despite these limitations, our results are largely consistent with subject-specific *in vivo* measurements, clinical observations and *in vivo* and *in vitro* studies of healthy LV-MV-AV dynamics.

5.5 Limitations

As explained in Part 1, the no-slip boundary condition in Abaqus SPH is not fully constrained. This limited imposition is likely to affect the flow solution in the wall boundary layer and limit the study of the small-scale flow features seen in the LV blood flow (207). Second, cardiac wall motion was prescribed according to the subject-specific MSCT imaging data. With this approach, the mesh deformation is independent of the solution of the fluid equations because all the nodes of the cardiac wall have prescribed displacements at each time step. The use of this method is based on the assumption that the flow-induced load on the cardiac wall is minor in comparison to the structural-induced load on the fluid flow (231). It is important to remember that as long the prescribed wall motion closely resembles the subject-specific MSCT images, the blood flow dynamics will be similar whether the wall motion is prescribed or computed by a coupled solution.

CHAPTER 6. SPECIFIC AIM 1B – PART 1, LV-VALVE DYNAMICS UNDER PRIMARY MITRAL REGURGITATION

6.1 Introduction

MV prolapse following rupture of the chordae tendineae is a major cause of primary MR, and is associated with several causes such as bacterial endocarditis, local myxomatous degeneration, connective tissue abnormalities, hypertrophic cardiomyopathy, and blunt chest trauma (232). Mild varieties of mitral chordae rupture generally involve separation of a single chorda, which can lead to minimum hemodynamic effects and requires neither intervention nor treatment. Rupture of multiple chordae, however, may cause moderate to severe acute or chronic MR (232). Studies have shown that chordae rupture may be either immediate onset or a progressive process in which minimal rupture precedes more extensive or even complete rupture (233). To restore normal MV function and prevent further pathologic progression, MV repair or replacement can be performed (232). A variety of surgical and transcatheter repair treatments are currently available, however, in many cases there is a sub-optimal selection of the treatment attributed to the complicated repair techniques and the mitral apparatus complex geometry that require extensive surgical experience and specialized skills (38).

Computational modeling of heart valve dynamics and function is an active research field that not only can allow an in–depth examination of the dynamics of the LV-valve complex under normal and diseased states, but can also offer potential to inform the therapeutic decision-making process (212). FE studies have been performed in the past

with the goal to investigate MV dynamics after chordae rupture. Kunzelman and colleagues (97, 98) were among the first to study the effects of chordae rupture and their repair on MV function. More recently, Kim at al. (99-101) and Sturla et al. (102, 103) evaluated the biomechanical characteristics of MV models with PML prolapse, and compared different repair techniques such as neo-chordae and leaflet resection. In these FE studies, chordae structure was mainly determined from published clinical data and ex vivo findings due to the limited resolution of the medical image data. Moreover, FE or structural-only models assume the hemodynamic pressure load is uniformly distributed over the leaflet surface, a factor which has been previously shown to affect valve dynamics (3, 136). Structural valve models are appropriate for simulation of quasi-static events such as closed valves, but in order to accurately model full dynamic/transient valve dynamics, an FSI modeling approach that accounts for the strong coupling between the large deformation of the leaflets and the intraventricular blood flow is required (3).

The first FSI model to investigate MV function with ruptured chordae was presented by Toma et al. (88). In this study, the importance of individual chordae on MV closure dynamics was assessed by simulating rupture in every of the 51 possible chordae branches. However, a rigid tube was used as an approximation of the LV domain, neglecting the cardiac wall motion and its direct effect on the blood flow. The severity of the resultant MR was also approximated by calculating the regurgitant orifice area, with no hemodynamic variables analyzed. In the study by Khodaei et al. (234), although the modeling approach included the LV geometry to account for a physiologic moving boundary, several critical simplifications such as an idealized MV geometry, the omission of the LA and AV geometries, and the modeling of only the valve closing phase limited

the findings of the study. Due to the complex mechanical coupling between the MV and the LV mediated through the PM, the chordae tendineae and the dynamic MA, rigorous modeling of MV dynamics under normal and diseased states should include the entire LH complex. Indeed, it has been determined that even with a rigid U-shaped LV model, the intraventricular mitral flow patterns are substantially different from that estimated using a tubular geometry (3).

In Specific Aim 1b – Part 1, we will make use of the subject-specific LH model previously developed and validated in Specific Aim 1a – Part 2 to investigate the coupled LV-valve pathological dynamics under primary MR following mitral chordae rupture. The FSI framework used in this study takes into account the complexity of the LH morphology, the large deformation experienced by the aortic and mitral leaflets and the cardiac wall, the anisotropic nonlinear elastic behavior of the valvular tissue, and the pulsatile hemodynamic loads during the entire cardiac cycle. FSI simulations of LH dynamics under physiologic (control) and seven chordae rupture conditions will be performed and compared, and the effects on the force balance of the mitral apparatus, leaflets deformation state, MR severity, LH hemodynamics and overall cardiac efficiency will be investigated.

6.2 Materials and Methods

Figure 29 presents our computational modeling protocol for investigation of LH dynamics following mitral chordae rupture. This protocol was composed of FSI simulation of physiologic LH function (control), virtual modeling of multiple levels of chordae rupture, FSI simulation of LH function after chordae rupture, and evaluation of the functional and biomechanics characteristics of the coupled LV-valve pathological dynamics.

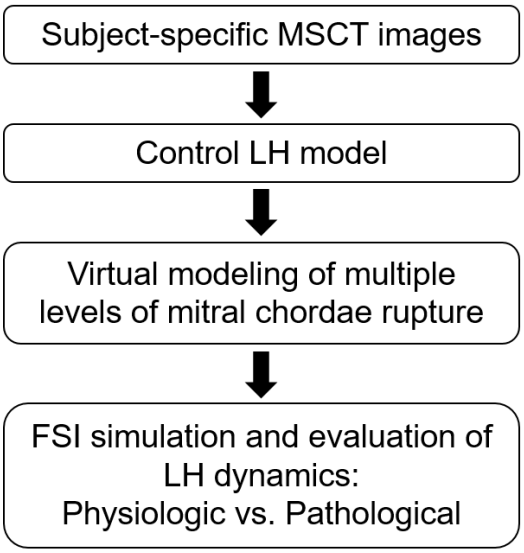

Figure 29. Computational modeling protocol for investigation of LH dynamics following mitral chordae rupture.

6.2.1 Subject-specific LH model

In this study, we employed the healthy LV-valve model developed in Specific Aim 1a – Part 2 (Subject 2). As seen in Figure 30A, this control LH model comprises all major cardiac structures, including the aortic root, AV, LV, MV and LA. As seen in Figure 30B, the detailed mitral chordae structure (number, position, length, branching, origins of the PM tips, and insertions into the leaflets) was clearly visible from the MSCT images, which had excellent clarity and crisp detail (73). Chordae were classified into five groups according to the respective insertion zone on the leaflets: anterior strut, anterior marginal, posterior marginal, posterior intermediate, and posterior basal (22). As shown in Figure 30D, marginal chordae insert into the leaflet free edge, intermediate chordae insert on the leaflet rough zone, and basal chordae insert closer to the leaflet base. High-quality images also allowed us to identify and delineate the chordae that protruded from the PM heads.

Simple point insertions were then used to model the distribution of the chordae origins on the PM tips. Identifying and creating the chordae to leaflet transition zone, on the other hand, is a nontrivial problem, since chordae seamlessly fuse into the leaflets and limited image resolution can prevent the complete detection of this detailed structure.

For the basal and strut chordae, the leaflet-chordae transition zone was easily identified from the MSCT images. Fork-shaped truss elements were used to follow the visible chordae splits and avoid local stress concentrations on the leaflets. For some of the intermediate and marginal chordae, however, the transition region was not clearly detected. Thus, the number of splits and their lengths were initially estimated and required further manual refinement. This optimization process aimed to quantitatively match the FE deformed MV systolic geometry with the subject-specific MSCT images (73). In summary, chordae originated from the APM and PPM tips, and distributed to the ventricular surface of the leaflets as presented in Table 7. A total of 17 chordae origins were modeled from the PM tips. Cross-sectional area values of 0.71 mm^2, 2.05 mm^2, and 0.38 mm^2 were assigned to basal/intermediate, strut, and marginal chordae, respectively (73). Each chord was modeled with up to 10 elements, with an average element length of 1.5 mm.

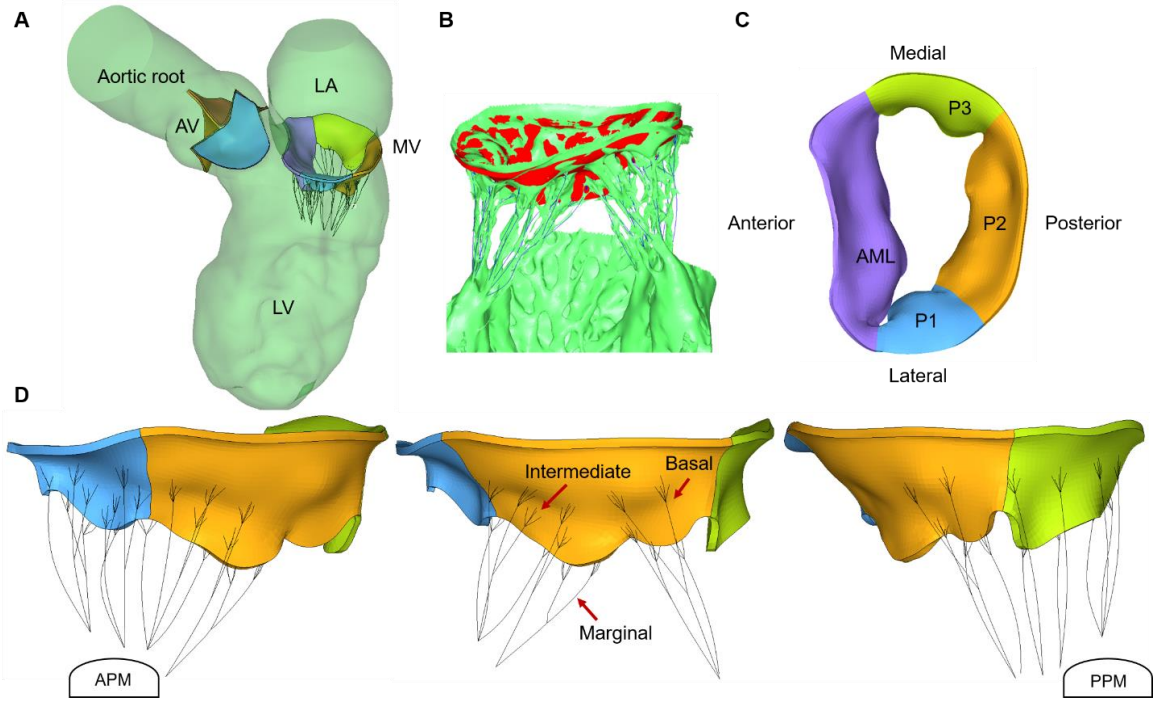

Figure 30. A) Control LH model, B) MV model reconstructed from MSCT images, C) top view of MV with four sub-regions, D) PML chordae groups. AML chordae not shown for clarity.

Table 7. Mitral chordae structure.

		From APM	From PPM
Number of chordae origins	AML	5	3
	PML	4	5
Number of chordae leaflet insertions	AML marginal	8	6
	AML strut	3	4
	PML marginal	7	6
	PML intermediate	7	1
	PML basal	5	6

6.2.2 Chordae rupture modelling

The control LH model was defined as having all mitral apparatus anatomical structures intact. PML prolapse is more prevalent than AML prolapse (235), usually involving ruptured chordae in the central scallop (P2), which then extends to the lateral P1 and P3 scallops (102, 103, 236, 237) (Figure 30C). Thus, the chordae rupture LH models were virtually created by modifying the control model, initially removing marginal and intermediate chordae elements in the individual PML scallops, and then progressing towards rupture of the basal chordae; causing partial or total double scallop prolapse. A total of seven chordae rupture LH models were created.

6.2.3 Boundary conditions

Pressure boundary conditions were applied at the atrial inlet and aortic outlet of the LH models. For the control model, a constant LA pressure of 20 mmHg was prescribed at the inlet, while an aortic pressure waveform, as seen in Figure 31, was applied at the outlet (208). In acute MR due to ruptured chordae, RV_{MV} in a normal-sized LA results in a marked increase in the atrial pressure (elevated V-wave) (238). Thus, the chordae rupture models employed a pathological atrial inlet pressure waveform (239), while the same aortic pressure waveform as in the control model was applied at the outlet.

Cardiac wall motion was prescribed as previously explained in Specific Aim 1a. In this study, the cardiac wall motion was kept the same for all LH models. This approach aims to replicate the instantaneous changes in cardiac dynamics during acute MR due to chordae rupture, when the LV has not yet remodeled, but the afterload is decreased as the

result of partial systolic emptying into the LA. Thus, the compensatory and cardiac remodeling mechanisms under chronic MR were not considered.

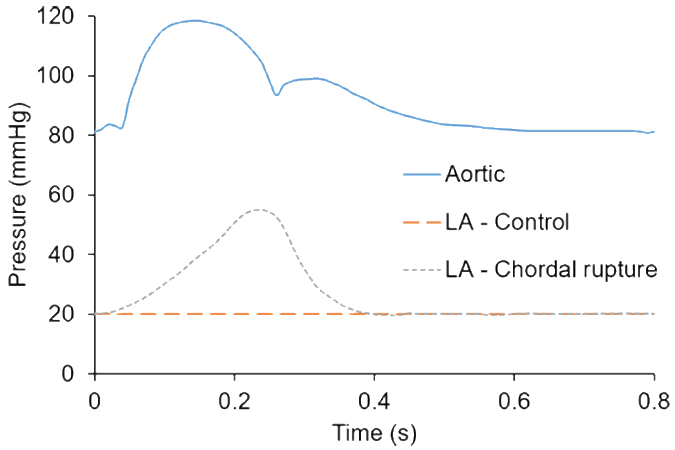

Figure 31. Aortic and LA pressure boundary conditions.

6.2.4 Data analysis

In addition to the structural and hemodynamics variables previously presented in Specific Aim 1a – Part 2, the following parameters were quantified in this study. The net force carried by the different chordae tendineae groups at peak systolic pressure. The force experienced by a particular chordae group was calculated as the sum of vectors representing the tension in each individual chorda attached to that chordae group. In order to facilitate visualization and analysis, LH models were grouped according to the PM from where the chordae ruptured.

In order to quantitatively grade the severity of MR for the different LH models, the RV_{MV} was determined by the time integral of the negative transmitral systolic flow, where RV_{MV} is equal to the sum of the closing volume and the leakage volume. In this study, the

closing volume was defined as the volume of blood flowing retrograde through the valve during its closure, and was quantified for all models from the start of negative transmitral flow at early systole until the control model reached a positive mitral flow, as indicated by the dotted line in Figure 32B. Any fluid volume accumulation after valve closure resulted from leakage and it was referred to as leakage volume. We note that for MR cases, there is no widely-accepted definition to distinguish between the closing and leakage volumes. The combination of the forward stroke volume (SV_{AV}) and the RV_{MV} is known as the total SV of the LV ($LVSV$), which was used to calculate the regurgitant fraction, $RF_{MV} = RV_{MV}/LVSV$

LV efficiency, an important measure of ventricular pump performance, is defined as the efficiency of energy transfer from the LV to the arterial system (240). This variable represents the percentage of total energy expenditure by the myocardium that is converted into external stroke work (SW). LV efficiency was calculated as fSW/PVA, where fSW is the forward SW, and was defined as the time integral of the continuous product of flow across the AV and the aortic pressure during systole (241). From a pressure-volume loop, PVA, known as the pressure volume area, represents the total mechanical energy generated by ventricular contraction, where $PVA = PE + SW$ (242). SW corresponds to the area of the pressure-volume loop, and characterizes the external mechanical work achieved by the heart to eject the $LVSV$. PE, or potential energy, on the other hand, is the mechanical energy that is available in the LV at end-systole that was not converted into external work and will be dissipated during relaxation (242).

6.3 Results

6.3.1 Global hemodynamic parameters

Figure 32 shows the computed volumetric flow rate through the AV and MV from systole to diastole for the LH models. The negative AV flow at early diastole in Figure 32A indicates backflow of blood into the LV during AV closure, while the negative systolic MV flow in Figure 32B indicates the backflow of blood into the LA due to MV closing and incompetence. During systole, the AV flow reached a peak value of 414 ml/s for the control model, while the minimum peak flow was obtained for the P2/P1 model, with a value of 169 ml/s. As seen in Figure 32B, this reduction in the aortic flow from the P2/P1 model coincided with the highest mitral regurgitant flow.

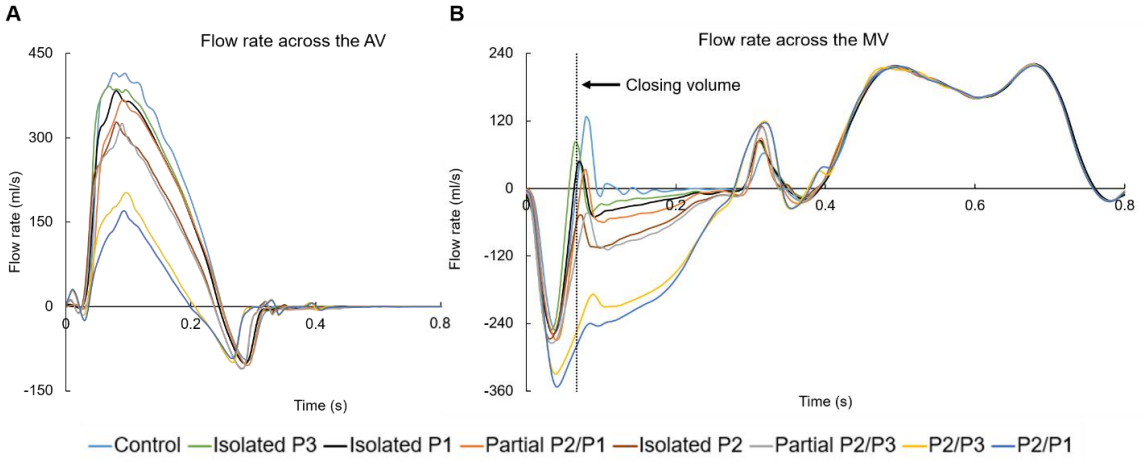

Figure 32. Flow rate across the AV and MV through the cardiac cycle. PML is divided into P1, P2 and P3 scallops.

Table 8 summarizes the main hemodynamic parameters. By using the RF_{MV} as a the parameter in the grading of MR severity (32), Table 8 shows that from the seven chordae rupture models, 3 can be classified as having mild MR, 2 moderate MR, and 2

severe MR. As per 2014 AHA/ACC guidelines (243), 2 chordae rupture models can be classified as having severe MR (RF_{MV} > 50%), while the other 4 models as having progressive MR (RF_{MV} < 50%). As expected, the RV_{AV} was similar for all LH models, with the lowest value obtained for the control model. From these results it can be seen that the severity of MR not only has an impact on the RV_{MV}, but also on the onset of AV closing (especially in the severe MR models) and on the RV_{AV} due to coupled valve dynamics.

Table 8. Summary of global hemodynamic parameters.

	Control	**Isolated P3**	**Isolated P1**	**Partial P2/P1**	**Isolated P2**	**Partial P2/P3**	**P2/P3**	**P2/P1**
RV_{AV} (ml)	4.27	4.34	4.63	4.73	4.61	5.05	4.62	4.72
MV closing volume (ml)	8.65	8.54	10.21	11.26	11.86	13.19	16.25	17.08
MV leakage volume (ml)	0.62	3.36	4.54	6.47	12.46	13.33	31.04	34.45
RV_{MV} (ml)	9.27	11.90	14.75	17.73	24.32	26.52	47.19	51.53
SV_{AV} (ml)	58.22	55.18	51.55	48.43	41.94	39.72	20.46	16.16
RF_{MV} (%)	13.74	17.74	22.25	26.80	36.70	40.04	69.76	76.13
MR severity (RF_{MV})	Mild	Mild	Mild	Mild	Moderate	Moderate	Severe	Severe

6.3.2 Chordae tension

Figure 33 shows the net force carried by the different chordae tendineae groups at peak systolic pressure. Table 9 presents the numerical values of Figure 33. In the control model, the highest PML chordae tension was found for the basal chordae, followed by the intermediate chordae, and lastly the marginal chordae. For the AML, the chordae tension was higher in the strut chordae than in the marginal chordae. When compared to the control model, Figure 33 shows that there was no evident change in the tension of AML marginal

chordae as the number of ruptured chordae increased. However, there was a noticeable increase in their tension (>20%) during total double scallop prolapse (i.e. P2/P3 and P2/P1 models). On the other hand, the tension in the strut chordae appeared to decrease as the number of ruptured chordae increased. This reduction was more than 20% during total double scallop prolapse.

In general, the tension in the PML basal chordae decreased as the as the number of ruptured chordae increased. Moreover, there was a clear reduction of more than 50% in their tension when partial or total double scallop prolapse occurred. In the isolated scallop prolapse models, as expected, the net PML marginal and intermediate chordae tensions decreased. However, in the partial double scallop prolapse models, marginal chordae tension increased more than 20% compared to the control model. When total double scallop prolapse occurred, while marginal chordae tension decreased and intermediate chordae tension increased in the P2/P1 model, the opposite trend occurred in the P2/P3 model, where marginal chordae tension increased and intermediate chordae tension decreased.

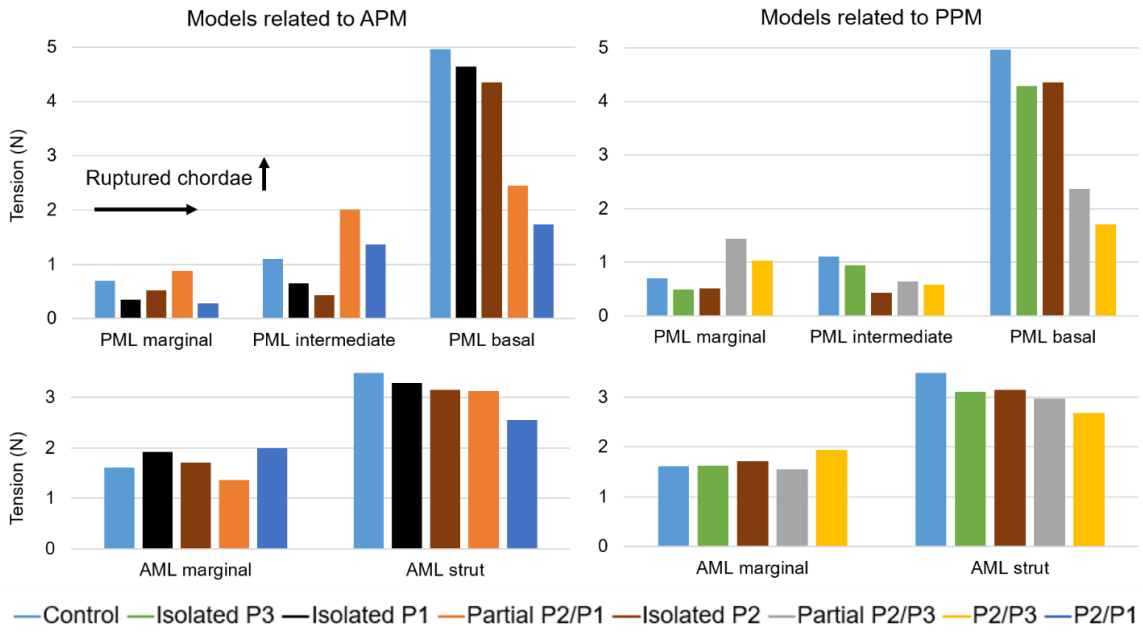

Figure 33. Chordae tension at peak systole. APM: anterolateral PM, PPM: posteromedial PM.

Table 9. Summary of chordae and PM forces (N) at peak systole, and percentage change compared to the control model.

	Control	Isolated P3		Isolated P1		Isolated P2		Partial P2/P1		Partial P2/P3		P2/P3		P2/P1	
	(N)	**(N)**	**(%)**	**(N)**	**(%)**	**(N)**	**(%)**	**(N)**	**(%)**	**(N)**	**(%)**	**(N)**	**(%)**	**(N)**	**(%)**
AML marginal	1.61	1.63	1.22	1.92	19.04	1.71	6.28	1.36	-15.64	1.55	-4.05	1.95	20.65	1.99	23.62
AML strut	3.49	3.11	-11.13	3.29	-5.97	3.15	-9.88	3.13	-10.39	2.98	-14.87	2.68	-23.34	2.56	-26.71
PML marginal	0.70	0.49	-30.00	0.35	-50.55	0.52	-25.87	0.88	26.51	1.43	105.04	1.03	47.08	0.28	-60.47
PML intermediate	1.11	0.94	-14.97	0.65	-41.54	0.43	-60.82	2.01	82.06	0.64	-42.28	0.58	-47.26	1.36	23.39
PML basal	4.97	4.28	-13.75	4.64	-6.48	4.35	-12.33	2.45	-50.58	2.37	-52.25	1.71	-65.62	1.74	-65.06
APM	6.15	5.43	-11.66	5.52	-10.20	5.39	-12.34	3.76	-38.77	5.99	-2.61	5.70	-7.32	2.45	-60.10
PPM	5.73	5.02	-12.39	5.32	-7.13	4.78	-16.59	6.08	6.08	2.98	-48.02	2.25	-60.79	5.48	-4.40

6.3.3 Leaflet stress

Figure 34 shows the maximum principal stress distribution across the mitral leaflets at peak systole. A stress value threshold of 0.5 MPa was applied such that relatively large stress values were displayed in grey, facilitating the comparison between all models.

6.3.3.1 Control model

As shown in Figure 34, full leaflet coaptation was clearly observed in the control model, as this was confirmed by the computed MV leakage volume of 0.62 ml. In the PML, high stress regions were observed in the P2 belly to basal region, with a maximum value of 0.34 MPa at the insertion of the basal chordae. Lower levels of tensile stress were found in the P1 and P3 scallops, even resulting in compressive stresses from the bucking or folding of the tissue. In all MV models, a similar pattern of stress distribution was observed in the AML, displaying large stresses in the belly region and close to the fibrous trigones along the MA, regardless of the presence of leaflet prolapse. For the control model, the maximum AML stress was 0.43 MPa, and was located close to the right fibrous trigone region and at the insertion of the strut chordae.

6.3.3.2 Chordae rupture models

PML stress distribution for the chordae rupture models differed from the control model. In the isolated scallop prolapse models, the free edge of the scallop was unrestricted and prolapsed towards the LA, whereas the belly region bent. However, an increase in the stress of the prolapsing scallop was not evident, and even seemed to become less tensile and more compressive. Between the three isolated scallop models, the maximum PML stress value

(0.46 MPa) occurred in the isolated P2 model, and was localized near the P2/P1 junction region where the remaining intact basal chordae were connected.

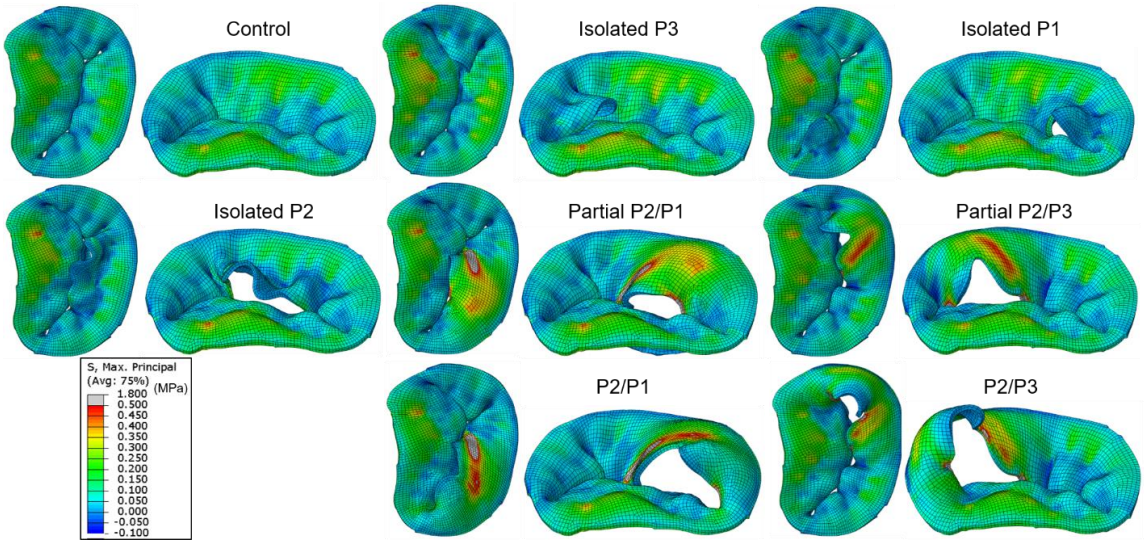

Figure 34. Stress distribution in the mitral leaflets at peak systole.

In the presence of partial or total double scallop prolapse, abnormal bulging of the PML was clearly found in all models. Overall, a broad band of large stresses (0.5-1.8 MPa) occurred in the belly region of the prolapsed segment. Additionally, high stress values (1.5-2.8 MPa) occurred near the scallop junction free edge regions, where the adjacent remaining marginal chordae were connected. Between the four double scallop prolapse models, the maximum stress (2.8 MPa) occurred in the P2/P3 model, and was localized near the free edge of the P2 scallop where the remaining intact marginal chordae were attached. In order to quantitatively compare the stress in the leaflets, Figure 35 shows the maximum principal stress values averaged over the four sub-regions of the mitral leaflets.

Leaflet coaptation and mitral annular regions were not included for the averaged stress calculation.

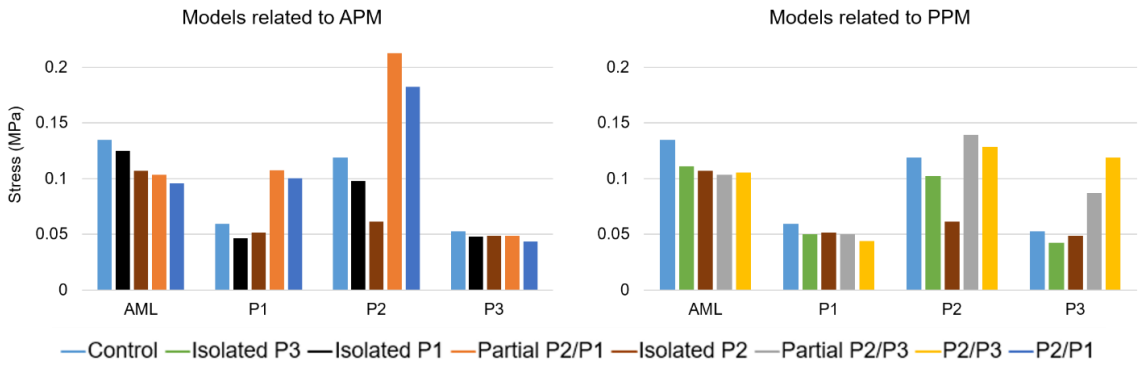

Figure 35. Averaged max. principal stress (MPa) in mitral leaflets at peak systole.

6.3.4 LH hemodynamics

Figure 36 shows the 3D velocity streamlines colored by velocity magnitude at peak systole. From the figure it is evident that chordae rupture causes a regurgitant jet into the LA, however, the structure and strength of this jet varies depending on the location and severity of the prolapse. Based on the jet direction, three types of MR jets were found: 1) an anterolaterally directed regurgitant jet was originated in the isolated P3 and P2/P3 models; 2) an anteromedially directed MR jet was found in the isolated P1, isolated P2, and P2/P1 models; and 3) an anteriorly directed central jet was developed in the partial P2/P1 and partial P2/P3 models. These 3D morphologies of the MV and flow structures obtained from the FSI simulations corresponded well to pathologic MR characteristics observed in 2D/3D echo and cardiac MRI data (99, 100, 103, 244). Additionally, Figure 36 shows that chordae rupture can produce eccentric and non-eccentric MR jets. An eccentric “wall-hugging” jet

that impinged the LA wall was visible in the 4 double scallop prolapse models. Conversely, a non-eccentric jet with more visible 3D flow features and flowing towards the central portion of the LA was found in the 3 isolated scallop prolapse models. Peak regurgitant velocity as well as peak aortic velocity for all models are presented in Table 10. Note that peak regurgitant velocity may not necessarily occur at peak systole.

Table 10. Summary of aortic and regurgitant jet velocities and LV efficiency.

	Control	**Isolated P3**	**Isolated P1**	**Partial P2/P1**	**Isolated P2**	**Partial P2/P3**	**P2/P3**	**P2/P1**
Peak aortic velocity (m/s)	2.69	2.41	2.31	2.38	2.23	2.07	1.33	1.19
Peak regurgitant velocity (m/s)	N/A	5.05	5.01	5.47	4.71	5.71	5.17	5.47
fSW (J)	0.89	0.84	0.78	0.74	0.63	0.60	0.31	0.24
SW (J)	1.02	1.01	1.01	1.00	0.98	0.98	0.93	0.91
LV efficiency (%)	75.64	71.82	67.59	63.98	55.93	53.20	28.64	22.86

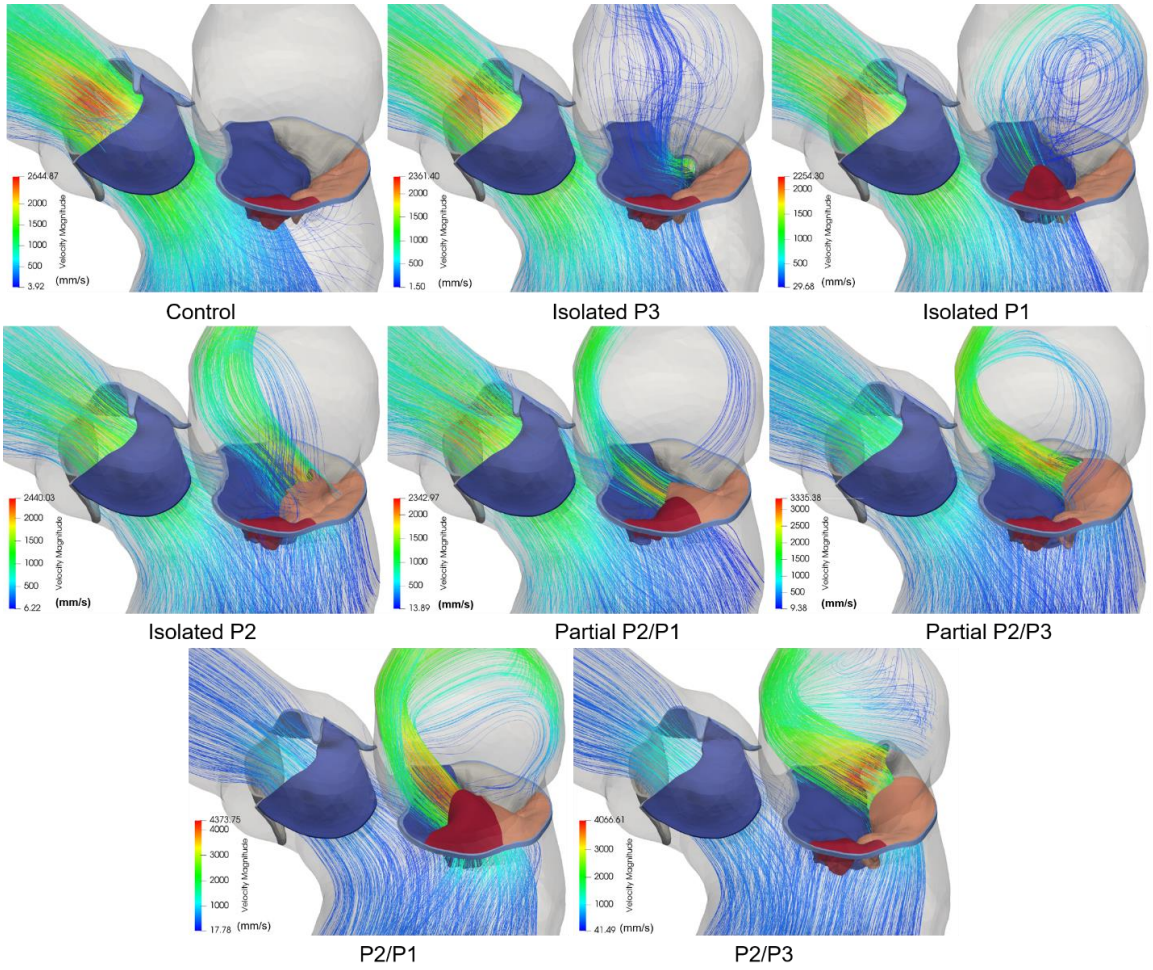

Figure 36. Velocity streamlines showing regurgitant jet structures at peak systole.

6.3.5 LV efficiency

Figure 37 shows a representative pressure-volume loop for the isolated P2 model. LV efficiency results are summarized in Table 10. As expected, the highest LV efficiency was found for the control model, with a value of 75.64%. MR due to ruptured chordae caused a reduction in the LV pump performance, from 71.82% in mild MR, down to 22.86% in severe MR.

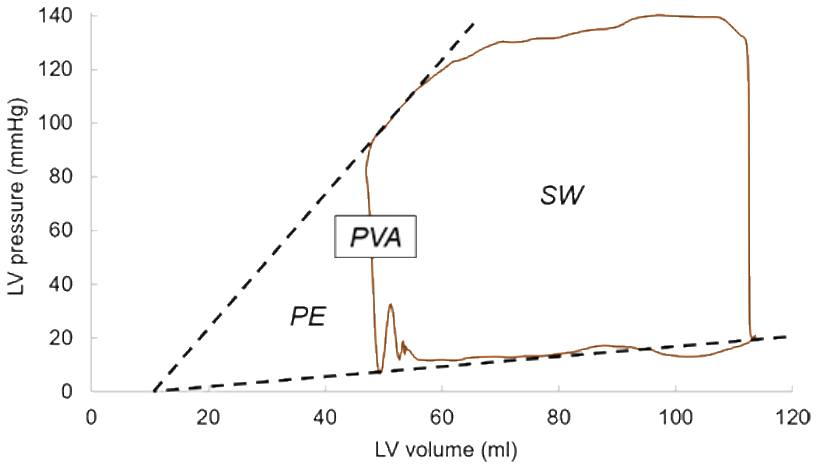

Figure 37. Representative pressure-volume loop for isolated P2 model.

6.4 Discussion

6.4.1 Mitral apparatus force balance

The results of this study showed that basal/strut chordae carried the majority of the systolic load acting on the leaflets (Figure 33). Further, basal/strut load decreased as the number of ruptured chordae increased. This reduction in the load was more than 50% for basal chordae when partial or total double scallop prolapse occurred, and more than 20% for strut chordae during total double scallop prolapse. This marked reduction in basal/strut chordae load, together with the corresponding increase in the marginal/intermediate chordae load could be caused by the reduction of the leaflet coaptation zone. A smaller coaptation area increases the tension of the remaining marginal/intermediate chordae, as they have to account for a higher pressure-bearing systolic load that otherwise would be absorbed by proper leaflet apposition. As it has been shown that the thinner marginal chordae are less

extensible (245, 246) and weaker than basal chordae (247), long-term results may lead to chordae elongation, further exacerbate chordae rupture, and eventually cause valve failure.

Chordae tension has previously been measured in vivo and in vitro under physiological and pathological conditions (22). However, due to inherent procedural difficulty and in order to avoid interference with normal valve dynamics, these studies have been unable to simultaneously measure the forces across all chordae groups, and instead, have averaged the tension measured in few chordae. Overall, these studies have found that the average tension in a single AML strut chord is the highest among all chordae groups, and that individual marginal chorda force is lower than strut/intermediate chordae forces (15, 248). When the chordae tensions for each chordae group were averaged in our control model, our simulations results seem to agree with the experimental findings, showing that a single AML strut chord is subjected to the highest average load, with a value of 0.5 N. Furthermore, PML and AML marginal chordae carried the lowest average loads, with values of 0.05 N and 0.12 N, respectively. In MV FE models with isolated P2 prolapse developed by Sturla et al. (102, 103), the total tension in the chordae located in the proximity of the prolapsing region ranged between 2.56 N and 3.99 N. The present FSI study showed, however, that marginal and intermediate chordae tensions in the isolated P2 prolapse model were 0.52 N and 0.43 N, respectively (Table 9). The discrepancy between our results and other computational studies could be due to differences in the numerical approaches, geometry, material properties, and boundary conditions.

The measurement of the PM forces is critical for the understanding of the mitral apparatus force balance and redistribution under pathological conditions. As seen in Table 9, the tension in the PM from where the chordae ruptured was reduced between 10%-17%

in the 3 isolated scallop prolapse models, more than 38% during partial double scallop prolapse, and around 60% during total double scallop prolapse. Contrary to our results, Sturla and colleagues (103) noticed a reduction in the PM force from a prolapsed MV to a repaired MV with neo-chordae, which should resemble a healthy MV. At peak systole, it is expected that the PM forces in a physiologic MV should be higher than of a prolapsed MV due to the larger leaflet area experiencing the transmitral pressure difference. Further, Sturla et al. (103) found that the combined PM tension under isolated P2 prolapse ranged between 13.58 N and 17.57 N, which is 30%-70% larger than the value found in our isolated P2 prolapse FSI model (10.17 N). For the control model, it can be seen that for both PM, the PML chordae carried between 54%-60% of the load. This distribution was not strongly affected in the isolated scallop prolapse models. Moreover, when partial or total double scallop prolapse occurred, the opposite PM did not show a significant increase or reduction in its tension, as the total load carried by the PML and AML chordae remained approximately the same as in the control model.

This capability to systematically quantify the force redistribution from the mitral leaflets to the PM from a healthy to a pathological state is a valuable tool that could lead to an improved understanding of how different pathologies and repair techniques influence LH dynamics and valve mechanics. For example, the use of neo-chordae has made a great number of complex MV pathologies amenable to repair rather than replacement (249). Nevertheless, determining the optimal number, location and proper length of neo-chordae remains a challenge (102). As shown by an elegant FE study by Sturla and colleagues (102, 103), small differences in the neo-chordae technique used can significantly alter native chordae forces and leaflet stresses, despite comparable macroscopic successful clinical

outcomes. Neo-chordae placement should aim to bring the coaptation region back into the LV inflow region, prevent post-repair systolic AML motion, and overcome MR. Thus, FSI models are required in order to quantify the flow across the valve and accurately simulate full dynamic valve behavior (3), both of which are essential in the simulation of MV repair because valvular dynamics are affected by the reduction of the effective valvular orifice and restricted motion of the leaflets themselves.

The FSI modeling framework developed in this study could overcome some of the weaknesses of the decoupled FE approach, and open the way to assess the coupled LV-valve fluid and structural mechanics before and after MV repair. Combined with clinical data, FSI computational models can provide highly controlled and quantitative analyses of the distinct effects of various valve repair/replacement techniques, pathophysiologic conditions, and anatomical variations on the coupled LH dynamics, and are thus advantageous over FE- or fluid-only computational models, and complementary to in vivo and in vitro models.

The development of these detailed cardiac computational models for functional evaluation and treatment planning is highly dependent on available clinical imaging modalities, since capturing anatomically accurate 3D images of the cardiac structures is a critical first step of any computational modeling endeavor. Currently, echo is the standard noninvasive clinical imaging modality to examine the cardiac function and valvular diseases. However, due to its limited spatial resolution, patient-specific detailed mitral chordae structure and distribution cannot be accurately captured or segmented (76). Other noninvasive 3D cardiac imaging modalities include cardiac MRI and MSCT. As shown in this study, high-quality MSCT images can enable accurate and detailed segmentation of

the valvular and sub-valvular structures of the LH. In case of low MSCT image quality, a complementary segmentation approach that uses optimization methods, parametric modeling using anatomic landmarks points of the valvular apparatus, or generalized anatomical models from literature-derived data, as commonly used in echo-derived computational models, would be required (8). Fortunately, recent developments in MSCT technology now allow rapid acquisition of volumetric datasets with high spatial and temporal resolution and unlimited 2D planar reconstruction post-processing capability. These new-generation MSCT scanners, together with a parallel rapid expansion of percutaneous valvular repair and replacement techniques have not only allowed that MSCT becomes the standard imaging modality in pre-procedural assessment, but that this imaging modality has the potential to play an important role in the diagnosis and evaluation of valvular pathologies (250).

6.4.2 Leaflet stress distribution

In the chordae rupture models where partial or total double scallop prolapse occurred, overall, a high-stress concentration was found in the prolapsed PML segment when compared to the control model. Our simulation results seem to agree with previous computational studies that have compared MV stresses under chordae rupture and normal/repaired states (100, 251, 252). For example, Kunzelman et al. (97) investigated MV dynamics under physiological and P2 chordae rupture states. Similar to our study, it was found that the leaflet stress increased during chordae rupture, and that stress concentrations were located close to the attachment point of the adjacent remaining native chordae. Similarly, Sturla et al. (103) found that the stress in the prolapsed P2 scallop increased during chordae rupture, indicating excessive loading of the remaining chordae

and adjacent leaflet tissue. Nevertheless, as seen in Figure 35, our study showed that chordae rupture in a specific scallop does not always involve an increase in the stress of the entire leaflet. For example, in the P1 and P3 isolated models, it was found that the average stress in the prolapsed scallop in fact decreased around 20%, while in the neighboring and opposite scallops decreased between 9%-18%. Moreover, in the isolated P2 model, the reduction in the stress of the P2 scallop was 50%, while in the neighboring scallops (i.e. P1 and P3) decreased between 8%-13%.

On the contrary, in the four models where partial or total double scallop prolapse occurred, the stress in the lateral (P1 or P3) scallops increased more than 65%, in the central (P2) scallop increased between 8%-80%, and in the healthy scallop decreased between 7%-25%. It is noteworthy that the average stress in the AML was also reduced as the number of ruptured chordae increased. This reduction was more than 20% when partial or total double scallop prolapse occurred. This indicates that PML chordae rupture also affects the stress distribution in the AML. It is reasonable to expect that these differences in tissue loading can cause the mitral leaflets to remodel and adapt to the geometric needs imposed by chordae elongation and rupture (253, 254), similar as chronic tension leads to permanent increases in size in bone, vessels, and skin (255-257). However, little is known about this phenomenon, in part due to the lack of a measuring technique that can accurately and parametrically quantify the MV mechanical state under different pathophysiological loads. The FSI modeling framework developed in this study can potentially allow for such measurements, which can provide invaluable data for exploring the basic mechanisms of tissue remodeling.

6.4.3 Pathologic LH hemodynamics

Accurate grading of MR severity is crucial for clinical decision making, prognosis, and timing of treatment intervention. The most common method for noninvasive assessment of MR is echo, however, accurate and reproducible quantification of the RV_{MV} is compromised by the presence of multiple jets, the dynamic regurgitant orifice, and geometrical assumptions of the mitral orifice and the LVOT (258). Moreover, given the possible eccentricity of the regurgitant jet into the LA with a marked Coanda effect, quantification of MR severity can be underestimated due to limitations of alignment, hydrodynamic principle assumptions using the PISA method, and Color Doppler jet size attenuation when the jet is wall hugging (259). Herein the importance of quantifying the RV_{MV} with a volumetric technique, that although is time consuming as it requires calculation of the SV and RV through the regurgitant and reference valves, has advantages in eccentric MR jets, multiple jets, and mid-to-late systolic MR.

As shown in Table 8 and Table 9, the modeling approach implemented in this study was able to assess MR severity by directly quantifying the RV_{MV}, which is a strong indicator of MV function, as well as its effect on the aortic blood flow. Moreover, this is the first computational work that reported different MR jet structures in the LA using an FSI framework. As seen in Figure 36, while some regurgitant jets followed the direction of the flow determined by the prolapsed segment; with a more central location, other Coanda jets appeared to be attracted towards the atrial wall. The results of this work could be used to better understand how the regurgitant flow features can affect LA enlargement (260), as well as echo assessment of MR by performing a systematic comparison of the different semi-quantitative and quantitative techniques. Heart pumping efficiency is also an important hemodynamic metric that can be studied with an integrative computational

approach. When MR was present, there was a progressive reduction in the LV pump efficiency in performing fSW, since the total SW was divided into the fSW and the ineffective work of the volume regurgitation into the LA. Impaired LV efficiency for the chordae rupture models was between 71.82% - 22.86%. Our model predictions seem to agree well with in vivo measurements under healthy and MR conditions [261]. For example, Kameyama et al. (242) found that the human LV efficiency is 69% ± 10% under physiological conditions.

It is also important to note that besides the expected increase in the MV leakage volume as the number of ruptured chordae increased (Table 8), a higher MV closing volume was also predicted; especially in the severe MR models. It was found that although the degree of MV opening and the timing of valve closure was similar for all LH models at end-diastole, the mitral leaflets coapt together faster in the control model. The reason behind this is that the basal chordae were the first to carry the pressure load early in systole, preventing the base of the PML to partially bulge upward into the LA due to the increased transmitral pressure, as it occurred in the LH models with partial or total double scallop prolapse. In the control model, this allowed that a larger leaflet area was perpendicular to the pressure gradient, therefore creating a larger closing force and causing the leaflets to coapt together faster. This finding underscores: a) the importance of basal chordae in optimizing MV closure, and b) the fact that blood flow dynamics and the structural mechanics of the valves should be modeled together using FSI in order to capture the full valve dynamics throughout the cardiac cycle.

In this study, we make a first attempt in relating the ventricular fluid dynamics with the valve mechanics during MR by modeling flow-leaflet interaction, leaflet coaptation,

and flow dynamics into, outward and within the LV. Studies like this are significant because it is known that for complex systems such as the heart, the structural deformation of the valves is intricately associated with the blood flow dynamics, and a deeper understanding of the interaction between the different components may lead to useful tools to diagnose and treat any abnormality of one part based on available information about the other. Performing FSI simulations of the LH dynamics to a satisfactory level, however, is not a trivial task. The main challenges to overcome are: 1) the large nonlinear deformation of the valve leaflets, 2) flow domain discontinuity due to rapid valve closure, and 3) the computation of flow-induced loads on evolving complex fluid-solid interfaces. Regardless of significant advances in the field, existing FSI methods using either a boundary conforming formulation such as the ALE method, or a non-boundary conforming formulation such as the IB method experience several complications (137, 262), mainly because the fluid mechanics are most conveniently described using the Eulerian formulation, while the solid equations are normally described in the Lagrangian formulation.

Using a Lagrangian description for both fluid and solid domains is a potential remedy to the simulation of FSI problems, and SPH is one of these methods. The meshless nature of SPH allows large deformations to be modeled more easily in cases where mesh-based methods would require dealing with expensive re-meshing and with a moving interface on a stationary mesh. Previous studies have concluded that the SPH method is a viable FSI technique to simulate the complex valve dynamics and the large-scale ventricular flow dynamics (86, 136, 156, 207, 208). Nevertheless, like any other numerical method, SPH has its own limitations and further developments are still required for SPH to compete with

established mesh-based methods. For example, in this study each cardiac cycle required approximately 5 days to run. As a result, the present FSI modeling framework cannot be used in a clinical setting and currently, is only suitable for a research environment. However, both FE and SPH solvers can use the GPU's extremely parallel architecture (88, 263, 264), which will significantly reduce the running time in the near future and avoid the need for a large computer cluster.

6.5 Limitations

There are some limitations that should be taken into account when interpreting the results of this study. First, in this parametric FSI study we adapted one previously validated healthy LH model to create seven chordae rupture cases, employing the same baseline conditions for all diseased models, with variations of chordae rupture location and number. Such well-controlled, side-by-side comparisons are difficult to obtain in real patient conditions. However, we acknowledge that a large cohort of patient-specific LH models needs to be developed and simulated to replicate clinical conditions and draw statistical conclusions. Second, there is no direct validation of the chordae rupture LH models. We assume that LH and valve computational models that have been validated under physiological conditions (73, 207, 208) can also accurately simulate some pathological states, such as acute MR due to chordae rupture. To allow for validation of the chordae rupture LH models, a retrospective study of patients with mitral leaflet prolapse scheduled for MV repair would be needed, and clinical measurements should be compared to FSI results.

Third, the FSI modeling protocol adopted in this study required a considerable amount of human effort to create the LH models and of computational time to run the FSI simulations, which is not compatible with its use in a routine clinical setting. We are currently developing methods to streamline and automate the model generation and simulation process to facilitate analysis of larger patient cohorts (265). Fourth, although alterations in tissue properties have been found when MV prolapse is caused by chordae rupture (266), the same mitral tissue properties and geometry (e.g. tissue thickness) were used for all models in this study. Therefore, simulation results may differ if patient-specific pathological tissue and geometrical data are incorporated. Finally, due to the inherent limitation of Abaqus SPH formulation, small-scale flow and turbulence features may not be accurately solved close to the cardiac wall. When particles are close to the wall, part of the supporting domain of the smoothing kernel will not be filled with SPH particles, affecting their integration accuracy. However, the combined effect of the smoothing kernel interpolation function near the wall and the node-to-surface contact interaction partially enforces the no-slip boundary condition.

CHAPTER 7. SPECIFIC AIM 1B – PART 2, LV-VALVE DYNAMICS UNDER SECONDARY MITRAL REGURGITATION AND BICUSPID AORTIC VALVE STENOSIS

7.1 Introduction

In contrast to degenerative or primary MR that results from the pathologic abnormality of the valvular tissue, secondary or functional MR occurs on a structurally normal MV as a result of alterations in LV geometry and function. Functional MR represents a major clinical challenge, since severe MR has poor prognosis in patients with heart failure and reduced LVEF (267, 268). In ischemic MR, pathological LV remodeling contributes to the apical, posterior and lateral displacement of the PM, with reduced LV contractility and abnormal MA contraction. The displacement of the PM results in traction on the mitral leaflets and restriction on leaflet motion. Moreover, inadequate closure of the MV contributes to increased tethering forces and reduced leaflet closing force (269, 270).

Using an undersized annuloplasty ring to improve leaflet coaptation is a common surgical treatment for functional MR. Significant recurrence of MR, however, has been reported following annuloplasty (271-273). Moreover, many patients with severe functional MR are not eligible for surgical MV repair due to multiple comorbidities and high surgical risk (274). Other treatments include leaflet resection, neochordae implantation, and edge-to-edge repair (272, 275-278). The highly complex structure and the interrelated function among the valve substructures and the continuous remodeling mechanisms of MR make MV treatment strategy difficult. Particularly for MV repair, the

success of a technique may be associated with the leaflet stress, MA force and chordae forces(279-281). Therefore, it is important to understand the LV-valve biomechanics under functional MR, in order to assess the effectiveness of repair strategies and determine the optimal strategy available for specific patients.

Computational studies have been useful in assessing the MV mechanics under normal and diseased conditions, as well as evaluating surgical MV repair techniques. MV repair by annuloplasty and MitraClip intervention was studied using patient-specific FE MV models derived from echocardiography data (282-284). However, due to the limited resolution of echo data, the locations of chordal insertion points and single-point chordal origins on the PM in these models were assumed. PM and MA dynamic motion from diastole to systole is essential for accurate simulation of leaflet closing behaviors using healthy MV models (285). Realistic chordae and leaflet reconstruction has been achieved based on Micro-CT, but Micro-CT cannot be applied in a clinical setting (286).

Hence, in Specific Aim 1b – Part 2, we aim to develop a patient-specific LH model with functional MR and concomitant BAV that includes detailed chordae tendineae structure and distribution, accurate leaflet geometry and thickness, dynamic MA and chordae origins, anisotropic hyperelastic material models, and human age- and gender-matched material properties. Despite the presence of traction on the MV leaflets caused by displacement of the PM, the initial MV geometry constructed from clinical images has been assumed stress-free in previous studies. In this study, we will introduce the tethering pre-tension force, the tension existing in the chordae prior to systole, which plays an important role in accurately simulating MV dynamics under functional MR. The patient-specific LH model will be validated first, by quantitatively comparing the closed MV

geometry obtained from the simulation with the in vivo MV geometry obtained from the clinical MSCT images at systole. MV model optimization, including chordae tethering adjustment and pretension will be performed until correct valve morphology and leaflet deformation are obtained. The second validation phase will consist of the comparison of the FSI hemodynamic results with the patient's echo measurements.

7.2 Materials and Methods

7.2.1 Patient information

A 71-year-old male patient with a mean aortic annulus diameter of 23 mm was referred for TAVR at Hartford Hospital (Hartford, CT). Pre-TAVR echo examination revealed classical low-flow, low-gradient severe AS, a BAV with eccentric coaptation between the non-coronary leaflet and fused left and right coronary leaflets, with no raphe between them (Sievers type 0 L/R) (56). Mild aortic insufficiency was detected. Moderate-to-severe functional MR was also found, with restricted PML motion and reduced leaflet coaptation, resulting in a posteriorly directed regurgitant jet. The LV wall thickness was normal, but the chamber was mildly dilated with severe global hypokinesis with regional variation. The LA was dilated despite a normal antero-posterior diameter.

7.2.2 Patient-specific LH model

The patient-specific LH model was created from the pre-TAVR cardiac MSCT images after obtaining approval from the Institutional Review Board. The MSCT images, acquired with a GE LightSpeed 64-channel volume CT scanner, had an in-plane resolution of 0.82 x 0.82 mm and a slice thickness of 0.625 mm. Ten phases of the cardiac cycle were

collected using an ECG-gated sequence. DICOM images were imported into Amira-Avizo (Thermo Fisher Scientific, MA) and 3D Slicer (www.slicer.org) software to segment the cardiac structures, which included the ascending aorta, aortic root, BAV, calcification, MV, chordae, LV and LA endocardial walls. HyperMesh software (Altair Engineering, Inc., MI) was then used to create a high quality FE mesh. Figure 38A shows the patient-specific LH model. Two calcific deposits were found in the fused leaflet, as well as one in the coronary ostia close to the right coronary artery.

The AV and MV geometries were segmented at mid-systole and mid-diastole, respectively, approximating their stress–free configuration (212). Similarly, the aortic root and ascending aorta were segmented at mid-systole. The patient-specific MV model used in this study was developed and validated in a previous work from our group that investigated MV dynamics under functional MR (287). Briefly, the detailed chordae structure (number, position, length, branching, origins of the PM tips, and insertions into the leaflets) was directly reconstructed from the MSCT images, as seen in Figure 38B. Chordae were classified into five groups: anterior strut (AS), anterior basal (AB), anterior marginal (AM), posterior basal (PB), and posterior marginal (PM). Cross-sectional area values of 0.38 mm^2, 0.71 mm^2 and 2.05 mm^2 were assigned to marginal, basal and strut chordae, respectively (73). A total of 18 chordae origins were modeled from the PM tips.

3D solid elements (eight-node hexahedral C3D8R/C3D8I elements, six-node wedge C3D6 elements, and four-node tetrahedral C3D4 elements) were used to discretize the ascending aorta, aortic root, BAV, calcification and MV. Stress/displacement truss elements (two-node linear T3D2 elements) were used for the mitral chordae, while shell elements (four-node quadrilateral S4 elements) were used to model the endocardial wall.

Two layers of elements were used across the mitral leaflet thickness. For the AML, the average thickness values for the leaflet belly and free edge were 1.26 mm and 2.09 mm, respectively. For the PML, the average thickness values of the leaflet belly and free edge were 1.31 mm and 1.57 mm, respectively (287). Four layers of elements were used across the ascending aorta/aortic root and BAV leaflet thickness, with a uniform total thickness of 2 mm and 0.7 mm, respectively.

After a mesh convergence study, average mesh sizes for the BAV, MV, chordae, aorta/aortic root and calcification were 0.25 mm, 0.7 mm, 1.5 mm , 1 mm and 0.5 mm, respectively. Leaflet mesh size was refined until stress results were not affected by mesh size, with results showing a variation within 5%. The total number of elements used for the BAV was 48,567, 6550 for MV, 860 for chordae, 183,130 for aorta/aortic root, and 42,650 for calcification. The BAV/aortic root and calcification shared the same nodes on the tissue-calcification interface, thus avoiding contact-related issues during the simulation. SPH particles were uniformly distributed in the domain with a spatial resolution of 0.8 mm, which led to approximately 1 million one-node (PC3D) elements.

An anisotropic hyperelastic material model, based on Holzapfel et al. (209, 288), was adopted to characterize the mechanical response of most cardiac tissues, while the isotropic hyperelastic Ogden material model (289) was used to characterize the mechanical properties of mitral chordae and aortic-mitral curtain. Material parameters were determined by fitting in-house multiprotocol biaxial and uniaxial testing data of human cardiac tissues. Table 11 lists the fitted material parameters. Calcification was assumed to be a linear-elastic material with a Young's modulus of 12.6 MPa and a Poisson ratio of 0.3 (112).

Table 11. Cardiac tissues material parameters.

MHGO model	C_{10} (kPa)	C_{01}	k_1 (kPa)	k_2	θ (°)	κ	D (kPa^{-1})
AV leaflets	0.017	147.262	39704.1	2352.96	0	0.317	5.0e-4
AML	0.285	61.303	9.295	99.684	0	0.333	5.0e-4
PML	0.101	33.191	10.756	48.495	27.98	0.089	5.0e-4
Sinuses	1.755	13.707	10.550	80.379	20.06	0	5.0e-4
Aorta	4.175	3.464	3.771	15.927	70.95	0.086	5.0e-4
Ogden model	μ_1 (MPa)	a_1	μ_2 (MPa)	a_2	μ_3 (MPa)	a_3	
Anterior marginal	17.824	17.808	17.660	17.797	17.592	17.768	
Anterior strut	24.342	11.338	10.332	11.167	14.914	11.188	
Anterior/posterior basal	10.256	16.579	10.654	16.554	10.671	16.554	
Posterior marginal	12.995	15.651	13.083	15.683	12.870	15.662	
Intervalvular fibrosa	1.505	21.400	11.207	21.400	1.441	21.400	

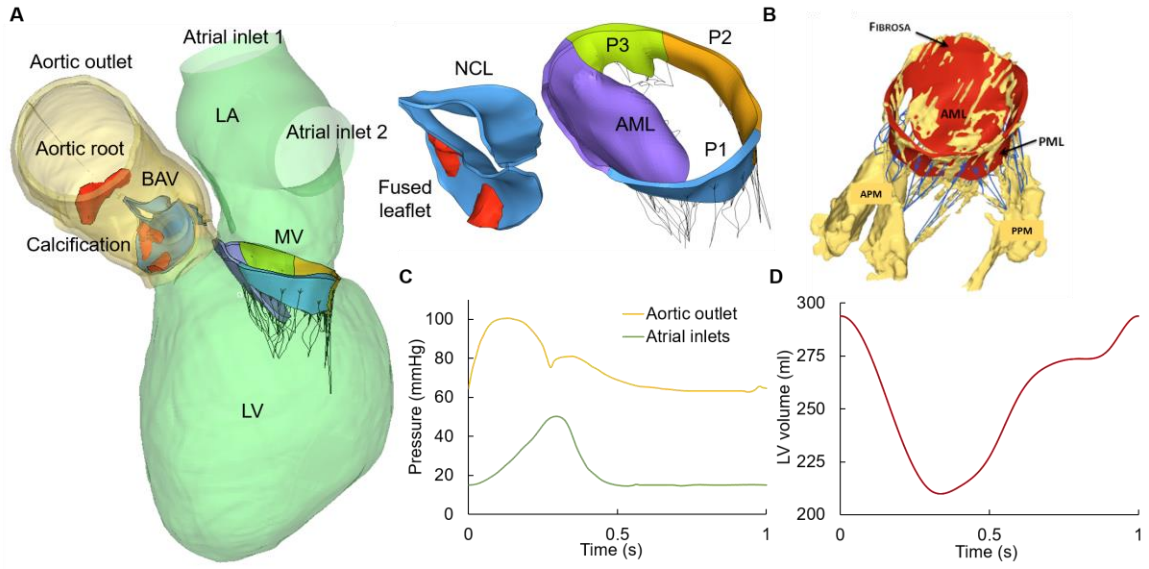

Figure 38. A) Patient-specific LH model reconstructed from the MSCT images, B) MV model from MSCT segmentation, C) Aortic and LA pressure waveforms, D) LV volume waveform.

7.2.3 Boundary conditions

Time-dependent pressure boundary conditions were applied at the two atrial inlets (pulmonary veins) and at the aortic outlet of the pre- and post-TAVR LH models. As seen in Figure 38C, a pathological atrial pressure waveform was prescribed at the inlets, with an elevated V-wave due to the regurgitant volume in the atrial cavity during systole (238). In order to match the patient's clinical data, the mean diastolic atrial pressure value was adjusted to be 12 mmHg, while the peak systolic and diastolic aortic pressure values were set to 100 mmHg and 63 mmHg, respectively.

Endocardial wall motion was imposed as a time-dependent nodal displacement boundary condition based on the ten cardiac phases from the MSCT images. A detailed

description of the cardiac wall motion modeling procedure can be found in Specific Aim 1a. Figure 38D shows the time-varying LV volume change waveform obtained from the FSI model. The patient's heart rate was approximately 60 bpm, corresponding to a cardiac cycle of 1 s. Note that FSI simulations begin at early systole. Two cardiac cycles were conducted and the results from the second cycle were analyzed herein.

7.2.4 Data analysis

7.2.4.1 Fluid parameters

As introduced in Part 1, the RV_{MV} and RV_{AV} were obtained by integrating the negative MV systolic flow rate curve and negative AV diastolic flow rate curve over time, respectively. The RV was defined as the sum of the valve closing and the leakage volumes. Similarly, the SV_{MV} and SV_{AV} were obtained by integrating the positive MV diastolic flow rate curve and positive AV systolic flow rate curve over time, respectively. MR severity was graded using the regurgitant fraction criterion (32), $RF_{MV} = RV_{MV}/LVSV$, where $LVSV$ is the total SV of the LV (SV_{AV} + RV_{MV}). AV effective orifice area was calculated as $EOA_{AV} = \frac{MSF}{51.6\sqrt{\Delta P}}$, where MSF is the root mean square systolic flow rate, and ΔP is the mean systolic pressure gradient (213).

7.2.4.2 Structural parameters

For the validation of the MV model, the distance error between the deformed MV and the ''true'' valve geometry obtained from the MSCT images during systole were computed in MATLAB as the point-to-node distance between the nodes of the deformed valve mesh and their corresponding projected points on the tissue surface segmented from the image

data (290). A point-to-node distance > 2 mm was considered unacceptable and required further model adjustment.

For the FSI simulation, tissue mechanics were evaluated by the average maximum principal stress values calculated in the BAV leaflets and MV leaflets during peak diastolic and systolic pressure, respectively. Chordae forces at peak systole were also reported as presented in Part 1. Briefly, the force experienced by a particular chordae group was calculated as the sum of vectors representing the tension in each individual chorda attached to that chordae group.

7.3 Results

7.3.1 MV optimization and validation

Due to the limitation of the MSCT image resolution, it was not possible to detect all of the chordae or the accurate chordae length. Therefore, the number of chordae and their lengths were estimated in the initial model and required optimization. The model was adjusted until the deformed MV model could closely match the true image model. If the surface of the valve leaflets were protruding towards the LA, the chordae in the vicinity were shortened. If a chorda was excessively tensioned and stretched the leaflet, it was then elongated. The chordae lengths were adjusted while keeping the insertion and origin points unchanged.

After 20+ iterations, it was determined that adjusting the chordae length alone was insufficient to accurately simulate the systolic MV deformation. Therefore, an existing chordae tethering force at diastole due to LV dilatation in this functional MR patient, which could further restrict the leaflet motion, was needed. This pre-existing force was generated

by shortening the length of the tethered chordae by 1.99 mm on average in a total of 8 chordae. The chordae origins were translated towards the annulus plane along the vector going from the chordae origin point to the insertion point by the magnitude of the chordae shortening. Hence, an additional step of pretension was added to the simulation process, where the translated origins were displaced from their adjusted locations to their original locations identified from MSCT to generate the pre-tension in the chordae. Approximately 50 iterations were performed to optimize the chordae lengths and degree of pre-tension.

Figure 39 shows the final optimized MV geometry after performing chordae optimization. The atrial, sagittal and isometric views of the valve demonstrated a good agreement between the deformed MV and the true image model at systole. During peak systole, a large regurgitant orifice was visible at the P1 and partial P2 regions. Figure 39d displays an overlay of the 2D projections of the regurgitant orifice in the deformed and true image models at systole. The 2D areas from the computational model and true image model were 60.55 and 51.86 mm^2, respectively.

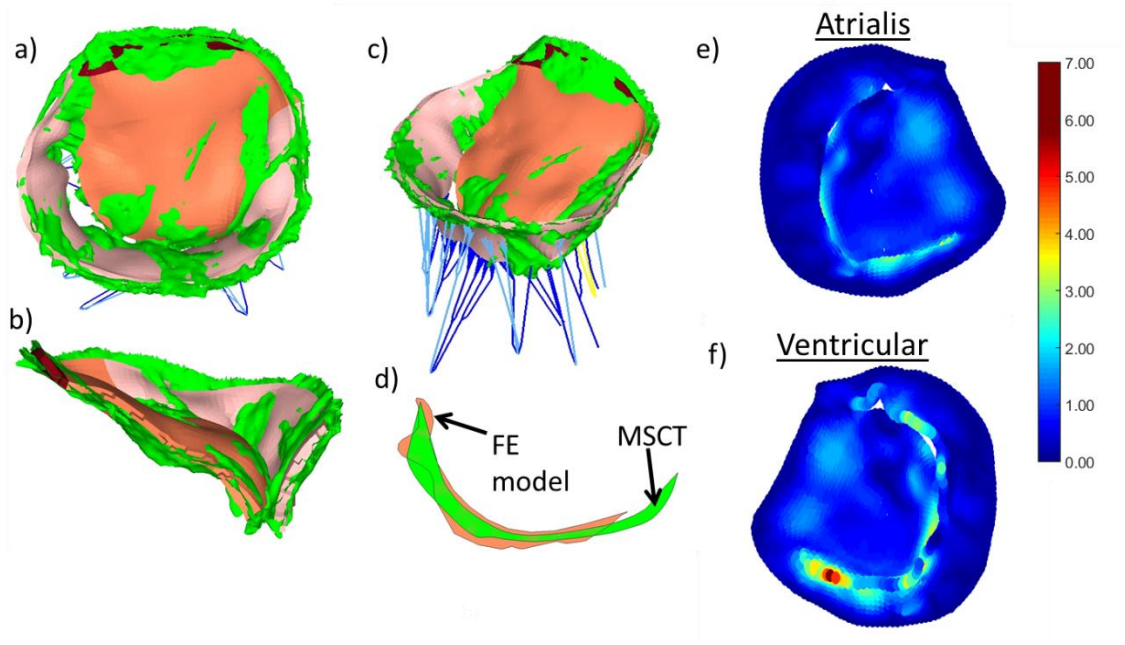

Figure 39. (a) Atrial, (b) sagittal and (c) isometric views of the deformed MV model overlapped with the true image model from MSCT at mid-systole, (d) the projected orifice areas of the deformed MV model and middle-systolic geometry from MSCT images; (e) atrial and (f) ventricular surface views of the calculated distance error maps at middle systole.

7.3.2 Global hemodynamic parameters and validation

Table 12 displays the computed hemodynamic parameters of the patient-specific LH model throughout the cardiac cycle. Numerical measurements are compared to the patient's available echo data. Generally, there is good quantitative agreement between the simulation results and the clinical data, which demonstrates that the SPH-FE FSI modeling framework can accurately simulate the patient-specific LH pathological dynamics. FSI simulation of BAV function revealed the classical low-flow low-gradient AS found clinically, with an $EOA_{AV} < 1\ cm^2$, mean systolic pressure gradient < 40 mmHg, and decreased LVEF < 50%. Similarly, FSI simulation of MV function demonstrated moderate-to-severe MR, which

was consistent with the patient's clinical echo examination. Additionally, Figure 40 shows the intraventricular velocity streamlines colored by velocity magnitude during peak systole. Due to the restricted PML motion, the pre-TAVR model displayed a posteriorly directed regurgitant jet, which qualitatively matched the Doppler color echo image shown in Figure 40.

Table 12. LH hemodynamics and echo comparison.

	FSI	**Echo**
SV_{AV} (ml)	46.28	43
RV_{AV} (ml)	9.34	–
SV_{MV} (ml)	74.64	–
RV_{MV} (ml)	37.59	–
RF_{MV} (%)	44.82	–
MR severity (RF_{MV})	Moderate-to-severe	Moderate-to-severe
LVEF (%)	28.55	25
AV peak gradient (mmHg)	34.82	34
AV mean gradient (mmHg)	23.97	20
AV peak velocity (m/s)	2.82	2.9
EOA_{AV} (cm^2)	0.77	0.67
E wave (m/s)	0.79	0.9
A wave (m/s)	0.54	0.6
E/A	1.47	1.5
MR peak gradient (mmHg)	118.59	–
MR peak velocity (m/s)	5.42	–

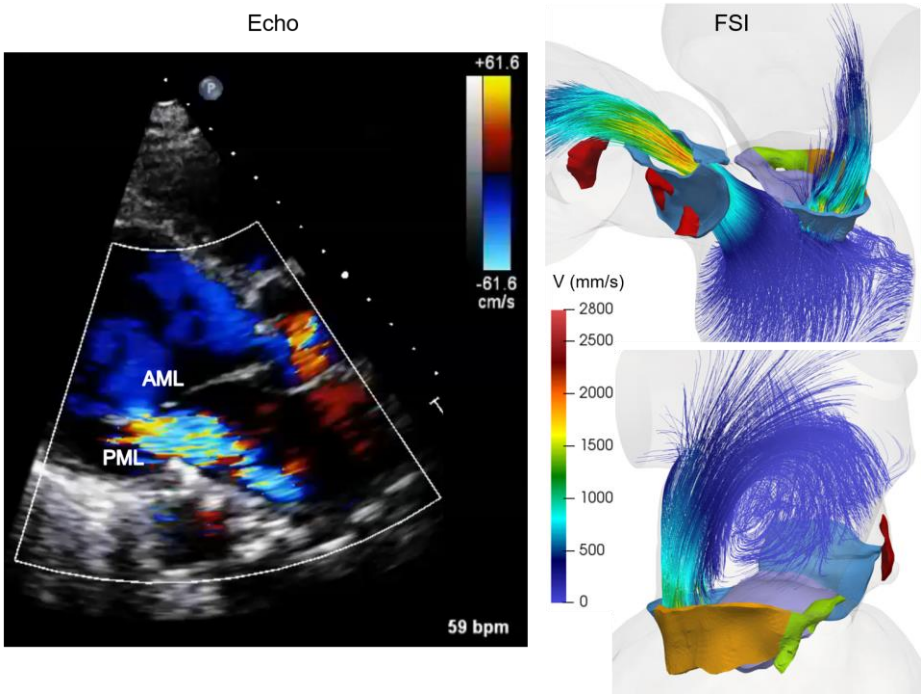

Figure 40. Doppler color echo image and FSI velocity streamlines showing regurgitant jet structures at peak systole.

7.3.3 Valve tissue mechanics

Table 13 presents the average stress values calculated for the AV leaflets and MV leaflets during peak diastolic and systolic pressure, respectively. Due to the restricted motion of the PML observed clinically, the average stress in the AML was generally higher than in the PML. However, the peak mitral leaflet stresses were located at the tethered PML chordae insertion regions, near the leaflet free-edge and basal chordae locations. Since this patient had a postero-lateral regurgitant gap with PML tethering near the APM, the LH model experienced high PML chordae forces when compared to AML chordae tensions. There was an imbalanced force distribution between the two PM, with APM force being higher than PPM force.

Table 13. LH tissue parameters.

	FSI
S_I^{AVRG} (MPa)	
AV	0.076
AML	0.126
PML	0.082
$F_{chordae}$ (N)	
AML marginal	1.14
AML strut	2.04
AML basal	3.84
PML marginal	6.13
PML basal	7.33

7.4 Discussion

7.4.1 MV deformation

The MV model developed in this study was able to accurately captured PML tethering by accounting for the pre-tension tethering forces in the chordae and the mitral leaflets. We observed high chordae forces on the tethering PM at both diastole and systole. Early experiments have suggested that tension on chordae and mitral leaflets existed not only at systole but also diastole (291, 292). Due to functional MR, LV dilation and apical displacement of the PM could cause more traction on the leaflets and thus prevent proper coaptation. Systolic chordae forces as well as leaflet stress and strain values have been studied both experimentally and computationally by simulating an MR state of the MV (106, 293-295). However, few studies have looked into the tension that exists in diastole under functional MR due to PM traction, and MV models at diastole state have mostly been assumed stress free (106, 282, 293, 296). For this patient case, a lack of annulus and ventricular contraction, large tenting angle and area were observed from the MSCT images,

as well as restricted PML motion from diastole to systole. From our simulations, we found that ignoring the tension in the chordae and leaflets during diastole would overestimate the leaflet coaptation for this patient, with 84% larger in average point-to-mesh distance error compared to the model with pretension. The results indicated that the existing pre-tension force in chordae and leaflets at diastole is essential in accurately replicating the in vivo MV dynamics.

7.4.2 Clinical validation

To the best of our knowledge, this is the first validated patient-specific computational model that simulated the LH dynamics under functional MR during the entire cardiac cycle. Comparison between simulation results and available echo data demonstrated good quantitative agreement, with some computed variables agreeing better with the echo measurements than others. First, it is generally noted that differences in terms of the SV_{AV}, RV_{MV}, LVEF, E wave, A wave, E/A ratio, and MR peak gradient and velocity were mostly below 10% (Table 12). It is also noted that the errors in the estimation of the AV peak and mean gradients, AV peak velocity and EOA_{AV} were below 20%. As with any image-based computational model, there exist sources of geometric and numerical uncertainties. Moreover, it is important to be aware of the inherent limitations and variability in the measurement of hemodynamic variables using echo (297). Echo examination is highly dependent on the experience of the operator, the technical quality of the study and on the patient's acoustic window (298).

7.5 Limitations

While, on one side, cardiac tissues were realistically described as nonlinear and anisotropic, on the other side, patient-specific cardiac tissue material properties were not available. Thus, tissues mechanical response was defined from an extensive human tissue database obtained from in-house multiprotocol biaxial and uniaxial tests. Second, since this study did not consider the zero stress–free configuration of the aortic wall, a rigid body constraint was assigned to the aortic root/ascending aorta wall elements during the FSI simulations. Third, the current SPH-FE FSI modeling framework involves a high computational cost. The FSI simulations required approximately 5 days to run one cardiac cycle in an Intel Xeon E5-2670 cluster. As a result, the present modeling methodology cannot be used in a clinical setting and currently, is only suitable for a research environment. Nevertheless, among other advantages, SPH is easy to parallelize. The ability to run both FE and SPH codes on GPUs will significantly reduce the running time in the near future and avoid the need for a computer cluster (299, 300).

CHAPTER 8. SPECIFIC AIM 2A – LV-VALVE DYNAMICS UNDER TRANSAPICAL NEOCHORDAE IMPLANTATION

8.1 Introduction

After the success of TAVR in treating severe AS, a great effort has been made in recent years on the development of minimally-invasive technologies for MV repair/replacement. In particular, transapical beating heart neochordae implantation has demonstrated potential effectiveness and safety in treating a subset of patients with primary MR (301). In the transapical chordae repair approach, ePTFE sutures are implanted on a beating-heart through a small incision under 2D/3D TEE guidance. Neochordae are anchored to the prolapsing leaflet segment on one end, and on the moving LV apex on the other end.

Although transapical neochordae implantation has been demonstrated to be safe and effective in patients with primary MR (302), this is still a technically demanding technology in the early stage of use. A number of issues such as residual leaflet prolapse when treating multi-scallop disease, determination of the optimal LV access site, suture number, placement and length, as well as proper patient selection to ensure a safe and durable repair remain to be studied in detail (301, 303). Moreover, it is important to highlight that the growing experience with this technique has been mainly in patients with isolated central prolapse (302). Therefore, limited knowledge about the biomechanical and clinical outcomes in patients with multi-scallop or paracommissural prolapse exists. Clearly, long-term, large-volume clinical studies as well as highly controlled biomechanical studies are needed to assess the definitive value of this therapeutic approach.

Cardiac computational modeling is a powerful tool that can help us to better understand the functional and biomechanical environment of the heart under physiologic, pathological and repaired conditions. FE studies have been performed in the past to evaluate MV dynamics under different repair techniques (97, 98), including traditional surgical neochordae implantation, where the sutures are attached to the PM tips (99, 101-103). Recently, a FE model was develop by Gaidulis and colleagues (304) to evaluate MV repair with transapical neochordae implantation. In particular, the effect of neochordae length on post-repair MV dynamics was investigated. However, for physiologically accurate simulations and rigorous evaluation of MV repair treatments, the intraventricular blood dynamics and the structural mechanics of the valves should be modeled together, an area where FSI is required (3, 76, 155).

In Specific Aim 2a, we employed the LH model with primary MR due to chordae rupture developed in Specific Aim 1b – Part 1 to simulate transapical neochordae implantation and better understand the biomechanical interaction between the neochordae and the LH complex. Neochordae implantation using three and four sutures was modeled under three clinically relevant prolapse conditions: isolated P2, multi-scallop P2/P3 and multi-scallop P2/P1. We investigated the effect of selecting an antero-lateral vs. a postero-lateral LV access site, and suboptimal neochordae length, compared to optimal suture length. An improved understanding of these aspects through a detailed and objective engineering approach is an important step towards the success of novel transcatheter MV interventions in the short- and long-term.

8.2 Materials and Methods

8.2.1 LH model

In this study, we employed the LH model with primary MR developed in Specific Aim 1b – Part 1. Three PML prolapse models that reproduce common clinical scenarios of acute chordae rupture were selected and analyzed: isolated P2, multi-scallop P2/P3 and multi-scallop P2/P1. Briefly, the isolated P2 prolapse model was created by removing marginal and intermediate chordae elements from the central scallop, while the multi-scallop prolapse models were created by progressing towards rupture of the basal chordae elements.

8.2.2 Transapical neochordae modelling

Neochordae were modeled as CV-4 ePTFE sutures (W.L. Gore & Associates, Inc., Flagstaff, AZ, USA) (305) with a constant cross-sectional area of 0.074 mm^2 (251), and using stress/displacement truss elements (T3D2) with an average element length of 1 mm. Mechanical properties derived from uniaxial tensile tests were obtained from literature (251, 306). In this study, virtual transapical neochordae procedures were modeled under optimal implantation conditions. That is, following the manufacture's recommendations (307) (308, 309). and the clinical step-by-step guide (305, 310).

Clinically, three or four neochordae are implanted on average in order to balance the tension per neochorda, provide structural support and avoid excessive mechanical stress on the leaflets (302). Thus, three (NC3) and four (NC4) neochordae were modeled in this study for each PML prolapse model, as seen in Figure 41 and Figure 42. Representative isolated P2 NC3 model showing the antero-lateral LV access site. Neochordae number and leaflet attachment location for the 6 post-repair models.. Each neochorda was modeled as

a simple suture loop, passing one end of the suture through the prolapsed scallop(s), while the two free ends were locked on the LV epicardium (305). Moreover, each neochorda was advanced and anchored to the leaflet as a single point attachment at individual nodes through the leaflet thickness. In real practice, the use of a girth hitch knot or a double-helix knot may reduce leaflet stress concentrations compared to our idealized knot modeling. As shown in Figure 41 and Figure 42, neochordae were uniformly distributed along the prolapsed scallop(s) and fixed 4 mm away from the leaflet free edge, as clinically recommended (305).

Two LV access sites were modeled for the neochordae origin: a postero-lateral (Figure 41) and an antero-lateral (Figure 42) (305) (308). These sites were located approximately 3 cm from the true apex of the heart. Moreover, the location of the epicardial and endocardial walls of the LV entry site was tracked from the subject-specific MSCT images during the cardiac cycle, and their motion was imposed as a time-dependent nodal displacement boundary condition (Figure 43A). Optimal neochordae length was initially determined from the baseline LH model as the distance between the affected scallop(s) and the LV access site at peak systole, and later tuned to maximize leaflet coaptation and minimize MR in the post-repair LH models.

Additionally to modeling ideal neochordae length, two suboptimal neochordae length configurations were simulated for the isolated P2 prolapse model when using NC4 and an antero-lateral LV entry site. Optimal suture length was altered by ± 4 mm, simulating apparently correct transapical neochordae techiques with a slight under-tension (optimal + 4 mm) and over-tension (optimal - 4 mm).

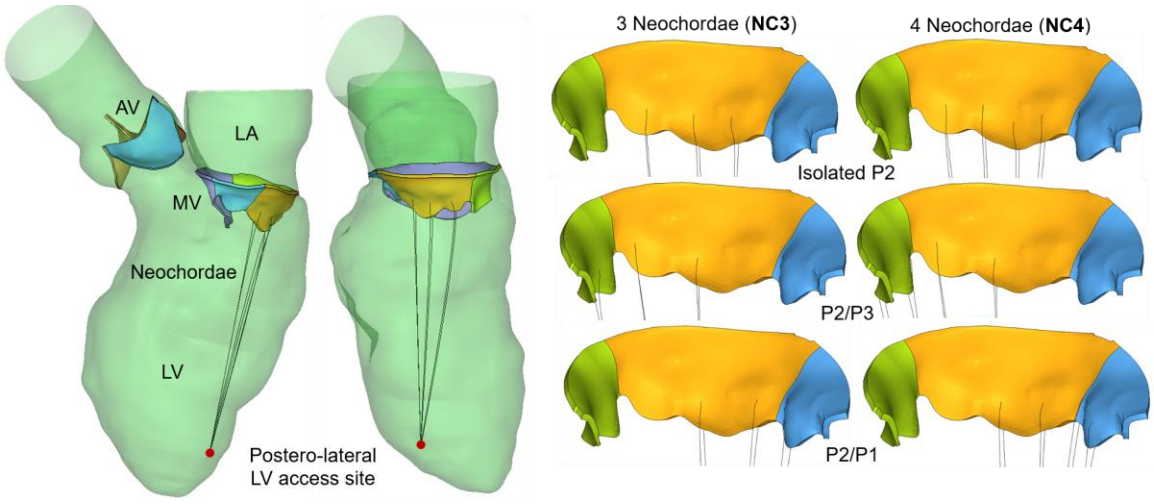

Figure 41. Representative isolated P2 NC3 model showing the postero-lateral LV access site. Neochordae number and leaflet attachment location for the 6 post-repair models.

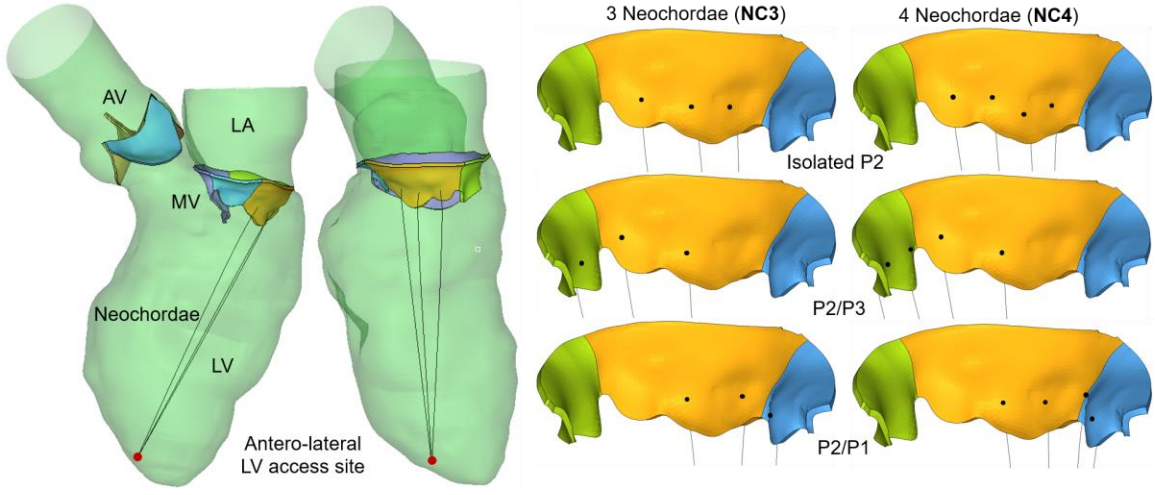

Figure 42. Representative isolated P2 NC3 model showing the antero-lateral LV access site. Neochordae number and leaflet attachment location for the 6 post-repair models.

8.2.3 Boundary conditions

Time-dependent pressure boundary conditions were applied at the LA inlet and aortic outlet of the LH models. As seen in Figure 43B, for the baseline and post-repair models, a constant atrial pressure of 20 mmHg was prescribed at the inlet, while a physiological aortic pressure waveform was applied at the outlet. In acute MR, the regurgitant volume in a normal-sized LA results in a marked increase in the atrial pressure during systole (238) (elevated V-wave). Thus, the pre-repair models employed a pathological LA inlet pressure waveform, while the same aortic pressure waveform as in the baseline/post-repair models was applied at the outlet.

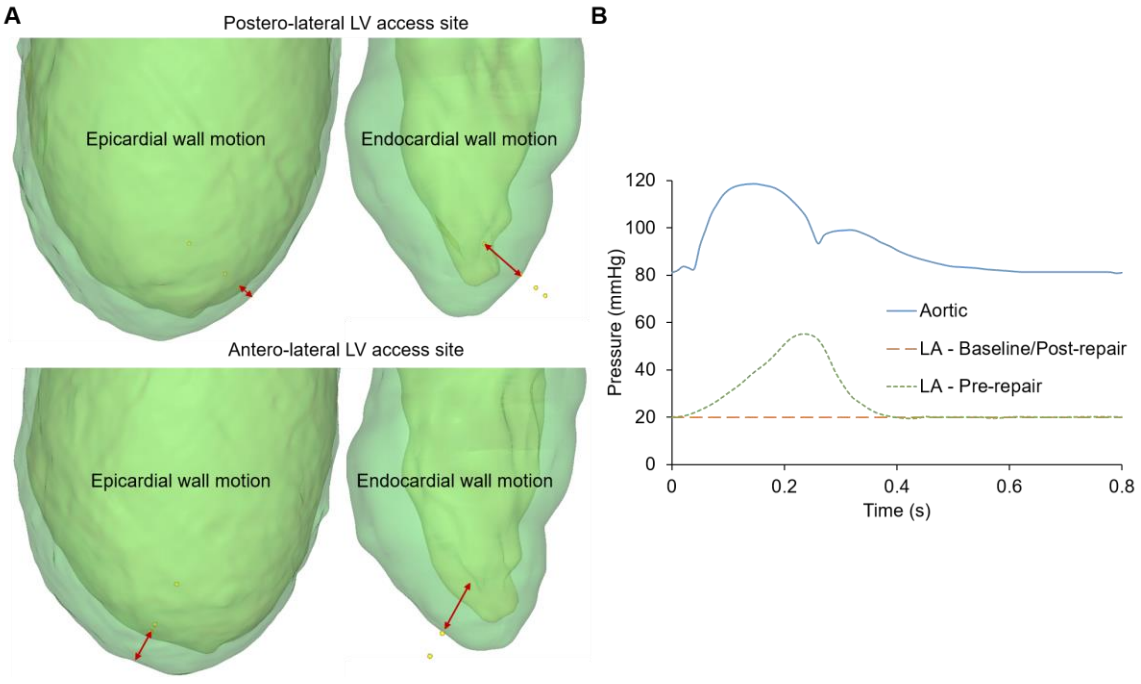

Figure 43. A) Epicardial and endocardial wall motion between peak diastole (green) and peak systole (yellow). B) Aortic and LA pressure boundary conditions.

8.2.4 Data analysis

A total of 18 LH FSI simulations were performed in this parametric study. One for the baseline model, three for the pre-repair models with chordae rupture, six for the post-repair models with optimal neochordae length (NC3 and NC4) and using a postero-lateral LV entry site, six for the post-repair models with optimal neochordae length (NC3 and NC4) and using an antero-lateral LV entry site, and two for the isolated P2 NC4 post-repair models with suboptimal neochordae length (optimal ± 4 mm) and using an antero-lateral LV entry site. In the text, "AL-NC" refers to the antero-lateral transapical neochordae configuration, while "PL-NC" refers to the postero-lateral configuration.

Baseline, pre- and post-repair LH dynamics were analyzed in terms of the following hemodynamic and structural biomechanical parameters: 1) SV_{AV}, SV_{MV}, RV_{AV}, RV_{MV}, RF_{MV}, and MR severity, 2) Native chordae tension ($F_{chordae}$), defined as the resultant force carried by the different chordae groups. The resultant force experienced by a particular chordae group was calculated as the sum of forces exerted by each native chorda attached to that chordae group, 3) PM force (F_{PM}), defined as the resultant reaction force exerted on the APM and PPM to bear the tension of the native chordae, 4) Neochordae tension (F_{NC}), defined as the resultant force exerted on the ePTFE sutures, 5) Percentage of the force carried by each neochorda ($F_{neochorda}$) relative to the total neochordae tension, 6) Peak value ($S_I^{MAX}{}_{NC}$) of the maximum principal stress on the neochordae, 7) Average ($S_I^{AVRG}{}_{MV}$) maximum principal stress in the MV leaflets. Leaflet free edge and annular regions were not included in the average stress calculation, 8) Peak value ($S_I^{MAX}{}_{MV}$) of the maximum principal stress on the mitral leaflets with location.

8.3 Results

8.3.1 LH hemodynamics

Table 14 and Table 15 show the LH hemodynamic parameters for the baseline, pre- and post-repair models with PL-NC and AL-NC configurations, respectively. For each post-repair model, the use of ePTFE sutures, regardless of the number used and location, resulted in the reposition of the prolapsed scallop(s) under the MA and acute reduction of MR. By using RF_{MV} as a quantitative parameter to grade the MR severity, Table 14 and Table 15 show that all post-repair models can be classified as having trivial MR, like the baseline model. The mitral flow rate curves through the cardiac cycle for the LH models are shown in Figure 44, respectively. As expected, the SV_{MV} was largely similar for all LH models, since the cardiac wall motion was assumed to remain unchanged.

Table 14. Hemodynamic parameters for the baseline, pre- and post-repair (optimal neochordae length) LH models under PL-NC configuration.

	Baseline	**Isolated P2**	**Isolated P2 NC3**	**Isolated P2 NC4**	**P2/P3**	**P2/P3 NC3**	**P2/P3 NC4**	**P2/P1**	**P2/P1 NC3**	**P2/P1 NC4**
SV_{AV} (ml)	58.22	41.94	59.11	59.12	20.46	57.22	58.08	16.16	58.94	57.72
RV_{AV} (ml)	4.27	4.61	4.47	4.61	4.62	4.67	4.61	4.72	4.63	4.70
SV_{MV} (ml)	62.54	61.36	63.78	63.79	63.60	63.32	63.23	63.42	63.57	62.99
RV_{MV} (ml)	9.27	24.32	10.05	10.15	47.19	11.39	10.56	51.53	10.17	10.54
RF_{MV} (%)	13.74	36.70	14.53	14.66	69.76	16.60	15.39	76.13	14.71	15.44
MR severity (RF_{MV})	Trivial	Moderate	Trivial	Trivial	Severe	Trivial	Trivial	Severe	Trivial	Trivial

Table 15. Hemodynamic parameters for the baseline, pre- and post-repair (optimal neochordae length) LH models under AL-NC configuration.

	Baseline	**Isolated P2**	**Isolated P2 NC3**	**Isolated P2 NC4**	**P2/P3**	**P2/P3 NC3**	**P2/P3 NC4**	**P2/P1**	**P2/P1 NC3**	**P2/P1 NC4**
SV_{AV} (ml)	58.22	41.94	58.98	57.26	20.46	57.78	58.14	16.16	59.39	59.11
RV_{AV} (ml)	4.27	4.61	4.53	4.62	4.62	4.29	4.36	4.72	4.23	4.56
SV_{MV} (ml)	62.54	61.36	63.55	62.99	63.60	62.87	62.88	63.42	64.02	63.59
RV_{MV} (ml)	9.27	24.32	9.81	11.02	47.19	10.13	9.85	51.53	9.58	9.74
RF_{MV} (%)	13.74	36.70	14.27	16.14	69.76	14.92	14.49	76.13	13.90	14.15
MR severity (RF_{MV})	Trivial	Moderate	Trivial	Trivial	Severe	Trivial	Trivial	Severe	Trivial	Trivial

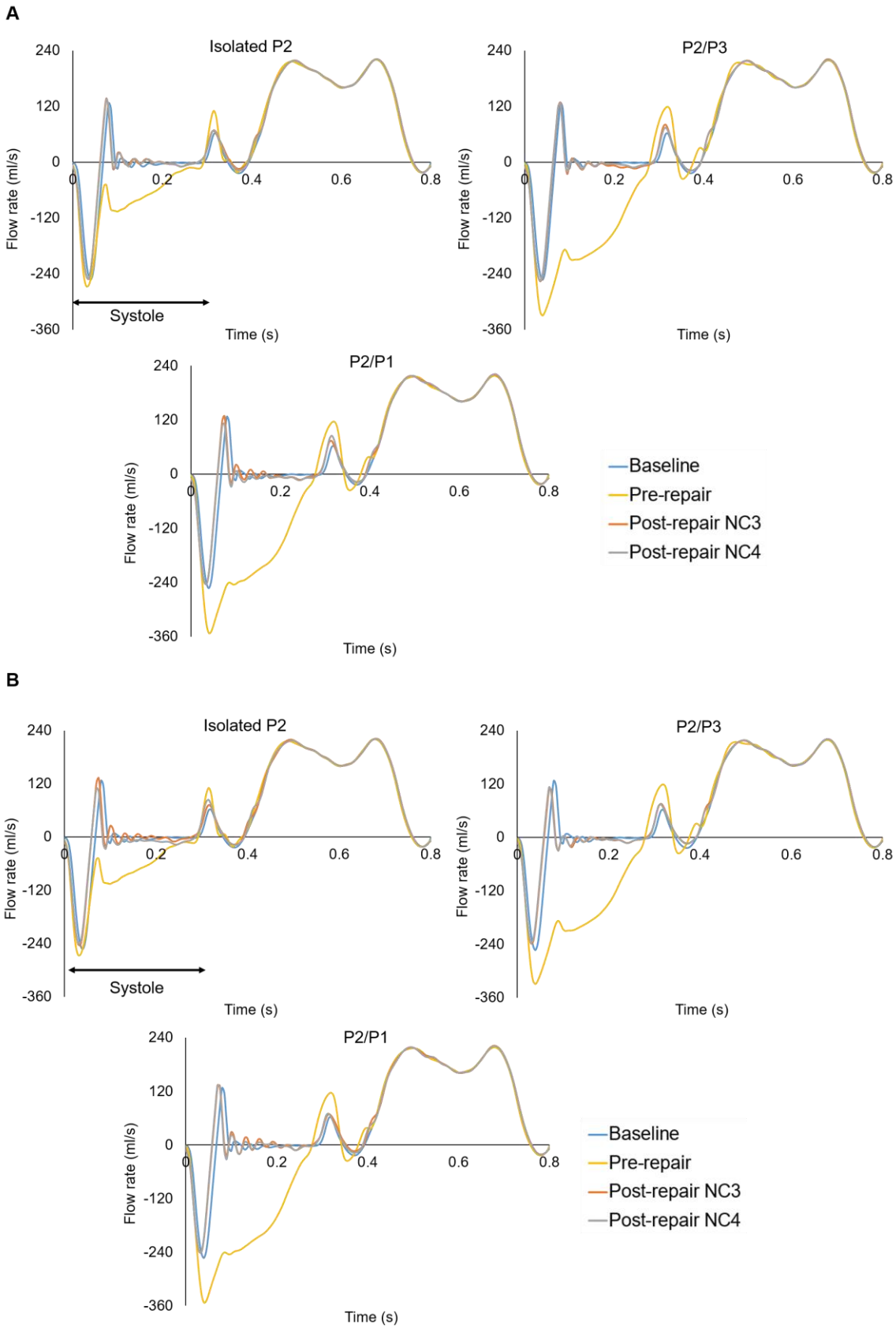
A
Isolated P2
P2/P3
P2/P1
Flow rate (ml/s)
Time (s)
Systole
Baseline
Pre-repair
Post-repair NC3
Post-repair NC4
B
Isolated P2
P2/P3
P2/P1
Flow rate (ml/s)
Time (s)
Systole
Baseline
Pre-repair
Post-repair NC3
Post-repair NC4

Figure 44. Flow rate curves (ml/s) across the MV throughout the cardiac cycle. A) PL-NC configuration, B) AL-NC configuration. The negative systolic mitral flow indicates the backflow into the LA due to MV closing and MR.

8.3.2 Native chordae tension – PL-NC

Forces on the different native chordae groups at peak systole are reported in Table 16 and Figure 45. When compared to the baseline model, AML marginal tension increased more than 30% for all post-repair models. On the other hand, AML strut tension was largely unchanged. As expected, PML chordae tension for the post-repair models was lower than for the baseline model, a direct result of the decreased number of native PML chordae available for coaptation.

For the isolated P2 post-repair models, PML chordae tension decreased between 30% - 50% in all chordae groups, when compared to the baseline model. For the P2/P3 post-repair models, PML marginal/basal and intermediate chordae tension decreased more than 60% and 30%, respectively. Similarly for the P2/P1 post-repair models, PML intermediate/basal and marginal chordae tension decreased more than 60% and 30%, respectively. Overall, native mitral chordae did not see noticeable differences in their tension when implanting NC3 or NC4 for each clinical scenario of MV prolapse.

Table 16. Structural parameters for the baseline, pre- and post-repair (optimal neochordae length) LH models under PL-NC configuration at peak systole.

	Baseline	Isolated P2	Isolated P2 NC3	Isolated P2 NC4	P2/P3	P2/P3 NC3	P2/P3 NC4	P2/P1	P2/P1 NC3	P2/P1 NC4
$F_{chordae}$ (N)										
AML marginal	1.61	1.71 (6.3)	2.24 (38.7)	2.35 (45.7)	1.95 (20.6)	2.18 (34.8)	2.23 (38.2)	1.99 (23.6)	2.41 (49.1)	2.36 (46.5)
AML strut	3.49	3.15 (-9.9)	3.58 (2.5)	3.60 (3.1)	2.68 (-23.3)	3.23 (-7.5)	3.30 (-5.7)	2.56 (-26.7)	3.67 (4.9)	3.60 (3.1)
PML marginal	0.70	0.52 (-25.9)	0.32 (-53.9)	0.45 (-36.2)	1.03 (47.1)	0.28 (-60)	0.24 (-65.2)	0.28 (-60.5)	0.41 (-41.3)	0.43 (-37.9)
PML intermediate	1.11	0.43 (-60.8)	0.57 (-48.5)	0.52 (-53.1)	0.58 (-47.3)	0.76 (-31.1)	0.73 (-33.7)	1.36 (23.4)	0.01 (-99.4)	0.02 (-98.2)
PML basal	4.97	4.35 (-12.3)	3.47 (-30)	3.13 (-37)	1.71 (-65.6)	1.87 (-62.3)	1.94 (-60.9)	1.74 (-65.1)	2.09 (-57.9)	2.10 (-57.7)
F_{PM} (N)										
APM	6.15	5.39 (-12.3)	5.18 (-15.7)	5.16 (-16)	5.70 (-7.3)	5.76 (-6.2)	5.82 (-5.4)	2.45 (-60.1)	3.19 (-48.2)	3.17 (-48.4)
PPM	5.73	4.78 (-16.6)	5.01 (-12.6)	4.88 (-14.8)	2.25 (-60.8)	2.56 (-55.4)	2.63 (-54.2)	5.48 (-4.4)	5.39 (-5.9)	5.35 (-6.6)
F_{NC} (N)	–	–	1.83	2.11	–	3.02	3.33	–	3.02	3.10
$F_{neochorda}$ (%)	–	–	35.8, 36.8, 27.4	26.8, 20, 34.2, 19.1	–	32.1, 27.8, 40.1	29.3, 25.8, 17.1, 27.9	–	27.3, 38.4, 34.3	19.7, 25.3, 27.4, 27.5
$S_i^{MAX}{}_{NC}$ (MPa)	–	–	9.08	9.74	–	16.37	13.16	–	15.67	11.55
$S_i^{AVRG}{}_{MV}$ (kPa)										
AML	135	107 (-20.7)	140.8 (4.3)	142.2 (5.3)	105.5 (-21.9)	139.9 (3.6)	140.1 (3.7)	96 (-28.9)	141.6 (4.9)	139.4 (3.2)
P1	59.2	51.5 (-13)	64.6 (9.1)	63.7 (7.6)	44.3 (-25.2)	63 (6.5)	62.7 (5.9)	100.4 (69.6)	137.1 (131.6)	132.6 (124.1)
P2	118.8	61.3 (-48.4)	178.2 (50)	191.8 (61.4)	128.7 (8.4)	164.8 (38.7)	176.6 (48.7)	182.6 (53.7)	191.7 (61.3)	183.9 (54.8)
P3	52.6	48.5 (-7.8)	58.4 (11)	61.7 (17.3)	119.0 (126.1)	163.3 (210.3)	153.8 (192.3)	43.6 (-17.1)	59.6 (13.2)	55.7 (5.9)
$S_i^{MAX}{}_{MV}$ (MPa)	0.43 - AML	0.52 - AML	0.71 – P2	0.67 – P2	2.80 – P2	1.66 – P3	1.56 – P3	2.25 – P2	1.04 – P2	1.29 – P2

$F_{neochorda}$ values from left to right correspond to neochorda located from P1 to P3 scallops.

Percentage variations with respect to the baseline model are reported in parenthesis.

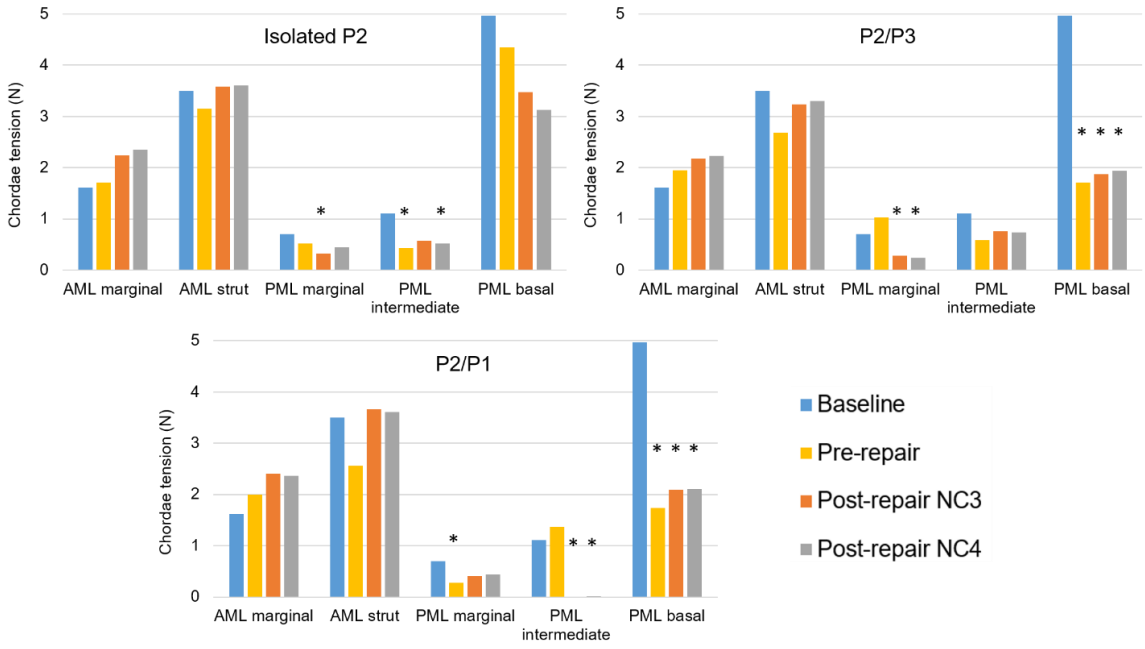

Figure 45. Native mitral chordae tension (N) at peak systole. Asterisks highlight a marked reduction (>50%) in chordae tension with respect to the baseline model.

8.3.3 Native chordae tension – AL-NC

Native chordae tension at peak systole are reported in Table 17 and Figure 46. When compared to baseline conditions, except for the isolated P2 NC4 model, post-repair models demonstrated an important increase (>30%) in AML marginal tension. AML strut tension on the other hand, revealed minimum changes between baseline and post-repair states. For the isolated P2 post-repair models, PML marginal/basal and intermediate tensions decreased >30% and ~50%, respectively. For the P2/P3 and P2/P1 post-repair models, PML basal tension decreased at least 50%, while PML marginal/intermediate tension decreased at least 35%. Overall, the different chordae groups did not see a noticeable

change in their total tension when implanting NC3 or NC4 for each clinical scenario of MV prolapse.

Table 17. Structural parameters for the baseline, pre- and post-repair (optimal neochordae length) LH models under AL-NC configuration at peak systole.

	Baseline	**Isolated P2**	**Isolated P2 NC3**	**Isolated P2 NC4**	**P2/P3**	**P2/P3 NC3**	**P2/P3 NC4**	**P2/P1**	**P2/P1 NC3**	**P2/P1 NC4**
$F_{chordae}$ (N)										
AML marginal	1.61	1.71 (6.3)	2.17 (34.8)	1.71 (5.7)	1.95 (20.6)	2.30 (42.7)	2.28 (41.4)	1.99 (23.6)	2.38 (47.7)	2.53 (56.9)
AML strut	3.49	3.15 (-9.9)	3.63 (4)	3.55 (1.6)	2.68 (-23.3)	3.27 (-6.4)	3.31 (-5.3)	2.56 (-26.7)	3.73 (6.7)	3.78 (8.1)
PML marginal	0.70	0.52 (-25.9)	0.33 (-53.4)	0.38 (-44.9)	1.03 (47.1)	0.27 (-61.7)	0.30 (-56.7)	0.28 (-60.5)	0.45 (-36)	0.39 (-43.9)
PML intermediate	1.11	0.43 (-60.8)	0.54 (-51.5)	0.52 (-53.4)	0.58 (-47.3)	0.65 (-40.8)	0.63 (-43)	1.36 (23.4)	0.09 (-91.6)	0.10 (-90.9)
PML basal	4.97	4.35 (-12.3)	3.51 (-29.3)	3.10 (-37.6)	1.71 (-65.6)	1.64 (-67)	1.65 (-66.8)	1.74 (-65.1)	2.22 (-55.4)	2.29 (-54)
F_{PM} (N)										
APM	6.15	5.39 (-12.3)	5.18 (-15.8)	4.84 (-21.3)	5.70 (-7.3)	5.47 (-11)	5.48 (-10.9)	2.45 (-60.1)	3.28 (-46.7)	3.36 (-45.4)
PPM	5.73	4.78 (-16.6)	5.00 (-12.7)	4.42 (-22.9)	2.25 (-60.8)	2.67 (-53.5)	2.69 (-53)	5.48 (-4.4)	5.59 (-2.5)	5.73 (0)
F_{NC} (N)	–	–	2.06	2.68	–	5.50	5.95	–	2.97	3.29
$F_{neochorda}$ (%)	–	–	35.3, 34.9, 29.8	29.8, 14.5, 33.3, 22.5	–	32, 37.5, 30.5	30, 30, 18.5, 21.5	–	26.2, 42.2, 31.6	18.1, 27.5, 27.8, 26.6
$S_i^{MAX}{}_{NC}$ (MPa)	–	–	9.8	12.07	–	27.87	24.13	–	16.91	12.35
$S_i^{AVRG}{}_{MV}$ (kPa)										
AML	135.0	107 (-20.7)	139.1 (3)	132.7 (-1.7)	105.5 (-21.9)	136.6 (1.2)	141.6 (4.9)	96 (-28.9)	140.4 (4)	145.1 (7.4)
P1	59.2	51.5 (-13)	63 (6.4)	63.3 (7)	44.3 (-25.2)	62.9 (6.2)	63.2 (6.8)	100.4 (69.6)	132.4 (123.8)	120.4 (103.5)
P2	118.8	61.3 (-48.4)	179.5 (51.1)	160.1 (34.8)	128.7 (8.4)	217.1 (82.7)	220.9 (85.9)	182.6 (53.7)	209.1 (76)	204.4 (72.1)
P3	52.6	48.5 (-7.8)	56.5 (7.3)	55.5 (5.6)	119 (126.1)	163.2 (210.1)	153.3 (191.4)	43.6 (-17.1)	59 (12.1)	57.9 (9.9)
$S_i^{MAX}{}_{MV}$ (MPa)	0.43 - AML	0.52 - AML	0.66 – P2	0.66 – P2	2.80 – P2	1.85 – P2	1.97 – P2	2.25 – P2	1 – P2	1.41 – P2

$F_{neochorda}$ values from left to right correspond to neochorda located from P1 to P3 scallops.

Percentage variations with respect to the baseline model are reported in parenthesis.

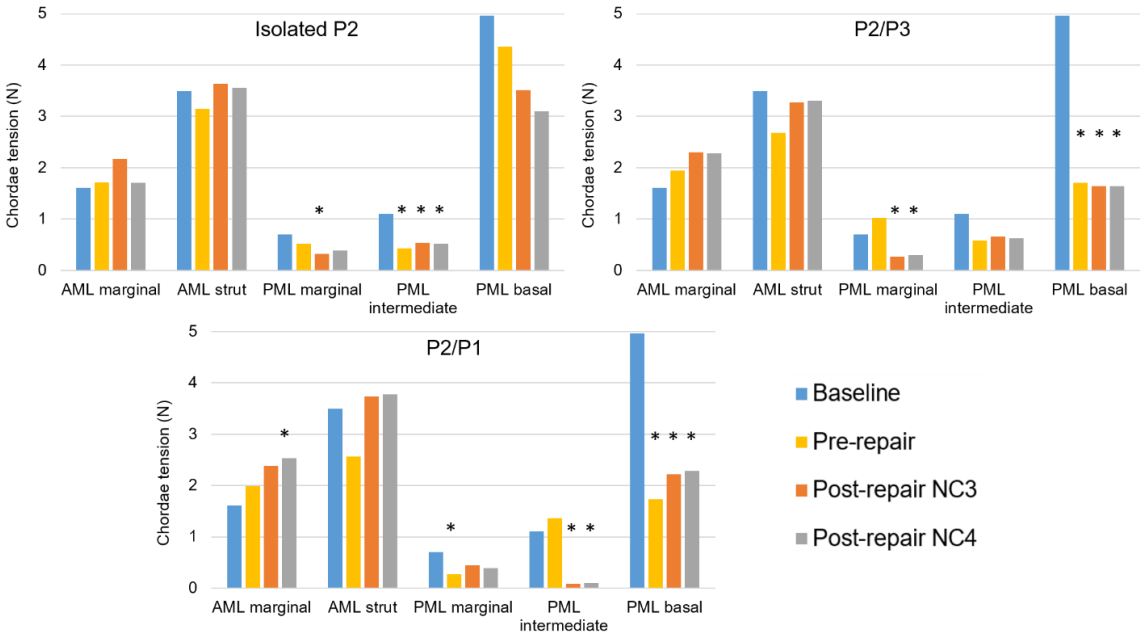

Figure 46. Native chordae tension (N) at peak systole. Asterisks highlight a marked reduction/increase (>50%) in chordae tension with respect to the baseline model (blue).

8.3.4 Neochordae and PM tension – PL-NC

Figure 47 shows the PM tension curves for the baseline model and the total neochordae tension curves for the post-repair models throughout the cardiac cycle. While the isolated P2 post-repair models had a total suture tension of ~2 N at peak systole, the P2/P3 and P2/P1 post-repair models reported a suture tension of ~3 N (Table 16). Moreover, the highest and lowest individual neochorda tensions between all post-repair models were 1.21 N and 0.42 N, respectively. No marked differences in terms of total neochordae tension were found when implanting NC3 or NC4 for each clinical scenario of MV prolapse.

8.3.5 Neochordae and PM tension – AL-NC

During peak systole, the isolated P2, P2/P3 and P2/P1 AL-NC post-repair models had a total suture tension between 2 N – 2.7 N, 5.5 N – 6 N, and 3 N – 3.3 N, respectively (Figure 47 and Table 17). Moreover, the highest and lowest individual neochorda tension values between all models were 2.06 N and 0.39 N, respectively. When comparing the use of NC3 and NC4, for the isolated P2 post-repair models, implanting NC4 showed a 30% increase in neochordae tension. For the P2/P3 and P2/P1 post-repair models, however, minor differences in total suture tension were reported.

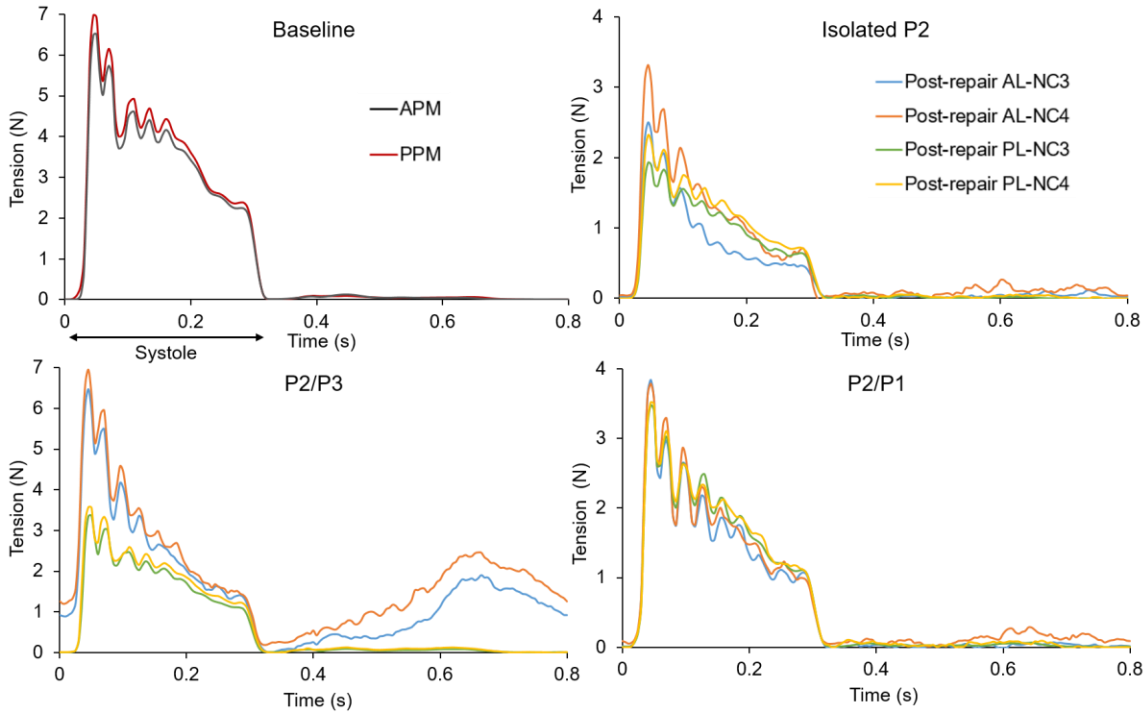

Figure 47. PM and total neochordae tension curves (N) for AL-NC and PL-NC configurations throughout the cardiac cycle.

8.3.6 Mitral leaflet stress – PL-NC

Figure 48 and Table 16 show the average stress calculated for each of the four mitral leaflet segments at peak systole. It was found that the AML stress seemed to return to a baseline state in all post-repair models, after decreasing during PML prolapse. For the isolated P2 models, the PML stress in the non-prolapsing scallops (i.e. P1 and P3) remained mostly unchanged between the baseline and post-repair states. The P2 stress, however, showed a marked variation, changing from a 50% reduction (compressive stress) in the pre-repair model, to a 50% increase (tensile stress) in the post-repair models, when compared to the baseline model.

In the P2/P3 and P2/P1 post-repair models, the stress in the non-prolapsing scallop (i.e. P1 and P3, respectively) returned to a baseline value after neochordae implantation, while in the lateral prolapsing scallop (i.e. P3 and P1, respectively) the stress increased >120% compared to the baseline model. Similarly, the central P2 prolapsing scallop saw an increase in the stress of at least 40%. Importantly, no significant differences in the average mitral leaflet stress were observed when implanting NC3 or NC4.

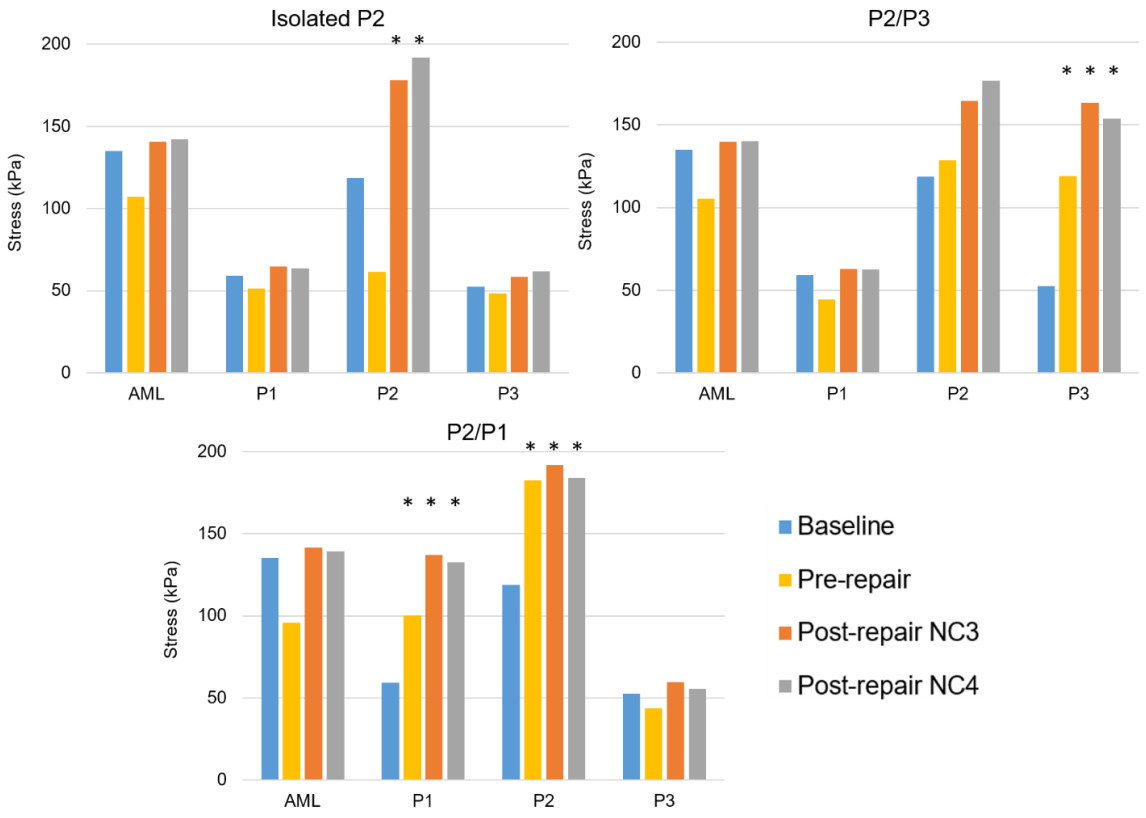

Figure 48. Average stress (kPa) in the mitral leaflets at peak systole. Asterisks highlight a marked increase (>50%) in leaflet stress with respect to the baseline model.

Additionally, Figure 49 shows the stress distribution across the mitral leaflets at peak systole. A similar pattern of stress distribution was observed in the AML for all models, displaying large stresses close to the fibrous trigones and at the insertion region of the strut chordae, regardless of the presence or repair of the prolapse. As seen in Table 16, for the baseline and isolated P2 pre-repair models, the peak stress was located in the AML, close to the right fibrous trigone, with values of 0.43 MPa and 0.52 MPa, respectively. For the P2/P3 and P2/P1 pre-repair models, the peak stress was located in the P2 scallop, near the scallop junction free edge region with values of 2.8 MPa and 2.25 MPa, respectively.

After neochordae repair, for the isolated P2 post-repair models, the peak stress increased ~100% in the P2 scallop when compared to the isolated P2 baseline model, and relocated close to the neochordae insertion zone, as seen in Figure 49. For the P2/P3 post-repair models, the peak stress was now located in the P3 scallop at the level of neochordae insertion region, with an increase of >600% when compared to the P2/P3 baseline model. Nevertheless, these peak stress values of the post-repair models were markedly lower than the value reported for the P2/P3 pre-repair model. The peak stress in the P2 scallop also increased >150% when compared to the P2 baseline model.

Likewise, for the P2/P1 post-repair models, the peak stress remained located in the P2 scallop but relocated close to neochordae insertion region, with an increase of >200% when compared to the isolated P2 baseline model. Again, these values are markedly lower than the value reported for the P2/P1 pre-repair model. Peak stress values in the P1 scallop and AML also increased >150% and 30%, respectively.

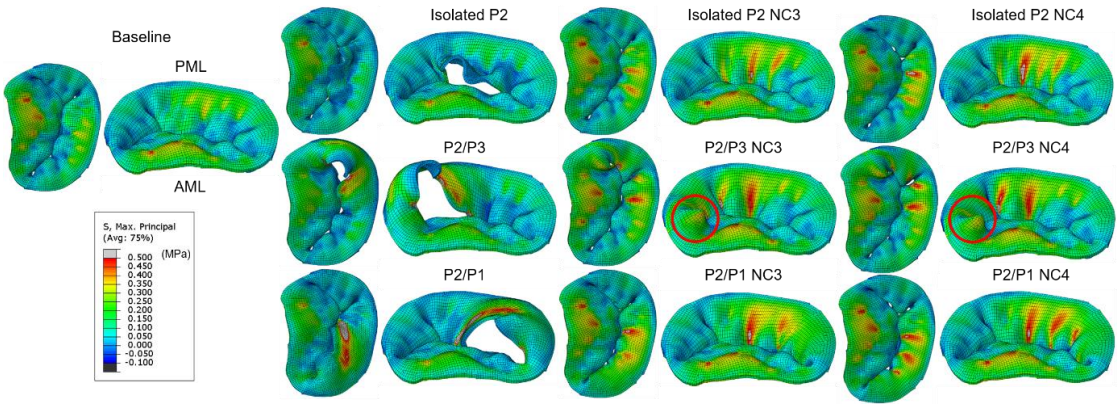

Figure 49. Stress distribution (MPa) in the mitral leaflets at peak systole. A stress value threshold of 0.5 MPa was applied such that relatively large stress values were displayed in grey, facilitating comparison between models. Red circles denote uneven coaptation regions. Native chordae and neochordae not shown for clarity.

8.3.7 Mitral leaflet stress – AL-NC

The average stress values at peak systole calculated for each of the four leaflet segments are presented in Figure 50 and Table 17. After transapical neochordae implantation, the average AML stress returned to a baseline value in all post-repair models, after decreasing during PML prolapse. For the isolated P2 post-repair models, the non-prolapsing PML scallops (i.e. P1 and P3) maintained physiological values, while the average stress in the central scallop increased >50% and >30% for the NC3 and NC4 models, respectively, when compared to the baseline model.

Similarly, for the P2/P3 and P2/P1 post-repair models, the non-prolapsing scallops (i.e. P1 and P3, respectively) maintained baseline values, while the average stress in the central scallop increased ~80%. There was also an important increase in the average stress of ~200% and >100% in the lateral prolapsing scallops (i.e. P3 and P1, respectively). Importantly, no significant differences in leaflet stress were observed when implanting NC3 or NC4.

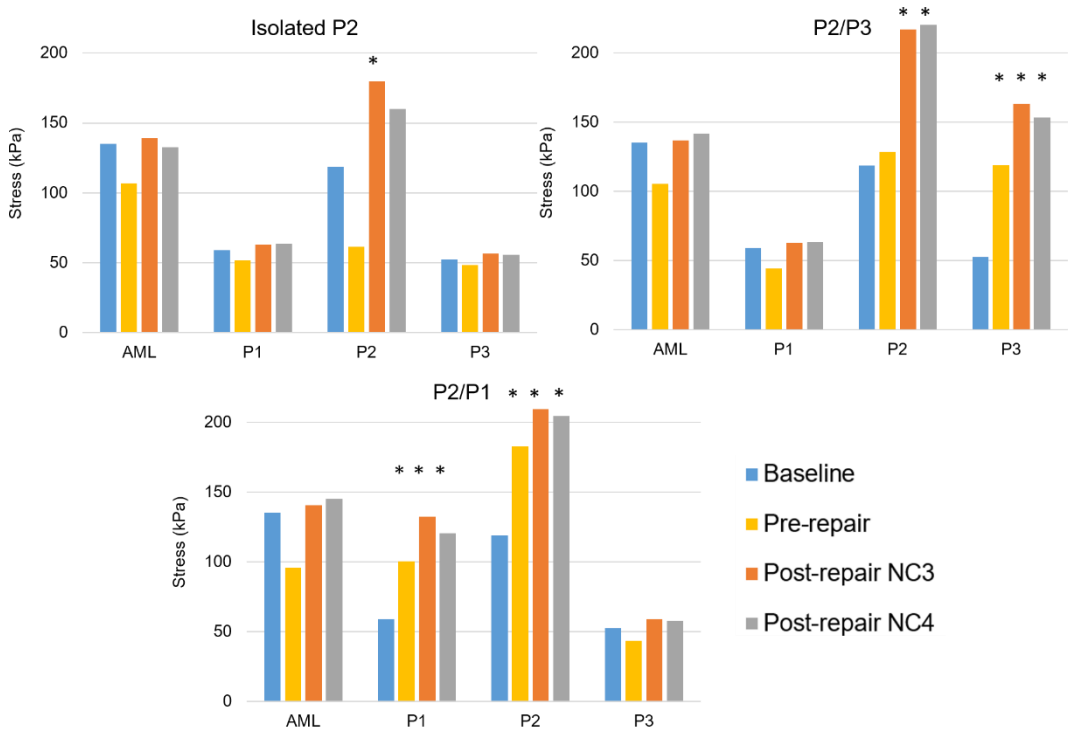

Figure 50. Average stress (kPa) in the MV leaflets at peak systole. Asterisks highlight a marked increase (>50%) in leaflet stress with respect to the baseline model (blue).

Figure 51 shows the stress distribution patterns across the mitral leaflets at peak systole. For the isolated P2 post-repair models, the peak stress in the central scallop increased ~100% when compared to the baseline model, and relocated close to neochordae insertion region, as seen in Figure 51. For the P2/P3 post-repair models, the peak stress was also located in the P2 scallop at the level of neochordae insertion, with an increase of >450% when compared to the baseline model. The peak stress in the P3 scallop also increased >350% from baseline to post-repair states. However, when compared to the P2/P3 pre-repair model, the peak P2 stress was markedly reduced from 2.8 MPa to 1.85 MPa – 2 MPa.

For the P2/P1 post-repair models, the peak stress was again situated in the P2 scallop at the level of neochordae implantation, and increased >200% when compared to the baseline model. The peak stress in the P1 scallop and AML also increased ~200% and >50% from baseline to post-repair states, respectively. However, when compared to the P2/P1 pre-repair model, the peak P2 stress actually decreased from 2.25 MPa to 1 MPa – 1.4 MPa.

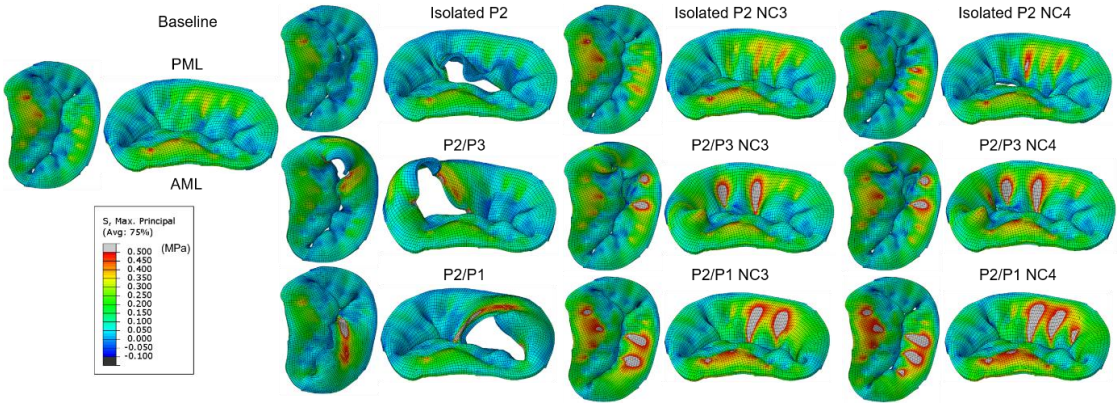

Figure 51. Stress distribution (MPa) in the MV leaflets at peak systole. A stress value threshold of 0.5 MPa was applied such that relatively large stress values were displayed in grey, facilitating comparison between models. Native chordae and neochordae not shown for clarity.

8.3.8 AL-NC vs PL-NC implantation

Table 18 compares the AL-NC vs. PL-NC biomechanical outcomes by presenting the percentage variations of the main hemodynamic and structural parameters of the AL-NC post-repair models with respect to the PL-NC post-repair models. In regard to the hemodynamic outcomes, no significant differences in MR reduction were found between AL-NC and PL-NC configurations. When comparing neochordae tension measurements at

peak systole, however, Figure 47 and Table 18 show a significant increase in the total suture tension (~80%) for the P2/P3 AL-NC post-repair models. The other two clinical scenarios of MV prolapse (i.e. isolated P2 and P2/P1) did not show noticeable changes in neochordae tension between AL-NC and PL-NC configurations.

Similarly, and from a leaflet stress perspective, the P2 scallop in the P2/P3 and P2/P1 AL-NC post-repair models showed a higher average leaflet stress than the PL-NC post-repair models, however, this increase was only important (>30%) for the P2/P3 AL-NC3 model. In contrast, no marked differences in the average stress were found in the other leaflet segments (Table 18). Finally, when comparing peak stresses in the leaflets, although minor differences in the peak stress were reported for the isolated P2 post-repair models, for the P2/P3 post-repair models, the P2 peak stress increased >100% for the AL-NC configuration, while the P3 peak stress saw a decreased of ~30%. Additionally, for the P2/P1 post-repair models, the peak stress in P3 and AML increased ~30% for the AL-NC configuration.

Table 18. Percentage variations of the hemodynamic and structural parameters for the AL-NC post-repair LH models with respect to the PL-NC post-repair LH models.

(%)	Isolated P2 NC3	Isolated P2 NC4	P2/P3 NC3	P2/P3 NC4	P2/P1 NC3	P2/P1 NC4
RV_{MV}	-2.39	8.57	-11.06	-6.72	-5.80	-7.59
RF_{MV}	-1.79	10.10	-10.12	-5.85	-5.51	-8.35
$F_{chordae}$						
AML marginal	-2.82	-27.44	5.86	2.32	-0.90	7.13
AML strut	1.46	-1.43	1.20	0.45	1.72	4.90
PML marginal	1.04	-13.69	-4.35	24.57	8.96	-9.61
PML intermediate	-5.78	-0.56	-14.09	-14.07	1267.75	403.79
PML basal	1.03	-0.85	-12.48	-15.12	5.89	8.79
F_{PM}						
APM	-0.03	-6.29	-5.12	-5.80	2.88	5.94
PPM	-0.06	-9.47	4.25	2.54	3.63	7.11
F_{NC}	12.43	27.06	81.99	78.73	-1.70	5.91
$S_I^{MAX}{}_{NC}$	7.93	23.92	70.25	83.36	7.91	6.93
$S_I^{AVRG}{}_{MV}$						
AML	-1.18	-6.68	-2.32	1.11	-0.90	4.07
P1	-2.51	-0.61	-0.26	0.88	-3.40	-9.20
P2	0.74	-16.51	31.74	25.05	9.11	11.12
P3	-3.32	-10.00	-0.07	-0.30	-1.01	3.86
$S_I^{MAX}{}_{MV}$	-7.69	-0.96	109.68	140.56	-3.47	9.18

Percentage variations with respect to the isolated P2 NC4 model with optimal neochordae length are reported in parenthesis.

8.3.9 Suboptimal neochordae length

Table 19 and Figure 52 compare the main hemodynamic and structural parameters for the isolated P2 AL-NC4 post-repair LH models with optimal and suboptimal neochordae lengths. From Figure 52A it is evident that while the over-tension model presented a similar

RV_{MV} as the optimal model, the under-tension model on the other hand, had a significant increase (>143%) in the $RV_{MV,}$ and can be determined to present moderate MR.

Concerning neochordae tension measurements (Figure 52B), as expected, under-tension of the neochordae resulted in a markedly lower total suture tension than in the optimal configuration, giving a value of 0.41 N at peak systole (Table 19). On the contrary, over-tension of the neochordae by 4 mm caused a significant increase in the total suture tension throughout the cardiac cycle, including the diastolic phase. At peak systole, shortened neochordae showed a tension of 12.22 N.

Finally, while a systematic decrease in the leaflet stress was quantified for the under-tension model, when compared to the optimal neochordae configuration, a systematic increase in AML and PML stress was quantified for the over-tension model (Figure 52D). Specifically, the central P2 scallop gave the highest stress variations between optimal and suboptimal neochordae configurations (Table 19).

Table 19. Hemodynamic and structural parameters for the isolated P2 AL-NC4 post-repair LH models with optimal and suboptimal neochordae lengths.

	Optimal	Under-tension	Over-tension
SV_{AV} (ml)	57.26	41.06	55.55
RV_{AV} (ml)	4.62	4.54	5.28
SV_{MV} (ml)	62.99	63.76	62.36
RV_{MV} (ml)	11.02	26.71 (142.9)	12.33 (11.9)
RF_{MV} (%)	16.14	39.41	18.16
MR severity (RF_{MV})	Trivial	Moderate	Trivial
$F_{chordae}$ (N)			
AML marginal	1.71	1.60 (-6.4)	3.56 (108.8)
AML strut	3.55	3.22 (-9.3)	4.27 (20.1)
PML marginal	0.38	0.43 (12.1)	0.54 (39.4)
PML intermediate	0.52	0.40 (-21.7)	0.39 (-24.8)
PML basal	3.10	4.27 (37.6)	2.16 (-30.4)
F_{PM} (N)			
APM	4.84	5.27 (9.0)	5.47 (13.1)
PPM	4.42	4.65 (5.1)	5.44 (23.0)
F_{NC} (N)	2.68	0.41 (-84.5)	12.22 (356)
$F_{neochorda}$ (%)	29.8, 14.5, 33.3, 22.5	29.0, 25.6, 17.9, 27.5	25.7, 9.0, 31.1, 34.2
$S_I^{MAX}{}_{NC}$ (MPa)	12.07	1.63 (-86.5)	56.47 (368)
$S_I^{AVRG}{}_{MV}$ (kPa)			
AML	132.7	109.7 (-17.3)	189.5 (42.8)
P1	63.3	54.2 (-14.3)	105.9 (67.3)
P2	160.1	65.7 (-58.9)	898.7 (461.2)
P3	55.5	48.7 (-12.3)	96.1 (73.0)

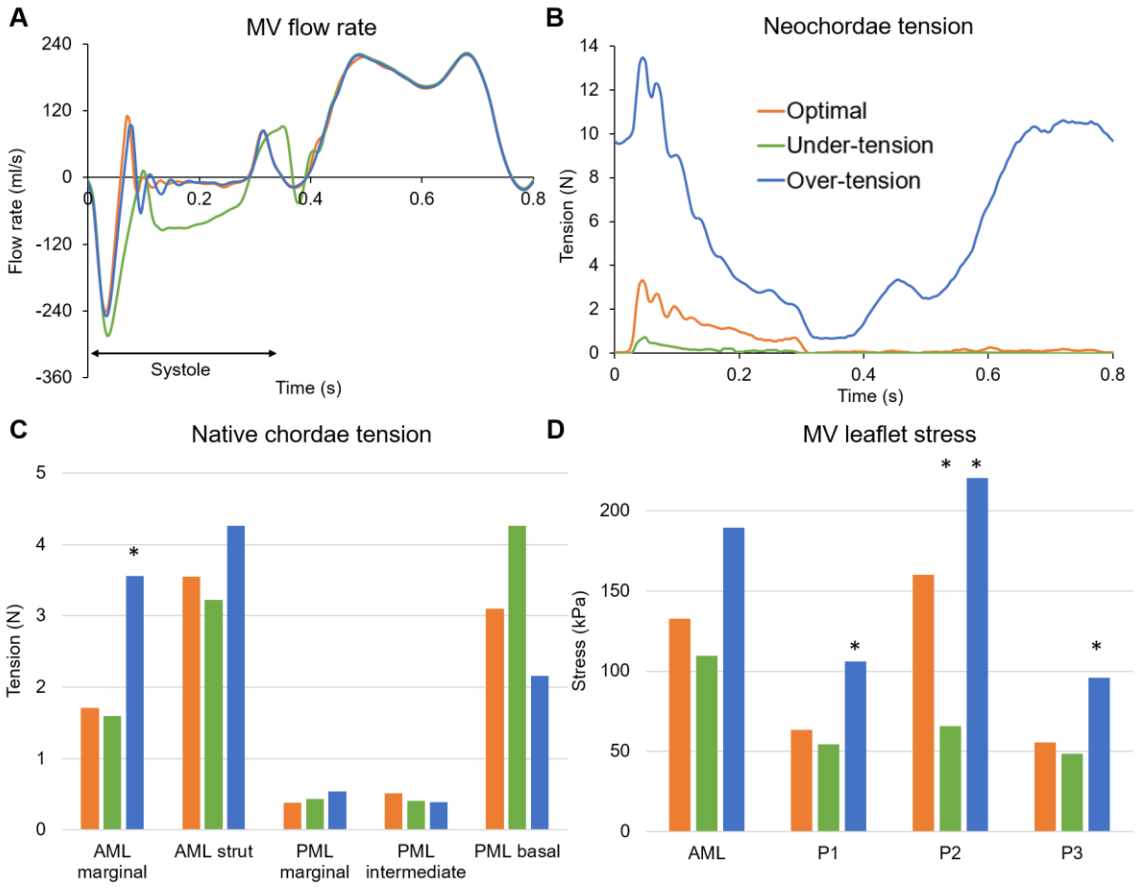

Figure 52. Isolated P2 AL-NC4 post-repair LH models with optimal and suboptimal neochordae lengths. A) Flow rate curves (ml/s) across the MV throughout the cardiac cycle. The negative systolic mitral flow indicates the backflow into the LA due to MV closing and MR, B) Total neochordae tension curves (N) throughout the cardiac cycle, C) Native chordae tension (N) at peak systole, D) Average MV leaflet stress (kPa) at peak systole. Asterisks highlight a marked reduction/increase (>50%) with respect to the isolated P2 AL-NC4 model with optimal neochordae length (orange).

8.4 Discussion

In this study, we evaluated the biomechanical effects of ePTFE suture number and length, LV access site, and complexity of PML prolapse on restoring baseline LH dynamics after transapical neochordae procedures. The present parametric study, to our knowledge, is the

first to assess the magnitude and time course of the force transfer between the mitral apparatus, the transapical neochordae and the blood flow at baseline, pre- and post-repair states using a FSI modeling framework. FSI modeling tools, as used in this study, are required to quantify the regurgitant flow across the MV, accurately simulate full dynamic/transient valve dynamics (3, 155), and assess the time course of the force transmitted through the neochordae to the LH structures during MV repair. These data, formerly inaccessible, are thus innovative. Direct quantitative comparison of the LV-valve mechanical environment between baseline and post-repair states is vital to evaluate the role of transapical neochordae implantation techniques in restoring physiologic-like cardiac dynamics. The main findings of this study were the following:

1) When using optimal neochordae length, PL-NC and AL-NC configurations resulted in successful MV repair from a hemodynamics perspective; regardless of the complexity of the prolapse lesion. From a tissue mechanics standpoint, however, the magnitude and distribution of the PML stress and native chordae tension had important changes between baseline and post-repair states.

2) No marked differences in intraventricular hemodynamics, native chordae tension and MV average stress were found when implanting NC3 or NC4 for each clinical scenario of MV prolapse. Neochordae tension, however, increased 30% when using AL-NC4 compared to AL-NC3 during isolated P2 prolapse repair. Moreover, for the P2/P1 AL-NC post-repair models, the peak P2 stress increased ~40% when using NC4.

3) For this patient case, selecting an antero-lateral LV entry site for the treatment of multi-scallop P2/P3 prolapse generated a significant increase in the neochordae tension

(~80%), P2 average stress (~30%), and P2 peak stress (>100%) with respect to a postero-lateral LV access site. No differences in MR reduction were found between AL-NC and PL-NC configurations.

4) Neochordae length tuning is critical. During isolated P2 prolapse repair when using an AL-NC configuration, although over-tension of the neochordae led to minimal hemodynamic changes in the RV_{MV}; compared to the optimal model, a significant increase in peak systolic neochordae tension (>300%), diastolic neochordae tension, and mitral leaflet average stress (40% - 460%) was quantified. Additionally, neochordae under-tension led to MR severity worsening from trivial to moderate; giving a similar RV_{MV} as the pre-repair model.

8.4.1 Baseline vs PL-NC biomechanics

Native chordae tension analysis showed that generally, PML chordae tension decreased at least 30% from baseline to post-repair states, while AML marginal tension increased >30%. Increased chordae tension can induce elongation of the chordae in the long term (219). When comparing pre- and post-repair states, Sturla and colleagues (102, 103) found that the tension in the PML marginal and basal chordae close to the prolapsing region decreased after the repair, partially transferring the load to the ePTFE sutures. We found a similar trend in this study. Nevertheless, we also showed that PML chordae tension was affected differently based on the number of prolapsed scallops. For the isolated P2 models, only basal chordae tension substantially decreased from pre- to post-repair states. For the P2/P3 and P2/P1 post-repair models, however, PML basal tension remained unchanged.

Interesting data were thus obtained, in particular concerning the force redistribution between marginal, intermediate and basal chordae.

In biomechanics, the presence of physiologic tissue stresses has long been considered closely related to tissue homeostasis (226). Following transapical neochordae implantation, the average leaflet stress substantially increased in the repaired scallop(s) when compared to the baseline model. Moreover, this increase was more noticeable during multi-scallop prolapse than during isolated scallop prolapse. On the other hand, it was observed that AML stress was not directly affected by the implantation of the ePTFE sutures, showing similar values as the baseline model. In terms of stress distribution, the peak stress relocated from the AML region in the baseline model, to the neochordae insertion region in all post-repair models. In addition, peak leaflet stress values increased significantly (~100%) for the isolated P2 post-repair models, and between 200% - 600% for the P2/P1 and P2/P3 post-repair models, when compared to the baseline model.

MV prolapse is commonly associated with alterations of the mitral apparatus tissue properties involving myxomatous degeneration (311). Although the detailed mechanisms for the development of MV prolapse in association with adverse tissue remodeling are still unclear, the underlying biomechanical goal of any optimal MV repair procedure is to restore normal valvular morphology, physiological loading and hemodynamic function. Our post-repair LH models demonstrated that both native chordae and mitral leaflets mechanical environments were affected by the implantation of the transapical sutures, with some chordae groups and leaflet segments not returning to physiologic-like biomechanical values. Although our data showed that, in some cases, post-repair native chordae tension and leaflet stress were markedly lower than in the pre-repair pathological state (Table 16),

changes in tissue deformation from those normally experienced under baseline conditions may lead to cellular responses and tissue remodeling that would ultimately dictate the extent of long-term durability of the MV repair procedures.

8.4.2 Baseline vs AL-NC biomechanics

When using optimal neochordae length, native chordae analysis showed that AML marginal tension increased >30%, while PML chordae tension decreased between 30% - 90% from baseline to post-repair conditions, depending on the specific chordae group (Table 17 and Figure 46). More importantly, the average stress substantially increased in the prolapsing scallop(s) after MV repair. This increase was more noticeable during multi-scallop prolapse than during isolated P2 prolapse, and in the lateral prolapsing scallop (i.e. P1 or P3) than in the central P2 scallop. Regarding the peak PML stress, stress magnitude in the P2 scallop increased ~100%, >200% and >450% for the isolated P2, P2/P1 and P2/P3 post-repair models, respectively. Similar to the findings of Gaidulis et al. (304) and Sturla at al. (102, 103, 312), neochordae implantation did not have important effects on the stress distribution and peak values across the non-prolapsing PML scallops.

Our results suggest that although transapical neochordae implantation may well regain normal MV coaptation and, at least in the short-term, treat MR, it may also deviate the MV leaflets from their normal physiological loading state. Valve leaflets have been shown to respond to increased stress by increasing collagen and proteoglycan synthesis, inducing a shift from predominantly type I to type III collagen. These changes can result in thicker but more compliant leaflets (313, 314), and may lead to cellular responses and tissue remodeling that would ultimately dictate the extent of the long-term durability of the

transapical neochordae procedure. It is important to remember that according to our data, although the peak PML stress from pre- to post-repair states markedly decreased, the average stress in the prolapsing scallop(s) actually increased (Table 17 and Figure 50). Clearly, further studies are necessary to determine the impact of transapical neochordae techniques on LV-MV biomechanics from pre- to post-repair states by means of reverse remodeling.

8.4.3 AL-NC vs PL-NC biomechanics

As shown in Table 18, a marked increase (>80%) in total suture tension and P2 peak stress was obtained for the P2/P3 AL-NC post-repair models, even though a similar RV_{MV} was quantified for both AL-NC and PL-NC configurations. We hypothesized that this increase in neochordae tension and P2 stress during AL-NC repair can be related to a less physiological anterior trajectory of the implanted sutures, together with a longer suture length; compared to a more posterior insertion which provides a more natural orientation for the neochordae, with the LV anchoring point close to the base of the PPM (103, 315). Future studies with a larger sample size are needed to further investigate the particular transapical AL-NC biomechanics when treating P2/P3 prolapse and to confirm these preliminary findings.

Despite apparent similarities between AL-NC and PL-NC procedures, some differences in the neochordae mechanics can be identified. It has been shown that neochordae insertion from the anterior aspect of the LV imparts both apical as well as anterior forces, the latter of which serves to decrease and stabilize the antero-posterior dimension of the mitral annulus, imparting a substantial annuloplasty effect (308). A

slightly more anterior entry site also modifies the working angle of the PML, stretches it below the AML, and thereby increases the potential leaflet coaptation (316). On the other hand, some studies do not recommend an excessively anterior LV access site for neochordae implanted on the PML, due to the unphysiologic crossing of the left ventricle outflow tract and the significant risk of interference with the native chordae that may lead to AML rupture (317). In the TACT (Transapical Artificial Chordae Tendinae) trial, better procedural outcomes were obtained when the LV access site was moved toward the ventricular postero-lateral wall (317).

It is important to highlight that current clinical experience is per protocol limited mainly to isolated P2 prolapse, not supporting therefore, the evidence that AL-NC or PL-NC procedures will be effective/ineffective on the wide spectrum of primary MR, such as AML, multi-scallop, bileaflet or paracommissural diseases (302, 318). Procedure refinements, especially the revision of the LV entry site will be critical when attempting to restore baseline MV dynamics. An optimal LV access site should not interfere with the MV subvalvular apparatus, preserve LV-valve physiology, reduce risk of coronary injuries, and preserve the best symmetry and force distribution between the neochordae.

8.4.4 Optimal neochordae mechanics

To date, our knowledge of transapical neochordae mechanics has previously relied upon few in vivo animal and human models (303, 319), as well as on MV FE-only models that did not consider the blood-tissue interaction (304). Due to inherent procedural difficulties in the experimental setup while avoiding interference with normal valve dynamics, or due to limitations in the computational capabilities, these studies have been unable to assess

the mechanical interdependence between the neochordae and the LV-valve complex through the entire cardiac cycle. Moreover, up to now, it remained unclear how forces were distributed along the neochordae when tightened to the antero-lateral human LV apex, and how they compared to PL-NC tension curves and to native chordae tension curves. Our FSI computational framework allowed for a direct quantification of these forces in a simulated human beating heart for the first time (Figure 47).

The PM tension curves obtained for the baseline model quantitatively agree with PM force measurements performed in an vivo animal setting (320, 321). In a recent in vivo human study (319), Grinberg and colleagues were able to measure real-time neochorda tension during PL-NC implantation. This in vivo model is the one that most approaches our MV repair computational modeling framework, with the measured suture tension curves quantitatively agreeing with our computed neochordae tension curves. Suture force increased rapidly during early systole until it reached a peak value. The initial shoulder of the force tracing was followed by a plateau between mid-systole, and then a rapid decline in force during end-systole. A recent large multicenter study that evaluated early and 1-year results of transapical neochordae implantation reported a 10% technical failure despite initial good echocardiography results (302). This suggest the need to refine the procedure and include innovative tools that provide valuable data to better understand the biomechanical implications of MV repair techniques. Measurement of neochordae tension could be one of these mechanistic parameters, and could help to homogenize the tension on each of the neochordae (319).

In an animal study by Jensen et al. (303), force measurements on one neochorda attached to the APM tip and to the postero-lateral LV wall were compared in eight pigs

with AML (A2 scallop) prolapse. Although no significant differences in peak and mid-systolic neochorda tension were found, the rate of change of neochorda force ($dF_{chordae}/dt_{max}$); which reflects the tension fluctuations in the sutures, was significantly higher in the transapical fixation group. It was suggested that such abnormal and faster suture tension fluctuations might be explained by the absence of the shock absorbing effect of the PM, or by the increased transapical neochorda length relative to the PM implantation length (306, 322). Table 20 shows the computed maximum slope ($dF_{chordae}/dt_{max}$) of the AL-NC and PL-NC tension curves shown in Figure 47. A marked increase in the slope (>30%) from PL-NC to AL-NC configurations was found for the isolated P2 and P2/P3 post-repair models. This means that under these patient conditions, suture tension increased more rapidly in the AL-NC implantation group than in the PL-NC group, resulting in more abnormal neochordae tension fluctuations.

Table 20. Maximum slope ($dF_{chordae}/dt_{max}$) of the neochordae tension curves for the post-repair LH models with optimal neochordae length.

		dF/dt_{max}
Isolated P2	AL-NC3	178.2
	AL-NC4	233.3
	PL-NC3	138.3
	PL-NC4	165.6
P2/P3	AL-NC3	372
	AL-NC4	377.6
	PL-NC3	242
	PL-NC4	285.9
P2/P1	AL-NC3	289
	AL-NC4	286
	PL-NC3	260.5
	PL-NC4	263.7

The abnormal fluttering of the transapical neochordae might predispose to leaflet tears, neochordae rupture and repair failure (315). Durability of ePTFE sutures is well established, with only a few cases of neochordae rupture reported in conventional MV repair surgery in the past 25 years (323). However, recent cases of late suture rupture after transapical neochordae implantation have been reported (322, 324, 325). The length of neochordae implanted transapically is often twice the length of those implanted in the PM tips under conventional repair. Some studies have suggested that suture rupture could be caused due to tractional and frictional forces (326), especially when using a loop-in-loop technique, where the frictional component of the tear could occur due to the friction between the two loops. Caimmi and colleagues (306) also suggested that the extra length of neochordae used during transapical MV repair may result in decreased durability of the sutures and cause higher internal friction forces. Overall, these findings suggest that careful evaluation of neochordae failure and possible complications should be performed on a patient-specific basis. If the suture rupture occurs at the MV leaflets, the repair of the valve can be completed with new neochordae or converted to conventional MV surgery. In the case of rupture from the apex site, however, surgeons must concern themselves with myocardial fragility (325).

8.4.5 Effect of neochordae number under optimal length

In general, no marked differences in terms of MV stress, native chordae tension, and neochordae tension were found when implanting NC3 or NC4 for each clinical scenario of MV prolapse studied herein. We hypothesized that this is due to the fact that in our numerical simulations the transapical sutures had an ideal length and were uniformly distributed along the prolapsed scallop(s). Neochordae tension, however, increased 30%

when using AL-NC4 compared to AL-NC3 during isolated P2 prolapse repair. Moreover, for the P2/P1 AL-NC post-repair models, the peak P2 stress increased ~40% when using NC4. The main objective of this first-of-its-kind parametric FSI study was to evaluate baseline, pre- and post-repair LH dynamics assuming optimal transapical MV repair procedures, as this capability represents a critical advantage of novel transcatheter therapies over traditional surgical techniques. In conventional surgical neochordae repair, suture length adjustment on arrested hearts relies mainly on the surgeon experience and on saline/ink tests. With the introduction of minimally-invasive repair techniques performed on a beating heart under real-time TEE guidance, it is now possible to fix the length of the neochordae to the optimal position; neither too long nor too short. This feature was exploited in this work.

Interestingly, even with an ideal neochordae configuration, a noticeably uneven alignment in MV coaptation in the posteromedial commissure was observed for the P2/P3 PL-NC post-repair models, as shown by the red circles in Figure 49. This could be due to the lack of millimetric suture length tuning or an uneven load distribution between the P3 scallop, the native chordae and the sutures. Indeed, it has been shown that suboptimal suture length tuning can affect the mitral apparatus biomechanics after traditional surgical neochordae repair (102). Our results are consistent with this finding, showing that the highest neochorda tension and peak leaflet stress between all post-repair models were obtained for the P2/P3 NC3 model, and were actually located in the P3 scallop (Table 16). Altogether, these results suggest that a precise and successful neochordae implantation treatment strongly depends on the patient-specific prolapse morphology and LV-valve anatomy.

8.4.6 Suboptimal neochordae length mechanics

Previous studies have suggested that suboptimal neochordae tensioning during conventional MV surgery can lead to leaflet stress hot spots, excessive localized increase of neochordae tension, and an unbalanced leaflet configuration (102). During treatment of isolated P2 prolapse, our analysis showed that while transapical sutures with an optimal length carried a net peak systolic load of 2.7 N; with a peak stress value of 12.07 MPa, over-tensioned neochordae carried a higher load of 12.2 N; with a peak stress value of 56.5 MPa (Table 19 and Figure 52). Thus, the net force exerted by the shortened sutures was 370% higher than for sutures with an optimal length, even though hemodynamic outcomes were very similar. Our study also found that the highest tension experienced by a single neochorda was 4.18 N, which corresponded to the over-tension model. This peak neochorda tension is, however, lower than the failure load of ePTFE CV-4 sutures of 16.36 N (327). These results suggest that under the specific anatomic, loading and neochordae conditions modeled in this patient case, early neochordae rupture is unlikely to occur due to excessively high tensile suture tension.

However, as shown in Figure 52B, a key finding of this study is that during suture overtension there was not only a significant increase in neochordae tension during systole but also during diastole. During the cardiac cycle there is a synchronized reciprocal behavior between the mitral annulus and the PM, with their mutual distance undergoing only minimal changes (328). Under baseline conditions, this phenomenon probably induces small elongations/shortenings of the native mitral chordae. Under transapical neochordae implantation, however, much larger changes in neochordae length can occur, since the distance between the mitral annulus and the LV apex decreases in systole and

increases in diastole. Thus, this phenomenon probably induces important elongations of the neochordae; which can be exacerbated if initial suture overtension is performed. These variations can generate an unwanted high neochordae tension during diastole, as shown in Figure 52B, that can be transferred to the repaired scallop as an unphysiological load. Furthermore, a slight over-tension is usually applied during neochordae final fixation as a result of early LV remodeling and volume reduction after the procedure (329). Overall, careful estimation of initial neochordae length as well as suture tension evolution during mid- to long-term follow-up seem critical.

8.5 Limitations

This study has several limitations that need to be considered when interpreting the results. First, the 3 pre-repair models and 14 post-repair models were virtually created from one previously validated subject-specific LH model. Thus, no population-based statements can be made and no statistical conclusions can be drawn. We acknowledge that a larger cohort of patient-specific LH models is needed to further assess the biomechanics of the transapical neochordae procedure. Nevertheless, well-controlled side-by-side comparisons such as the ones obtained in this parametric study are difficult to obtain in a clinical setting. Second, although cardiac tissue properties were age- and gender-matched, we utilized healthy human valvular tissue material properties obtained from in-house multiprotocol biaxial tests due to the limited availability of patient-specific diseased human valvular tissue data. Third, this study aimed to evaluate the changes in LH biomechanics immediately after neochordae implantation. Thus, the same cardiac wall motion was maintained before and after the treatment procedures without considering any compensatory cardiac remodeling mechanisms. Finally, the use of SPH comes with its

disadvantages. The no-slip boundary condition is not fully constrained in the Abaqus SPH formulation. This limited imposition is likely to affect the flow solution in the boundary layer and limit the study of the small-scale flow features seen in the cardiac flow. However, in Specific Aim 1 we showed that the large-scale intraventricular hemodynamics as well as the heart valve tissue mechanics obtained using the proposed SPH-FE FSI method are in agreement with in vivo, in vitro and in silico measurements.

CHAPTER 9. SPECIFIC AIM 2B – LV-VALVE DYNAMICS UNDER TRANSCATHETER AORTIC VALVE REPLACEMENT AND CONCOMITANT MITRAL REGURGITATION

9.1 Introduction

The AV and MV are coupled via a common fibrous continuity known as the aortic-mitral curtain or intervalvular fibrosa (17). As a result, physiologic function of either of these two valves involves the complementary function of the other (330). A better understanding of the aortic-mitral structural coupling and the ability to accurately assess biomechanical changes in different treatment scenarios is important, especially in the context of heart valve intervention planning and post-procedural assessment, where these changes will not only have an impact on valve dynamics but also on LV function. A prime example of aortic-mitral functional complexity is during the treatment of severe AS in the presence of secondary significant MR.

The prevalence of moderate-to-severe concomitant MR in patients undergoing TAVR ranges from 20% – 33% (331), with significant impact on prognosis (332, 333). Albeit, MR is inherently left untreated in this setting, and its severity may decrease, remain unchanged or even increase following the procedure (334, 335). The design of the two TAV devices currently used, balloon-expandable (BEV) and self-expandable (SEV) valves, might also contribute to the observed differences and add complexity to the interpretation of the results. The SEV consist of a nitinol stent with a more prominent protrusion into the LVOT, and self-expansion that has less radial force to surpass the

resistance of the calcified, oval-shaped aortic annulus, compared to the BEV stent (336). Some observational studies have pointed towards a higher degree of MR improvement in patients treated with a BEV as compared to a SEV (337-339), while others have found no differences (340).

A thorough evaluation of aortic-mitral coupling and MR response after TAVR is of particular importance in the current era, where operable patients at low surgical risk are increasingly referred for TAVR. The presence of significant MR with low likelihood of MR improvement may influence the selection of combined surgical AV replacement with MV repair/replacement therapies in such patients. As existing clinical data on the direction and magnitude of MR severity following TAVR have demonstrated conflicting evidence and constitute a current clinical dilemma, a quantitative engineering analysis of the underlying synchronized reciprocal behavior and biomechanical AV-LV-MV coupling during and after TAVR can potentially provide the basis for an individualized treatment approach and better procedural planning.

Patient-specific computer simulations for transcatheter interventions can be helpful in quantifying the interaction of a broad spectrum of devices with the human tissue/organs, based on the integration of detailed anatomic and biomechanical parameters in an objective and reproducible manner (341). In the TAVR population, however, no patient-specific computational models have been developed to analyze the effect of TAVR on aortic-mitral coupling and MR severity for patients with severe AS and concomitant MR. Thus, the main objectives of Specific Aim 2b are: 1) to model the TAVR procedure and analyze the influence of TAV type and stent implantation height on aortic-mitral structural coupling and function, and 2) simulate and validate the post-TAVR LH dynamics with the goal to

quantify the immediate changes in MR severity, identify the determinants of MR improvement, and compare SEV and BEV performance.

9.2 Materials and Methods

9.2.1 Patient-specific LH model

In this study, we employed the patient-specific LH model with functional MR developed and validated in Specific Aim 1b – Part 2. Briefly, pre-TAVR examination revealed moderate-to-severe functional MR with restricted PML motion, resulting in a posteriorly directed regurgitant jet. The measured aortic annulus was 23 mm. During the TAVR procedure, a 26 mm first generation BEV Edwards SAPIEN device was successfully deployed. Post-operative echo examination showed a correct TAV deployment, absence of PVL, while moderate-to-severe MR remained.

9.2.2 Balloon-expandable TAV model

A generic BEV model, based on a 26 mm first-generation Edwards SAPIEN device was used in this study (112). As seen in Figure 53A, the TAV consists of three components: stainless steel stent, skirt and bovine pericardium leaflets. The stent, which was generated using depictions in the literature, had an external nominal diameter of 26 mm, a frame height of 16.1 mm, and a rectangular cross section of 0.4 x 0.55 mm for the frame struts. 3D solid elements (eight-node hexahedral C3D8I elements) were used to model the stent, while 3D membrane elements (M3D4) were used to model the fully enclosed balloon, which resembled the Edwards RetroFlex 3 balloon geometry. Two layers of 3D solid elements (eight-node hexahedral C3D8R elements) were used to model the TAV leaflets,

with a uniform total thickness of 0.28 mm. The skirt was modeled by shell elements (three-node triangular S3 elements). The attachment line of the TAV leaflets to the stent are curved from the commissures downwards to the leaflet cusps, having a scallop leaflet shape similar to that of the Edwards SAPIEN valve design. TAV leaflets bovine pericardium properties, as shown in Table 21, were obtained from our previous studies that characterized the mechanical properties of chemically-treated pericardial tissues (342, 343), as presented in APPENDIX A. The stent was modeled as an elastic-plastic material with the properties of 316 stainless steel with a Young's modulus of 193 GPa, a Poisson ratio of 0.3, and initial yield stress of 340 MPa (344).

9.2.3 Self-expandable TAV model

A generic SEV model, based on a 26 mm first-generation Medtronic CoreValve device was used in this study (130). As seen in Figure 53B, the SEV consists of a Nitinol stent, skirt and porcine pericardium leaflets. Two layers of 3D solid elements were used to model the TAV leaflets and the stent, while shell elements were used for the skirt. Abaqus (3DS, Dassault Systéms, Paris, France) built-in superelasticity material library was used to model the Nitinol stent, with austenite elasticity of 50 GPa, austenite Poisson's ratio of 0.3, martensite elasticity of 25 GPa, and martensite Poisson's ratio of 0.3 (344). TAV leaflets had a thickness of 0.28 mm and porcine pericardium properties obtained from our previous studies that characterized the mechanical properties of chemically-treated pericardial tissues (342, 343). TAV leaflets porcine pericardium properties, as shown in Table 21, were obtained from our previous studies that characterized the mechanical properties of chemically-treated pericardial tissues (342, 343).

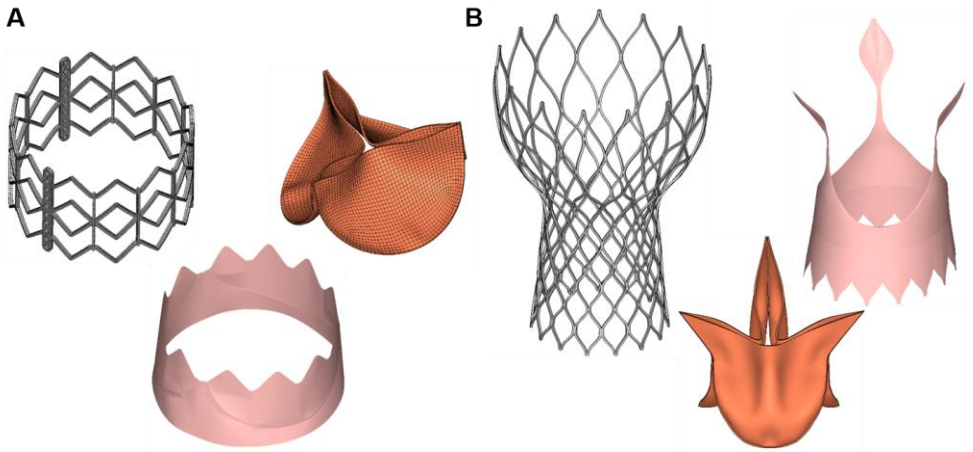

Figure 53. A) Balloon-expandable valve (BEV) model, B) Self-expandable valve (SEV) model.

Table 21. TAV leaflet material parameters.

MHGO model	C_{10} (kPa)	C_{01}	k_1 (kPa)	k_2	θ (°)	κ	D (kPa^{-1})
Bovine pericardium	6.358	16.734	13.415	96.850	0	0	5.0e-4
Porcine pericardium	1.2606	33.7972	386.842	276.732	0	0.1	5.0e-4

9.2.4 FE modelling of TAVR procedure – BEV

The TAVR procedure with a BEV was simulated in four major steps (111, 112). In order to accurately evaluate the impact of TAVR on MR severity, the patient-specific myocardium surrounding the aortic root, aortic-mitral curtain, MV and proximal LV/LA endocardial walls was also reconstructed from the MSCT images and integrated in the LH model, as seen in Figure 54B.

Step 1 - Stent crimping: Initially, the nominal stent was positioned coaxially within the aortic root and centered into the aortic annulus. The crimped stent and balloon geometries were obtained by applying a radial displacement on two cylindrical-surface sheaths. The stent was crimped to an exterior diameter of 8 mm (24 Fr catheter), as seen in Figure 54A, and positioned in a way that the TAV commissures had the same orientation as the native aortic sinuses. The AV leaflets were pre-opened with a cone-shaped catheter to simulate the effect of the insertion of the delivery system across the AV.

To quantify the impact of BEV deployment height on LH dynamics and MR severity, the axial positioning of the stent with respect to the aortic annulus plane was parametrized to replicate three clinical deployment configurations: 1) Midway, denoted as post-TAVR 50%. The conventional manufacture's recommendation for the Edwards SAPIEN system is to position the mid-point (i.e., 50:50) of the stent at the aortic annulus plane (345). 2) Post-TAVR 30%, defined as a slightly higher device implantation, with 30% of the stent located below the aortic annulus. 3) Post-TAVR 10%, defined as a high device implantation, with only 10% of the stent located below the aortic annulus plane. The aortic annulus plane was defined as the virtual plane formed by joining the points of basal attachment of the BAV leaflets (345).

Step 2 - Balloon inflation: The mechanical response of the fluid-filled balloon expansion was modeled by the surface-based fluid cavity method, capable of simulating the coupling between the deformation of the balloon and the fluid inside (112). The balloon was pressurized for 0.25 s until it was fully inflated. This method was initially calibrated to ensure a correct nominal stent size after balloon inflation.

Step 3 - Stent recoil: The internal pressure of the balloon was decreased over a time period of 0.25 s. Therefore, the stent recoiled and stabilized, and the native AV leaflets adopted a more natural open position.

Step 4 - TAV leaflet and skirt positioning: The TAV leaflets and skirt were not included during the stent deployment procedure, but were added after stent recoil. Their effect on the biomechanical interaction between the stent and the native aortic tissue has been shown to be negligible (122) The TAV leaflets were mounted in the deformed stent using a virtual assembly method (346). Briefly, the nodes lying on the leaflet attachment and along the commissures were mapped onto the stent frame through a set of non-uniform imposed displacements, ensuring an appropriate final leaflet position.

During TAVR modeling, the ascending aorta and myocardium were constrained at their distal ends allowing only rotational degrees of freedom. The balloon was constrained at its distal and proximal ends in order to mimic the bond to the catheter and avoid rigid body motion. The kinetic energy was monitored to ensure that the ratio of kinetic energy to internal energy remained under 10%. The resulting deformed LH models after BEV stent recoil were used to assess post-TAVR LH dynamics using FSI modeling.

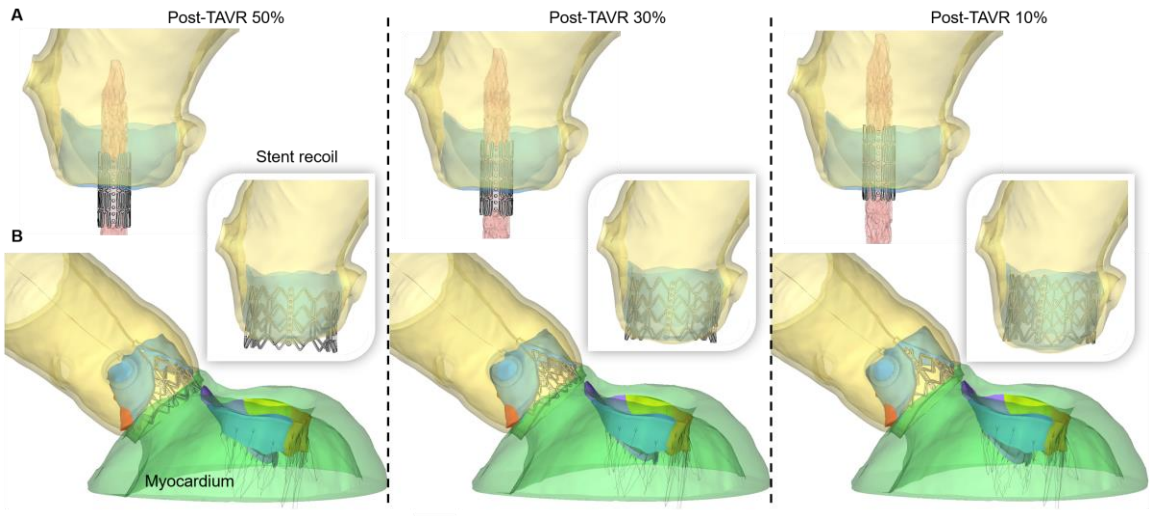

Figure 54. A) Crimped BEV stent at the three deployment heights, B) LH models with myocardium after TAVR deployment and stent recoil.

9.2.5 FE modelling of TAVR procedure – SEV

The TAVR procedure with a SEV was simulated in three major steps:

Step 1 - Stent crimping: The nominal SEV stent was positioned coaxially within the aortic root and centered into the aortic annulus. Next, the stent was crimped to an exterior diameter of 6 mm (18 Fr catheter), as seen in Figure 55A, by applying a radial displacement field to a cylindrical-surface sheath. Finally, the AV leaflets were pre-opened with a cone-shaped catheter to simulate the effect of the insertion of the delivery system across the valve. Pre-dilatation of the AV with a balloon was not simulated during the virtual procedure.

To quantify the impact of SEV implantation depth on aortic-mitral coupling and MR severity, the axial positioning of the stent with respect to the aortic annulus was

parametrized to replicate three possible clinical scenarios: 1) Optimal, the conventional manufacture's recommendation for the CoreValve system is to position the lowest point of the crimped stent ~5 mm below the aortic annulus (347), 2) High, defined as 3.6 mm higher than the optimal stent position, and 3) Low, defined as 3.6 mm lower than the optimal stent position.

Step 2 – Stent release: The deployment of the crimped stent was simulated by axially displacing the cylindrical sheath away from the aortic root, followed by a stent-tissue interaction phase to stabilize the dynamic component of the system and its contacts. The aorta and myocardium were constrained at their distal ends allowing only rotational degrees of freedom. The friction coefficient between the stent and cardiac tissues was assumed to be 0.1 (130), a frictionless contact was defined between the outer stent surface and the inner sheath surface, while a self-contact formulation was used for the stent. In order to reach a quasi-static state, viscous-elastic damping was added. This value was monitored to ensure that it did not exceed 0.8% of the total system energy. The kinetic energy was also monitored to ensure that the ratio of kinetic energy to internal energy remained under 10%.

Step 3 - TAV leaflet and skirt positioning: The TAV leaflets and sealing skirt were added as previously explained. The pressure gradient was neglected during the TAVR procedure, since in the clinical setting rapid pacing is applied during device deployment. The deformed LH geometries, as shown in Figure 55B, were extracted from the FE simulations and used to assess the post-TAVR LH dynamics using FSI.

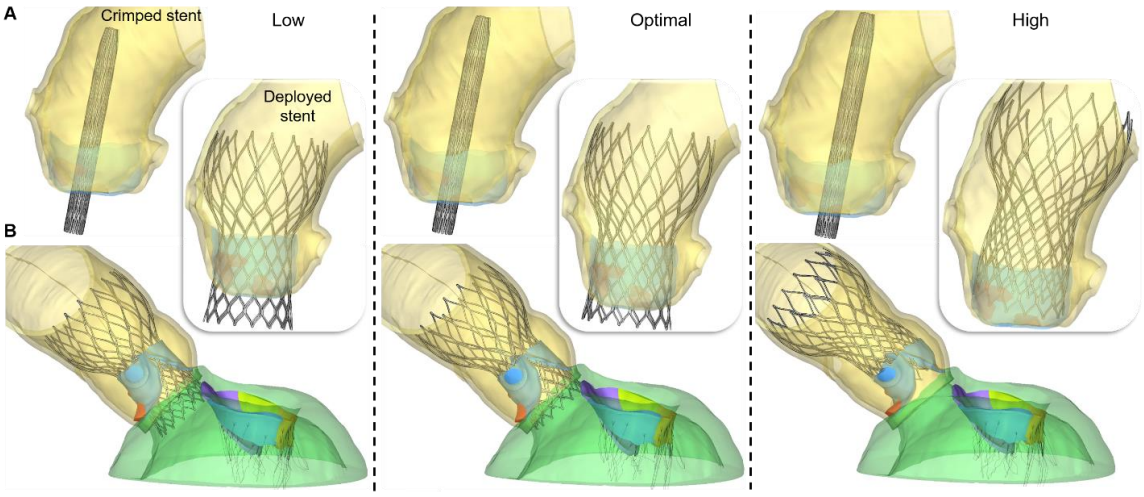

Figure 55. A) Crimped SEV stent at the three deployment heights, B) LH models with myocardium after TAVR deployment.

9.2.6 Boundary conditions

Time-dependent pressure boundary conditions were applied at the two atrial inlets (pulmonary veins) and at the aortic outlet of the pre- and post-TAVR LH models, as previously explained in Specific Aim 1b – Part 2. Pressure boundary conditions and cardiac wall motion were kept the same for the pre- and post-TAVR LH models, simulating immediate post-operative LH dynamics, without considering the cardiac remodeling mechanisms that occur over time after TAVR.

9.2.7 Data analysis

9.2.7.1 Aortic-mitral geometrical parameters

Aortic-mitral structural coupling during TAVR was evaluated in terms of the geometrical parameters shown Figure 56. The following measurements were obtained during systole:

a) aortic annulus and MA areas, b) antero-posterior (AP) distance, defined as the distance between mid-anterior and mid-posterior MA points, c) anterolateral-posteromedial (AL-PM) distance, d) inter-commissural (CC) distance, e) MA height, defined as the maximum vertical distance between the highest and lowest points of the saddle-shaped MV, f) aortic-mitral angle, defined as the angle between the planes of the MA and the aortic annulus, g) aortic-mitral distance, defined as the centroid distance between the MA and the aortic annulus, h) aortic annulus motion, defined as the longitudinal excursion of the aortic annulus during TAVR, and i) anterior and posterior MA motion, defined as the posterior displacement of the MA during TAVR.

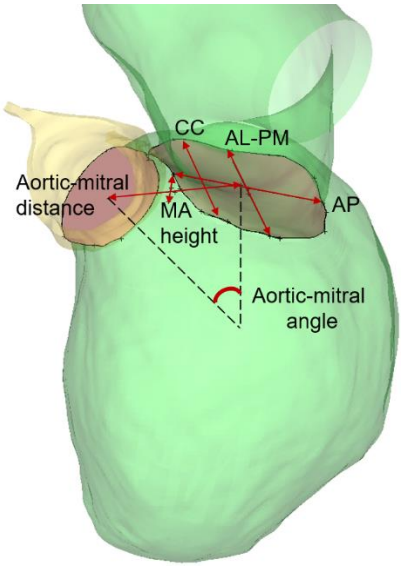

Figure 56. Aortic-mitral geometrical parameters.

9.2.7.2 Fluid parameters

As introduced in Specific Aim 1b – Part 2, the following hemodynamic parameters were quantified: SV_{AV}, SV_{MV}, RV_{AV}, RV_{MV}, RF_{MV}, MR severity, LVEF, LV mean systolic pressure, AV mean and peak gradients, AV peak velocity, EOA_{AV}, E wave, A wave, E/A ratio, MR peak and mean gradients, and MR peak velocity

9.2.7.3 Structural parameters

The three stent deployment heights for the BEV and SEV models were analyzed and compared during the TAVR procedure in terms of peak (S_I^{MAX}) and average (S_I^{AVRG}) maximum principal stress values in the BAV leaflets, sinus, calcification and MA, contact radial force between the stent and aortic root, and stent deformation. To facilitate comparison between different models and avoid the bias caused by local high stress concentration, only the 99-percentile values of the peak stress were evaluated (348). Moreover, leaflet annular regions were not included in the average stress calculation in order to avoid boundary effects. The contact radial force between the recoiled stent and surrounding cardiac tissues was calculated as $RF = \sum_{i=1}^{n_s} rf_{i,post}$, where n_s is the total number of nodes in the stent, and $rf_{i,post}$ is the radial contact force at each stent node after recoil. Stent deformation was evaluated by quantifying stent eccentricity and recoil. Stent eccentricity, which assess the conformity of the stent deformation after recoil, was calculated as the ratio of the maximum stent diameter to minimum stent diameter. BEV stent recoil was determined as $(D_{min}\ expanded - D_{min}\ recoiled)/D_{min}\ expanded$, where D_{min} is the minimum stent diameter during fully balloon expansion and stent recoil.

These two metrics were calculated at three different cross-sections of the stent (i.e. bottom, middle and top) with the mean value reported.

Additionally, post-TAVR tissue mechanics were evaluated by the average maximum principal stress values calculated in the AV/TAV leaflets and MV leaflets during peak diastole and systole, respectively. Chordae forces ($F_{chordae}$) at peak systole were also reported. The force experienced by a particular chordae group was calculated as the sum of vectors representing the tension in each individual chorda attached to that chordae group.

9.3 Results

9.3.1 TAVR-in-BAV biomechanics – BEV

Figure 54A shows the crimped BEV stent geometry at the three deployment heights, while Figure 54B shows the final deformed geometries after balloon deflation and stent recoil. No severe leaflet overhanging or potential risk for coronary obstruction were observed. The shortest distance between the coronaries and the native leaflets was found to be 7.5 mm for the post-TAVR 10% case, which was between the left coronary ostia and the fused leaflet free edge. No evident gaps between the recoiled stent and the native annular tissue were observed in the post-TAVR LH models, which was later confirmed in the FSI blood flow simulations by absence of PVL.

The stress distribution on the native AV leaflets after stent recoil is presented in Figure 57. Similar stress distribution patterns were observed for the three implantation configurations, where peak values were located in regions in contact with the higher portion of the stent for the post-TAVR 30% and 10% models, and in the leaflet-root

attachment region close to the commissures for the post-TAVR 50% case, as shown by the red circles in Figure 57. Another leaflet region that experienced high stress values was the leaflet belly region in contact with the large calcification deposit due to the stiffer material properties. For the aortic root, high stress values were found at the leaflet-root attachment lines, especially in the fused leaflet commissures.

As presented in Table 22, the highest deployment model (post-TAVR 10%) resulted in higher peak stress values in the leaflets, sinus and calcification regions. The highest peak stress in the anterior MA, however, was found for the midway implantation model (post-TAVR 50%), a direct result of a larger aortic-mitral curtain tissue in contact with the stent. The contact radial force between the recoiled stent and surrounding cardiac tissues is listed in Table 22. The post-TAVR 10% model gave the highest contact force, with a value of 108 N, while the post-TAVR 50% case gave the lowest contact force, with a value of 98 N. Stent eccentricity and recoil values are also presented in Table 22. All three stents showed a similar eccentricity, maintaining a nearly uniform circular pattern. Stent recoil, however, was lower for the midway implantation model (3.3%) than for the highest implantation model (6.2%).

Table 22. TAVR-in-BAV biomechanical parameters after BEV stent recoil.

	Post-TAVR 50%	Post-TAVR 30%	Post-TAVR 10%
S_I^{MAX} (MPa)			
Native AV leaflets	2.75	2.93	3.15
Sinus	2.11	2.16	2.34
Calcification	1.88	1.95	2.02
Anterior MA	0.151	0.064	0.036
Posterior MA	0.012	0.024	0.014
S_I^{AVRG} (MPa)			
Native AV leaflets	0.74	0.88	1.01
Sinus	0.31	0.31	0.3
Contact radial force (N)	98.13	104.09	107.79
Stent eccentricity	1.05	1.08	1.07
Stent recoil (%)	3.30	5.75	6.17

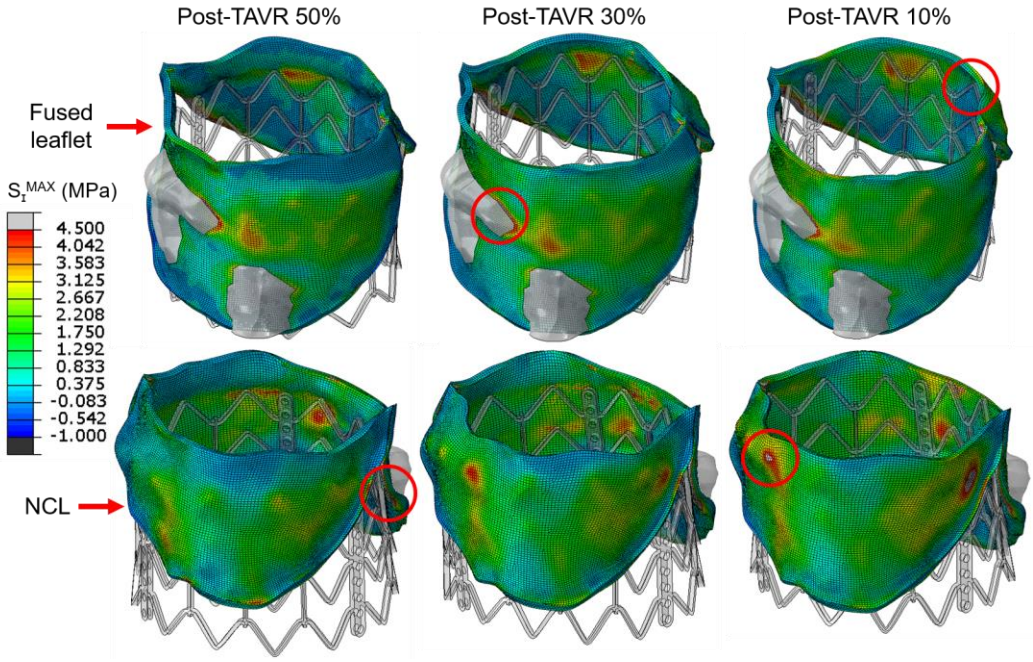

Figure 57. Stress distribution (MPa) in the AV leaflets after BEV stent recoil. Red circles denote regions of peak stress values. A maximum stress value threshold of 4.5 MPa was applied such that higher stress values were displayed in grey, facilitating comparison between models.

9.3.2 TAVR-in-BAV biomechanics – SEV

Figure 55 shows the crimped and deployed SEV stent geometries at the three implantation depths. No potential risk for coronary obstruction was observed after TAVR. No evident gaps between the stent and aortic tissues were observed following TAVR, which was later confirmed in the FSI simulations by the absence of PVL. Figure 58 presents the stress distribution on the AV leaflets after stent deployment. Similar stress patterns were observed for the three implantation configurations, with high stress values found in the fused leaflet, especially in the upper half of the leaflet. For the high implantation model, the NCL also presented high stress values in the upper region of the leaflet. As shown by the red circles, peak stress values were located in the leaflet-root attachment line close to the commissures, in the leaflet free edge in contact with the stent, and in the fused leaflet belly region in contact with the large calcification deposit.

Table 23 summarizes the peak (S_I^{MAX}) and average (S_I^{AVRG}) stress values in the aortic tissues, the stent-tissue contact force, and stent eccentricity. The high deployment model gave the highest peak and average stress values in the AV leaflets, the lowest peak stress values in the calcification and MA, and the lowest stent-tissue contact force. All three SEV stents showed a similar deformation, with an eccentricity value of ~1.08.

Table 23. TAVR-in-BAV biomechanical parameters after SEV stent deployment.

	Low	Optimal	High
S_I^{MAX} (MPa)			
Native AV leaflets	1.16	1.31	1.88
Sinus	0.80	0.89	0.90
Calcification	0.82	0.97	0.57
Anterior MA	0.250	0.141	0.024
Posterior MA	0.046	0.048	0.020
S_I^{AVRG} (MPa)			
Native AV leaflets	0.22	0.27	0.40
Sinus	0.10	0.12	0.09
Contact radial force (N)	31.70	39.55	28.79
Stent eccentricity	1.09	1.08	1.08

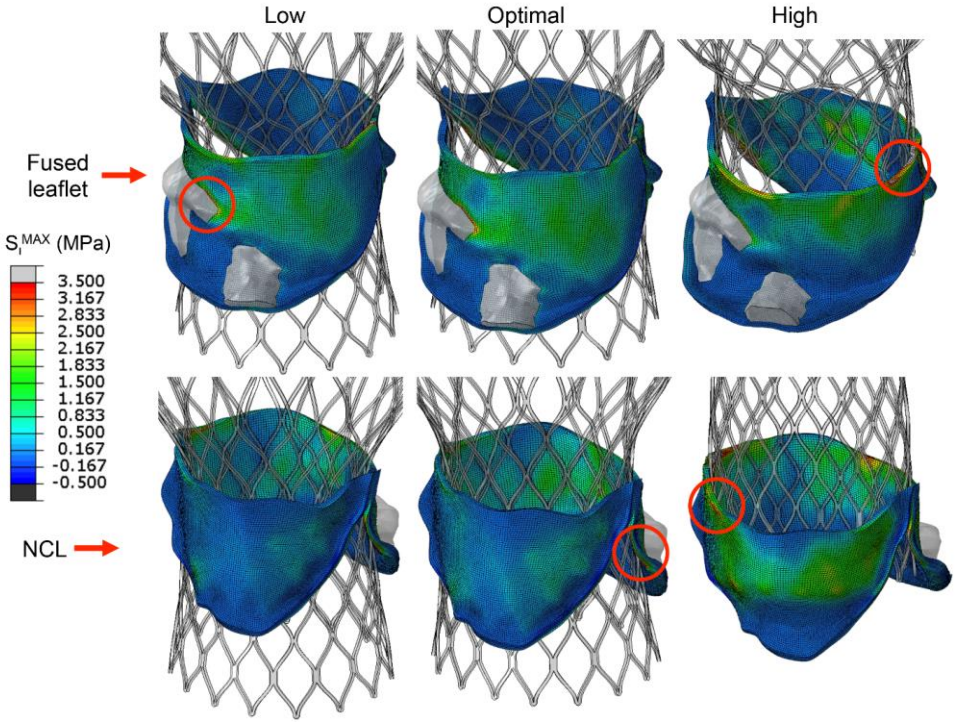

Figure 58. Stress distribution (MPa) in the AV leaflets after SEV deployment. Red circles denote regions of peak stress values. A maximum stress value threshold of 3.5 MPa was applied such that higher stress values were displayed in grey, facilitating comparison between models.

9.3.3 BEV impact on MR: structural changes

Figure 59 and Table 24 present the aortic-mitral structural coupling before and after TAVR during peak systole. We found an important reduction in the MA height from pre- to the post-TAVR 50% model (15%), however, as the stent implantation height increased, the MA height increased instead; up to 8% for the post-TAVR 10% case. Additionally, the aortic-mitral angle decreased between 5% - 10% following TAVR, with a smaller systolic angle in the highest implantation model than in the midway implantation model. Although the MA area (~3.2%), AP distance (~4.3%) and aortic-mitral distance (~4.5%) decreased in all post-TAVR models, there were no evident changes when comparing these before and after TAVR. Similarly, both AL-PM distance (~3%) and aortic annulus area (~2%) had a slight tendency to increase after TAVR. In regards to the aortic annulus motion, it was found that this anatomic structure was displaced ~3.3 mm towards the LVOT during TAVR, and this motion seemed to decrease as the stent implantation height increased. Moreover, the anterior MA was also displaced ~2.5 mm posteriorly during TAVR, again, this motion decreased as the implantation height increased. Finally, Figure 59 shows the aortic-mitral complex before and after TAVR during peak systolic flow. Although it is evident that the regurgitant orifice area decreased in all post-TAVR models, MR was still present. Moreover, the post-TAVR 50% model exhibited the smallest regurgitant orifice area, which was later confirmed by quantification of the RV_{MV}.

Table 24. Aortic-mitral geometrical parameters during systole – BEV.

	Pre-TAVR	**Post-TAVR 50%**	**Post-TAVR 30%**	**Post-TAVR 10%**
Aortic annulus area (cm^2)	4.93	5.13	5.00	4.94
MA area (cm^2)	11.40	10.97	11.04	11.10
AP distance (mm)	35.53	33.29	34.30	34.41
AL-PM distance (mm)	39.54	40.97	40.58	40.66
CC distance (mm)	31.14	31.18	30.80	30.94
MA height (mm)	6.00	5.10 (-15)	6.18 (3)	6.49 (8)
Aortic-mitral angle (º)	123.05	116.88 (-5)	112.81 (-8)	111.23 (-10)
Aortic-mitral distance (mm)	28.46	27.48	27.06	26.97
Aortic annulus motion (mm)	–	3.87	3.15	2.82
Anterior MA motion (mm)	–	3.28	2.31	1.92
Posterior MA motion (mm)	–	1.00	0.76	0.48

Percentage variations with respect to the pre-TAVR model are reported in parenthesis.

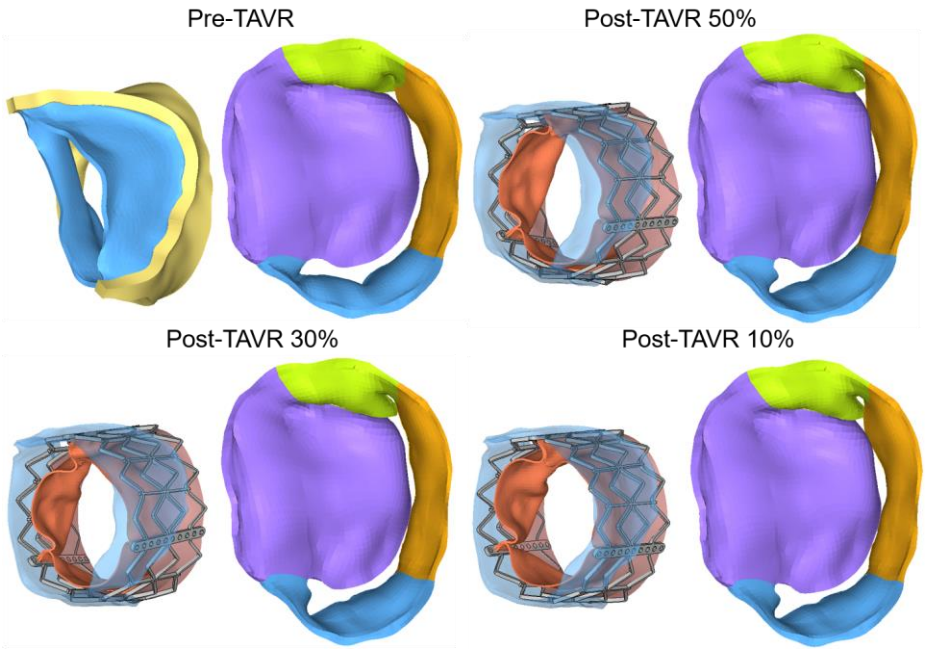

Figure 59. Aortic-mitral coupling at peak systole when using a BEV.

9.3.4 SEV impact on MR: structural changes

From Figure 60 it is evident that although the MV regurgitant orifice area appeared to decrease in most post-TAVR models, MR was still present. As presented in Table 25, we quantified a marked reduction (>20%) in the MA height from pre- to post-TAVR states, with the highest reduction found for the optimal implantation model (35%). Similarly, the aortic-mitral angle decreased (~10%) after low and optimal configurations. Although the aortic-mitral distance (~4.2%), MA area (~2.5%), AP distance (<1%), and CC distance (<1%) decreased in all post-TAVR models, there were no significant changes when comparing these before and after TAVR. Similarly, both AL-PM distance and aortic annulus area had a slight tendency to increase after TAVR. Regarding the displacement of the valve annuli, it was found that the anterior MA was displaced posteriorly ~1.6 mm

during the TAVR procedure, while the aortic annulus was displaced ~2.6 mm towards the LVOT. Importantly, this annuli motion seemed to increase as the stent implantation height increased.

Table 25. Aortic-mitral geometrical parameters during systole – SEV.

	Pre-TAVR	**Low**	**Optimal**	**High**
Aortic annulus area (cm^2)	4.93	4.96	5.01	4.94
MA area (cm^2)	11.40	11.19	11.15	10.99
AP distance (mm)	35.53	35.90	35.20	34.62
AL-PM distance (mm)	39.54	39.58	40.21	39.78
CC distance (mm)	31.14	30.82	31.02	30.74
MA height (mm)	6.00	4.43 (-26)	3.93 (-35)	4.66 (-22)
Aortic-mitral angle (º)	123.05	111.26 (-10)	110.10 (-11)	121.26
Aortic-mitral distance (mm)	28.46	27.48	27.14	27.17
Aortic annulus motion (mm)	–	1.61	2.93	3.14
MA motion (mm)	–	1.17	1.67	1.88

Percentage variations with respect to the pre-TAVR model are reported in parenthesis.

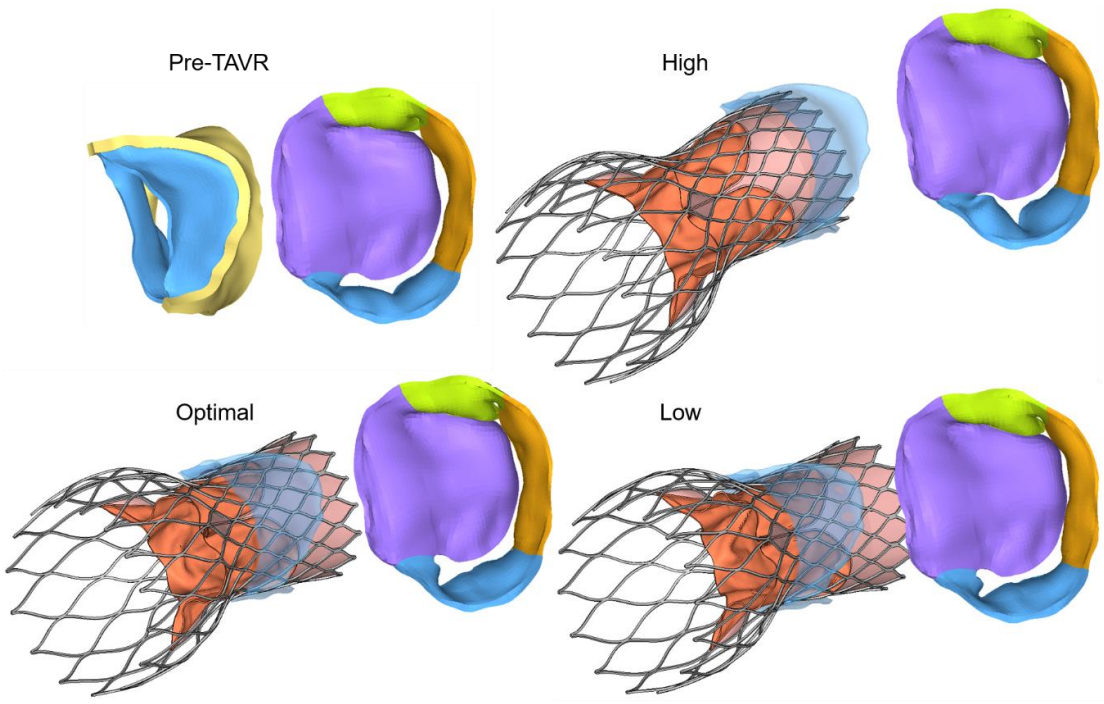

Figure 60. Aortic-mitral coupling at peak systole when using a SEV.

9.3.5 BEV impact on MR: hemodynamic changes

Figure 61 shows the flow rate waveforms across the AV an MV throughout the cardiac cycle for the pre- and post-TAVR LH models. The negative aortic flow at end-systole (Figure 61A) indicates the retrograde blood flow into the LV during AV closure, while the negative systolic mitral flow (Figure 61B) indicates the backflow of blood into the LA due to MV leaflet closing and MR. Diastolic inflow rates (positive) across the MV were approximately the same for all models, since LV size and motion remained unchanged immediately post-TAVR. As expected, the pre-TAVR LH model had the lowest peak aortic flow and SV_{AV}, as seen in Figure 61A. Following TAVR, correction of the AV obstruction led to an immediate reduction in the LV systolic pressure, which decreased the pressure

gradient across the AV and MV, and therefore led to a reduction in the RV_{MV} and an increase in the SV_{AV}.

As shown in Table 26, improved LV function and hemodynamic success of the procedure was found in all post-TAVR LH models, as confirmed by the reduction of MR and AV/MR peak velocities, and by the increase in the EOA_{AV}. The greater degree of MR improvement (10%) was for the post-TAVR 50% model; which based on the RF_{MV} criterion can now be classified as moderate MR. When compared to the pre-TAVR model, the degree of MR severity remained unchanged for the post-TAVR 30% and 10% models.

When comparing the pre- and post-TAVR aortic flow rate waveforms shown in Figure 61A, a noticeable change in the onset time of BAV/TAV closure was found. The TAV device had a distinct slower closure and higher closing volume compared to the native BAV leaflets, with the highest RV_{AV} obtained for the post-TAVR 10% model. Pre-procedural mild aortic regurgitation, found clinically in the patient's echo examination, was also detected in the pre-TAVR computational model, as shown by the negative diastolic aortic flow (Figure 61A). Aortic regurgitation was resolved following TAVR, both in the real clinical case and in the FSI simulations. Moreover, the absence of PVL in all post-TAVR LH models matched the post-operative echo findings.

Additionally, Figure 62 shows the intraventricular velocity streamlines colored by velocity magnitude during peak systole. Due to the restricted PML motion, the post-TAVR models displayed a posteriorly directed regurgitant jet. The regurgitant jet structures were similar between the post-TAVR models, with an eccentric "wall-hugging" jet that impinged the postero-lateral atrial wall, with a similar MR peak velocity (Table 26).

Overall, when compared to the patient-specific post-TAVR echo data, numerical results corresponded well to the echo measurements (Table 26), which demonstrate the accurate predictive capabilities of our patient-specific modeling methodology, that is, the simulated TAVR procedure using FE analysis, followed by the simulated post-TAVR LH dynamics using FSI analysis. Nevertheless, some differences between the echo and FSI data were found, especially regarding the AV pressure gradients. These differences, which will be later discussed, are in line with the inherent uncertainties in the echo flow recordings and the image-based computer simulations.

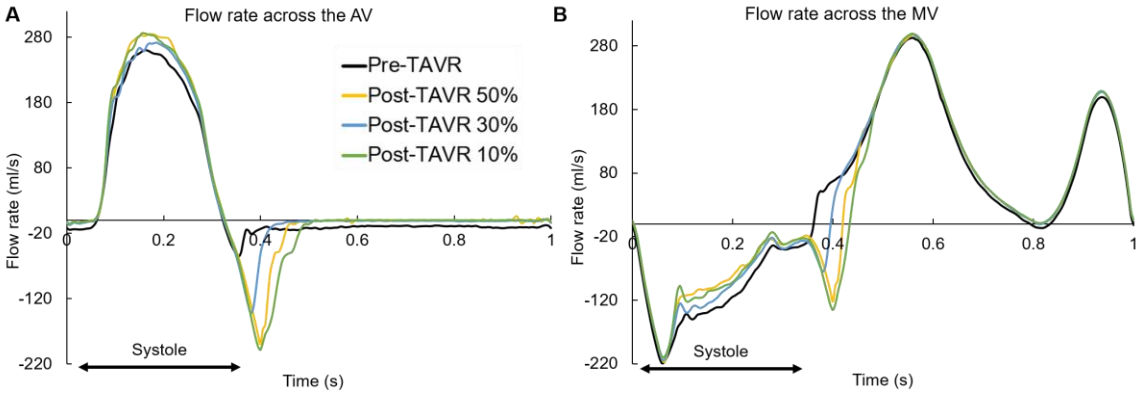

Figure 61. Flow rate (ml/s) across the A) AV and B) MV throughout the cardiac cycle.

Table 26. Pre- and post-TAVR LH hemodynamics and post-TAVR echo comparison – BEV.

	Pre-TAVR	**Post-TAVR 50%**	**Post-TAVR 30%**	**Post-TAVR 10%**	**Post-TAVR Echo**
SV_{AV} (ml)	46.28	52.24	49.11	51.94	48
RV_{AV} (ml)	9.34	11.43	7.21	15.39	–
SV_{MV} (ml)	74.64	74.54	76.93	72.72	–
RV_{MV} (ml)	37.59	33.84	34.8	35.89	32
RF_{MV} (%)	44.82	39.32	41.48	40.87	–
MR severity (RF_{MV})	Moderate-to-severe	Moderate	Moderate-to-severe	Moderate-to-severe	Moderate-to-severe
LVEF (%)	28.55	29.30	28.56	29.90	30
AV peak gradient (mmHg)	34.82	22.64	24.12	23.88	16.6
AV mean gradient (mmHg)	23.97	11.98	12.54	12.53	8.4
AV peak velocity (m/s)	2.82	1.74	1.73	1.70	2.0
EOA_{AV} (cm^2)	0.77	1.20	1.12	1.17	1.4
E wave (m/s)	0.79	0.80	0.83	0.88	0.87
A wave (m/s)	0.54	0.54	0.57	0.58	0.54
E/A	1.47	1.48	1.47	1.51	1.6
MR peak gradient (mmHg)	118.59	114.09	110.87	112.76	108
MR peak velocity (m/s)	5.42	4.92	4.91	4.93	5.2

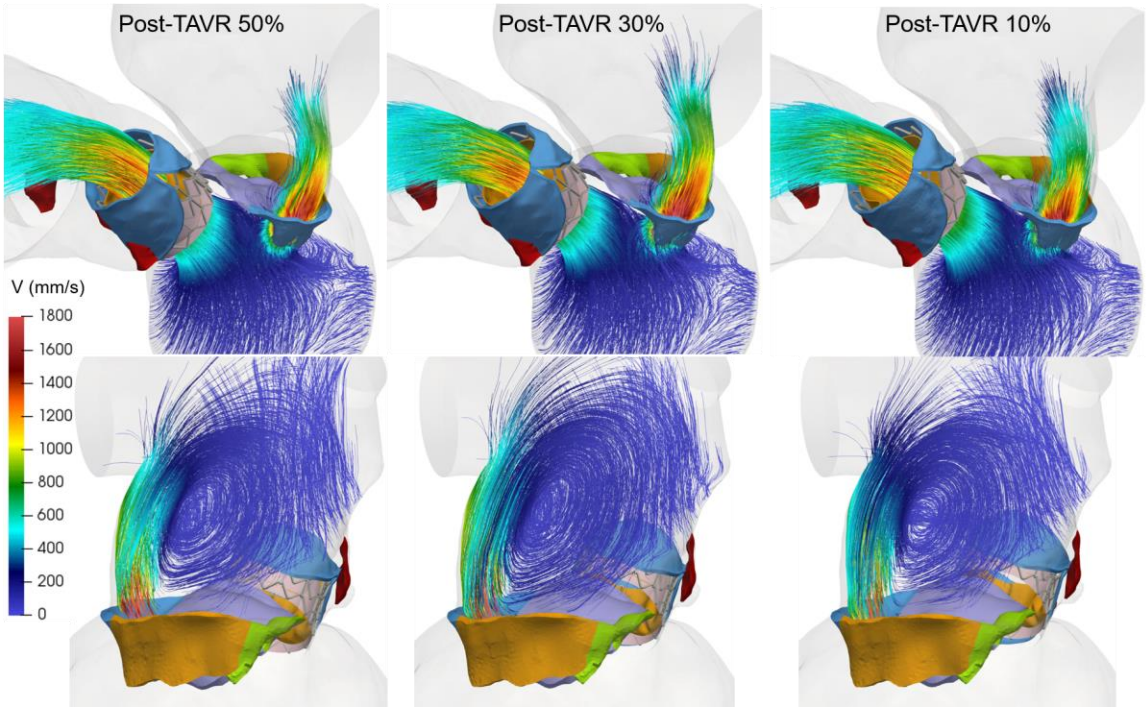

Figure 62. Post-TAVR velocity streamlines showing the regurgitant jet structures at peak systole.

9.3.6 SEV impact on MR: hemodynamic changes

Several findings can be described from Figure 63 and Table 27. First, improved systolic function and hemodynamic success of the procedure was found in the post-TAVR models, given by lower AV peak/mean pressure gradients, AV peak velocity, MR mean pressure gradient, and MR peak velocity, and higher EOA_{AV} and SV_{AV}. Second, the greater degree of MR improvement (~10%) was for the high deployment model; which based on the RF_{MV} criterion can now be classified as moderate MR. The degree of MR severity remained unchanged for the low and optimal models. Third, the optimal model gave a higher RV_{MV} than the pre-TAVR model (40.49 vs 37.59 ml). Due to the coupled valve dynamics and

mass conservation, this model also gave a slightly lower SV_{AV} than the pre-TAVR model (43.97 vs 46.28 ml). Fourth, central aortic regurgitation was resolved following TAVR for the low and optimal implantation models, while the SEV of the high deployment model did not fully close until mid-diastole (Figure 63A). No PVL was quantified in any of the post-TAVR models, as found clinically. Finally, Figure 64 shows the intraventricular velocity streamlines colored by velocity magnitude during peak systole.

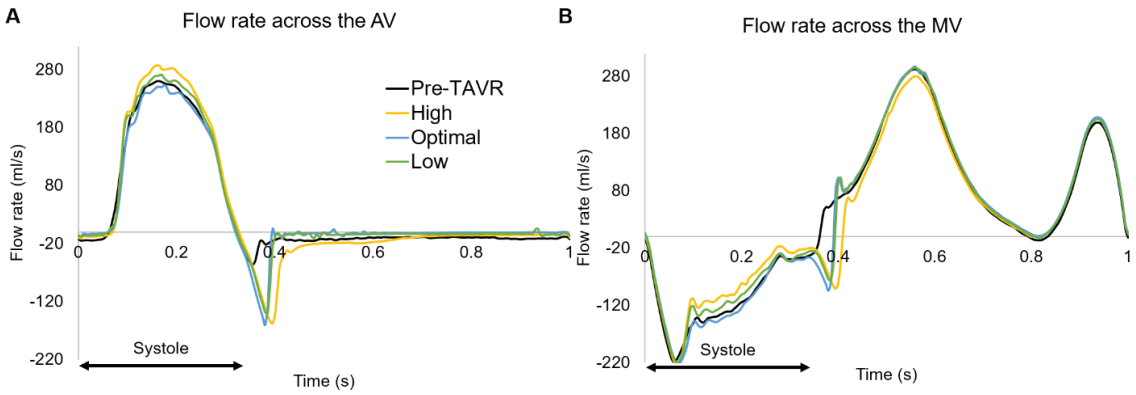

Figure 63. Flow rate (ml/s) across the A) AV and B) MV throughout the cardiac cycle.

Table 27. Pre- and post-TAVR FSI hemodynamics – SEV.

	Pre-TAVR	Low	Optimal	High
SV_{AV} (ml)	46.28	47.89	43.97	51.01
RV_{AV} (ml)	9.34	7.91	6.87	15.19
SV_{MV} (ml)	74.64	76.12	77.60	69.54
RV_{MV} (ml)	37.59	35.96	40.49	33.65
RF_{MV} (%)	44.82	42.89	47.94	39.75
MR severity (RF_{MV})	Moderate-to-severe	Moderate-to-severe	Moderate-to-severe	Moderate
LVEF (%)	28.55	28.54	28.75	28.82
LV mean systolic pressure (mmHg)	95.15	91.16	89.38	91.59
AV peak gradient (mmHg)	34.82	27.32	27.78	28.13
AV mean gradient (mmHg)	23.97	15.66	15.69	16.24
AV peak velocity (m/s)	2.82	1.76	1.66	1.70
EOA_{AV} (cm^2)	0.77	1.00	0.93	1.04
E wave (m/s)	0.79	0.80	0.78	0.67
A wave (m/s)	0.54	0.56	0.56	0.49
E/A	1.47	1.44	1.40	1.36
MR mean gradient (mmHg)	57.25	51.83	52.85	50.90
MR peak velocity (m/s)	5.42	5.18	5.13	4.89

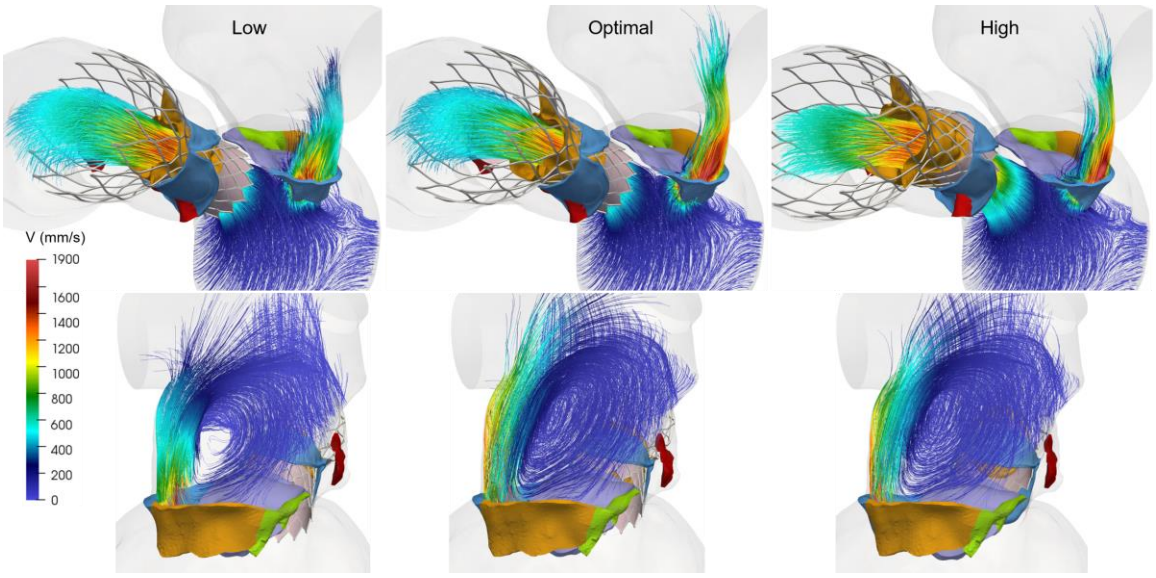

Figure 64. Post-TAVR velocity streamlines showing the regurgitant jet structures at peak systole.

9.3.7 Post-TAVR biomechanics – BEV

Table 28 presents the average stress values calculated for the AV/TAV leaflets and MV leaflets during peak diastole and systole, respectively. It was found that the average stress in the AML was at least 20% lower following TAVR, potentially due to morphological changes caused by the posterior displacement of the anterior MA during the procedure. Due to the restricted motion of the PML observed clinically, the average stress in the PML did not show significant changes between pre- and post-TAVR states. Although the average stress in the AML was generally higher than in the PML before and after TAVR, it was found that the peak mitral leaflet stresses were actually located at the tethered PML chordae insertion regions, near the leaflet free-edge and basal chordae locations.

Since this patient had a postero-lateral regurgitant gap with PML tethering near the APM, the LH models experienced high PML chordae forces when compared to AML chordae tensions. There was an imbalanced force distribution between the two PM, with anterior PM force being higher than posterior PM force. Due to anatomic changes in the MV and the mitral apparatus force redistribution following TAVR, AML strut tension increased at least 50%, while AML marginal and basal chordae tensions decreased between 17% - 36%. Similarly, PML basal tension decreased at least 15%, while PML marginal chordae showed no evident changes in their tension. It is important to note, however, that the total AML and PML chordae tensions were largely unchanged during pre- and post-TAVR states, and between the different three deployment models, which suggest that mitral leaflet tethering was not improved immediately after TAVR, but that there was a force redistribution between the different components of the mitral apparatus, in particular concerning changes in tension between marginal, basal and strut chordae.

Table 28. Pre- and post-TAVR tissue mechanics – BEV.

	Pre-TAVR	**Post-TAVR 50%**	**Post-TAVR 30%**	**Post-TAVR 10%**
S_I^{AVRG} (MPa)				
AV/TAV	0.076	0.151 (99)	0.161 (112)	0.149 (96)
AML	0.126	0.090 (-29)	0.101 (-20)	0.102 (-19)
PML	0.082	0.082 (0)	0.079 (-4)	0.076 (-7)
$F_{chordae}$ (N)				
AML marginal	1.14	0.95 (-17)	0.92 (-19)	0.86 (-24)
AML strut	2.04	3.23 (59)	3.13 (54)	3.05 (50)
AML basal	3.84	2.47 (-36)	2.90 (-25)	2.84 (-26)
PML marginal	6.13	6.95 (13)	6.50 (6)	6.05 (-1)
PML basal	7.33	5.58 (-24)	6.05 (-18)	6.24 (-15)

Percentage variations with respect to the pre-TAVR model are reported in parenthesis.

9.3.8 Post-TAVR biomechanics – SEV

Following TAVR, AML stress decreased between 5% - 21%, while PML stress decreased between 14% - 42%, potentially due to the reduction in the MR driving force. As shown in Table 29, the AML was subjected to a higher stress than the PML before and after TAVR. An imbalanced chordae force distribution was quantified for the pre- and post-TAVR models; a result of the restricted PML motion and postero-lateral chordae tethering. A higher tension was found for the PML chordae than for the AML chordae. Following TAVR, there was a force redistribution between the different chordae groups. AML and PML basal chordae tension decreased at least 36% and 22%, respectively, while AML marginal/strut and PML marginal chordae tension either increased or decreased depending on the stent implantation depth. More importantly, the total chordae tension decreased following TAVR (~20 N vs ~15 N) for the low and high implantation models, which suggests an improvement of mitral leaflet tethering. This phenomenon was not quantified for the optimal deployment model.

Table 29. Pre- and post-TAVR tissue mechanics – SEV.

	Pre-TAVR	**Low**	**Optimal**	**High**
S_I^{AVRG} (MPa)				
AV/TAV	0.076	0.113	0.106	0.108
AML	0.126	0.120 (-5)	0.109 (-14)	0.099 (-21)
PML	0.082	0.048 (-42)	0.071 (-14)	0.056 (-32)
$F_{chordae}$ (N)				
AML marginal	1.14	0.90 (-21)	1.14	1.28 (13)
AML strut	2.04	2.67 (31)	3.07 (51)	1.82 (-11)
AML basal	3.84	2.42 (-37)	2.48 (-36)	2.31 (-40)
PML marginal	6.13	4.25 (-31)	6.91 (13)	5.41 (-12)
PML basal	7.33	5.19 (-29)	5.72 (-22)	4.99 (-32)

Percentage variations with respect to the pre-TAVR model are reported in parenthesis

9.4 Discussion

The main contribution of the present study was a comprehensive analysis of TAVR impact on aortic-mitral coupling, MR severity and LH dynamics in a rigorously developed and validated patient-specific model. Specifically, this work presented an engineering mechanics study that:

1) Investigated the impact of TAV type and stent deployment height on aortic-mitral coupling and TAVR-host biomechanical interaction.

2) Quantified that during TAVR, due to mechanical compression of the stent against the aortic-mitral curtain, the anterior MA was displaced posteriorly while the aortic annulus was displaced towards the LVOT.

Moreover, the new knowledge learned from a clinical perspective include:

1) Although improved systolic function was quantified for all post-TAVR models, no marked differences in early MR improvement/worsening (<10%) were noted at the three implantation depths, independent of TAV type.

2) For this patient case, the BEV highest deployment model resulted in higher stresses in the native leaflets, contact radial force and stent recoil, while the BEV midway implantation model gave better hemodynamic performance and MR reduction.

3) For this patient case, the SEV high implantation model gave the highest reduction in the RV_{MV} and MR severity, and the lowest stent-tissue contact force. On the contrary, the SEV optimal implantation model gave a higher RV_{MV} (~8%) than the pre-

TAVR model, the highest stent-tissue contact force, and no mitral leaflet tethering improvement.

4) Acute changes in MR severity following TAVR were predominantly related to: i) structural changes in the aortic-mitral complex caused by the grade of stent apposition and device anchoring, and ii) hemodynamic changes in global LV afterload/impedance caused by the relief of the AV obstruction.

9.4.1 TAVR-in-BAV

Patient-specific modeling of TAVR in a BAV patient under various procedural scenarios provided quantifiable information about device anchoring and the interaction between the stent, the aortic-mitral curtain and the native valve. The BEV highest deployment model (post-TAVR 10%) led to higher peak stresses in the AV leaflets, sinus and calcification, as well as higher contact radial force, stent recoil and average leaflet stress. These results are in agreement with a FE study by Bianchi et al. (127) that found that after stent recoil the high deployment model resulted in higher leaflet and sinus stresses, as well as higher contact forces than the midway deployment model. In our study, the peak stresses were generally found in the leaflet region in contact with the upper stent struts, in the leaflet-root attachment lines, and in the transition region between calcification and leaflet tissue. Altogether, these results could indicate a higher risk for tissue damage and potential for aortic root injury or rupture for the highest stent positioning, as compared to a slightly lower or midway implantation configuration. This is especially important in the BAV space, as rates of annular rupture have been reported in some series to be as high as 5.3% using the balloon-expandable SAPIEN XT valve (349). Moreover, under BAV disease, the

TAV is usually implanted higher (+4 mm above the annulus) and anchored at the tightest part of the BAV commissures, with an often higher final implantation depth due to the anchoring effect of the calcification (350).

Device apposition and, therefore, a correspondent measure of stent anchoring can be approximated by measuring the contact radial force, pressure or area between the stent and its surrounding tissue (111, 121). Previous in vitro and computational studies have aimed to improve the understanding of the relationship between radial force and TAVR performance (336, 351). Up to now, however, the value of this critical force for TAVR-in-BAV was unknown. Our simulation results showed that the radial force for the three implantation models when using a BEV ranged between 205 – 230 N, and 98 – 108 N during fully stent expansion and after stent recoil, respectively. These forces, which increased as the implantation height increased, are markedly higher than the radial forces for a tricuspid AV reported by Egron et al. (336) and Wang et al. (111) between 100 – 150 N during fully stent expansion. This difference in contact radial force between bicuspid and tricuspid AV anatomies may be important clinically, since TAV oversizing is common in TAVR-in-BAV in order to prevent significant PVL, especially with the older-generation TAV models.

While radial dilatation is usually desired for proper device anchoring and to avoid dislocation of the implant, an excess in radial force may also lead to impairment of the conduction system, leading to left bundle branch or even complete atrioventricular conduction block. Indeed, PVL and high pacemaker implantation rates have been one of the main limitations of TAVR-in-BAV (352), with reported pacing rates of up to 25.5% for the balloon-expandable TAV (353). It has been postulated that the higher incidence of

cardiac conduction disorders and permanent pacemaker implantation rates in TAVR-in-BAV are related with difficulty in valve positioning and asymmetric expansion due to the irregular leaflet shape, heavy calcification and the inability to achieve a coaxial position during valve deployment (353). For the patient-specific case studied herein, a symmetrical expansion of the BEV stent was obtained, as supported by a stent eccentricity value close to one for the three deployment models (Table 22). This positive outcome can be explained by the less complex BAV type present in this patient, which was Sievers type 0 L/R without aortic root dilatation. The absence of a raphe and excessive bulky calcification, especially in the LVOT, allowed an apparently safe stent positioning with a circular uniform expansion, with no post-operative PVL found in this patient, agreeing with the clinical findings.

9.4.2 Effect on TAVR on MR severity

Following TAVR, several clinical studies have found the etiology and severity of MR to have varying effects on short- and long-term mortality (335, 337, 354). Less is known, however, on the changes in MR severity post-TAVR, with single-center and multicenter registry studies often giving conflicting results (334, 335, 337, 355). Given the paucity of high-quality data on this topic, the American Heart Association's guidelines and the European Society of Cardiology have opted not to make recommendations on concomitant MR treatment in patients undergoing TAVR. Nevertheless, with the previous knowledge of physiologic aortic-mitral reciprocal behavior (356), some echo studies have aimed to identify the structural changes in the aortic-mitral complex that may influence MR degree following TAVR (355, 357, 358). Although these imaging studies have greatly enhanced our understating of the aortic-mitral coupling in this setting, the use of 2D/3D echo only

allows a semi-quantitative analysis of the AV-MV anatomy and coupled function. Taking into account the fast-paced developments in transcatheter valve therapies, there is a need for more robust quantitative methods for objective and accurate assessment of AV-MV coupled dynamics. The patient-specific computational model developed in this study provided a quantitative engineering analysis of the relationship between MR severity and the 3D structural changes of the aortic-mitral continuity throughout the cardiac cycle following TAVR in a virtual human beating heart.

In agreement with previous clinical imaging studies (357, 358), our analysis showed that during TAVR procedure the MA height decreased in the post-TAVR models compared with the pre-TAVR model. Interestingly, with a higher BEV stent implantation configuration, we found that the MA height increased instead; up to 8% for the post-TAVR 10% model. The aortic-mitral angle also decreased, with a narrower angle in the highest implantation model than in the midway implantation model. Narrower distances between the center of the aortic and mitral annuli matched changes in the aortic-mitral angle. The reports by Shibayama et al. (355) and Vergnat et al. (358) are also consistent with the present study, showing that the MA area, AP distance and AL-PM distance did not significantly changed after TAVR. A critical finding of this study was that during TAVR, the aortic annulus was displaced longitudinally towards the LVOT, while the anterior MA was displaced posteriorly. Particularly, the posterior displacement of the anterior MA suggests an actual mechanical effect of the TAV stent on the aortic-mitral curtain. We also found that the post-TAVR model that gave a worse MR than the pre-TAVR model (SEV optimal) presented the highest stent-tissue contact force, and no mitral leaflet tethering improvement (Table 23 and Table 29).

Overall, these results give a plausible mechanistic proposition for early MR improvement following TAVR. Geometric perturbation of the aortic-mitral fibrous continuity during TAVR can contribute to improved MV leaflet coaptation and decreased leaflet tethering, therefore reducing MR. These mechanistic parameters may suggest early avenues of MR improvement, such as contact force between the TAVR stent and the surrounding tissue, with potential compression of the aortic-mitral continuity. While existing medical imaging modalities to assess the impact of TAVR on MR severity are post-operative and lack high reproducibility, novel and more powerful tools, such as the patient-specific computer simulations presented in this work, can enhance our understanding of the biomechanical interaction between the device and the host, and may eventually help to improve TAVR procedure characteristics and optimal patient selection to ensure best patient care in AS with concomitant MR.

From a hemodynamics perspective, after relief of AV obstruction by TAVR, acute reduction of the LV afterload accounted for an improvement in systolic function and better hemodynamic balance. In fact, LV pressure immediately decreased following TAVR, and consequently, the MR pressure gradient decreased, which contributed to a reduction in the pathological retrograde flow through the MV. Although AV peak and mean pressure gradients were similarly reduced among the three post-TAVR models, there was a trend towards a higher reduction of the MR pressure gradient among those models with improved MR. Assessment of MR severity by echocardiography under severe AS can be challenging and relies on several mathematical assumptions. For example, MR jet velocity may increase due to a high LV pressure. A large color Doppler jet with a high driving velocity but small effective regurgitant orifice area is probably not severe MR, and is likely to

appear less severe after TAVR (359). On the other hand, moderate-to-severe MR may lead to underestimation of the severity of the AS, since the decreased SV_{AV} due to MR lowers the flow across the valve and, hence, the AV velocity and gradient (360). To the best of our knowledge, this is the first computational study to directly quantify the changes in the LV-valve hemodynamics pre- and post-TAVR under different TAV configurations, and to accurately measure the RV_{MV} irrespective of MR jet geometry and geometric assumptions.

9.4.3 SEV vs BEV performance

Procedural characteristics, including the type of TAV, may also influence the post-operative degree of MR. When comparing the BEV and SEV results, we found no significant changes in the RV_{MV} (<10%) following TAVR, independent of the TAV type. It should be emphasized that in both studies, the same patient-specific computer model was used, and post-TAVR dynamics were simulated under the same loading and boundary conditions. Although no marked changes occurred in the degree of MR, some differences were identified when comparing SEV and BEV device performance. First, there was a trend towards a more consistent MR reduction with the BEV, whereas the likelihood of improvement was lower and less predictable when using a SEV; with mixed MR improvement/deterioration results depending on the deployment height. As shown in Table 26 and Table 27, when comparing SEV vs. BEV performance at an optimal implantation depth, while the SEV model gave a higher RV_{MV} than the pre-TAVR model (40.49 vs 37.59 ml), the BEV model gave a lower RV_{MV} (33.84 vs 37.59 ml). Moreover, while the optimal SEV model was the only post-TAVR model that resulted in worsening of MR, the optimal BEV model led to the highest decrease in the RV_{MV} between the three BEV implantation

models (361). These results are in agreement with clinical studies that point toward a greater degree of MR reduction in patients treated with a BEV as compared to a SEV (337-339, 362, 363).

Several TAV-related factors have been postulated to help explain these differences in MR outcome: i) It has been suggested that the longer frame of the SEV may anatomically or functionally interfere with the AML, especially in the presence of a low implantation (364, 365). This was not confirmed in a large CoreValve series (366) or found in this computational study. In line with this hypothesis is the observation that a deep positioning of the SEV could be correlated with MR worsening (364), although this has not been observed in all studies (367). Our data also rule out this phenomenon for this patient computer model, since MR worsening only occurred in the post-TAVR model with an optimal implantation height. ii) The first generation CoreValve device has been associated with a higher degree of PVL, which may maintain volume overload and contribute to a less MR improvement (368, 369). PVL, however, was not quantified in any of our post-TAVR models. Moreover, the first-generation SEV has now been replaced by newer and enhanced versions with low PVL rates and are usually implanted at a shallower depth than the older generation CoreValve device.

The second key finding was obtained when comparing the results of the SEV and BEV models that gave the greater degree of MR reduction. We identified four mechanistic parameters that appear to be associated with early MR improvement, independent of the TAV type: stent-tissue contact force, aortic-mitral angle, aortic annulus displacement and MA displacement. Specifically, the post-TAVR models with the lowest contact force, highest aortic-mitral angle, and highest valve annuli compression led to the greatest MR

reduction, when compared to the other two SEV/BEV implantation models. As such, it could be hypothesized that a TAVR deployment configuration that causes a large compression of the aortic-mitral continuity without an excessive stent-tissue contact force should be used. Clearly, the biomechanical mechanism of MR evolution after TAVR is multifactorial, and appears to be mediated by several structural and hemodynamic changes. Moreover, a large comparative study would be required to establish a more definitive framework to guide appropriate TAV selection.

9.5 Limitations

Several limitations should be taken into consideration when interpreting our findings. First, in this study only one patient-specific anatomy was examined, and as such the specific results regarding the TAVR biomechanics and its impact on MR severity cannot be assumed to represent the entire population. However, the validity of the results stands due to their comparative nature. Second, while, on one side, cardiac tissues were realistically described as nonlinear elastic, on the other side, patient-specific cardiac tissue material properties were not available. Thus, tissues mechanical response was defined from an extensive human tissue database obtained from in-house multiprotocol biaxial and uniaxial tests. Estimation of in vivo material parameters inversely from medical images would be ideal to produce more accurate predictive results (370).

Third, since this study did not consider the zero stress–free configuration of the aortic wall, a rigid body constraint was assigned to the aortic root/ascending aorta wall elements during the pre- and post-TAVR FSI simulations; however, deformable tissue properties were attributed during the TAVR FE simulations. For the same reason, aortic

wall pre-stress state was neglected during the TAVR FE analysis. This assumption, which will be tacked in a future study, could lead to uncertainties on the computed stresses as well as in the tissue compliance (371-373). The pre-stress assumption of the native leaflets might have a small impact on the solution since the transvalvular pressure is very small during TAV deployment.

Fourth, post-operative MSCT images were not available, thus it was not possible to compare the deformed TAV stent geometries from the simulations with post-TAVR clinical images. However, the current study still enabled us to compare different implantation configurations and evaluate the impact of stent depth on several clinically relevant parameters. Finally, the current SPH-FE FSI modeling framework involves a high computational cost. The FE TAVR simulations required approximately 3 days to run while the pre- and post-TAVR FSI simulations required approximately 5 days to run one cardiac cycle in an Intel Xeon E5-2670 cluster. As a result, the present modeling methodology cannot be used in a clinical setting and currently, is only suitable for a research environment. Nevertheless, among other advantages, SPH is easy to parallelize. The ability to run both FE and SPH codes on GPUs will significantly reduce the running time in the near future and avoid the need for a computer cluster (299, 300). Advances in machine learning techniques could also eventually render real-time biomechanical analysis for time-sensitive clinical applications (374).

CHAPTER 10. SPECIFIC AIM 2C – LV-VALVE DYNAMICS UNDER MITRACLIP AND ANNULOPLASTY IMPLANTATION

10.1 Introduction

The percutaneous edge–to-edge MV repair technique using MitraClip (Abbott Vascular, Santa Clara, CA) is the most widely used minimally-invasive treatment option for patients with symptomatic MR and high surgical risk (375). Based on the surgical method by Alfieri, AML and PML are clipped, which results in a double-orifice valve. Although MitraClip was recently approved by the FDA for treatment of significant functional MR, two large randomized clinical trials showed apparently conflicting results. While the COAPT trial showed that MitraClip is associated with a lower rate of hospitalization for heart failure and lower all-cause mortality within 24 months of follow-up, compared with using medical therapy alone (376), the MITRA-FR trial did not show significant differences between the intervention and control groups (377).

Differences in the two trials are likely to be related to level of functional MR, medical management, operator experience and most importantly, to patient selection (378); with markedly improved outcomes in the setting of a disproportionately larger severity of MR relative to LV volumes after optimizing medical therapy for heart failure (379). Indeed, several studies have shown that persistence of moderate-to-severe MR after MitraClip is associated with a considerably higher 1-year mortality (380-382), such that MR reduction to moderate or less is of paramount importance. Thus, it is clear that for a successful MitraClip procedure: i) a multidisciplinary team needs to be involved, ii) procedural

techniques need to be optimized, and iii) physicians should individualize treatments in accordance with patient characteristics and perform careful preoperative planning to select patients who would benefit the most from the procedure.

In this context, there is a clear indication for a better mechanistic understanding and further improvement of the MitraClip technique under functional MR. Particularly, patient-specific computer simulations could help to better understand the complex biomechanical interaction between the device and the human host, predict device performance (efficacy) and possible complications (safety). This may eventually allow physicians to personalize treatments strategies and select patients who would benefit the most from the MitraClip procedure with a higher level of accuracy, thereby improving clinical outcomes.

Computational simulations using FE analysis have been useful in assessing MV biomechanics under healthy and diseased conditions, as well as in evaluating the functional and structural effects of different surgical and transcatheter MV repair techniques (293, 383). While several FE studies have modeled the edge-to-edge and MitraClip procedures under degenerative MR (96, 384-388), to the best of our knowledge, no computational study has to date evaluated the impact of MitraClip on MV biomechanics under functional MR. Previously, Lau and colleagues (92) investigated the effect of the edge-to-edge surgical technique on an idealized MV model with a dilated but static MA and healthy chordae structure with no leaflet tethering.

In Specific Aim 2c, we employed the previously validated patient-specific LH model with functional MR developed in Specific Aim 1b – Part 2 to simulate the MitraClip procedure and assess the biomechanical interaction between the device and the host. The

FSI framework implemented in this study allowed us to investigate the impact of central and lateral MitraClip placement, as well as combined MitraClip and annuloplasty therapies on biomechanical outcomes, and post-clip LH structural and fluid dynamics.

10.2 Materials and Methods

10.2.1 Patient-specific LH model

In this study, we employed the patient-specific LH model with functional MR developed and validated in Specific Aim 1b – Part 2. Briefly, echo examination revealed moderate-to-severe MR with a tethered PML with restricted motion and reduced leaflet coaptation. The LVEF was estimated to be 25%. The LV thickness was normal but the chamber was mildly dilated. The patient-specific LH model, shown in Figure 65A, was composed of the ascending aorta, aortic root, AV, calcification, MV, LV and LA endocardial walls, detailed chordae structure and distribution, accurate leaflet geometry and thickness, dynamic MA and chordae origins, anisotropic hyperelastic material models, and human age- and gender-matched material properties. Additionally, chordae tethering forces due to PM displacement were accounted for accurate modeling of MV dynamics under FMR, as explained in Specific Aim 1b – Part 2.

10.2.2 MitraClip model

The clip model was simplified as two rectangular rigid plates with dimensions similar to the real MitraClip device. Figure 65B illustrates the clip model used in this study and the real MitraClip device. The length of each plate was 9 mm and the width was 5 mm. As shown in Figure 65B, a reference node was defined at the middle bottom edge of each

plate, allowing each arm to rotate with respect to its own reference node. A connector element connecting the two reference nodes was defined in order to impose mutual kinematic constraints. During the simulations, the relative motion of the two clip arms was constrained by the connector element to prevent relative displacement between them. Based on the location of the regurgitant gap, two MitraClip placement locations were simulated in this study: i) central positioning, between the AML and P2 scallop, and ii) lateral positioning, between the AML and P1 scallop.

10.2.3 Annuloplasty ring model

There are several models of ring available for use in MV repair in various shapes (partial vs complete, flat vs saddle-shape) and with different material properties (rigid vs semi-rigid vs flexible). Under functional MR, the standard annuloplasty treatment involves the use of a ring that reduces the antero-posterior diameter of the MA. Thus, in this study we used a complete ring based on the Carpentier-Edwards Classic ring (Edwards Lifesciences, Irvine, California). Following the selection guidelines for the Classic ring (389), a 38 ring size was chosen based on the similarity between the surface area of the device and the surface area of the AML. The 3D ring shape and dimensions were obtained from literature. However, rather than implanting a virtual ring with its full cross-sectional geometry, ring implantation was simplified as prescribed boundary conditions on the MA.

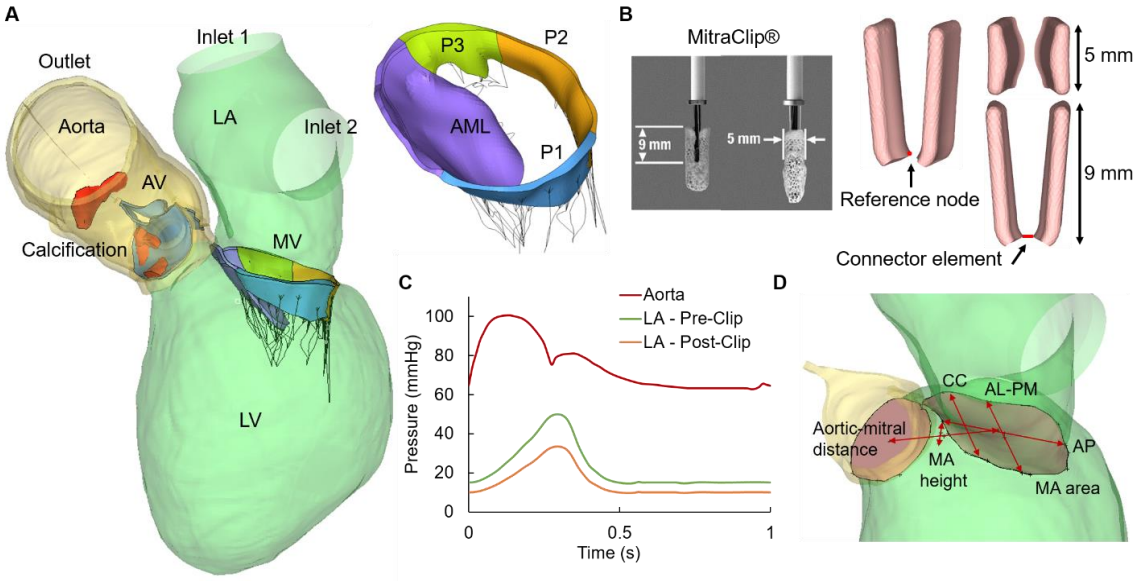

Figure 65. A) Patient-specific LH model, B) Real and simplified MitraClip devices, C) Aortic and LA pressure waveforms, D) MV geometrical parameters. AV: aortic valve, LV: left ventricle, LA: left atrium, MV: mitral valve, AML: anterior mitral leaflet, PML: posterior mitral leaflet is divided into lateral P1 scallop, central P2 scallop and medial P3 scallop.

10.2.4 FE modelling of MitraClip and annuloplasty procedures

10.2.4.1 Step 1 – MV closure

Simulation of MV closure under systolic pressure and chordae tethering has been described in detail in our previous studies (287, 390). Briefly, since the patient had moderate-to-severe MR with PML tethering and dilated LV, pre-existing forces within the posterior chordae at diastole were modeled in the first sub-step of the simulation. Thus, before running the FE simulations, a total of 8 posterior chordae were shortened by translating the chordae origins towards the MA plane along the original direction of the chordae. At the beginning of the simulations, those chordae origins were initially displaced to their original

locations to generate the tethering tension. After those chordae origins reached their original locations on the PM tips, a rough contact with no separation behavior was enforced to connect the chordae with the PM tips (287). The reaction force on each node of the MA was output at the end of this first sub-step. Next, the dynamic motion of the MA and chordae origins from diastole to systole obtained from the MSCT images was applied as a nodal displacement boundary condition(287). The clinically measured transmitral pressure gradient of 114 mmHg was then applied to the ventricular surface of the leaflets to simulate MV closure. At the end of this step, the two MitraClip arms rotated so that the clip opened at 120 degrees.

10.2.4.2 Step 2 – Clip attachment

Clip grasping to the mitral leaflets was modeled at diastole when the valve just started to open. Initially, displacement boundary conditions on the MA and chordae were applied so that the mitral apparatus restored to a diastolic position and the leaflets opened due to the release of the pressure on the ventricular surface. Next, the MA nodal displacement boundary condition was replaced by the MA reaction forces obtained in Step 1 from the pretension simulation at diastole to account for the tension within the MA during diastole. Meanwhile, to grasp the leaflets, the two clip arms rotated back to a closed position until a gap of 4 mm was left between the upper end of the two arms (391). At the end of the step, rough contact with no possible slippage and no separation behavior was initiated between the arms and the mitral leaflets. The clip arms remained mutually parallel but could rotate/tilt following the interaction with the leaflets. During all simulation steps, nodes on the septal wall of the myocardium were fixed to prevent excessive cardiac motion.

10.2.4.3 Step 3 – Annuloplasty ring

To align the virtual ring with the MA plane, least-square planes were created for both the ring and the MA. The ring was rotated until its least square plane was parallel to that of the MA. Next, middle anterior and posterior portions of the ring were aligned with the middle anterior and posterior portions of the MA until the ring was positioned such that the anterior portion of the ring overlaped with the anterior MA as much as possible, avoiding excessive displacement of the LVOT.

Following ring alignment, a total of 18 node clusters uniformly distributed along the MA were identified as boundary nodes; each cluster contained 3 adjacent nodes. On the virtual ring, 18 uniformly distributed nodes were also identified. Suturing of the annuloplasty ring to the MA was mimicked in the FE simulations by imposing kinematic displacements on the 18 node clusters on the MA from their original locations to the locations of the 18 corresponding nodes identified on the virtual ring. During this step, the boundary conditions on the chordae origins were unfixed to allow PM movement. Meanwhile, a point load equivalent to the reaction force obtained at each chordae origin from the pretension simulation was applied to the same chordae origin to account for the tension within the chordae due to leaflet tethering at diastole. No separation between the clip and the leaflets was maintained in this step. The deformed LH geometries were extracted from the FE simulations and used to assess the post-clip LH dynamics using FSI.

10.2.5 Boundary conditions

Time-dependent pressure boundary conditions were applied at the two LA inlets (pulmonary veins) and at the aortic outlet of the pre- and post-clip models, as previously

explained in Specific Aim 1b – Part 2. Cardiac wall motion was kept the same for all pre- and post-clip models, simulating immediate post-operative LH dynamics, without considering any possible cardiac remodeling mechanisms that occur over time after MitraClip. In functional MR, the regurgitant volume in the LA cavity results in an elevated V-wave pressure during systole (238). Thus, the pre-clip model employed a pathological LA inlet pressure waveform, as seen in Figure 65C. After MitraClip implantation, the LA pressure was decreased by 33% (392) (393).

10.2.6 Data analysis

10.2.6.1 MV geometrical parameters

Morphologic changes in the MV during MitraClip were evaluated in terms of the geometrical parameters shown Figure 65D. The following measurements were obtained during systole: a) antero-posterior (AP) distance, defined as the distance between mid-anterior and mid-posterior MA points, b) anterolateral-posteromedial (AL-PM) distance, c) MA spherecity index (ASI), defined as the ratio between AP and AL-PM distances, d) inter-commissural (CC) distance, e) MA height to inter-commissural width ratio (AHCWR), defined as the ratio between MA height and the CC distance f) MA area, and g) aortic-mitral distance, defined as the centroid distance between the MA and the aortic annulus.

10.2.6.2 Fluid parameters

As introduced in Specific Aim 1b – Part 2, the following LH hemodynamic parameters were quantified throughout the cardiac cycle: SV_{AV}, SV_{MV}, RV_{AV}, RV_{MV}, RF_{MV}, MR

severity, LVEF, LV mean systolic pressure (LV-MSP), LV end-diastolic pressure (LV-EDP), peak systolic pressure gradient (PSPG), mean systolic pressure gradient (MSPG), AV peak velocity, EOA_{AV}, peak diastolic pressure gradient (PDPG), mean diastolic pressure gradient (MDPG), E and A wave velocities, EOA_{MV}, MR mean pressure gradient (MR-MPG), MR mean velocity, and EROA. EOA_{MV} was calculated as $\frac{MDF}{31\sqrt{\text{MDPG}}}$, where MDF is the root mean square diastolic flow rate (214). Similarly, EROA was defined as $\frac{MRF}{31\sqrt{\text{MR-MPG}}}$, where MRF is the root mean square regurgitant flow rate.

10.2.6.3 Structural parameters

During the MitraClip procedure, the average maximum principal stress (S_1^{AVRG}) in the MV leaflets was quantified from the FE simulations. To avoid the bias caused by local high stress concentration, only the 99-percentile values of the peak stress values were evaluated (348). Moreover, leaflet annular regions were not included in the average stress calculation in order to avoid boundary effects. From the FSI simulations, pre- and post-clip MV biomechanics were evaluated by the S_1^{AVRG} in the MV leaflets during peak systole and diastole. AML and PML chordae forces ($F_{chordae}$) were also reported. The force experienced by a particular chordae group was calculated as the sum of vectors representing the tension in each individual chorda attached to a specific leaflet. Finally, the anatomic MV orifice area (AMVOA) was quantified throughout the cardiac cycle. The least square plane of the MA was calculated at each time point of the cardiac cycle. The AMVOA was then measured as the projected 2D area of the leaflets free edge on the MA least square plane. The regurgitant orifice area and opening orifice area values were obtained by selecting the minimum and maximum AMVOA values during systole and diastole, respectively.

10.3 Results

10.3.1 MitraClip impact on LH dynamics: MV geometry

Table 30 presents the changes in MV geometry during MitraClip implantation. The AP distance and ASI markedly decreased (>20%) after MitraClip for the central model, with or without ring. Similarly, the MA area and aortic-mitral distance had a tendency to decrease for all clip models, but these changes were not significant when compared to pre-clip conditions. Furthermore, although the AL-PM distance and CC distance increased in all post-clip models, these changes were comparable before and after MitraClip. Generally, using a lateral clip led to the smallest changes in MV geometry, while using a central clip + ring led to the biggest anatomical changes. Table 30 also presents the average stress (S_I^{AVRG}) in the MV leaflets during the clipping procedure. The PML was subjected to a higher stress than the AML for all clip models, with the central + ring model giving the highest leaflet stress values.

Table 30. MV anatomical and biomechanical parameters pre- and post-clip.

	Pre-Clip	**Lateral**	**Central**	**Central + Ring**
AP distance (mm)	34.37	31.90	27.37 (-20)	25.28 (-26)
AL-PM distance (mm)	39.83	41.96	43.28	45.71
ASI	0.86	0.76	0.63 (-27)	0.55 (-36)
CC distance (mm)	33.87	35.22	34.90	37.42
AHCWR	0.14	0.16	0.11	0.12
MA area (cm^2)	11.40	10.37	10.04	9.40
Aortic-mitral distance (mm)	28.32	25.06	24.43	23.38
S_I^{AVRG} AML (MPa)	–	0.101	0.084	0.113
S_I^{AVRG} PML (MPa)	–	0.108	0.099	0.152

Marked percentage variations with respect to the pre-clip model are reported in parenthesis.

10.3.2 MitraClip impact on LH dynamics: Intraventricular hemodynamics

Figure 66 shows the flow rate waveforms across the valves throughout the cardiac cycle for the pre- and post-clip models. The positive flow indicates the forward flow towards the aorta (Figure 66A) and the LV (Figure 66B) during systole and diastole, respectively. In contrast, the negative flow indicates the backward blood flow due to valve closure and regurgitation. Table 31 summarizes the main hemodynamic parameters quantified for the pre- and post-clip models from the FSI simulations.

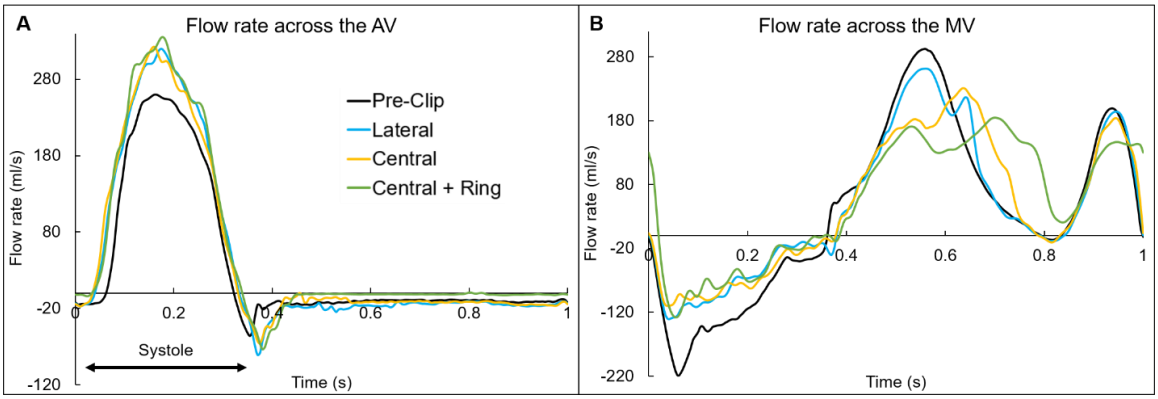

Figure 66. Flow rate (ml/s) across the A) AV and B) MV throughout the cardiac cycle.

Several important findings can be described during systole: First, successful MitraClip therapy led to an immediate hemodynamic improvement by decreasing the RV_{MV}, and due to the coupled valve dynamics and mass conservation, a concomitant increase in the forward SV_{AV}. The greater degree of MR improvement, based on the RF_{MV} criterion, was for the central + ring model (46%). Nevertheless, all post-clip models can now be classified as moderate MR. Second, MR reduction promoted LV unloading and a

decrease in preload, manifested by an increase in the LV-MSP and a decrease in the LV-EDP, as seen in Figure 67C. The central + ring model presented the greatest decrease in LV preload.

Third, the LVEF decreased post-Clip by less than 4%. Despite the slight reduction in the total LVEF, the effective LVEF markedly increased, as evidenced by an increase in the SV_{AV} between 27 – 32%. Fourth, the MR-MPG increased after the procedure due to the decrease in the LA pressure and the increase in the LV-MSP. The peak MR velocity and EROA, on the other hand, decreased after MitraClip. Fifth, improvement in the systolic hemodynamic profile after clip implantation was also associated with a decrease in the PSPG and MSPG (Figure 67A), and an increase in the EOA_{AV}.

Similarly, important findings were identified during the diastolic phase: First, narrowing of the MV orifice after MitraClip caused higher PDPG and MDPG (Figure 67B), as well as higher MV inflow velocities. The MDPG increased from 1.35 mmHg pre-clip up to 7.47 mmHg when using a central clip + ring. Second, as seen in Figure 66B, the MV inflow curve profile changed pre- and post-clip. Due to the decrease in the EOA_{MV} and the greater resistance to flow in the double-orifice valve post-clip, there was a decrease in the early E-wave dominant flow. The decrease in the E-wave flow curve was higher for the clip + ring model, which presented the lowest EOA_{MV}.

Table 31. Pre- and post-clip LH hemodynamics.

	Pre-Clip	Lateral	Central	Central + Ring
SV_{AV} (ml)	46.28	58.81	58.55	61.21
RV_{AV} (ml)	9.34	13.18	10.42	4.78
SV_{MV} (ml)	74.64	70.22	71.57	75.70
RV_{MV} (ml)	37.59	23.88	23.59	19.51
RF_{MV} (%)	44.82	28.88	28.72	24.17
MR severity (RF_{MV})	Moderate to severe	Moderate	Moderate	Moderate
LVEF (%)	28.55	28.15	27.96	27.47
LV-MSP (mmHg)	97.64	102.89	105.83	105.83
LV-EDP (mmHg)	15.96	9.67	8.39	0.92
PSPG (mmHg)	34.82	30.74	30.58	33.90
MSPG (mmHg)	23.97	20.97	20.7	21.34
AV peak velocity (m/s)	2.82	2.72	2.8	2.8
EOA_{AV} (cm^2)	0.77	0.94	0.93	0.96
PDPG (mmHg)	4.32	8.91	9.05	9.17
MDPG (mmHg)	1.35	4.33	6.16	7.47
E wave (m/s)	0.79	0.96, 1.46	1.43, 1.29	1.41, 1.36
A wave (m/s)	0.54	0.71, 1.2	1.31, 1.15	1.32, 1.28
EOA_{MV} (cm^2)	4.1	2.19	1.76	1.53
MR-MPG (mmHg)	57.25	75.24	76.65	76.66
MR peak velocity (m/s)	5.42	4.61	4.83	4.89
EROA (cm^2)	0.5	0.28	0.26	0.25

E and A wave velocity values from left to right correspond to the double/triple orifices located from P1 to P3 scallops.

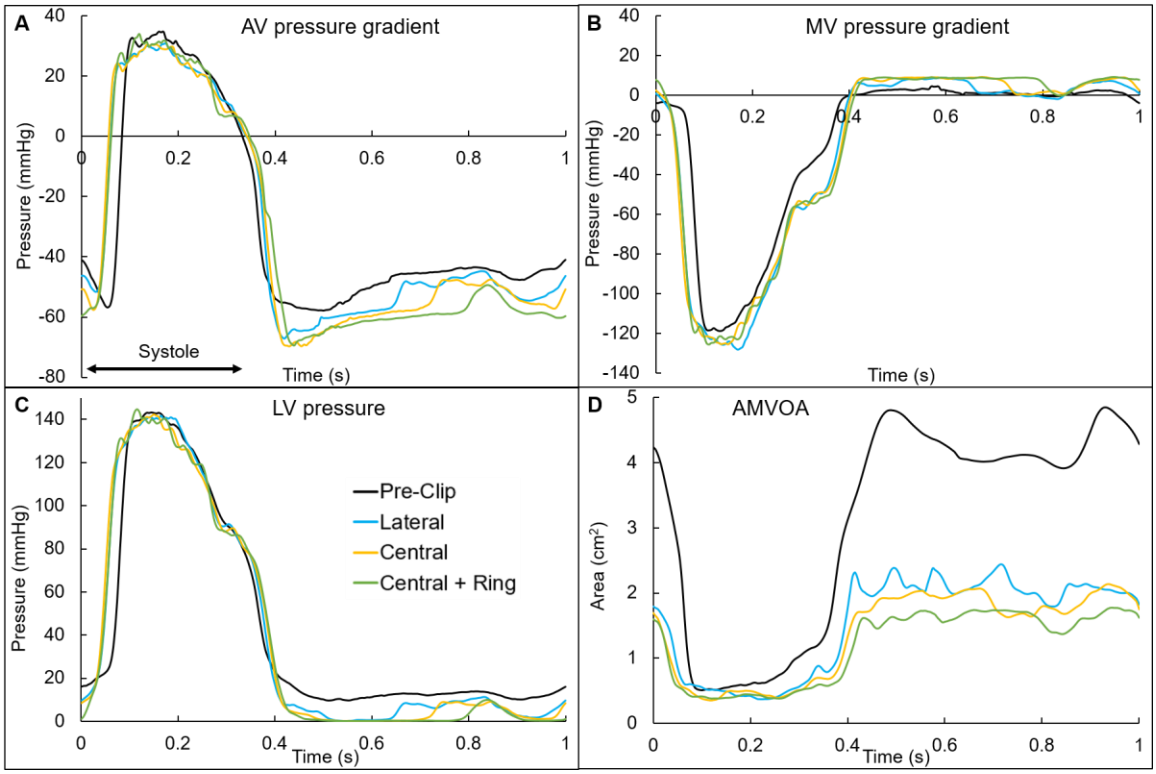

Figure 67. A) AV pressure gradient, B) MV pressure gradient, C) LV pressure, and D) AMVOA throughout the cardiac cycle.

Figure 68 shows the intraventricular velocity streamlines colored by velocity magnitude during peak systole. Due to the restricted PML motion, the pre-clip model displayed a posteriorly directed regurgitant jet, which qualitatively and quantitatively matched the regurgitant jet measured clinically (361). The regurgitant jet structure was similar between pre- and post-clip configurations, with an eccentric "wall-hugging" jet that impinged the postero-lateral LA wall. The strength and velocity of the jet, however, decreased following MitraClip (Table 31).

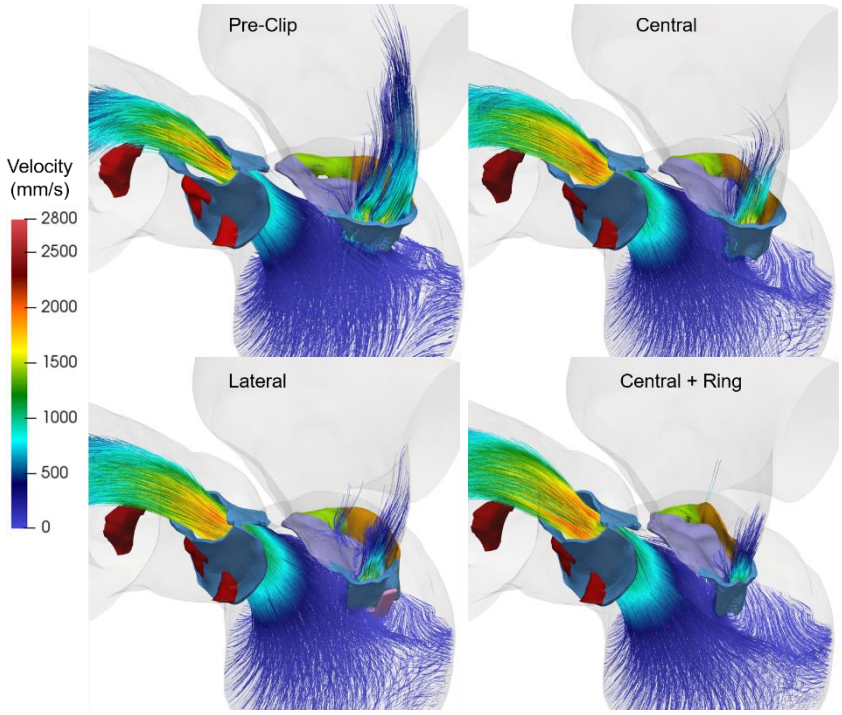

Figure 68. Pre- and post-clip velocity streamlines showing the regurgitant jet structures during systole.

Finally, Figure 69 shows the velocity streamlines during peak diastole. Marked differences in the inflow flow structure and magnitude were observed pre- and post-clip, as well as between the different clip models. MitraClip implantation significantly altered the LV hemodynamics by creating a double-jet configuration due to the double-orifice MV. Moreover, the post-clip jets were not oriented towards the apex, but towards the LV wall, where they impinge leading to higher near-wall velocities than the pre-clip model, especially for the central + ring model. The induced double-jet configuration appears with a deeper jet penetration inside the LV. As shown in Table 31, due to the reduced orifice areas, the jets had much higher velocities than the central jet observed before clip

implantation. Additionally, the different orifice sizes caused differences in the peak jet velocities.

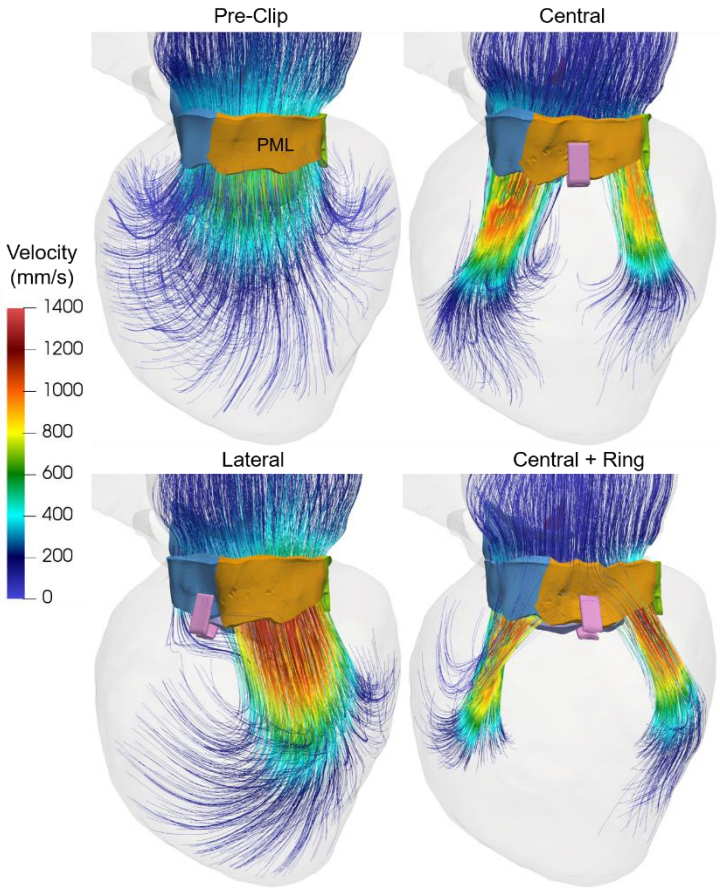

Figure 69. Pre- and post-clip velocity streamlines showing the intraventricular blood flow during diastole.

10.3.3 MitraClip impact on LH dynamics: MV tissue mechanics

Table 32, Figure 70A and Figure 70C present the average (S_I^{AVRG}) stress in the MV leaflets and the chordae tension during peak systole pre- and post-clip. From Figure 70A it can be seen that both AML and PML were subjected to a higher systolic stress after the

procedure. This increase in the leaflet stress was significant (>50%) for the PML when using a lateral clip or a central clip + ring. Figure 71 shows the stress distribution patterns across the MV leaflets at peak systole. Before clip implantation, peak stress values in the AML were located at the right and left trigones, while peak values for the PML were distributed along the MA region and at the basal chordae insertion region. Following clip attachment, areas of high stress concentration were relocated near the clip arms for all configurations. As seen in Figure 70C, since this patient had a postero-lateral regurgitant gap with PML tethering, the pre- and post-clip models experienced a higher total PML chordae systolic tension when compared to AML chordae tension. After MitraClip, the chordae attached to the AML were subjected to a lower tension compared to the pre-clip model, while PML chordae were under a higher tension. These differences were only important (>30%) when a lateral clip was implanted.

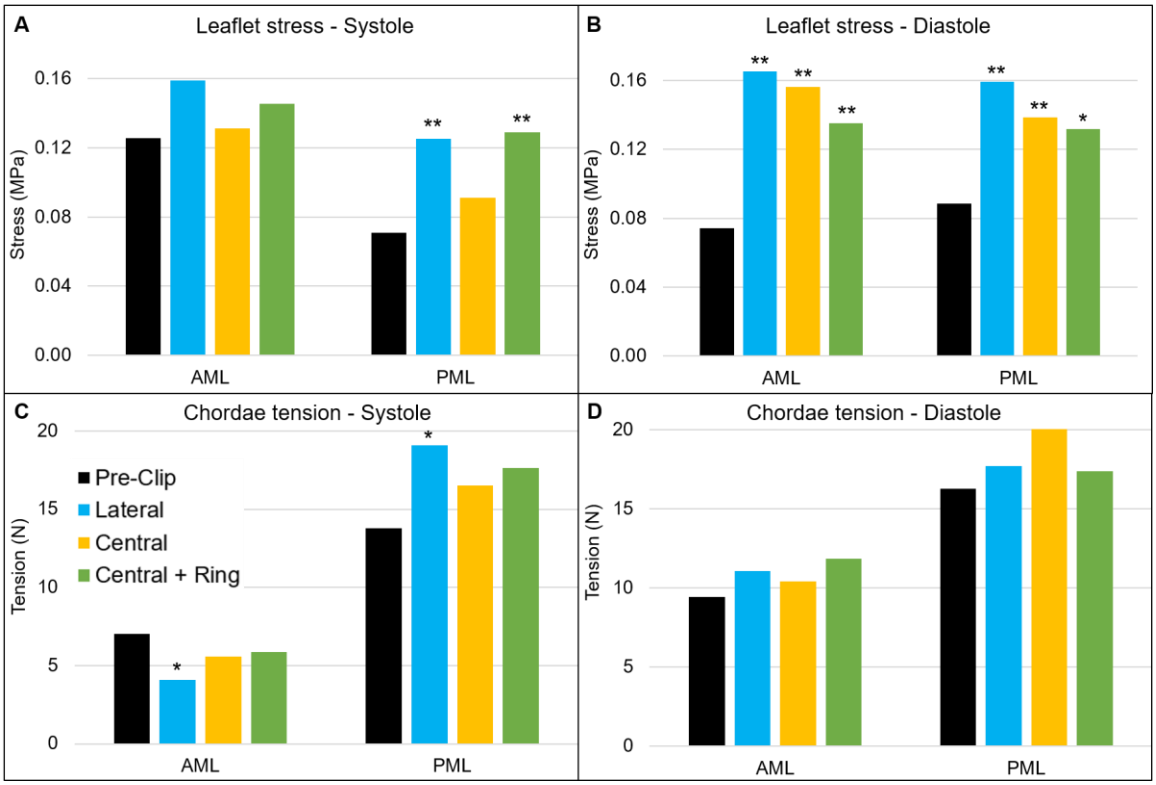

Figure 70. A) Leaflet stress during systole, B) Leaflet stress during diastole, C) Chordae tension during systole, and D) Chordae tension during diastole.

Table 32. Pre- and post-clip MV biomechanics during systole.

	Pre-Clip	**Lateral**	**Central**	**Central + Ring**
S_1^{AVRG} (MPa)				
AML	0.126	0.159 (26)	0.131 (5)	0.145 (16)
PML	0.071	0.125 (76)	0.091 (28)	0.129 (82)
$F_{chordae}$ (N)				
AML	7.04	4.07 (-42)	5.59 (-21)	5.88 (-16)
PML	13.79	19.06 (38)	16.50 (20)	17.63 (28)
AMOVA - regurgitant orifice area (cm^2)	0.51	0.38 (-26)	0.37 (-29)	0.35 (-33)

Percentage variations with respect to the pre-clip model are reported in parenthesis.

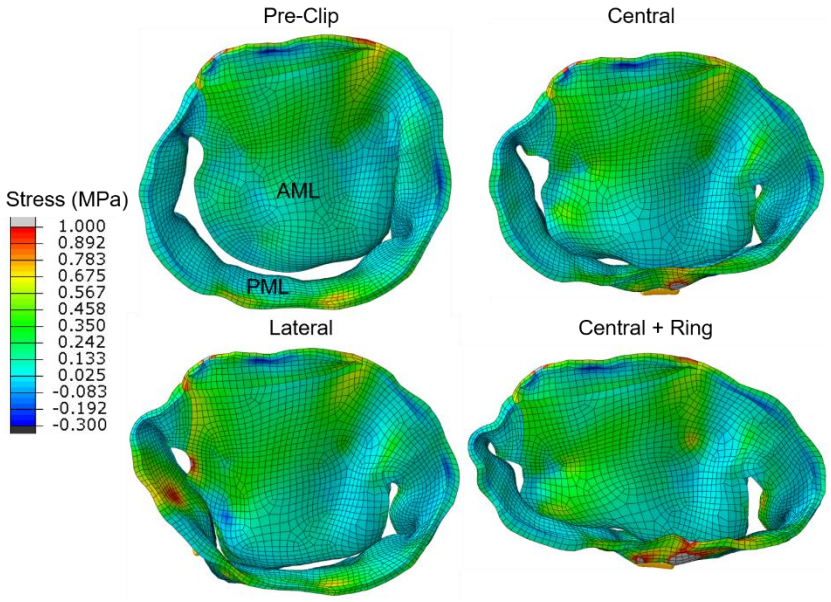

Figure 71. Stress distribution on the MV leaflets during systole.

Regarding the diastolic phase, Table 33, Figure 70B and Figure 70D show the average leaflet stress and the chordae tension. A significant increase (>50%) in AML and PML stress was quantified for all post-clip models. Moreover, the lateral model gave the highest increase in leaflet stress, while the central + ring model gave the lowest stress increase. As seen in Figure 72, similar stress distribution patterns were observed in the MV leaflets for all post-clip models during diastole. In the AML, peak stresses relocated near the clip arms and along strut and marginal chordae insertion regions. In the PML, peak stresses extended from the free edge at the level of the clip arms towards the P2 annular region, close to the insertion of the basal chordae. In regard to diastolic chordae forces, Figure 70D shows that although AML and PML chordae tension had a tendency to increase after the procedure, there were no significant changes when comparing these before and after MitraClip. Similarly, we observed higher chordae forces during diastole than systole

for all pre- and post-clip models, which could be attributed to the diastolic restriction of the MV leaflets caused by PM relocation and LV dilatation.

Table 33. Pre- and post-clip MV biomechanics during diastole.

	Pre-Clip	**Lateral**	**Central**	**Central + Ring**
S_I^{AVRG} (MPa)				
AML	0.074	0.165 (122)	0.156 (110)	0.135 (82)
PML	0.088	0.159 (80)	0.139 (57)	0.132 (49)
$F_{chordae}$ (N)				
AML	9.43	11.04 (17)	10.42 (11)	11.85 (26)
PML	16.25	17.71 (9)	20.92 (29)	17.36 (7)
AMVOA - opening orifice area (cm^2)	4.85	2.46 (-49)	2.14 (-56)	1.79 (-63)

Percentage variations with respect to the pre-clip model are reported in parenthesis.

Finally, Figure 67D shows the AMVOA throughout the cardiac cycle. During systole, the AMVOA markedly decreased (>20%) from 0.51 cm^2 to ~0.36 cm^2 after MV repair, with the highest reduction (33%) obtained for the central + ring model (Table 32). During diastole, the AMVOA decreased significantly (>50%) for all post-clip models, with the highest reduction (63%) quantified for the central + ring model (Table 33). Furthermore, the pre-clip double-peaked AMVOA curve during diastole changed to a flat curve post-clip, similarly as the MV inflow curve seen in Figure 66B.

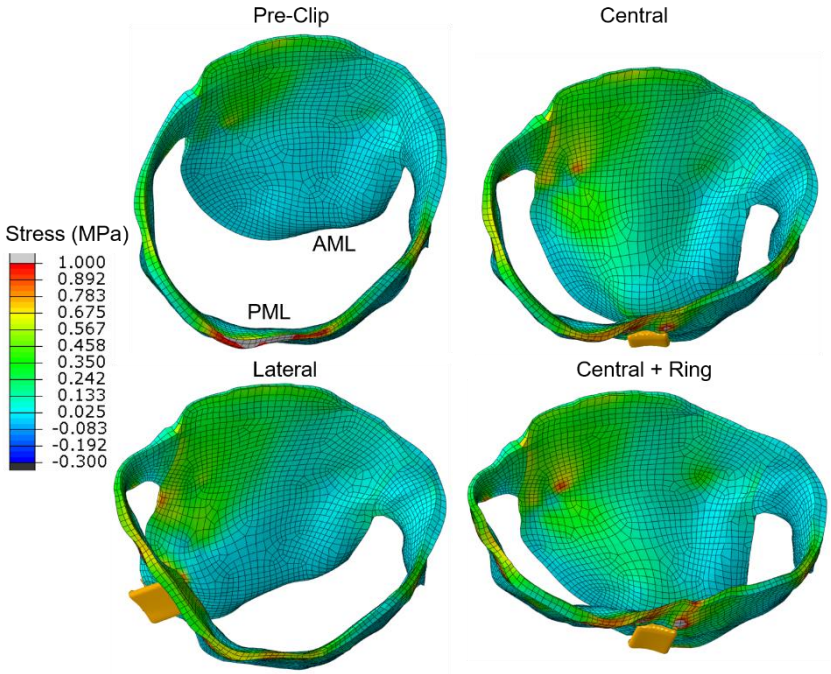

Figure 72. Stress distribution on the MV leaflets during diastole.

10.4 Discussion

The results of this study can be summarized as follows: First, MitraClip induced acute morphologic changes in the MV geometry. Clip implantation resulted in a marked decrease of the AP distance by up to 26%, and a non-significant decrease and increase of the MA area and AL-PM distance, respectively. Consequently, there was a significant reduction of the ASI together with a non-significant decrease in the AHCWR, suggesting that MitraClip therapy leads to a more elliptical and planar MA. Second, MV leaflet stress increased throughout the cardiac cycle after clip placement, with a significant increase during diastole by up to 122% and 80% for the AML and PML, respectively.

Third, MitraClip was accompanied by the reduction of the AMVOA during diastole by up to 63% for the central + ring model, while the systolic AMVOA decreased by up to 33% for the same model, resulting in improved but incomplete MV coaptation. Additionally, MitraClip altered the temporal course of the diastolic AMVOA and MV inflow profiles from double-peaked curves to more flattened curves. Fourth, the immediate reduction in the RV_{MV} achieved by MitraClip resulted in an acute increase in the forward flow (>27%), in addition to favorable changes in LV loading conditions by reducing the LV-EDP and LA pressure, and increasing the LV-MSP. For this patient case, while implanting a central clip + ring resulted in the highest improvement in LV systolic function and magnitude of reduction in the regurgitant flow (46%), this clip configuration also led to the highest degree of MS by increasing the MDPG to 7.47 mmHg.

10.4.1 Effects on MV geometry

The acute effects of MitraClip on the MV geometry under functional MR have been investigated in a few clinical studies using echocardiography (394-396). Similar to these investigations, we found a marked reduction in the AP distance together with a non-significant increase of the AL-PM distance, especially when a central clip + ring were implanted (Table 30). These changes were accompanied by comparable changes in the CC distance pre- and post-clip (397), and by a non-significant reduction in the MA area, as found in previous studies (394, 398). Some studies, however, have demonstrated a significant decrease of the MA area after MitraClip (395, 396). Nonetheless, this decrease is secondary to reduced AP distance after the procedure. Our results suggest that reshaping of the MA with a significant reduction of the AP distance contributes to a reduction of MR after MitraClip. Previous investigations have pointed that reduction in AP distance might

be an indicator of clinical benefit (396, 399, 400). This finding could be critical in a procedure in which patient selection is fundamental. Further studies in a larger population may be required to confirm such correlation. As a whole, it appears that the MitraClip device limits MV dilation by exerting traction on the MA (398); mainly in the antero-posterior direction, analogous to a partial annuloplasty procedure. The small changes in the CC distance can be explained by the presence of the aortic-mitral continuity and the fibrous trigones, which is a region less prone to large deformations than the posterior MA, which is mainly muscular and more prone to dilatation (401).

The decrease of the AP distance together with the increase in the AL-PM distance resulted in a significant reduction of the ASI in the central clip models, which confirms the reshaping of the MA from a rounder to a more oval shape. The reduction in the MA sphericity index has been quantified in patients with functional MR undergoing surgical MV repair with annuloplasty ring (402). AHCWR and aortic-mitral distance also decreased after MitraClip, but these changes were non-significant. The AHCWR is a measure of the MA non-planarity and describes its 3D shape. Our results suggest a flatter MA post-clip during systole, which can be related with the increased LV pressure and the more elliptical MA (403, 404). Overall, these findings, although not directly related to clinical outcomes, might be of interest for future studies determining independent anatomic implantation goals that predict sustained procedural success. Computational-based MV analysis, such as the one performed in this study, allows for a detailed quantitative understanding of the acute changes in MV geometry after MitraClip in an objective and reproducible manner. Further studies need to investigate the dynamic changes in the MV geometry at additional time points during the cardiac cycle and when using different clip numbers and positions.

10.4.2 Structural effects on the MV

MV leaflet stress increased throughout the cardiac cycle after MitraClip procedure, in particular next to the site of clip insertion. This increase was significant (>50%) in all post-clip models during peak diastole (Table 33). Moreover, during systole, AML stress was higher than PML stress for all pre- and post-clip models (Table 32), a direct result of the restricted PML motion caused by chordae tethering. During diastole, however, AML and PML had comparable stress values for each respective model. These results are congruent with the findings from Lau et al. (92) that showed that during diastole the MV leaflet stress can be up to 200% higher after MitraClip when treating MA dilatation, with respect to a physiological MV model. Morgan et al. [(388)] showed, on the other hand, that MitraClip resulted in similar or reduced MV leaflet stress values, relative to the MV model with no clip. However, the latter FE study was performed on a MV model with leaflet prolapse or primary MR, which is a different MV disease in its etiology and pathophysiology than functional MR.

During diastole, the MV leaflets were subjected to abnormal stresses up to 27% (lateral model) and 52% (central model) higher than during systole. For the central + ring model, however, the leaflets were subjected to comparable stress values during systole and diastole. Thus, the use of an annuloplasty ring in combination with MitraClip appeared to i) give the lowest increase in leaflet stress during diastole with respect to the pre-clip model, and ii) induce a more homogeneous stress state in both leaflets when comparing systolic and diastolic states. These findings have a particular impact upon transcatheter MV repair techniques and their durability, whereby MitraClip is the only repair procedure implemented.

Given that FDA approval for treatment of functional MR was recently granted, and that latest European guidelines implemented MitraClip as recommendation for the treatment of functional MR with a recommendation class IIb, level of evidence C (405), it is expected that MitraClip as non-surgical treatment option will revolutionize the treatment of functional MR. In vitro studies have shown that increased leaflet stress can alter proteoglycan and collagen synthesis, resulting in leaflet thickening with an increased compliance (104, 313). Moreover, under in vivo conditions the MitraClip device has been reported to gradually be encapsulated by connective tissue, have thicker fibrous capsules, and incite a fibrous reaction that results in the formation of a tissue bridge within the clip arms (406). Taken together, careful planning seems necessary to select respondent patients and to determine optimal clip placement. The biomechanical insight provided by FSI computational analyses such as the one developed in this study may aid in the better understanding of the biomechanical impact that MitraClip has on the load distribution and deformation of the LV-valve complex in the short- and long-term.

10.4.3 Effects on anatomic MV orifice area

We report, to our knowledge, the first set of time-dependent in-silico continuous AMVOA measurements pre- and post-clip, and under different clipping configurations (Figure 67D). We quantified a reduction in the diastolic and systolic AMVOA by up to 63% and 33%, respectively (Table 32 and Table 33). The computational-based approach implemented herein allowed us to directly quantify the true AMVOA at the level of the leaflet free edge throughout the cardiac cycle with high reproducibility. Clinically, this parameter could be assumed to represent an invasive measurement using catheterization or the “ground truth”.

Nevertheless, for better comparability of clinical results and simulation results, we also quantified the EOA_{MV} and EROA by using the mathematical formulation that relates the pressure drop across the valve and the flow rate, and by combining the continuity and orifice equations (213, 214). Similarly, we measured a reduction in the EOA_{MV} and EROA after MitraClip by up to 63% and 50%, respectively (Table 31). Congruent with our results, a recent 3D TEE study by Noack et al. (394) found that the EOA_{MV} and EROA decreased by up to 65% and 67%, respectively. Previous works have also shown a decrease in the EOA_{MV} of ~53% after the procedure (407, 408). In the latter studies, the EOA_{MV} was calculated with 3D planimetry in the proximity of the commissures, which can lead to an overestimation of the post-clip EOA_{MV}. This could help to explain the larger decrease in EOA_{MV} quantified in our study.

The clinical assessment of the continuous MV orifice area during MitraClip pre-procedural planning and evaluation is technical challenging due to the 3D dynamic MV orifice, the limited capacity for echocardiographic measurement of areas below 0.5 cm^2, and different TEE and Doppler-derived measurement techniques (408). When comparing our diastolic and systolic AMVOA values (Table 32 and Table 33) with our EOA_{MV} and EROA values (Table 31), we observed the same trend towards a decrease of the MV opening and regurgitant orifice areas pre- vs post-clip, and when using a lateral clip vs. central clip + ring. However, we also quantified that overall, the echocardiographic method (EOA_{MV} and EROA) underestimates the true MV orifice (AMVOA) (408), especially the regurgitant orifice area after MitraClip, with an error up to 30%.

Currently, there is no gold-standard method to measure the MV orifice area during MitraClip procedure. Moreover, in the absence of a reference method for its assessment

pre- and post-clip, it is challenging to determine the best echocardiography method to use. Our findings demonstrated for the first time the dynamic changes in the true MV orifice area before and after MitraClip in a patient with functional MR, and as such, it allows a fundamental improvement of the understanding of MV leaflet kinematics in patients with MR. This could provide useful information toward patient selection and procedural optimization for treatment with transcatheter edge-to-edge MV repair devices.

Interestingly, this study also showed that MitraClip therapy altered the temporal MV leaflet kinematics, especially during diastole. Before MitraClip, a twin-peaked AMVOA curve was quantified, which can be explained by early MV inflow (E wave) followed by atrial contraction (A wave). After clip implantation, the double-peaked AMVOA curve changed to a mostly flat curve (Figure 67D). Although some clinical studies have detected this diastolic flattening of the AMVOA curve (409), it was suggested this was caused by the prevalence of atrial fibrillation in the patients studied. But unlike previous reports, we prescribed the same LA wall motion pre- and post-clip in our virtual patient-specific model. Thus, we hypothesize the diastolic changes in the profile of the AMVOA and MV inflow curves post-clip are related to the MS caused by the narrower and double-orifice MV.

10.4.4 Effects on LH fluid dynamics

10.4.4.1 Impact on residual MR

Up to now, the most important hemodynamic parameters that determine procedural success after MitraClip are residual MR and increased transmitral pressure gradient (MDPG). Even moderate MR after the procedure has been associated with increased mortality (410),

particularly in patients with impaired LV function (411). Indeed, residual MR is discussed as one of the main drivers for worse patient outcome undergoing MitraClip implantation in the MITRA-FR trial, compared with the COAPT trial, with 50% residual MR ≥ 2 in MITRA-FR, and 31% residual MR ≥ 2 in COAPT after 1 year (376, 377). In our study, the post-clip model that gave the highest residual MR was the lateral clip model, followed closely by the central clip model (Table 31). Importantly, all post-clip models presented moderate MR. The post-repair finding of moderate MR is considered a suboptimal outcome for the MitraClip procedure (412). Such a determination would often contribute to the consideration to deploy additional clips.

As a general guideline, additional clips should not be placed if the patient has a mean MDPG ≥ 4 mmHg (413), which was the case for all our post-clip models. Thus, implantation of a second clip was not modeled in this study. The decision to proceed with a second clip is complex and based on the degree of reduction of MR with the first clip, residual MR, MDPG, EOA_{MV}, improvement in hemodynamics, and the technical feasibility of placing a second clip. Regardless of whether 1 or more clips are deployed, the currently recommended approach relies on an overall echocardiographic assessment of MR severity integrating multiple parameters (414, 415), some of which are not validated in the specific MitraClip clinical scenario, are limited by operator dependence, or are difficult to obtain with TEE imaging (298, 416-418).

10.4.4.2 Impact on MV diastolic pressure gradient

The benefit from MR reduction can be counterbalanced by the formation of MS. In cohorts of patients undergoing surgical annuloplasty for functional MR, development of MS was

associated with reduced patient functional capacity as assessed by the 6-minute walk test (419). Similarly, an increased MDPG after surgical MV repair was associated with reduced functional capacity (420) Bertrand et al. (421) stressed the relevance of the EOA_{MV} after annuloplasty to treat functional MR for the long-term outcome. After MitraClip, the creation of a double-orifice MV is often associated with an increase in the MDPG (422, 423). The abrupt change of the LV hemodynamic status from elevated preload caused by MR, to elevated afterload caused by MS and decrease of the low-impedance regurgitant flow into the LA can have a major impact on procedural outcomes. A recent study by Neuss and colleagues (424) found that MS after MitraClip has a negative impact on long-term clinical outcomes. A cutoff value was found at 5 mmHg for invasively and 4.4 mmHg for echocardiographically measured MDPG. Based on this threshold value, implantation of a central clip, with or without ring, caused MS in our patient model. In clinical studies, the frequency of MS at discharge has been reported to occur in approximately 25 - 35% of patients (424, 425). Overall, accurate quantification of the MDPG seems critical to optimize MitraClip procedural outcomes, as the goal is to find an acceptable compromise between residual MR and transmitral gradient.

As previously explained, TEE echocardiography and color Doppler are the tools available to assess both residual MR and MDPG. In clinical practice, the pressure drop across the MV during MitraClip is usually calculated using the simplified Bernoulli equation and the maximum velocity measured by TEE or Doppler-derived echocardiography (426, 427). An in vitro study (428) that investigated the effect of MitraClip on the MDPG found a good agreement between the MDPG measured with Doppler echocardiography and invasively (peak: 9 vs. 7 mmHg, mean: 4 vs 3 mmHg). This

study, however, also found that alignment of the Doppler probe is essential to limit measurement errors. At the peak of the E-wave, the jet velocity was approximately three times higher than the central line velocity, while at the peak of the A-wave, the jet velocity was about six times higher. Maisano et al. (429) also showed that an error up to 35% could be obtained in the estimation of the MDPG depending on the location of the velocity measurement. Thus, Doppler measurements are operator dependent and strongly influenced by LV function, LA compliance, and loading conditions (430). In addition, some Doppler echocardiographic methods have not been adequately validated in a double-orifice MV (431). Under these limitations, evaluation of directly measured hemodynamic parameters pre- and post-clip should be included to support decision making. In our study, all hemodynamic LH variables, including the MDPG and residual MR were accurately calculated using the velocity and pressure fields obtained by the simulation algorithms.

10.4.4.3 Impact on intraventricular hemodynamics

A few research attempts have been conducted to study the impact of MitraClip on LV fluid dynamics (432, 433). Using an in vitro model, Jeyhani et al. (428) showed that vortex development in the LV during diastole was significantly different after MV repair. MitraClip significantly increased the amplitude of the Reynolds and viscous shear stresses, as well as the number of high shear regions in the LV. By means of CFD simulations of different suture lengths and positions, Hu and colleagues (434, 435) demonstrated that while clipping at a commissural location maintained the single vortex structure observed in a normal LV, central and lateral clipping created two jets and vortex rings entering the ventricular cavity in the diastolic phase. Each jet was deflected laterally and impinged on the septal and lateral LV walls. Highest energy loss was found in the impingement regions,

whereas energy losses in the vortices were generally low. Another important takeaway was that decreasing the total orifice area enhanced this energy loss.

The results of our study detected potentially harmful changes in LV flow dynamics. Two jets downstream of the MV were formed when the clip was implanted at the central and lateral positions. The inflow velocity, PDPG, MDPG, and jet deflection angle all increased in the central + ring model, compared to the central model. Lateral clipping demonstrated a LV flow field closest to that of the pre-clip MV. The peak velocities across the MV were strongly affected by the total cross-sectional area of the orifices. From Figure 69 it is clear that the jets impinged the LV wall as they were deviated laterally due to the reduction in the MV orifice area. This deflection can compromise the fluid mechanics such as rapid dissipation of the large LV anterior vortex (434). Subsequently, the blood ejection from the LVOT may be affected by increasing the LV inflow energy dissipation in diastole and recycling in systole. Although previous computational and in vitro studies provided initial insights on the LV flow after MitraClip, the LV-MV complex used was a simplified model without the inclusion of realistic LV geometry and leaflet configurations. It is uncertain how these assumptions would influence the vortex dynamics and jet deflection. An improved understanding of the LH-device hemodynamics using FSI models that are more accurate may help to optimize MitraClip placement. We are currently working on performing a quantitative analysis of the pre- and post-clip intraventricular blood flow dynamics and energetic parameters that have been associated with maladaptive changes and LV reshaping (436, 437).

10.4.5 From color to quantitative hemodynamic assessment

In daily MitraClip routine, the interventional team has to face several difficult situations or "gray zones" from a decisional standpoint. Many questions commonly present. What should be done in the case of a residual MR? In case of a second or third clip implantation, would the adjunctive benefit of more MR reduction be nullified by the incremental increase of the MDPG? What should be done in the case of MR reduction, but a significant increase in transmitral gradient? The answers to these questions are not always clear, suggesting that procedural assessment should be performed in a more integrated way, taking into account both conventional methods (color jet and echocardiographic gradient) and continuous real-time hemodynamic measurements.

Indeed, intraprocedural assessment of LA pressure has been described as a helpful tool during MitraClip (438, 439). Ikenaga et al. (440) showed that changes in pulmonary vein flow following MitraClip can predict recurrent MR, and have an important and independent association with long-term outcomes. Kuwata et al. (392) also demonstrated the value of real-time monitoring of LA pressure during MitraClip to predict clinical outcomes. An increase in LA mean pressure was predictive of worse clinical outcomes at short-term follow-up, independent from echocardiographic findings. As intraprocedural decisions have a strong impact on procedural outcomes, long-term results and prognosis, the clinical message from these studies is extremely relevant for the interventional community: evaluation of MitraClip should shift from a solely echocardiography-based color Doppler assessment to a more integrated hemodynamic-based approach.

To the best of our knowledge, this is the first patient-specific FSI study to directly quantify the changes in LH hemodynamics and tissue mechanics pre- and post-clip under different MitraClip configurations throughout the cardiac cycle in a virtual human beating-

heart. FSI modeling tools, as used in this study, are required to quantify the regurgitant flow across the MV, accurately simulate full dynamic/transient valve dynamics (3, 155), and shift the conventional MitraClip paradigm from a solely anatomic approach, towards a more functional and physiological approach based on objective hemodynamic data. Much needed clinically relevant flow indicators may be obtained by applying the modeling approach herein proposed to the analysis of MitraClip procedure, as well as to gain insight into the different clinical scenarios that are currently critical for this minimally-invasive procedure. The same concept should could applied to other structural MV interventions, including MV replacement.

10.5 Limitations

The present study has several limitations. The main one is its small sample size. This study only used one previously validated patient-specific functional MR model. A large cohort of patient-specific models would be necessary to draw conclusions with confidence. Second, simulations results were not validated against post-procedural clinical data, since the patient studied herein did not undergo MitraClip therapy. Nevertheless, this study allowed for a systematic investigation of various biomechanical scenarios resulting from the MitraClip procedure. Such well-controlled side-by-side comparisons under the same patient and loading conditions are challenging to obtain in a clinical setting. Third, although cardiac tissue properties were age- and gender-matched, they were not patient-specific. Estimation of in vivo material parameters inversely from medical images would be ideal to produce more accurate predictive results. Fourth, only one clip placement was simulated in order to avoid significant MS. Implantation of additional clips is clinically common, as

residual MR after MitraClip is associated with higher mortality than that for patients without MR.

CHAPTER 11. SUMMARY

Specific Aim 1a – Part 1 investigated the capability of SPH, a fully Lagrangian mesh-free method, to simulate the bulk blood flow dynamics in two realistic LV models. 3D geometries and wall motion of the LV, proximal LA and aortic root were extracted from Cine-MR and MSCT imaging data. SPH simulation results were analyzed and compared with those obtained using a traditional CFD numerical method, and to in vivo 4D PCMR and echocardiography data, in terms of the large-scale blood flow phenomena usually clinically measured. A quantitative comparison of the velocity field and global flow parameters between the in silico models and the in vivo data showed a reasonable agreement, given the inherent uncertainties and limitations in the modeling and imaging techniques. The results of this study indicated the capability of SPH as a promising computational tool for predicting clinically relevant large-scale LV flow information, and serve as the cornerstone for the development of the SPH-FE FSI modeling framework.

Specific Aim 1a – Part 2 presented a fully-coupled FSI framework that combined SPH and nonlinear FE method to investigate the coupled AV and MV structural response and the bulk LV hemodynamics in a subject-specific LH model during the entire cardiac cycle. The FSI model incorporated valve structures that considered native asymmetric leaflet geometries, nonlinear elastic material models, and human material properties. Comparison of FSI results with subject-specific echocardiography data demonstrated that the SPH-FE approach was able to quantitatively predict the opening and closing times of the valves, the MV leaflet opening and closing angles, and the large-scale intraventricular flow phenomena with reasonable agreement. Moreover, comparison of FSI results with a

LV model without valves revealed substantial differences in the flow field. Peak systolic velocities obtained from the LV-valve model and the LV model without valves were 2.56 m/s and 1.16 m/s, respectively, compared to the Doppler echo data of 2.17 m/s. The developed SPH-FE FSI framework represents a further step towards modeling patient-specific coupled LH dynamics, and has the potential to improve our understanding of cardiovascular physiology. Moreover, successful completion of Specific Aim 1a serves as a basis for the investigation of pathological and post-procedural LH dynamics in Specific Aim 1b and Specific Aim 2, respectively.

MV dynamics depends on a force balance across the mitral leaflets, the chordae tendineae, the mitral annulus, the papillary muscles and the adjacent LV wall. Chordae rupture disrupts the link between the MV and the LV, causing primary MR. In Specific Aim 1b – Part 1, a FSI modeling framework was implemented to investigate the impact of chordae rupture on the LH dynamics and severity of MR. A control and seven chordae rupture LH models were developed to simulate a pathological process in which minimal chordae rupture precedes more extensive chordae rupture. Different non-eccentric and eccentric regurgitant jets were identified during systole. Cardiac efficiency was evaluated by the ratio of external stroke work. MV structural results showed that basal/strut chordae were the major load-bearing chordae. An increased number of ruptured chordae resulted in reduced basal/strut tension, but increased marginal/intermediate load. Chordae rupture in a specific scallop did not necessarily involve an increase in the stress of the entire prolapsed leaflet.

Functional MR is a significant complication of LV dysfunction and strongly associated with a poor prognosis. In Specific Aim 1b – Part 2, a patient-specific LH FSI

model with functional MR was developed. The model included detailed chordae tendineae structure and distribution, accurate leaflet geometry and thickness, dynamic MA and chordae origins, tethering pre-tension forces, nonlinear elastic material models, and human age- and gender-matched material properties. The MV structural model was validated by comparing the simulation results from valve closure simulation with the in vivo geometry at systole. It was found that the MV model could not replicate the in vivo geometry without the application of tethering pre-tension force in the chordae at diastole. Upon applying the pre-tension force and performing model optimization by adjusting the chordae length, position, and leaflet length, a good agreement between the computational model and the in vivo model was established. Additionally, the accuracy and predictability of the FSI framework were validated with echocardiography hemodynamic data. This work represents a further step towards patient-specific modeling of pathological LH dynamics, and has the potential to improve our understanding of the biomechanical mechanisms and treatment of primary and functional MR.

Transapical beating heart neochordae implantation is an innovative MV repair technique that has demonstrated promising clinical results in patients with primary MR. However, as clinical experience continues to increase, neochordae implantation criteria have not been fully standardized. Quantifying the complex biomechanical interaction and interdependence between the LH structures and the neochordae during this procedure is needed. Specific Aim 2a investigated the effect of i) selecting an antero-lateral ventricular access site; compared to a postero-lateral one, and ii) suboptimal neochordae length; compared to optimal suture length, on restoring baseline LH dynamics. Neochordae implantation using three and four sutures was simulated under three clinically relevant

PML prolapse conditions: isolated P2, multi-scallop P2/P3 and multi-scallop P2/P1. Baseline, pre- and post-repair LH dynamics were evaluated using a FSI modeling framework. Despite the absence of residual MR in all post-repair models with optimal neochordae length, the average and peak stresses in the repaired scallop(s) increased >40% and >100%, respectively, compared with the baseline state. Additionally, PML native chordae tension decreased at least 30%, while AML marginal chordae tension increased >30%.

Selecting an antero-lateral ventricular entry site for the treatment of P2/P3 prolapse generated a significant increase (>80%) in neochordae tension and central scallop peak stress, with respect to a postero-lateral access site. Neochordae length tuning is critical. During isolated P2 prolapse repair, although over-tension of the neochordae led to minimal hemodynamic changes in the regurgitant volume; compared to using an optimal suture length, a significant increase in peak systolic neochordae tension (>300%), diastolic neochordae tension, and mitral leaflet average stress (40% - 460%) was quantified. Additionally, neochordae under-tension led to regurgitation severity worsening; giving a similar regurgitant volume as the pre-repair model. We report, to our knowledge, the first set of time-dependent in silico human neochordae tension measurements during transpical neochordae repair. This parametric FSI study represents a further step towards an improved understanding of the biomechanical outcomes of transapical neochordae techniques.

The AV and MV function in a reciprocal interdependent fashion. However, the impact of TAVR on the aortic-mitral continuity and early post-procedural MR severity are poorly understood. Using a comprehensive computational engineering FSI framework, Specific Aim 2b evaluated the structural and hemodynamic impact of TAVR on aortic-

mitral continuity and MR severity in a rigorously developed and validated patient-specific LH model with AS and concomitant functional MR. The TAVR procedure was virtually simulated using BEV and SEV devices at three implantation heights. Pre- and post-TAVR LH dynamics as well as intra-operative biomechanics were analyzed. The accuracy and predictability of the modeling framework were validated with pre- and post-operative echo data.

No significant differences in early MR improvement/worsening (<10%) were noted at the three implantation depths when compared to the pre-TAVR state. The highest deployment BEV model resulted in higher stresses in the native leaflets, contact radial force and stent recoil, while the midway implantation BEV model gave better hemodynamic performance and MR reduction in this patient case. The high deployment SEV model resulted in a higher stress in the native aortic leaflets, lower stent-tissue contact force, and higher MR reduction for this patient case. When comparing SEV vs. BEV performance at an optimal implantation height, the SEV model gave a higher regurgitant volume than the pre-TAVR model (40.49 vs 37.59 ml), while the BEV model gave the lowest regurgitant volume (33.84 vs 37.59 ml). Acute improvement in MR was i) due to the mechanical compression of the stent against the aortic-mitral curtain, ii) due to an immediate drop in the LV pressure and transmitral pressure gradient. Contact force, aortic-mitral angle, and valve annuli compression were identified as possible mechanistic parameters that may suggest avenues for early MR improvement. Albeit a single real clinical case, it is our hope that such detailed engineering computational analysis could shed light into the underlying biomechanical mechanisms of TAVR impact on MR.

Percutaneous edge-to-edge repair of MR sing the MitraClip has been established as an option for high-risk and inoperable patients with degenerative MR, as well as for patients with functional MR who failed medical therapy. MitraClip was recently approved in the US for treatment of functional MR, which significantly expands the number of patients that can be treated with this device. Specific Aim 2c quantified the morphologic changes and evaluated the biomechanical interaction between the MitraClip device and the LH complex of a real patient case with functional MR using FSI modeling. MitraClip implantation using a central and a lateral clip, as well as combined annuloplasty procedure were simulated in a patient-specific model that integrated detailed geometries of the LH structures, incorporated age- and gender-matched nonlinear elastic human material properties, and accounted for chordae tethering forces. AP distance, ASI, anatomic regurgitant orifice area, and anatomic opening orifice area decreased by up to 26%, 36%, 33% and 63% when compared to the pre-clip model, respectively. MitraClip implantation immediately improved the hemodynamic profile and promoted LV unloading, but imposed a non-physiologic configuration and loading on the mitral apparatus, with anterior and posterior leaflet stress significantly increasing up to 122% and 80% during diastole, respectively. For this patient case, while implanting a central clip + ring resulted in the highest improvement in LV systolic function and magnitude of reduction in the regurgitant flow (46%), this clip configuration also led to the highest degree of mitral stenosis. FSI modeling as used here can be a powerful tool to examine the complex MitraClip-host biomechanical interaction.

CHAPTER 12. CONCLUSIONS AND FUTURE WORK

12.1 Specific Aim 1

12.1.1 Conclusions

12.1.1.1 Specific Aim 1a

In Specific Aim 1a, the first subject-specific LH FSI model that includes detailed valve structures, cardiac wall deformation, nonlinear elastic material models, human cardiac tissue material properties, and pulsatile hemodynamic loads throughout the cardiac cycle was developed. A detailed quantitative comparison of FSI results with those of subject-specific in vivo measurements, clinical observations and in vivo and in vitro studies has been presented. Despite some modeling simplifications and limitations, FSI results were in reasonable quantitative agreement. This study demonstrated the ability of the SPH-FE FSI framework to model the physiologic valves structural response and the bulk intraventricular hemodynamics in a subject-specific LH model during the entire cardiac cycle. The development of a FSI framework which is capable of reproducing the coupled LH dynamics in an accurate and practical way not only enhances our basic understanding of the functional morphology of these structures, but is also needed to obtain clinically relevant results, and to better understand the implications of a broad spectrum of valve repair and intervention replacement procedures.

12.1.1.2 Specific Aim 1b

Specific Aim 1b – Part 1 investigated the impact of PML chordae rupture on LH dynamics and severity of primary MR. We performed a parametric computational study that simultaneously quantified and analyzed chordae forces, PM forces, leaflet stresses, intraventricular hemodynamics and cardiac efficiency in the sequential transition from a physiological state to severe acute MR through multiple levels of chordae rupture. A detailed mechanistic understanding of the mitral apparatus force redistribution and coupled fluid and structural LH dynamics can give deeper insight into the pathophysiologic developmental mechanisms of MV prolapse due to chordae rupture, allow for evaluation and prediction of interventional treatments, and ultimately support improved clinical outcomes.

Specific Aim 1b – Part 2 evaluated the LH dynamics in a rigorously developed and validated patient-specific model with BAV, low-flow low-gradient AS, and functional MR. This study showed that the incorporation of pre-tension tethering forces improved the modeling accuracy of MV dynamic function. A computational method was carried out to optimize the chordae length in combination of adjusting the leaflet height to model the effect of pre-tension. The results showed that the MV model can closely replicate the in vivo valve geometry at systole from MSCT images. Moreover, FSI results showed good quantitative agreement when compared to the patient's available echo data, which demonstrates that the SPH-FE FSI modeling framework can accurately simulate the patient-specific LH pathological dynamics under severe AS and concomitant functional MR. Overall, Specific Aim 1b provided a comprehensive investigation of the LH dynamics under various MR conditions, BAV, and AS, which enabled by the FSI framewrokd is not only expected to unfold new perspectives for the understanding of cardiac physiology in

the setting of heart valve pathology, but can offer potential for patient-specific clinical diagnostic and prognostic information.

12.1.2 Future work

Though the subject- and patient-specific LH models developed in Specific Aim 1 are the first of their kind, there is still room for improvement. For example, cardiac wall motion was prescribed based on in vivo medical imaging data. The use of this one-way FSI coupling method is based on the assumption that the flow-induced load on the cardiac wall is minor in comparison to the structural-induced load on the fluid flow (231). The biggest advancement to our SPH-FE FSI modeling framework would be the inclusion of the mechanical deformation of the myocardium. Cardiac function involves a considerable range of spatial scales and different tightly coupled multi-physics problems. In the muscle, the electrical stimuli propagates through the myocytes causing the cardiac muscle contraction, which in turn exerts work upon the blood inside the atria and ventricles. Therefore, from the computational mechanics standpoint, the heartbeat is a tightly coupled fluid-electro-mechanical problem. The final objective is to model the pumping action of a heart. Nevertheless, despite the extensive work done in experimental and computational research of multi-physics heart modeling (441), up to now, there is no reference of a coupled scheme that includes electrophysiology, solid, and fluid mechanics of the whole human heart.

The use of human age- and gender-matched cardiac tissue properties is a substantial improvement over animal tissue properties. Nevertheless, there are limitations of using tissue properties from human cadaveric hearts. First of all, ex vivo tissue properties are not

patient-specific. Rather, tissue properties are selected from a cadaveric heart with similar characteristics to the patient of interest. This requires a thorough testing database of human tissue properties from an array of patients with differing ages, genders, and degrees of disease because all these factors can significantly impact the tissue response. The ultimate goal would be to obtain patient-specific tissue properties inversely from medical images using the inverse FE method (442, 443), a multi-resolution direct search approach (444), or machine learning algorithms (445). However, such approaches have not been applied to heart valve tissues. Accurate identification of in vivo nonlinear, anisotropic mechanical properties of cardiac tissues of individual patients has long been regarded as one of the critical challenges in the field of cardiovascular biomechanics. Along the same lines, mechanical properties of heart valve tissues are known to be dependent on a variety of factors such as degree of calcification, aging, and disease conditions. Thus, future studies could investigate how different pathophysiological conditions affect the opening/closing speed and shape of the valves, and how the dynamics of the valve in turn affects the LV hemodynamics.

Although in this study we focused on the left side of the heart, the developed FSI computational modeling framework can be easily adapted for simulation of right heart dynamics, including the tricuspid and pulmonary valves, and for the modeling of different valve repair/replacement procedures. The capability of SPH for cardiac modeling where complex geometries and large deformations are present should be taken advantage of. This research is advancing the capability for large-scale computational modeling of cardiac dynamics. In the long term, patient-specific cardiac computational models may be developed based on this research, and could be used as a valuable pre- and intra-operative

planning tool. Furthermore, the data from this research may be used to develop low-order flow models that can serve as a complementary tool for multiple purposes such as BHV design and optimization, and multiscale modeling of the cardiovascular system.

12.2 Specific Aim 2

12.2.1 Conclusions

12.2.1.1 Specific Aim 2a

In Specific Aim 2a, we quantified the complex biomechanical interaction between the neochordae and the LH structures under various PML prolapse scenarios, neochordae number, LV access sites and neochordae lengths using an integrative FSI computational framework. Despite MR reduction and restoration of leaflet coaptation in all post-repair LH models, transapical neochordae implantation altered the mitral apparatus biomechanical environment compared with a baseline state. We report original quantitative biomechanical data regarding leaflet stress magnitude and distribution, cardiac hemodynamics, and native and neochordae forces throughout the cardiac cycle during baseline, pre- and post-repair states under a broad spectrum of prolapse scenarios and neochordae implantation configurations. Direct comparison of the LV-valve biomechanical environment between baseline and post-repair states is imperative to evaluate the role of transapical neochordae technologies in restoring physiologic-like cardiac dynamics and demonstrate non-inferiority to conventional surgical MV repair procedures. While we are approaching the limits of existing in vitro, animal and clinical models to quantify the time-dependent force exchange between the LV-valve structures and minimally-invasive repair devices, the development of innovative and more powerful

tools, such as the FSI computer simulations presented in this work, may eventually help to determine the mid- to long-term biomechanical outcomes of transapical neochordae procedures.

12.2.1.2 Specific Aim 2b

MR is commonly found in conjunction with severe AS, but concomitant significant MR in the setting of TAVR is typically left untreated. In this era of transcatheter interventions advances, prediction of MR magnitude and direction following TAVR is critical but remains difficult in individual patients. With these challenges in mind, in Specific Aim 2b, we performed a comprehensive computational engineering analysis to investigate the impact of TAVR on MR severity, aortic-mitral coupling, TAVR-in-BAV device performance, and pre- and post-TAVR LH dynamics in a retrospective real clinical case.

No significant changes in MR severity were identified following TAVR with different TAV types and implantation heights. Our results demonstrated that the biomechanical mechanism of MR evolution after TAVR is clearly multifactorial. The structural coupling of the AV-MV is a relationship that undergoes measurable changes following TAVR as the stent compresses the aortic-mitral continuity. Moreover, we showed that correcting the AS abruptly reduces LV systolic pressure, which results in a lower transmitral systolic pressure gradient, which in turn reduces the pathological retrograde flow through the MV. Mechanistic intra-procedural predictors that may suggest early avenues of MR improvement were identified.

Although this work is limited by its small sample size and is not designed to specifically answer questions about the late post-procedural period, it does report a novel

and promising approach for elucidating the biomechanical mechanisms through which TAVR can influence early MR severity. Further development and validation of the computational modeling techniques in a large cohort of patients could eventually enable the use of such techniques for an individualized treatment approach and ultimately support improved clinical outcomes.

12.2.1.3 Specific Aim 2c

Feasibility and safety of MitraClip has been largely described in a variety of studies and case-reports. Results concerning efficacy and durability, however, are not entirely satisfactory. Additionally, results tend to be less impressive immediately after the procedure compared to surgical MV repair. In this era of booming technology, the collaboration between industry and academia is of utmost importance in order to bring further advancements in the field of percutaneous treatment of MV disease. In Specific Aim 2c, the acute LH hemodynamic and structural changes during and after MitraClip therapy were evaluated. Although this patient-specific FSI study provided further evidence to support that MitraClip is a viable approach to treat functional MR by improving LV systolic function and promoting LV unloading, clip implantation also imposed a non-physiologic configuration and loading on the LV-valve complex, especially during diastole. FSI modeling as used here can be a powerful and versatile tool that can pinpoint specific biomechanical implications and potentially play an important role in elucidating the optimal setting and efficacy of percutaneous MV repair procedures.

12.2.2 Future work

The insights derived from the data presented in Specific Aim 2 have important clinical implications; however, those insights should be supported by a few other studies. Firstly, in this study, the deformed LH geometries after neochordae, MitraClip, annuloplasty and TAVR procedures obtained using FE analysis were used as the initial stress-free geometries for the post-procedural FSI simulations, thus the induced stress state from the repair/replacement procedures was neglected. Additional studies should investigate if this assumption is valid in such complex simulations, or integrate the FE and FSI models in a single simulation file. However, as all of the measurements and analyses in this work are the first of their kind, such exploration is beyond the scope of this thesis.

Secondly, the cardiac geometries obtained from the in vivo MSCT images for the development of the subject- and patient-specific LH models were assumed to be in their stress-free state. However, cardiac structures are continuously under a loaded and pressurized state. Several computational methods have been proposed to compute the load-free configuration and the pre-stress of different structures of the cardiovascular system, especially large arteries. These include manual trial-and-error techniques, as well as automatic inverse techniques such as solving the inverse elastostatics problem, and shape matching techniques. In order to obtain realistic patient-specific tissue compliance and hemodynamics, the LH pre-stress needs to be accounted for in the computational formulation using the load-free state of the cardiac structures. Our lab recently demonstrated the feasibility and potential of using machine learning techniques as a fast surrogate of FE-based inverse methods to recover the zero-pressure geometry of the human thoracic aorta (373). Future studies should investigate the capabilities of this method to compute the stress-free geometry of the remaining LH structures. These two additions

would not only make the FSI modeling framework more physiologically accurate but would also open up the possibility of tackling more clinical issues in cardiac physiology.

In recent years, there has been immense interest in the evaluation of blood flow dynamics in cardiac function analysis for their ability to provide independent and prognostic information over conventional measures (446-448). The LH hemodynamics computed in the current study were from clinically relevant large-scale intraventricular flow features present in the heart. As recent studies have shown that some parameters derived from this intraventricular flow field can be associated with changes in LV dimensions and function in different clinical conditions (436, 437, 449), futures studies should aim to quantify these intraventricular vortex and flow energetic indices from our FSI models. The occurrence of maladaptive changes after transcatheter valve repair/replacement procedures may stimulate further research in the field with the aim to identify intraventricular flow patterns associated with LV reshaping and positive/negative clinical outcomes.

Finally, Specific Aim 2 outlined a number of biomechanical implications resulting from repairing the MV under degenerative and functional MR, and from replacing the AV under low-flow low-gradient stenosis, and BAV. Numerous additional future studies should follow to enhance, further, and/or complement the present work. For example, a larger parameter sweep could be performed which also includes other valvular diseases, stages of the disease (e.g. LV remodeling), hemodynamic conditions (e.g. heart rate, blood pressure), tissue properties, cardiac anatomy variability, next-generation catheter-based devices, etc. This study represents an effort to bring personalized medicine closer to reality. The tools developed in this study may one day be used for the prediction of device

performance and complications through patient screening, optimal device placement, rational device selection, and improved device design. This advance would help medical device companies by providing better devices that can be developed more quickly and with fewer physical design cycles. Most importantly though, personalized medicine will benefit the patients, providing reduced complication rates through better patient screening, patient-device pairing, and optimized placement.

CHAPTER 13. FUNDING AND OTHER SUPPORT

This work was primarily supported by grants from the National Heart, Lung, and Blood Institute of the National Institutes of Health (R01HL104080 and R21HL127570), and by a Fulbright-Colciencias Fellowship.

Special thanks is given to Holifield Farms, who graciously donated fresh porcine hearts for use in the study of APPENDIX A.

APPENDIX A. BIOMECHANICAL CHARACTERIZATION OF CHEMICALLY-TREATED FETAL, CALF AND ADULT BOVINE PERICARDIUM

A.1 Introduction

Biosprosthetic heart valves (BHV) designed to be implanted surgically or percutaneously are commonly made from bovine pericardium (BP), porcine pericardium or porcine aortic valve tissue (450). Due to adequate biological and mechanical properties, wide availability, and rigorous quality control related to intensive battery farming, adult BP (ABP) or calf BP (CPB) are considered as biomaterials of choice to manufacture BHV (451). The pericardial sac is a fibrous meshwork with varying degrees of collagen orientation and constituent components throughout the sac (452), and thus is considered to be mechanically anisotropic (453). Several studies have analyzed and compared the fiber architecture, mechanical properties and morphology of fresh and chemically treated BP, with and without the application of stress or strain constraints during tissue fixation (454-457). A function-structure relationship between collagen alignment and the mechanical behavior of the BP has been identified, where collagen fiber orientation and fiber diameter play a paramount role in the overall tissue behavior (454, 458).

It is also known that the mechanical properties of collagenous tissues change with growth, maturation and aging (459). For example, it has been shown that tendon elastic modulus and ultimate stress increase with maturity (460) (461-463). Nonetheless, knowledge regarding the age-related changes in the mechanical properties of BP xenografts

is highly limited. A recent study by Sizeland et al. (2014) (464) found significant differences in the tissue tensile response between glutaraldehyde-treated (GL-treated) ABP and neonatal BP. The markedly thinner neonatal tissue showed a higher elastic modulus and a higher ultimate tensile strength (UT_S) than ABP. While yielding important quantitative information, uniaxial mechanical testing is non-physiologic for soft tissues as the coupling of the tissue's directional response is ignored. Additionally, it is still not clear whether the effect of maturation and aging on the mechanical behavior of the BP is orientation-dependent. Clearly, multi-protocol biaxial mechanical data are necessary for the complete mechanical characterization of the BP.

The strength and thickness of leaflet tissues are of crucial importance for the required lifetime of the biomaterial, but also for valve delivery in applications such as percutaneous BHV replacement. The first generation of transcatheter aortic valves required the use of 18-Fr, 22-Fr, and 24-Fr delivery sheaths. This translates into minimal vessel diameters of 6 mm, 7 mm, and 8 mm in noncalcified arteries (465). The new generation of transcatheter aortic valves further reduces the device profile, allowing for delivery sheaths as small as 14 Fr (466). In the rapidly growing field of minimally-invasive heart valve replacement, it is clear that the industry is trending towards lower-profile devices that minimize incisions and simplify advancement of the catheter through small and/or tortuous arteries. However, the size of the delivery catheter system is limited by the minimum crimped diameter of the valve, which is in turn determined by the crimping profile of the stent, but mainly by the thickness of the BP tissue.

Younger BP has been shown to be thinner than CBP and ABP (464), giving it a potential physical advantage for percutaneous BHV production. However, a detailed

understanding of the age-dependent anisotropic mechanical properties of the BP remains unknown. Therefore, the objective of the present study was to investigate and compare the mechanical response of chemically treated ABP, CBP and fetal BP (FBP) through comprehensive mechanical testing and structural analysis. An improved understanding and utilization of the BP mechanical properties may ultimately result in BHV designs with more predictable performance and improved durability, as well as enable percutaneous valve technologies to develop the minimal profile size required to improve the advancement of the catheter through small and/or tortuous arteries and reduce adverse events.

A.2 Materials and Methods

A.2.1 Tissue preparation

Fresh pericardial sacs were obtained from 10 adult (12-24 months old), 11 calf (6-12 months old) and 11 fetal (third trimester of gestation) cattle from Animal Technologies, Inc. (Tyler, TX). The fresh pericardia were stored in cryopreservant solution (10% dimethyl sulfoxide and 90% culture medium RPMI 1640) at −80 °C until fixation could be performed. Cryopreservation has been shown to retain the native tissue`s structural integrity and mechanical properties (467) (468). Prior to testing, the pericardia were thawed via the published protocol (467) and cut into flat sheets. Regions of the pericardial sacs with defects such as cuts or tears and those in which the pericardial ligaments could not be clearly distinguished were excluded.

The tissue was pinned slightly around the edges to hold flat, and any adherent adipose tissue and loose surface fibers were carefully removed prior to treatment. Care was

taken with the handling of the pericardium to not stretch the material to avoid changes in fibril alignment (453). Tissue treatment and fixation were performed in two steps at room temperature. First, the flat pericardium was immersed in a container of 0.625% glutaraldehyde and placed on an orbital shaker at 100 rpm for 2 hours. In the second step, the tissue was treated with a crosslinking anti-calcification solution composed of formaldehyde, ethanol, and Tween 80 (Sigma Aldrich, St. Louis, MO), and placed on an orbital shaker at 100 rpm for 18 hours. Treated pericardium was then stored at 4°C in 0.25% glutaraldehyde for a minimum of 48 hours prior to testing.

Selection of testing samples was based on the orientation of macroscopically visible collagen fibers, uniform thickness and local homogeneity. First, visual inspection of the pericardium sheets under a light source was used to identify a potential local preferred fiber direction. Biaxial testing samples were cut into a 20 mm x 20 mm square such that the preferred fiber direction and the cross-preferred fiber direction aligned with the X1 and X2 directions of the device's loading axes, respectively (Figure 73A). Second, if after biaxial testing an isotropic response was obtained from the sample, mechanical alignment consisting of sample rotation was performed until an anisotropic response was acquired.

Uniaxial testing samples adjacent to the biaxial samples were carefully cut into a "dog-bone" shape using a stencil with a central zone 30 mm long x 3 mm wide to ensure failure in the center region and to minimize grip effects. Each sample was cut in such a way as to insure that the preferred fiber direction was parallel with the loading axis of the tensile device. Sample thickness was measured and averaged in five different places with a Mitutoyo 7301 rotating thickness gage (Aurora, IL) with an accuracy of ± 0.01 mm.

A.2.2 Planar biaxial mechanical testing

Planar biaxial testing was conducted following the methods detailed in Sacks and Sun (2003) (469). Briefly, four graphite markers delimiting a square approximately 2 mm x 2 mm in size were glued to the central region of the tissue surface for optical strain measurements. Specimens were immersed in saline solution for at least 30 minutes prior to testing to allow for tissue hydration. Samples were then mounted in a trampoline fashion and tested in aqueous 0.9% NaCl solution at 37 °C. A stress-controlled test protocol was utilized (469), wherein the ratio of the normal Lagrangian stress components T_{11}:T_{22} was kept constant with $T_{12} = T_{21} = 0$. Preconditioning of up to 40 cycles, with a rest period of 25 s between each set of 10 consecutive cycles was performed to reduce tissue hysteresis and achieve a stable tissue response. Seven successive protocols were performed using the ratios T_{11}:T_{12} = 1:0.75, 1:0.5, 1:0.3, 1:1, 0.75:1, 0.5:1, 0.3:1 with 10 cycles per run. Tissue samples were assumed to be incompressible and planar, and the unloaded reference markers were obtained using the post-preconditioning state.

Stiffness and extensibility in both the preferred fiber direction (X1) and cross-preferred fiber direction (X2) were computed from the equibiaxial stress-strain curves as material metrics. Tissue stiffness was quantified by means of the secant modulus at three equibiaxial stress values: 1) 60 kPa for tissue response under small load, 2) 250 kPa to examine tissue response at a physiological level (455), and 3) 500 kPa for a high stress state, representing areas of the valve that may experience greater stress (i.e. attachment to stent, commissure regions). Linear regression was used to calculate the extensibility in the high-modulus linear region (Figure 73B). In addition, the degree of anisotropy (DA) was analyzed using the ratio of Green strains, E_{11} / E_{22}, at maximum equibiaxial loading.

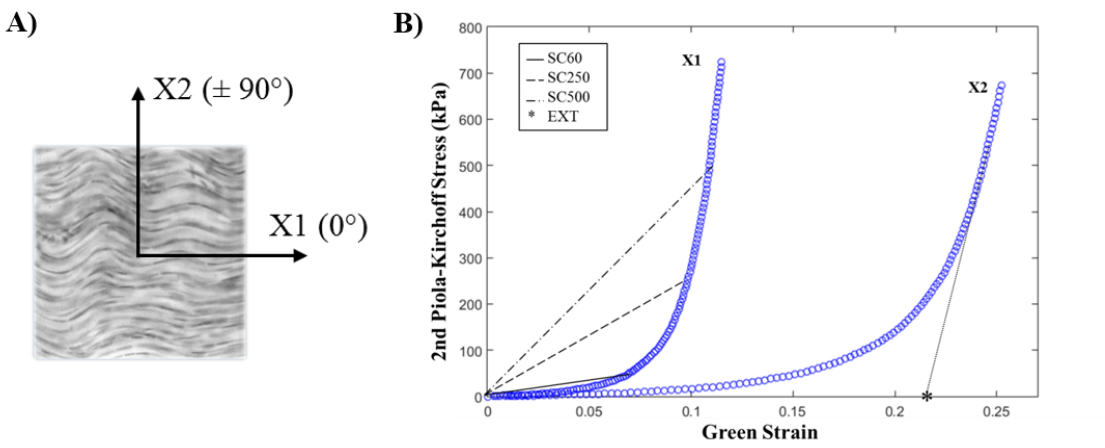

Figure 73. A) Orientation of BP biaxial samples, B) Representative equibiaxial stress-strain curve and calculated parameters. EXT: Extensibility, SC60: Secant modulus at 60 kPa, SC250: Secant modulus at 250 kPa, and SC500: Secant modulus at 500 kPa, for both X1 and X2 directions.

A.2.3 Uniaxial mechanical testing

Testing was conducted using a TestResources 100Q Universal Testing Machine (Shakopee, MN). Four graphite optical markers were placed on the narrow portion of the samples for optical strain measurements. The axial force was measured by means of a 500 lbf load cell (TestResources SM-500-294). The specimens were mechanically fixed to specially-designed anti-slip clamps, and special care was taken to avoid damage during clamping while avoiding slippage from the grips. The specimens were immersed in saline solution for at least 1 hour before testing and continuously hydrated after mounting to allow for optimal tissue hydration during testing.

All specimens were mechanically preconditioned by means of a series of 10 loading–unloading cycles estimated to 30% of the maximum load prior to testing (data not

shown) (470). The samples were then loaded at a rate of 50 mm/min until failure. A CCD camera was used to capture optical marker motion, while an in-house LabVIEW (National Instruments, Austin, TX, USA) program was used to simultaneously correlate the markers' location and load information with each video frame. Stress–strain curves were obtained and analyzed using an in-house Matlab code. The UT_S and ultimate tensile strain (UT_E) were determined from the uniaxial data, defined by the peak stress and maximum deformation withstood by the samples prior to failure, respectively. Tissue stiffness was also quantified by means of the tangent modulus defined as the slope of the stress-strain curve in the high-modulus linear region.

A.2.4 Multiphoton microscopy

To corroborate the visual findings of the local preferred fiber direction and quantify the orientation of the collagen fibers, tested biaxial samples were imaged using second harmonic generation (SHG). Tissues were imaged on a Zeiss 710 NLO inverted confocal microscope (Carl Zeiss Microscopy, LLC, Thornwood, NY, USA) equipped with a mode-locked Ti:Sapphire Chameleon Ultra laser (Coherent Inc., Santa Clara, CA) in combination with non-descanned detection (NDD). The laser was set to 800 nm and emission was filtered from 380–430 nm (471). Samples were kept hydrated with saline solution during imaging to prevent drying artifacts and covered with #1.5 coverslips. SHG was collected using a Plan-Apochromat 40x oil immersion objective. Zeiss ZEN software was used to visualize and export image stacks for analysis. Image resolution was set to 1024 x 1024 pixels at 12-bit pixel depth.

A.2.5 Local collagen fiber orientation and distribution

Estimation of a local preferred fiber direction for each z-stack was done using a semiautomatic ImageJ-Matlab in-house code (The Mathworks, Inc., Natick, MA). First, OrientationJ (472), an ImageJ (473) plug-in developed for directional analysis, was used to generate a weighted histogram of local angles between ±90° for each optical slice, where 0° aligned to the X1 biaxial axis and ±90° to the X2 axis (Figure 73A). The local collagen fiber orientation was evaluated pixel-by-pixel based on the structure tensor, commonly used in image processing (474). Next, the individual histograms at each slice were combined and normalized using Matlab to calculate a mean local angular histogram for each BP sample.

A.2.6 Histology

Ten samples for each age group were selected for quantitative histological analysis after biaxial testing. Samples were cut into strips parallel to the X1 direction of the biaxial test fixture, fixed in 10% neutral buffered formalin and embedded in paraffin. Sections cut at 5-μm thickness were stained in picrosirius red solution for one hour (reagents from Sigma Aldrich, St. Louis, MO). The slides were then washed in acidified water, three changes of 100% ethanol, and xylene before being mounted in a resinous medium and coverslipped. Picrosirius red staining was used in conjunction with circularly polarized light microscopy to assess collagen fiber thickness and organization. Fiber thickness determines the color, changing from green to yellow to orange to red with increasing thickness (475). This principle can be used to quantify the relative proportion of collagen fiber maturity in the tissue. For example, yellow-orange strong birefringence would be assigned to mature thick collagen fibers, whereas newly-synthesized thin collagen fibers would display a weak birefringence associated with a greenish color (476).

The proportion of different colored fibers was assessed using published methods (477). Briefly, images from four different locations in each sample were viewed with the use of a N-Achroplan 10x objective on an Axio Scope.A1 microscope (Carl Zeiss Microscopy, LLC, Thornwood, NY) equipped with filters to provide circularly polarized illumination, recorded by a AxioCam MRc Rev.3 digital camera (Carl Zeiss Microscopy, LLC, Thornwood, NY) and analyzed using an in-house Matlab code. Images were resolved into their hue, saturation and value components. A histogram of hue frequency was obtained from the resolved 8-bit hue images, which contained 256 colors, defined as follows: red 2 to 9 and 230 to 256, orange 10 to 38, yellow 39 to 51, and green 52 to 128 (477). The number of pixels within each hue range was determined and expressed as a percentage of the total number of collagen pixels, which in turn was expressed as a percentage of the total number of pixels in the image analyzed to give collagen content.

A.2.7 Constitutive modelling

For this study, two different constitutive models were used to fit the experimental data. BP was assumed to be an incompressible, anisotropic, nonlinear, hyperelastic material (478). Exponential descriptions in terms of the Green strain have the benefits of being invertible and fairly simple to interpret. Thus, the first model utilized was a Fung-type model (479) with the strain energy function given by

$$W = \frac{c}{2}(e^{Q} - 1)$$
$$Q = A_1E_{11}^2 + A_2E_{22}^2 + 2A_3E_{11}E_{22} + A_4E_{12}^2 + 2A_5E_{11}E_{22} + 2A_6E_{22}E_{12} \quad (13)$$

where c and A_i are material parameters. Formulations based on polynomials and exponentials of strain invariants are also common in the literature and have been implemented into many standard FE packages. The second model used was a fiber-reinforced material model based on the work of Holzapfel et al. (2000) (480) and Gasser et al. (2006) (481), as presented in Specific Aim 1a – Part 2.

Each constitutive model was fit simultaneously to the mean response of the seven stress-controlled protocols for each age group to provide material parameters for the computational modeling simulations. The goodness-of-fit was determined by the correlation coefficient based on a nonlinear regression model in Matlab. The average material parameters obtained from the individual responses of the specimens are not given since the parameters (and their averages) are not individually meaningful; only as a set do the parameters completely describe the biaxial data.

A.2.8 Statistical analysis

All measurements are presented as a mean ± standard deviation. The One Way Analysis of Variance (ANOVA) test was implemented in SigmaPlot (V11.0, Systat Software Inc., San Jose, CA). If statistical differences were found ($P<0.05$), pairwise multiple comparisons were performed using the Holm–Sidak or the Dunn`s methods. Student's t-tests were used when two groups were compared. Probability values $P< 0.001$ were considered to indicate a high statistically significant difference.

A.3 Results

A.3.1 Tissue thickness

The mean thickness was 0.451 ± 0.0278 mm for ABP, 0.321 ± 0.0294 mm for CBP, and 0.231 ± 0.0167 mm for FBP. There was a high statistically significant difference between the three age groups ($P<0.001$), with FBP having approximately half the thickness of ABP (Table 34).

Table 34. Mean and standard deviation values for material metrics calculated from the equibiaxial and uniaxial tests.

	ABP (n=10)	**CBP (n=11)**	**FBP (n=11)**
Tissue thickness (mm)	0.451 ± 0.0278	0.321 ± 0.0294	0.231 ± 0.0167
Secant modulus X1 – 60 kPa (MPa)	1.903 ± 0.831	1.651 ± 0.790	0.896 ± 0.185
Secant modulus X1 – 250 kPa (MPa)	3.816 ± 1.199	4.030 ± 1.922	2.650 ± 0.570
Secant modulus X1 – 500 kPa (MPa)	6.041 ± 1.832	6.824 ± 3.164	4.625 ± 0.872
Secant modulus X2 – 60 kPa (MPa)	0.817 ± 0.242	0.733 ± 0.167	0.485 ±0.128
Secant modulus X2 – 250 kPa (MPa)	1.814 ± 0.371	1.763 ± 0.312	1.358 ±0.249
Secant modulus X2 – 500 kPa (MPa)	2.989 ± 0.538	2.946 ± 0.460	2.357 ± 0.348
DA	0.541 ± 0.092	0.504 ± 0.172	0.520 ± 0.107
Extensibility X1	0.0734 ± 0.0175	0.0803 ± 0.0292	0.0993 ± 0.0235
Extensibility X2	0.153 ± 0.0256	0.157 ± 0.0164	0.189 ± 0.0291
UT_S (MPa)	21.087 ± 4.144	22.438 ± 5.619	12.324 ± 4.352
Uniaxial Tangent modulus (MPa)	110.714 ± 30.824	101.834 ± 34.014	46.001 ± 15.344
UT_E	0.449 ± 0.0622	0.460 ± 0.0901	0.608 ± 0.0704

A.3.2 Biaxial mechanical response

The mean equibiaxial stress–strain curves in the preferred and cross-fiber directions for the three age groups are shown in Figure 74. In general, the mean curves exhibited the well-known nonlinear stress-strain response of soft tissues. The initial portion of the curves, known as the toe region, had a high deformation/low stress characteristic due to the un-crimping of collagen fibers and elasticity of elastin. Collagen fibers were then progressively recruited and dominated the stiff mechanical response at higher stress levels. A more gradual transition from low to high stiffness regions was observed in FBP, while ABP and CBP had a more pronounced rapid stiffening effect at the transitional region in both directions. From Figure 74 it can also be seen that all of the tested tissues exhibited anisotropic behavior, being much less extensible in the preferred fiber direction.

From Figure 75 and Table 34 it can be seen that a significant difference in tissue stiffness was observed in the preferred fiber direction at 60 kPa, where ABP and CBP were significantly stiffer than FBP ($P<0.001$ and $P=0.016$, respectively). Similarly, at 250 kPa ABP was significantly stiffer than FBP ($P=0.029$), and although CBP had a higher stiffness than FBP at this stress value, this difference cannot be considered statistically significant. A similar trend was observed at 500 kPa in the preferred fiber direction, but this also cannot be considered statistically significant. In the cross-preferred fiber direction, however, ABP and CBP were significantly stiffer than FBP at all stress values ($P<0.001$ and $P=0.007$ at 60 kPa respectively, $P=0.007$ and $P=0.010$ at 250 kPa respectively, and $P=0.010$ at 500 kPa), see Figure 75 and Table 34. There was no statistically significant difference in tissue stiffness between the ABP and CBP groups at all stress values.

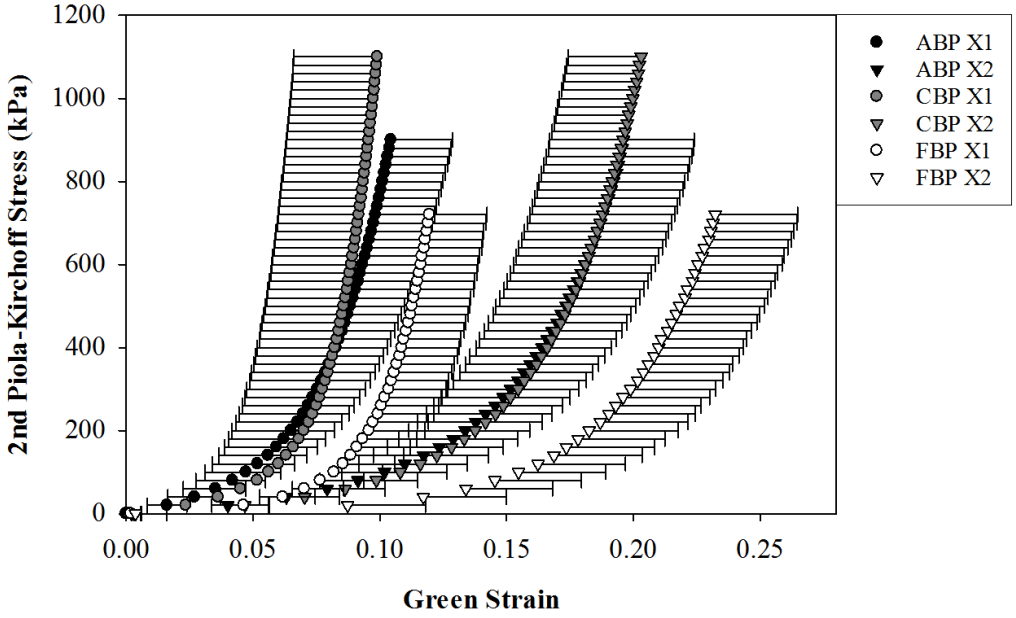

Figure 74. Equibiaxial response data for ABP, CBP and FBP, presented as mean curves with standard deviation bars.

To further illustrate the differences in mechanical properties between the three age groups, linear regression was used to calculate the extensibility at the high-modulus linear region of the stress-strain curves (see Figure 76, Table 34). As expected, FBP showed a higher extensibility than ABP and CBP, with a statistically significant difference in the cross-preferred fiber direction (P=0.007 and P=0.011, respectively). CBP samples exhibited a similar strain range to ABP samples. The mean DA values for the three age groups indicated that the BP specimens exhibited anisotropic behavior, where the cross-fiber direction doubled the strain value found in the preferred fiber direction at all ages (Table 34). The DA was not significantly different between the three age groups. Overall,

ABP and CBP demonstrated a markedly higher stiffness than FBP, while FBP was significantly thinner and more compliant than the ABP and CBP groups.

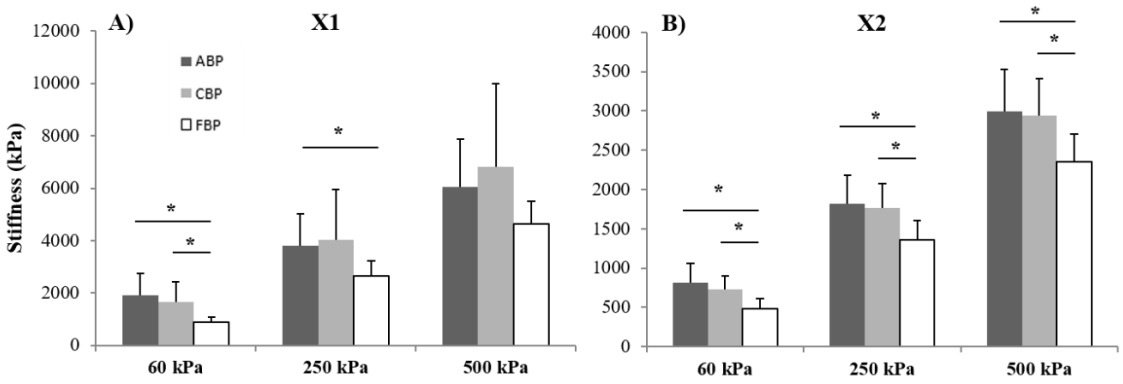

Figure 75. Mean and standard deviation of stiffness measurements calculated as secant modulus at three stress levels for ABP, CBP and FBP. (*) indicates a statistically significant difference while (**) indicates a high statistically significant difference.

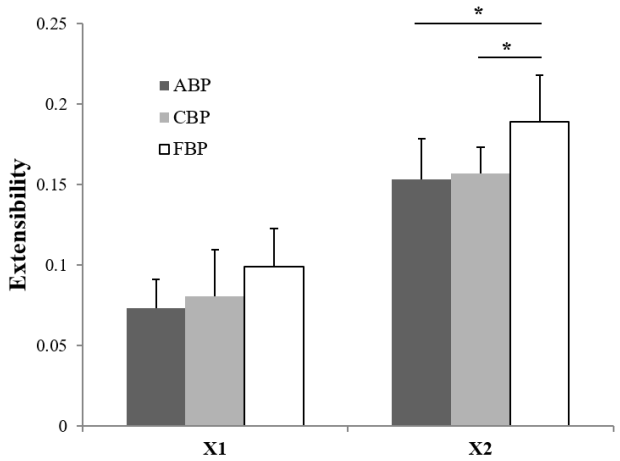

Figure 76. Mean and standard deviation of extensibility measurements for ABP, CBP and FBP. (*) indicates a statistically significant difference.

A.3.3 Uniaxial failure

The UT_S of ABP and CBP is found to be much greater than for FBP, with a high statistically significant difference ($P<0.001$) (Figure 77A). On the other hand, the UT_E was significantly greater for FBP than for ABP and CBP samples ($P<0.001$) (Figure 77B). These tensile properties reflect the significantly higher tangent modulus of the ABP and CBP tissue compared with the FBP ($P=0.003$ and $P=0.007$, respectively) (Table 34), and is in agreement with the biaxial data presented. There was no statistically significant difference in tensile properties between the ABP and CBP groups.

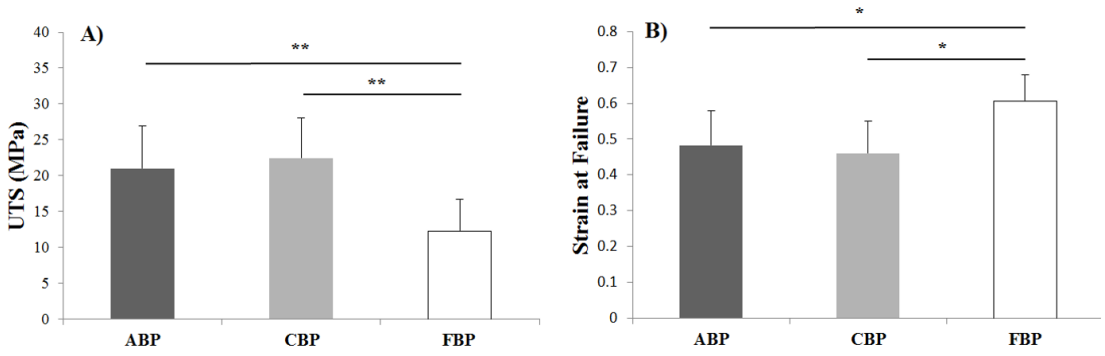

Figure 77. Mean and standard deviation of A) UT_S measurements and B) UT_E measurements for ABP, CBP and FBP. (*) indicates a statistically significant difference while (**) indicates a high statistically significant difference.

A.3.4 SHG imaging and local angle analysis

SHG microscopy is a nondestructive imaging tool that allows for clear visualization of collagen fibers throughout connective tissue without staining or pretreatment (482). Regarding the estimation of local collagen fiber orientation, Figure 78D, E, F shows an

example of the local angle distributions for BP samples of different ages. The measured preferred fiber orientation of these samples agrees with the fiber architecture visually identified under the light source, with peak angles around 10°, 8° and 4° for ABP, CBP and FBP samples, respectively. As can be seen in the mean local angular histograms, the angular values obtained with the ImageJ-Matlab in-house code are in line with the way the samples were positioned in the biaxial device. By identifying the preferred and cross-preferred fiber directions, errors caused by intra- and inter-specimen structural variations can be reduced, providing a means for the improved characterization and modeling of the mechanical properties of the BP.

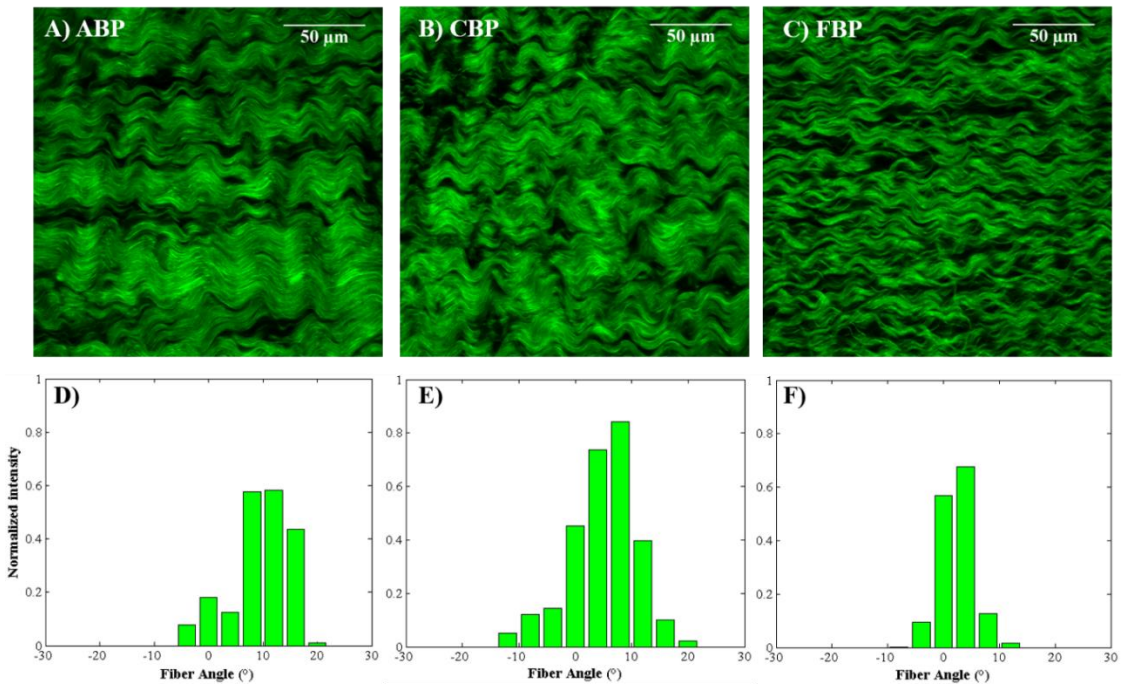

Figure 78. Representative SHG images for ABP, CBP and FBP (A-C) and estimation of local collagen fiber orientation (D-F).

Examination of collagen fibril architecture clearly indicates a different structural arrangement between the FPB tissue and the ABP/CBP groups (Figure 78A, B, C). At the fetal stage, small collagen fibers were primarily arranged parallel with the X1 loading axis. However, some regions showed fibers traversing and interweaving with other fibrils, which were not aligned with the principal axis (Figure 79C). In general, SHG images of FBP showed loosely packed small collagen fibers that lacked the typical mature closely packed collagen morphology. On the other hand, the collagen architecture of the adult and calf samples indicated a more organized collagenous matrix. Thick collagen bundles were still predominantly parallel to the X1 direction in a dense wavy pattern, although with an apparent increased crimp period (Figure 79A,B). Collagenous tissues typically fall into two categories: one composed of typically large, closely packed fibers, and the other composed of more uniform fibers of smaller average diameter with larger inter-fiber spaces (483).

A.3.5 Histological analysis

The picrosirius polarization method is simple, sensitive and specific for collagen staining. In conjunction with circularly polarized light, it is particularly useful to quantify the collagen content and study the organization and thickness of collagen fibers (475). Histological images revealed that the FBP samples contained more immature collagen fibers than those of the ABP and CBP samples (Figure 79). Collagen color (hue) quantitative examination of the images substantiated this finding, with a statistically significant difference in the percentage of green thin fibers between ABP and FBP (1.969% versus 5.548%, $P<0.001$), and between CBP and FBP (2.629% versus 5.548%, $P<0.001$), where the proportion of thin newly synthesized fibers decreased with increasing age. Although the differences between the three age groups for the yellow-orange (thick)

collagen fibers did not achieve statistical significance, our SHG results indicate changes in collagen fiber structure during BP tissue maturation.

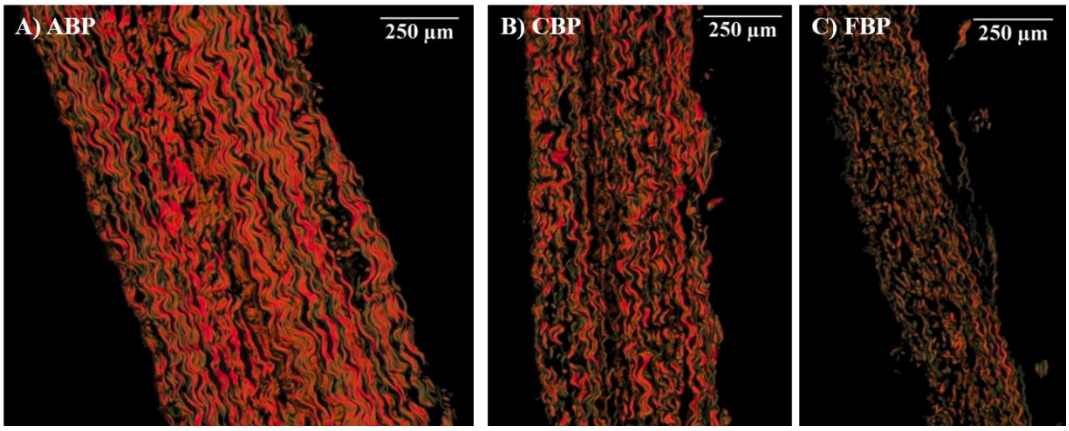

Figure 79. Representative picrosirius red-stained cross-sections for A) ABP, B) CBP, and C) FBP.

A.3.6 Constitutive modelling fit

The two constitutive models successfully fit the experimental data quantitatively in both the preferred and cross-preferred fiber directions. The material parameters and r^2 values for each age group obtained from the two models fit are summarized in Table 35. The mean seven-protocol stress–strain curves with the corresponding fit are shown in Figure 80. The individual parameters for each sample and r^2 values are listed in Table 36,

Table 37 and

Table 38 for the modified-Holzapfel model.

Table 35. Material parameters for the Fung and Modified-Holzapfel models.

Fung model								
	$c\ (kPa)$	A_1	A_2	A_3	A_4	A_5	A_6	r^2
ABP	21.88	58.25	27.87	4.49	5.54	-1.43	0.62	0.98
CBP	10.71	104.62	39.89	-4.60	9.89	1.80	-0.15	0.98
FBP	4.54	76.36	33.85	0.61	7.23	1.17	-0.008	0.98

Modified-Holzapfel model							
	$c_1\ (kPa)$	c_2	$k_1\ (kPa)$	k_2	D	$\Theta\ (deg)$	r^2
ABP	11.58	41.37	34.61	7.13	0.0005	0	0.97
CBP	14.16	30.57	55.21	3.84	0.0005	8.6	0.96
FBP	12.83	9.21	40.83	1.66	0.0005	15.4	0.97

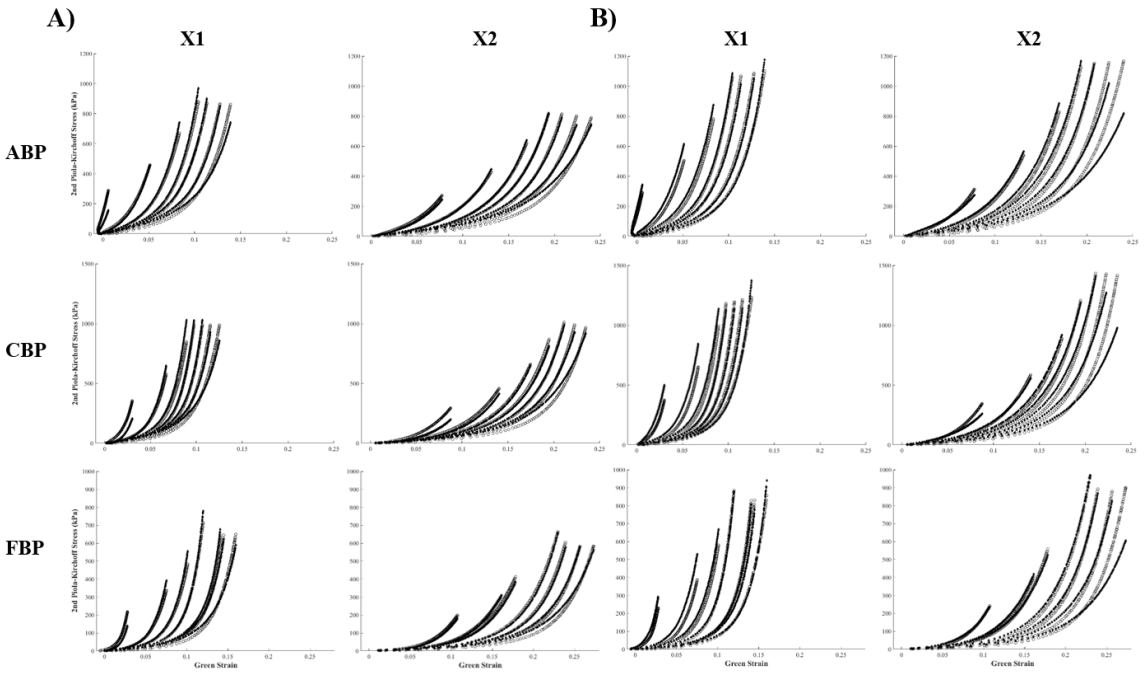

Figure 80. Mean responses of the seven experimental protocols (open circles) for ABP, CBP and FBP with A) fit to Fung model (solid diamonds), and B) fit to modified-Holzapfel model (solid diamonds).

Table 36. Individual APB material parameters for the Modified-Holzapfel model.

c_2	$k_1\,(kPa)$	k_2	$c_1\,(kPa)$	kappa	$\Theta\,(deg)$	r^2
7.476	57.491	14.651	14.706	0.000	0.000	0.971
12.599	44.854	46.487	4.477	0.000	0.000	0.955
10.864	198.394	16.649	8.334	0.000	0.000	0.966
13.326	24.103	58.410	9.317	0.000	0.000	0.973
10.257	56.497	26.584	5.190	0.000	0.000	0.969
11.151	5.802	60.969	12.584	0.000	18.677	0.960
9.646	29.807	13.855	4.880	0.000	0.000	0.961
10.924	17.544	34.441	6.412	0.000	0.000	0.970
12.852	22.735	49.923	5.116	0.000	0.000	0.943
14.599	39.965	159.399	11.735	0.000	14.407	0.922

Table 37. Individual CPB material parameters for the Modified-Holzapfel model.

c_2	$k_1\,(kPa)$	k_2	$c_1\,(kPa)$	kappa	$\Theta\,(deg)$	r^2
12.228	22.596	59.077	5.570	0.000	0.000	0.955
15.088	338.596	438.799	5.181	0.172	0.000	0.947
16.302	170.374	321.873	3.336	0.113	9.373	0.962
13.899	0.244	31.591	1.560	0.000	90.000	0.954
13.232	4.065	61.644	5.084	0.000	0.000	0.954
13.948	522.786	84.803	1.687	0.130	0.000	0.987
16.735	13.416	96.851	6.358	0.000	0.000	0.948
13.604	5.450	68.675	5.747	0.000	0.000	0.937
11.201	34.070	27.854	5.066	0.000	0.000	0.950
11.847	46.574	157.574	3.669	0.204	0.000	0.957
10.974	3.710	87.112	9.489	0.010	0.000	0.966

Table 38. Individual FPB material parameters for the Modified-Holzapfel model.

c_2	$k_1\,(kPa)$	k_2	$c_1\,(kPa)$	kappa	$\Theta\,(deg)$	r^2
12.618	1.646	28.692	1.546	0.000	0.000	0.913
10.172	64.281	64.510	2.327	0.119	8.895	0.982
12.860	2.732	20.421	3.421	0.000	0.000	0.927
15.654	48.178	98.776	0.519	0.167	0.002	0.961
12.805	46.280	194.971	4.714	0.187	0.001	0.964
11.214	15.470	44.285	1.879	0.056	5.275	0.954
7.788	2.075	25.084	3.865	0.040	19.568	0.948
11.509	17.494	61.585	3.576	0.070	0.000	0.952
14.314	2.927	76.390	1.431	0.000	0.000	0.973
11.319	8.674	101.780	1.202	0.082	0.000	0.927
8.273	121.310	59.493	5.233	0.000	0.000	0.877

A.4 Discussion

A.4.1 Tissue properties related to collagen maturation and aging

The age-related changes that manifest in the increased stiffness and mechanical strength of the CBP and ABP tissues can be attributed primarily due to the intermolecular cross-linking of the collagen. The molecular mechanisms involved during growth, maturation and aging of collagenous tissues are well known and comprise two different mechanisms, a precise enzymatic process during development and maturation, and a subsequent non-enzymatic adventitious reaction with glucose and its oxidation products during aging, a process referred to as glycation (459). Although both of these processes affect the mechanical properties of collagenous tissues, the most dramatic changes in stiffness and mechanical strength occur between embryonic growth and maturity (484), as observed between the FBP group and the ABP/CBP groups in this study. This age-related stiffening of the BP is consistent with findings previously reported in other connective tissues such as cartilage (485) and tendons (463), as well as with human and porcine valves (486) (487).

The histological analysis revealed a statistically significant difference in the percentage of green collagen fibers between the three tissue groups, where the proportion of thin fibers decreased with increasing age. The results of the histological analysis are in line with the findings of the SHG microscopy, showing that the FBP samples are mainly composed of small collagen fibers.. Collagen's ultimate tensile strength, in the range of 1 MPa, is directly proportional to the diameter of the fibrils (458). Thus, thicker fibers in the mature collagen will be stronger than the thinner fibers observed in the younger collagen (488) (489) (490). However, with increasing diameter, the flexibility of the tissue also

decreases and a reduction in the ability to resist crack propagation can be observed. Conversely, the plastic deformation, or creep, is directly related to the proportion of small diameter fibrils (491).

Regarding tissue elongatiom, there was a significant difference in the extensibility between the fetal and mature tissues, where FBP showed a higher extensibility than ABP and CBP. When viewed under SHG microscopy, the FBP tissue appeared to exhibit a higher waviness than the CPB and ABP samples. This crimp is believed to act as a shock absorber system and is responsible for the initial low-slope “toe region” of the biological stress–strain curve. The higher extensibility found in the FBP tissue can be ascribed to the lower level of crimp period of the fiber network, resulting in a higher elongation at alignment and a higher elongation at break. With increasing age, the crimp amplitude decreases and crimp wavelength increases thus decreasing the shock absorbing effect (492). The finding that extensibility decreases with collagen maturation and aging is consistent with previous age-related studies in tendon collagen (493), human aortic valves (494) and in porcine mitral and aortic valves (487).

A.4.2 Comparison with BP tissue properties reported in the literature

To the author's knowledge, the only published study that has mechanically assessed and compared the age-related differences in BP was developed by Sizeland et al. (2014) (464). GL-treated neonatal (4-7 days old) and adult (18-24 months) BP samples were subjected to uniaxial testing. Beyond the limited uniaxial tensile methodology reported, the authors found that neonatal pericardium had a significantly higher elastic modulus and UT_S than ABP. On the other hand, the UT_E was significantly higher for ABP than for neonatal BP.

An opposite trend was observed in the uniaxial testing results of this study. It is important to note that the fetal tissue used in our study was obtained during the third trimester of cattle gestation, while the neonatal tissue used by Sizeland and colleagues was obtained from cattle between 4-7 days old. Additionally, it was not clear from the study what type of tissue presorting and preconditioning, if any, were carried out. Although this age difference and testing criteria could help to explain the discrepancies in the mechanical properties, current literature generally agrees that in collagenous tissues the stiffness and UT_S increase with maturity (460) (484) (487), as found in this study.

The results of this study are also consistent with previous reports regarding the mechanical properties of chemically treated CBP (495). Recently, uniaxial tensile tests performed by Gauvin et al. (2012) (496) showed an UT_S for GL-treated CBP of approximately 25 MPa, while Bai et al. (2013) (497) reported an UT_S of 29 MPa and 25 MPa for GL-treated and decellularized CBP, respectively. Further uniaxial loading tests were performed on native and GL-treated BP by Hulsmann et al. (2013) (498). The UT_E value of 50% obtained for the fixed tissue is comparable to the value found in this study for CBP. The results of this study are also consistent with previous reports regarding the UT_E (499) (500) and UT_S (501) (502) of BP.

Concerning stiffness, it is accepted to define the elastic modulus as the slope of the stress-strain curve in the linear portion of it. However, there is a plurality of biomechanical parameters used in the literature, because of the pseudoelastic nature of soft tissues. Reported values for the elastic modulus of GL-treated BP under uniaxial loading range from 10 MPa up to 190 MPa (496, 498). A study done on decellularized BP samples showed similar values of elastic modulus as presented in this study (92.9 ± 21.6 MPa)

(502). Similarly, Sanchez et al. (2010) (503) reported an elastic modulus for GL-treated ABP with three different fiber orientations (0°, 45° and 90°). For the ABP samples at 0° fiber orientation, as defined in this study, Sanchez and colleagues found a stiffness value of 105 MPa, a finding consistent with this study.

Even though uniaxial tensile testing is advantageous for the determination of failure properties, biaxial testing can provide more complex insight into the coupling of the tissue directional response. Until now, only limited studies on the mechanical properties of chemically treated or fresh BP using biaxial testing were available (453, 456, 457, 495), which did not quantify the age-dependent mechanical differences. The Sacks group investigated the relationship between BP mechanical properties and tissue structure, suggesting that the local collagen fiber architecture plays a major role in determining the degree of mechanical anisotropy (454, 504, 505). The results of this study are in line with the above findings, showing that the BP stress–strain response is highly anisotropic.

A.4.3 Implications for BHV manufacturing

In this study, three main findings can be highlighted in relation to the identification of an optimal BP candidate biomaterial for manufacturing BHV. First, there were no statistically significant differences in the mechanical properties between the ABP and CBP tissues. Therefore, CBP is as strong but significantly thinner than ABP. These findings suggest (and support the current tissue selection process (457)) that CBP may be a better tissue source for the design of BHV, especially in the manufacturing of percutaneous heart valve technologies. Second, although FBP was significantly thinner than CBP and ABP, the fetal tissue was also significantly more extensible and more compliant than the adult and calf

tissues. It has been shown that heterogeneity in the structure and properties of the BP, with particularly high extensibility in a particular site, can cause stretching of the leaflet and result in prolapse (506). One could argue that the decreased thickness of the FBP would enable percutaneous BHV to develop smaller profile configurations. However, FBP—having the mechanical properties and characteristics described herein— should be used with caution and additional tissue characterization is needed before it can be considered as a suitable biomaterial for BHV design.

Third, biaxial mechanical testing revealed that the mechanical behavior of the BP was quantitatively consistent with the specimen local fiber architecture. The high compliance of the aortic valve leaflet along its radial direction allows the leaflet to be stretched in the diastolic cycle, while the circumferential stiffness is important for supporting the high transvalvular pressure (507). Such anisotropic properties of the valve leaflets are important for proper valve function (508); however, there is no evidence that the current process on fabrication of BP BHV considers the direction of the tissue fibers with respect to the flow. Based on the findings of this study, it is suggested that in order to mimic the native response of native valve leaflets, BP specimens with good structural uniformity should be oriented in a way such that the preferred fiber direction aligns with the circumferential direction of the leaflet, thus increasing stiffness in that direction; while the cross-preferred fiber direction should be aligned along the radial direction, enhancing leaflet apposition.

A.4.4 Modelling of BP leaflets

This study provides the first complete set of multi-protocol biaxial mechanical data for BP tissues of varying age. Biaxial testing provided independent control of stresses along perpendicular axes and information regarding the changes in coupling between the primary fiber and cross-fiber directions in BP tissue. BP demonstrated complex, highly anisotropic mechanical behavior, including pronounced mechanical coupling between the preferred and cross-preferred fiber directions. In fact, mechanical coupling between the axes produced negative strains along the preferred fiber direction in some samples subjected to non-equibiaxial loading. Additionally, our biaxial data clearly demonstrated the impact of maturation and age on the mechanical behavior of the BP, both in terms of stiffening and extensibility. Taken together, these results demonstrate the importance of utilizing multiaxial constitutive relationships within finite element models to accurately predict the mechanical response of BP. The constitutive models developed throughout this study, which describe the mechanical behavior of adult, calf and fetal BP tissues to a high degree of accuracy, may now be implemented in finite element models to study the biomechanics of a widely used BHV biomaterial.

A.5 Limitations

There are some limitations in this study. First, BP sacs were cryopreserved prior to fixation and testing. However, cryopreservation has been shown to ensure the structural integrity of collagenous tissues (509, 510) (511) (512) (513, 514). Vinci et al. (2013) (515) investigated the mechanical properties of decellularized cryopreserved human pericardium. Uniaxial tensile loading tests revealed equivalent elastic modulus, UT_S and UT_E of the decellularized tissue, before and after the cryopreservation, in comparison with the fresh tissue. Second, the sample size for the three age groups was relatively small; a

larger sample size would provide more statistical power in analyzing the data. Considering the effects of age on the mechanical properties of biomaterials, another limitation was the relatively narrow age range between the CBP and the ABP tissues compared to the broader age range between the FBP and the CBP tissues. A larger sample size including BP tissue between birth and 6 months of age would facilitate a deeper understanding and comparison of the age-dependent mechanical properties of the BP.

REFERENCES

1. Nishimura RA, Otto CM, Bonow RO, Carabello BA, Erwin JP, Guyton RA, O'Gara PT, Ruiz CE, Skubas NJ, Sorajja P. 2014 AHA/ACC guideline for the management of patients with valvular heart disease. Circulation. 2014:CIR. 0000000000000031.

2. Doost SN, Ghista D, Su B, Zhong L, Morsi YS. Heart blood flow simulation: a perspective review. Biomedical engineering online. 2016;15(1):101.

3. Lau K, Diaz V, Scambler P, Burriesci G. Mitral valve dynamics in structural and fluid–structure interaction models. Medical engineering & physics. 2010;32(9):1057-64.

4. Mittal R, Seo JH, Vedula V, Choi YJ, Liu H, Huang HH, Jain S, Younes L, Abraham T, George RT. Computational modeling of cardiac hemodynamics: Current status and future outlook. Journal of Computational Physics. 2016;305:1065-82. doi: http://dx.doi.org/10.1016/j.jcp.2015.11.022.

5. Halevi R, Hamdan A, Marom G, Lavon K, Ben-Zekry S, Raanani E, Bluestein D, Haj-Ali R. Fluid–structure interaction modeling of calcific aortic valve disease using patient-specific three-dimensional calcification scans. Medical & biological engineering & computing. 2016;54(11):1683-94.

6. Einstein DR, Del Pin F, Jiao X, Kuprat AP, Carson JP, Kunzelman KS, Cochran RP, Guccione JM, Ratcliffe MB. Fluid–structure interactions of the mitral valve and left heart: comprehensive strategies, past, present and future. International Journal for Numerical Methods in Biomedical Engineering. 2010;26(3-4):348-80.

7. Borazjani I. A review of fluid-structure interaction simulations of prosthetic heart valves. Journal of long-term effects of medical implants. 2015;25(1-2).

8. Chandran KB, Kim H. Computational mitral valve evaluation and potential clinical applications. Annals of biomedical engineering. 2015;43(6):1348-62.

9. Pinnock C, Lin T, Jones R, Smith T. Fundamentals of anaesthesia: Cambridge University Press; 2002.

10. Dahl SK. Numerical simulations of blood flow in the left side of the heart2012.

11. Markl M, Kilner PJ, Ebbers T. Comprehensive 4D velocity mapping of the heart and great vessels by cardiovascular magnetic resonance. Journal of Cardiovascular Magnetic Resonance. 2011;13(1):1.

12. Pedrizzetti G, La Canna G, Alfieri O, Tonti G. The vortex [mdash] an early predictor of cardiovascular outcome? Nature Reviews Cardiology. 2014;11(9):545-53.

13. Carlhäll CJ, Bolger A. Passing strange. Circulation: Heart Failure. 2010;3(2):326-31.

14. Pedrizzetti G, Domenichini F. Nature optimizes the swirling flow in the human left ventricle. Physical review letters. 2005;95(10):108101.

15. Jimenez JH, Soerensen DD, He Z, He S, Yoganathan AP. Effects of a saddle shaped annulus on mitral valve function and chordal force distribution: an in vitro study. Annals of biomedical engineering. 2003;31(10):1171-81.

16. Salgo IS, Gorman JH, Gorman RC, Jackson BM, Bowen FW, Plappert T, Sutton MGSJ, Edmunds LH. Effect of annular shape on leaflet curvature in reducing mitral leaflet stress. Circulation. 2002;106(6):711-7.

17. Yacoub MH, Kilner PJ, Birks EJ, Misfeld M. The aortic outflow and root: A tale of dynamism and crosstalk. Annals of Thoracic Surgery. 1999;68(3 SUPPL.):S37-S43.

18. Carpentier A. Cardiac valve surgery-the" French correction". J Thorac cardiovasc surg. 1983;86:323-37.

19. Carpentier A, Adams D, Filsoufi F. Carpentier’s Reconstructive Valve Surgery. From Valve Analysis to Valve Reconstruction. İmprint of Elsevier. Missouri. Year Book.95-110.

20. Yacoub MH, Kilner PJ, Birks EJ, Misfeld M. The aortic outflow and root: a tale of dynamism and crosstalk. The Annals of thoracic surgery. 1999;68(3):S37-S43.

21. Lam J, Ranganathan N, Wigle E, Silver M. Morphology of the human mitral valve. Circulation. 1970;41(3):449-58.

22. Rabbah J-PM, Saikrishnan N, Siefert AW, Santhanakrishnan A, Yoganathan AP. Mechanics of healthy and functionally diseased mitral valves: a critical review. Journal of biomechanical engineering. 2013;135(2):021007.

23. Benjamin EJ, Blaha MJ, Chiuve SE, Cushman M, Das SR, Deo R, de Ferranti SD, Floyd J, Fornage M, Gillespie C. Heart disease and stroke statistics—2017 update: a report from the American Heart Association. Circulation. 2017;135(10):e146-e603.

24. De Backer O, Piazza N, Banai S, Lutter G, Maisano F, Herrmann HC, Franzen OW, Sondergaard L. Percutaneous transcatheter mitral valve replacement: an overview of devices in preclinical and early clinical evaluation. Circulation Cardiovascular interventions. 2014;7(3):400-9. Epub 2014/06/20. doi: 10.1161/circinterventions.114.001607. PubMed PMID: 24944303.

25. Nkomo VT, Gardin JM, Skelton TN, Gottdiener JS, Scott CG, Enriquez-Sarano M. Burden of valvular heart diseases: a population-based study. Lancet. 2006;368(9540):1005-11. doi: 10.1016/S0140-6736(06)69208-8. PubMed PMID: 16980116.

26. Nishimura RA, Vahanian A, Eleid MF, Mack MJ. Mitral valve disease—current management and future challenges. The Lancet. 2016;387(10025):1324-34.

27. . Available from: https://www.houstonheartvalvesurgeon.com/mitral-valve-regurgitation.

28. Borger MA, Alam A, Murphy PM, Doenst T, David TE. Chronic ischemic mitral regurgitation: repair, replace or rethink? The Annals of thoracic surgery. 2006;81(3):1153-61. Epub 2006/02/21. doi: 10.1016/j.athoracsur.2005.08.080. PubMed PMID: 16488757.

29. Kumanohoso T, Otsuji Y, Yoshifuku S, Matsukida K, Koriyama C, Kisanuki A, Minagoe S, Levine RA, Tei C. Mechanism of higher incidence of ischemic mitral regurgitation in patients with inferior myocardial infarction: quantitative analysis of left ventricular and mitral valve geometry in 103 patients with prior myocardial infarction. The Journal of thoracic and cardiovascular surgery. 2003;125(1):135-43.

30. Agricola E, Oppizzi M, Maisano F, De Bonis M, Schinkel AF, Torracca L, Margonato A, Melisurgo G, Alfieri O. Echocardiographic classification of chronic ischemic mitral regurgitation caused by restricted motion according to tethering pattern. European Journal of Echocardiography. 2004;5(5):326-34.

31. Daimon M, Saracino G, Gillinov AM, Koyama Y, Fukuda S, Kwan J, Song JM, Kongsaerepong V, Agler DA, Thomas JD. Local dysfunction and asymmetrical deformation of mitral annular geometry in ischemic mitral regurgitation: a novel computerized 3D echocardiographic analysis. Echocardiography. 2008;25(4):414-23.

32. Zoghbi WA, Enriquez-Sarano M, Foster E, Grayburn PA, Kraft CD, Levine RA, Nihoyannopoulos P, Otto CM, Quinones MA, Rakowski H. Recommendations for evaluation of the severity of native valvular regurgitation with two-dimensional and Doppler echocardiography. Journal of the American Society of Echocardiography. 2003;16(7):777-802.

33. Gillinov AM, Tantiwongkosri K, Blackstone EH, Houghtaling PL, Nowicki ER, Sabik JF, Johnston DR, Svensson LG, Mihaljevic T. Is prosthetic anuloplasty necessary for durable mitral valve repair? The Annals of thoracic surgery. 2009;88(1):76-82.

34. Alfieri O, De Bonis M, Lapenna E, Regesta T, Maisano F, Torracca L, La Canna G, editors. "Edge-to-edge" repair for anterior mitral leaflet prolapse. Seminars in thoracic and cardiovascular surgery; 2004: Elsevier.

35. Alfieri O, De Bonis M, Lapenna E, Maisano O, Torracca L, La Canna G. The edge-to-edge technique for Barlow's disease. 2004.

36. Acker MA, Parides MK, Perrault LP, Moskowitz AJ, Gelijns AC, Voisine P, Smith PK, Hung JW, Blackstone EH, Puskas JD. Mitral-valve repair versus replacement for severe ischemic mitral regurgitation. New England Journal of Medicine. 2014;370(1):23-32.

37. Adams DH, Anyanwu AC. The cardiologist's role in increasing the rate of mitral valve repair in degenerative disease. Current opinion in cardiology. 2008;23(2):105-10.

38. Nelson JS, Bolling SF, editors. Who is doing mitral valve surgery in the United States? Seminars in thoracic and cardiovascular surgery; 2012: Elsevier.

39. Chiam PT, Ruiz CE. Percutaneous transcatheter mitral valve repair: a classification of the technology. JACC: Cardiovascular Interventions. 2011;4(1):1-13.

40. Administration USFaD. FDA approves expanded indication for two transcatheter heart valves for patients at intermediate risk for death or complications associated with open-heart surgery. 2016.

41. Iung B, Vahanian A. Epidemiology of valvular heart disease in the adult. Nature reviews Cardiology. 2011;8(3):162-72. doi: 10.1038/nrcardio.2010.202. PubMed PMID: 21263455.

42. Bonow RO, Carabello BA, Chatterjee K, de Leon AC, Jr., Faxon DP, Freed MD, Gaasch WH, Lytle BW, Nishimura RA, O'Gara PT, O'Rourke RA, Otto CM, Shah PM, Shanewise JS, American College of Cardiology/American Heart Association Task Force on Practice G. 2008 focused update incorporated into the ACC/AHA 2006 guidelines for the management of patients with valvular heart disease: a report of the American College of Cardiology/American Heart Association Task Force on Practice Guidelines (Writing Committee to revise the 1998 guidelines for the management of patients with valvular heart disease). Endorsed by the Society of Cardiovascular Anesthesiologists, Society for Cardiovascular Angiography and Interventions, and Society of Thoracic Surgeons. Journal of the American College of Cardiology. 2008;52(13):e1-142. doi: 10.1016/j.jacc.2008.05.007. PubMed PMID: 18848134.

43. Vahanian A, Alfieri O, Andreotti F, Antunes MJ, Baron-Esquivias G, Baumgartner H, Borger MA, Carrel TP, De Bonis M, Evangelista A, Falk V, Lung B, Lancellotti P, Pierard L, Price S, Schafers HJ, Schuler G, Stepinska J, Swedberg K, Takkenberg J, Von Oppell UO, Windecker S, Zamorano JL, Zembala M, Guidelines ESCCfP, Joint Task Force on the Management of Valvular Heart Disease of the European Society of C, European Association for Cardio-Thoracic S. Guidelines on the management of valvular heart disease (version 2012): the Joint Task Force on the Management of Valvular Heart Disease of the European Society of Cardiology (ESC) and the European Association for Cardio-Thoracic Surgery (EACTS). Eur J Cardiothorac Surg. 2012;42(4):S1-44. doi: 10.1093/ejcts/ezs455. PubMed PMID: 22922698.

44. Rodes-Cabau J. Transcatheter aortic valve implantation: current and future approaches. Nature reviews Cardiology. 2012;9(1):15-29. doi: 10.1038/nrcardio.2011.164. PubMed PMID: 22083020.

45. Nombela-Franco L, Ribeiro HB, Urena M, Allende R, Amat-Santos I, DeLarochellière R, Dumont E, Doyle D, DeLarochellière H, Laflamme J, Laflamme L, García E, Macaya C, Jiménez-Quevedo P, Côté M, Bergeron S, Beaudoin J, Pibarot P, Rodés-Cabau J. Significant Mitral Regurgitation Left Untreated At the Time of Aortic Valve Replacement: A Comprehensive Review of a Frequent Entity in the Transcatheter Aortic Valve Replacement Era. Journal of the American College of Cardiology. 2014(0). doi: http://dx.doi.org/10.1016/j.jacc.2014.02.573.

46. Webb J, Pasupati S, Humphries K, Thompson C, Altwegg L, Moss R, Sinhal A, Carere R, Munt B, Ricci D, Ye J, Cheung A, Lichtenstein S. Percutaneous transarterial aortic valve replacement in selected high-risk patients with aortic stenosis. Circulation. 2007;116(7):755-63.

47. De Chiara B, Moreo A, De Marco F, Musca F, Oreglia J, Lobiati E, Bruschi G, Belli O, Mauri F, Klugmann S. Influence of CoreValve ReValving System implantation on mitral valve function: an echocardiographic study in selected patients. Catheter Cardiovasc Interv. 2011;78(4):638-44. doi: 10.1002/ccd.23045. PubMed PMID: 21805556.

48. Durst R, Avelar E, McCarty D, Poh KK, Friera LF, Llano MF, Chu J, Anumandla AK, Rodriguez LL, Mack MJ, Hanzel G, Kodali SK, Hung J, Picard MH. Outcome and improvement predictors of mitral regurgitation after transcatheter aortic valve implantation. J Heart Valve Dis. 2011;20(3):272-81. PubMed PMID: 21714416.

49. Giordana F, Capriolo M, Frea S, Marra WG, Giorgi M, Bergamasco L, Omede PL, Sheiban I, D'Amico M, Bovolo V, Salizzoni S, La Torre M, Rinaldi M, Marra S, Gaita F, Morello M. Impact of TAVI on mitral regurgitation: a prospective echocardiographic study. Echocardiography. 2013;30(3):250-7. doi: 10.1111/echo.12050. PubMed PMID: 23190425.

50. Samim M, Stella PR, Agostoni P, Kluin J, Ramjankhan F, Sieswerda G, Budde R, der Linden M, Samim M, Hillaert M, van Herwerden L, Doevendans PA, van Belle E. Transcatheter aortic implantation of the Edwards-SAPIEN bioprosthesis: insights on early benefit of TAVI on mitral regurgitation. Int J Cardiol. 2011;152(1):124-6. doi: 10.1016/j.ijcard.2011.07.042. PubMed PMID: 21840071.

51. Tzikas A, Piazza N, van Dalen BM, Schultz C, Geleijnse ML, van Geuns RJ, Galema TW, Nuis RJ, Otten A, Gutierrez-Chico JL, Serruys PW, de Jaegere PP. Changes in mitral regurgitation after transcatheter aortic valve implantation. Catheter Cardiovasc Interv. 2010;75(1):43-9. doi: 10.1002/ccd.22197. PubMed PMID: 19739261.

52. Hutter A, Bleiziffer S, Richter V, Opitz A, Hettich I, Mazzitelli D, Ruge H, Lange R. Transcatheter aortic valve implantation in patients with concomitant mitral and tricuspid regurgitation. Ann Thorac Surg. 2013;95(1):77-84. doi: 10.1016/j.athoracsur.2012.08.030. PubMed PMID: 23063197.

53. Unger P, Dedobbeleer C, Vanden Eynden F, Lancellotti P. Mitral regurgitation after transcatheter aortic valve replacement: does the prosthesis matter? Int J Cardiol. 2013;168(2):1706-9. doi: 10.1016/j.ijcard.2013.03.055. PubMed PMID: 23582437.

54. Fedak P, Verma S, David T, Leask R, Weisel R, Butany J. Clinical and pathophysiological implications of a bicuspid aortic valve. Circulation. 2002;106(8):900-4.

55. Sabet HY EW, Tazelaar HD, Daly RC. . Congenitally bicuspid aortic valves: a surgical pathology study of 542 cases (1991 through 1996) and a literature review of 2715 additional cases. . Mayo Clin Proc. 1999;74:14 –21.

56. Sievers H-H, Schmidtke C. A classification system for the bicuspid aortic valve from 304 surgical specimens. The Journal of Thoracic and Cardiovascular Surgery. 2007;133(5):1226-33.

57. Roberts WC, Ko JM. Frequency by decades of unicuspid, bicuspid, and tricuspid aortic valves in adults having isolated aortic valve replacement for aortic stenosis, with or without associated aortic regurgitation. Circulation. 2005;111(7):920-5. Epub 2005/02/16. doi: 10.1161/01.cir.0000155623.48408.c5. PubMed PMID: 15710758.

58. Etz CD, Misfeld M, Borger MA, Luehr M, Strotdrees E, Mohr F-W. Current indications for surgical repair in patients with bicuspid aortic valve and ascending aortic ectasia. Cardiology research and practice. 2012;2012.

59. Wenk JF, Zhang Z, Cheng G, Malhotra D, Acevedo-Bolton G, Burger M, Suzuki T, Saloner DA, Wallace AW, Guccione JM. First finite element model of the left ventricle with mitral valve: insights into ischemic mitral regurgitation. The Annals of thoracic surgery. 2010;89(5):1546-53.

60. Dahl SK, Vierendeels J, Degroote J, Annerel S, Hellevik LR, Skallerud B. FSI simulation of asymmetric mitral valve dynamics during diastolic filling. Computer methods in biomechanics and biomedical engineering. 2012;15(2):121-30.

61. Le TB, Sotiropoulos F. On the three-dimensional vortical structure of early diastolic flow in a patient-specific left ventricle. European Journal of Mechanics-B/Fluids. 2012;35:20-4.

62. McQueen D, Peskin C. Shared-memory parallel vector implementation of the immersed boundary method for the computation of blood flow in the beating mammalian heart. The Journal of Supercomputing. 1997;11(3):213-36.

63. Su B, Zhong L, Wang X-K, Zhang J-M, Tan RS, Allen JC, Tan SK, Kim S, Leo HL. Numerical simulation of patient-specific left ventricular model with both mitral and aortic valves by FSI approach. Computer Methods and Programs in Biomedicine. 2014;113(2):474-82. doi: http://dx.doi.org/10.1016/j.cmpb.2013.11.009.

64. Peskin CS. Flow patterns around heart valves: a numerical method. Journal of computational physics. 1972;10(2):252-71.

65. McQUEEN DM, Peskin CS, Yellin EL. Fluid dynamics of the mitral valve: physiological aspects of a mathematical model. American Journal of Physiology-Heart and Circulatory Physiology. 1982;242(6):H1095-H110.

66. Peskin CS. Numerical analysis of blood flow in the heart. Journal of computational physics. 1977;25(3):220-52.

67. Peskin CS. The immersed boundary method. Acta numerica. 2002;11:479-517.

68. Yin M, Luo X, Wang T, Watton P. Effects of flow vortex on a chorded mitral valve in the left ventricle. International Journal for Numerical Methods in Biomedical Engineering. 2010;26(3-4):381-404.

69. Gao H, Feng L, Qi N, Berry C, Griffith B, Luo X. A coupled mitral valve--left ventricle model with fluid-structure interaction. arXiv preprint arXiv:170401960. 2017.

70. Kunzelman KS, Cochran R. Stress/strain characteristics of porcine mitral valve tissue: parallel versus perpendicular collagen orientation. Journal of cardiac surgery. 1992;7(1):71-8.

71. Weinberg EJ, Shahmirzadi D, Mofrad MRK. On the multiscale modeling of heart valve biomechanics in health and disease. Biomechanics and modeling in mechanobiology. 2010;9(4):373-87.

72. Prot V, Skallerud B. Nonlinear solid finite element analysis of mitral valves with heterogeneous leaflet layers. Computational Mechanics. 2009;43(3):353-68.

73. Wang Q, Sun W. Finite element modeling of mitral valve dynamic deformation using patient-specific multi-slices computed tomography scans. Annals of biomedical engineering. 2013;41(1):142-53.

74. Stevanella M, Maffessanti F, Conti CA, Votta E, Arnoldi A, Lombardi M, Parodi O, Caiani EG, Redaelli A. Mitral valve patient-specific finite element modeling from cardiac MRI: application to an annuloplasty procedure. Cardiovascular Engineering and Technology. 2011;2(2):66-76.

75. Lee C-H, Carruthers CA, Ayoub S, Gorman RC, Gorman JH, Sacks MS. Quantification and simulation of layer-specific mitral valve interstitial cells deformation under physiological loading. Journal of theoretical biology. 2015;373:26-39.

76. Gao H, Qi N, Feng L, Ma X, Danton M, Berry C, Luo X. Modelling mitral valvular dynamics-current trend and future directions. Int J Numer Method Biomed Eng. 2016. doi: 10.1002/cnm.2858. PubMed PMID: 27935265.

77. Wong VM, Wenk JF, Zhang Z, Cheng G, Acevedo-Bolton G, Burger M, Saloner DA, Wallace AW, Guccione JM, Ratcliffe MB. The effect of mitral annuloplasty shape in ischemic mitral regurgitation: a finite element simulation. The Annals of thoracic surgery. 2012;93(3):776-82.

78. Baillargeon B, Costa I, Leach JR, Lee LC, Genet M, Toutain A, Wenk JF, Rausch MK, Rebelo N, Acevedo-Bolton G. Human cardiac function simulator for the optimal design of a novel annuloplasty ring with a sub-valvular element for correction of ischemic mitral regurgitation. Cardiovascular engineering and technology. 2015;6(2):105-16.

79. Rausch MK, Zöllner AM, Genet M, Baillargeon B, Bothe W, Kuhl E. A virtual sizing tool for mitral valve annuloplasty. International journal for numerical methods in biomedical engineering. 2017;33(2).

80. Einstein D, Reinhall P, Nicosia M, Cochran R, Kunzelman K. Dynamic finite element implementation of nonlinear, anisotropic hyperelastic biological membranes. Computer Methods in Biomechanics & Biomedical Engineering. 2003;6(1):33-44.

81. Einstein DR, Kunzelman KS, Reinhall PG, Nicosia MA, Cochran RP. Non-linear fluid-coupled computational model of the mitral valve. J Heart Valve Dis. 2005;14(3):376-85.

82. Kunzelman K, Einstein DR, Cochran R. Fluid–structure interaction models of the mitral valve: function in normal and pathological states. Philosophical Transactions of the Royal Society of London B: Biological Sciences. 2007;362(1484):1393-406.

83. Watton P, Luo X, Yin M, Bernacca G, Wheatley D. Effect of ventricle motion on the dynamic behaviour of chorded mitral valves. Journal of Fluids and Structures. 2008;24(1):58-74.

84. Ma X, Gao H, Griffith BE, Berry C, Luo X. Image-based fluid–structure interaction model of the human mitral valve. Computers & Fluids. 2013;71:417-25.

85. Gao H, Ma X, Qi N, Berry C, Griffith BE, Luo X. A finite strain nonlinear human mitral valve model with fluid-structure interaction. International journal for numerical methods in biomedical engineering. 2014;30(12):1597-613.

86. Toma M, Einstein DR, Bloodworth CH, Cochran RP, Yoganathan AP, Kunzelman KS. Fluid–structure interaction and structural analyses using a comprehensive mitral valve model with 3D chordal structure. International Journal for Numerical Methods in Biomedical Engineering. 2016.

87. Toma M, Jensen MØ, Einstein DR, Yoganathan AP, Cochran RP, Kunzelman KS. Fluid–structure interaction analysis of papillary muscle forces using a comprehensive mitral valve model with 3D chordal structure. Annals of biomedical engineering. 2016;44(4):942-53.

88. Toma M, Bloodworth CH, Pierce EL, Einstein DR, Cochran RP, Yoganathan AP, Kunzelman KS. Fluid-structure interaction analysis of ruptured mitral chordae tendineae. Annals of biomedical engineering. 2017;45(3):619-31.

89. Nash MP, Hunter PJ. Computational mechanics of the heart. Journal of elasticity and the physical science of solids. 2000;61(1-3):113-41.

90. Chen W, Gao H, Luo X, Hill N. Study of cardiovascular function using a coupled left ventricle and systemic circulation model. Journal of biomechanics. 2016;49(12):2445-54.

91. Quarteroni A, Lassila T, Rossi S, Ruiz-Baier R. Integrated Heart—Coupling multiscale and multiphysics models for the simulation of the cardiac function. Computer Methods in Applied Mechanics and Engineering. 2017;314:345-407.

92. Lau K, Díaz-Zuccarini V, Scambler P, Burriesci G. Fluid–structure interaction study of the edge-to-edge repair technique on the mitral valve. Journal of biomechanics. 2011;44(13):2409-17.

93. Votta E, Maisano F, Soncini M, Redaelli A, Montevecchi FM, Alfieri O. 3-D computational analysis of the stress distribution on the leaflets after edge-to-edge repair of mitral regurgitation. Journal of Heart Valve Disease. 2002;11(6):810-22.

94. Dal Pan F, Donzella G, Fucci C, Schreiber M. Structural effects of an innovative surgical technique to repair heart valve defects. Journal of biomechanics. 2005;38(12):2460-71.

95. Avanzini A. A computational procedure for prediction of structural effects of edge-to-edge repair on mitral valve. Journal of biomechanical engineering. 2008;130(3):031015.

96. Mansi T, Voigt I, Georgescu B, Zheng X, Mengue EA, Hackl M, Ionasec RI, Noack T, Seeburger J, Comaniciu D. An integrated framework for finite-element modeling of mitral valve biomechanics from medical images: application to MitralClip intervention planning. Medical image analysis. 2012;16(7):1330-46.

97. Kunzelman K, Reimink MS, Verrier ED, Cochran RP. Replacement of mitral valve posterior chordae tendineae with expanded polytetrafluoroethylene suture: a finite element study. Journal of cardiac surgery. 1996;11(2):136-45.

98. Reimink M, Kunzelman K, Cochran R. The effect of chordal replacement suture length on function and stresses in repaired mitral valves: a finite element study. The Journal of heart valve disease. 1996;5(4):365-75.

99. Rim Y, Laing ST, McPherson DD, Kim H. Mitral valve repair using ePTFE sutures for ruptured mitral chordae tendineae: a computational simulation study. Annals of biomedical engineering. 2014;42(1):139-48.

100. Rim Y, Choi A, McPherson DD, Kim H. Personalized computational modeling of mitral valve prolapse: Virtual leaflet resection. PloS one. 2015;10(6):e0130906.

101. Choi A, McPherson DD, Kim H. Neochordoplasty versus leaflet resection for ruptured mitral chordae treatment: Virtual mitral valve repair. Computers in Biology and Medicine. 2017;90:50-8.

102. Sturla F, Votta E, Onorati F, Pechlivanidis K, Pappalardo OA, Gottin L, Milano AD, Puppini G, Redaelli A, Faggian G. Biomechanical drawbacks of different techniques of mitral neochordal implantation: When an apparently optimal repair can fail. The Journal of thoracic and cardiovascular surgery. 2015;150(5):1303-12. e4.

103. Sturla F, Onorati F, Votta E, Pechlivanidis K, Stevanella M, Milano AD, Puppini G, Mazzucco A, Redaelli A, Faggian G. Is it possible to assess the best mitral valve repair in the individual patient? Preliminary results of a finite element study from magnetic resonance imaging data. The Journal of thoracic and cardiovascular surgery. 2014;148(3):1025-34.

104. Kunzelman KS, Quick DW, Cochran RP. Altered collagen concentration in mitral valve leaflets: biochemical and finite element analysis. The Annals of thoracic surgery. 1998;66(6):S198-S205.

105. Maisano F, Redaelli A, Soncini M, Votta E, Arcobasso L, Alfieri O. An annular prosthesis for the treatment of functional mitral regurgitation: Finite element model analysis of a dog bone–shaped ring prosthesis. The Annals of thoracic surgery. 2005;79(4):1268-75.

106. Votta E, Maisano F, Bolling SF, Alfieri O, Montevecchi FM, Redaelli A. The Geoform disease-specific annuloplasty system: a finite element study. The Annals of thoracic surgery. 2007;84(1):92-101.

107. Xu C, Jassar AS, Nathan DP, Eperjesi TJ, Brinster CJ, Levack MM, Vergnat M, Gorman RC, Gorman JH, Jackson BM. Augmented mitral valve leaflet area decreases leaflet stress: a finite element simulation. The Annals of thoracic surgery. 2012;93(4):1141-5.

108. Morrel WG, Ge L, Zhang Z, Grossi E, Guccione J, Ratcliffe M. Effect of mitral annuloplasty device shape and size on leaflet and myofiber stress following repair of posterior leaflet prolapse: a patient-specific finite element simulation. The Journal of heart valve disease. 2014;23(6):727-34.

109. Choi A, Rim Y, Mun JS, Kim H. A novel finite element-based patient-specific mitral valve repair: virtual ring annuloplasty. Bio-medical materials and engineering. 2014;24(1):341-7.

110. Capelli C, Bosi G, Cerri E, Nordmeyer J, Odenwald T, Bonhoeffer P, Migliavacca F, Taylor AM, Schievano S. Patient-specific simulations of transcatheter aortic valve stent implantation. Medical & biological engineering & computing. 2012;50(2):183-92.

111. Wang Q, Sirois E, Sun W. Patient-specific modeling of biomechanical interaction in transcatheter aortic valve deployment. Journal of Biomechanics. 2012;45(11):1965-71. doi: https://doi.org/10.1016/j.jbiomech.2012.05.008.

112. Wang Q, Kodali S, Primiano C, Sun W. Simulations of transcatheter aortic valve implantation: implications for aortic root rupture. Biomechanics and modeling in mechanobiology. 2015;14(1):29-38.

113. Auricchio F, Conti M, Morganti S, Reali A. Simulation of transcatheter aortic valve implantation: a patient-specific finite element approach. Computer methods in biomechanics and biomedical engineering. 2014;17(12):1347-57.

114. Gunning PS, Vaughan TJ, McNamara LM. Simulation of self expanding transcatheter aortic valve in a realistic aortic root: implications of deployment geometry on leaflet deformation. Annals of biomedical engineering. 2014;42(9):1989-2001.

115. Wang Q, Primiano C, McKay R, Kodali S, Sun W. CT image-based engineering analysis of transcatheter aortic valve replacement. JACC: Cardiovascular Imaging. 2014;7(5):526-8.

116. Gessat M, Hopf R, Pollok T, Russ C, Frauenfelder T, Sündermann SH, Hirsch S, Mazza E, Székely G, Falk V. Image-based mechanical analysis of stent deformation: concept and exemplary implementation for aortic valve stents. IEEE Transactions on Biomedical Engineering. 2013;61(1):4-15.

117. Grbic S, Mansi T, Ionasec R, Voigt I, Houle H, John M, Schoebinger M, Navab N, Comaniciu D, editors. Image-based computational models for TAVI planning: from CT images to implant deployment. International Conference on Medical Image Computing and Computer-Assisted Intervention; 2013: Springer.

118. Sturla F, Ronzoni M, Vitali M, Dimasi A, Vismara R, Preston-Maher G, Burriesci G, Votta E, Redaelli A. Impact of different aortic valve calcification patterns on the outcome of transcatheter aortic valve implantation: a finite element study. Journal of biomechanics. 2016;49(12):2520-30.

119. Xuan Y, Krishnan K, Ye J, Dvir D, Guccione JM, Ge L, Tseng EE. Stent and leaflet stresses in a 26-mm first-generation balloon-expandable transcatheter aortic valve. The Journal of thoracic and cardiovascular surgery. 2017;153(5):1065-73.

120. Xuan Y, Krishnan K, Ye J, Dvir D, Guccione JM, Ge L, Tseng EE. Stent and leaflet stresses in 29-mm second-generation balloon-expandable transcatheter aortic valve. The Annals of thoracic surgery. 2017;104(3):773-81.

121. Morganti S, Brambilla N, Petronio AS, Reali A, Bedogni F, Auricchio F. Prediction of patient-specific post-operative outcomes of TAVI procedure: The impact of the positioning strategy on valve performance. Journal of Biomechanics. 2016;49(12):2513-9. doi: https://doi.org/10.1016/j.jbiomech.2015.10.048.

122. Bailey J, Curzen N, Bressloff NW. Assessing the impact of including leaflets in the simulation of TAVI deployment into a patient-specific aortic root. Computer Methods in Biomechanics and Biomedical Engineering. 2016;19(7):733-44. doi: 10.1080/10255842.2015.1058928.

123. Bailey J, Curzen N, Bressloff NW. The impact of imperfect frame deployment and rotational orientation on stress within the prosthetic leaflets during transcatheter aortic valve implantation. Journal of biomechanics. 2017;53:22-8.

124. Bosi GM, Capelli C, Cheang MH, Delahunty N, Mullen M, Taylor AM, Schievano S. Population-specific material properties of the implantation site for transcatheter aortic valve replacement finite element simulations. Journal of biomechanics. 2018;71:236-44.

125. Schultz C, Rodriguez-Olivares R, Bosmans J, Lefevre T, De Santis G, Bruining N, Collas V, Dezutter T, Bosmans B, Rahhab Z. Patient-specific image-based computer simulation for theprediction of valve morphology and calcium displacement after TAVI with the Medtronic CoreValve and the Edwards SAPIEN valve. EuroIntervention. 2016;11(9):1044-52.

126. Hopf R, Sündermann SH, Born S, Ruiz CE, Van Mieghem NM, De Jaegere PP, Maisano F, Falk V, Mazza E. Postoperative analysis of the mechanical interaction between stent and host tissue in patients after transcatheter aortic valve implantation. Journal of biomechanics. 2017;53:15-21.

127. Bianchi M, Marom G, Ghosh RP, Fernandez HA, Taylor Jr JR, Slepian MJ, Bluestein D. Effect of Balloon-Expandable Transcatheter Aortic Valve Replacement Positioning: A Patient-Specific Numerical Model. Artificial Organs. 2016;40(12):E292-E304. doi: 10.1111/aor.12806.

128. de Jaegere P, De Santis G, Rodriguez-Olivares R, Bosmans J, Bruining N, Dezutter T, Rahhab Z, El Faquir N, Collas V, Bosmans B. Patient-specific computer modeling to predict aortic regurgitation after transcatheter aortic valve replacement. JACC: Cardiovascular Interventions. 2016;9(5):508-12.

129. Bianchi M, Marom G, Ghosh RP, Rotman OM, Parikh P, Gruberg L, Bluestein D. Patient-specific simulation of transcatheter aortic valve replacement: impact of deployment options on paravalvular leakage. Biomechanics and modeling in mechanobiology. 2019;18(2):435-51.

130. Mao W, Wang Q, Kodali S, Sun W. Numerical parametric study of paravalvular leak following a transcatheter aortic valve deployment into a patient-specific aortic root. Journal of biomechanical engineering. 2018;140(10):101007.

131. Lavon K, Marom G, Bianchi M, Halevi R, Hamdan A, Morany A, Raanani E, Bluestein D, Haj-Ali R. Biomechanical modeling of transcatheter aortic valve replacement in a stenotic bicuspid aortic valve: deployments and paravalvular leakage. Medical & biological engineering & computing. 2019:1-15.

132. Brouwer J, Gheorghe L, Nijenhuis VJ, ten Berg JM, Rensing BJ, van der Heyden JA, Swaans MJ. Insight on patient specific computer modeling of transcatheter aortic valve implantation in patients with bicuspid aortic valve disease. Catheterization and Cardiovascular Interventions. 2019;93(6):1097-105.

133. Kopanidis A, Pantos I, Alexopoulos N, Theodorakakos A, Efstathopoulos E, Katritsis D. Aortic flow patterns after simulated implantation of transcatheter aortic valves. Hellenic J Cardiol. 2015;56:418-28.

134. Vahidkhah K, Javani S, Abbasi M, Azadani PN, Tandar A, Dvir D, Azadani AN. Blood stasis on transcatheter valve leaflets and implications for valve-in-valve leaflet thrombosis. The Annals of thoracic surgery. 2017;104(3):751-9.

135. Basri AA, Zuber M, Zakaria MS, Basri EI, Aziz AFA, Ali RM, Tamagawa M, Ahmad KA. The hemodynamic effects of paravalvular leakage using fluid structure interaction; Transcatheter aortic valve implantation patient. Journal of Medical Imaging and Health Informatics. 2016;6(6):1513-8.

136. Mao W, Li K, Caballero A, Sun W. Fully-coupled Fsi Simulation of Bioprosthetic Heart Valve Using Smoothed Particle Hydrodynamics. Cardiology. 2016;134(2):178.

137. Ghosh R, Marom G, Rotman O, Slepian MJ, Prabhakar S, Horner M, Bluestein D. Comparative Fluid-Structure Interaction Analysis of Polymeric Transcatheter and Surgical Aortic Valves' Hemodynamics and Structural Mechanics. Journal of biomechanical engineering. 2018.

138. Kandail HS, Trivedi SD, Shaikh AC, Bajwa TK, Daniel P, Jahangir A, LaDisa Jr JF. Impact of annular and supra-annular CoreValve deployment locations on aortic and coronary artery hemodynamics. Journal of the mechanical behavior of biomedical materials. 2018;86:131-42.

139. Wu W, Pott D, Mazza B, Sironi T, Dordoni E, Chiastra C, Petrini L, Pennati G, Dubini G, Steinseifer U. Fluid–structure interaction model of a percutaneous aortic valve: comparison with an in vitro test and feasibility study in a patient-specific case. Annals of biomedical engineering. 2016;44(2):590-603.

140. Go AS, Mozaffarian D, Roger VL, Benjamin EJ, Berry JD, Blaha MJ, Dai S, Ford ES, Fox CS, Franco S. Heart disease and stroke statistics—2014 update. Circulation. 2013:01. cir. 0000441139.02102. 80.

141. Hughes TJR, Liu WK, Zimmermann TK. Lagrangian-Eulerian finite element formulation for incompressible viscous flows. Computer Methods in Applied Mechanics and Engineering. 1981;29(3):329-49. doi: http://dx.doi.org/10.1016/0045-7825(81)90049-9.

142. Shahriari S, Hassan I, Kadem L, editors. Validation of a Smoothed Particle Hydrodynamics Code for Internal Flow Simulations: Application to Hemodynamics in a Realistic Left Heart Cavity Model. ASME 2010 3rd Joint US-European Fluids Engineering Summer Meeting collocated with 8th International Conference on Nanochannels, Microchannels, and Minichannels; 2010: American Society of Mechanical Engineers.

143. Liu G-R. Meshfree methods: moving beyond the finite element method: Taylor & Francis; 2009.

144. Monaghan JJ. Smoothed particle hydrodynamics. Annual review of astronomy and astrophysics. 1992;30:543-74.

145. Liu M, Liu G. Smoothed particle hydrodynamics (SPH): an overview and recent developments. Archives of computational methods in engineering. 2010;17(1):25-76.

146. Morris JP, Fox PJ, Zhu Y. Modeling low Reynolds number incompressible flows using SPH. Journal of computational physics. 1997;136(1):214-26.

147. Hu XY, Adams NA. A multi-phase SPH method for macroscopic and mesoscopic flows. Journal of Computational Physics. 2006;213(2):844-61.

148. Zhu Y, Fox PJ, Morris JP. A pore-scale numerical model for flow through porous media. International journal for numerical and analytical methods in geomechanics. 1999;23(9):881-904.

149. Shahriari S, Hassan I, Kadem L. Modeling unsteady flow characteristics using smoothed particle hydrodynamics. Applied Mathematical Modelling. 2013;37(3):1431-50.

150. Sinnott M, Cleary PW, Prakash M, editors. An investigation of pulsatile blood flow in a bifurcation artery using a grid-free method. Fifth International Conference on CFD in the Process Industries, CSIRO, Melbourne, Australia; 2006.

151. Yamaguchi T, Ishikawa T, Imai Y, Matsuki N, Xenos M, Deng Y, Bluestein D. Particle-based methods for multiscale modeling of blood flow in the circulation and in devices: challenges and future directions. Annals of biomedical engineering. 2010;38(3):1225-35.

152. Müller M, Schirm S, Teschner M. Interactive blood simulation for virtual surgery based on smoothed particle hydrodynamics. Technology and Health Care. 2004;12(1):25-31.

153. Liu X CM, Duraiswamy N. Fluid–Structure interaction analysis of prosthetic aortic valve using abaqus smoothed particle hydrodynamic (SPH) analysis. ASME emerging technologies' 6th frontiers in biomedical devices conference & exhibition; Irvine, CA2011.

154. Kulp S, Gao M, Zhang S, Qian Z, Voros S, Metaxas D, Axel L, editors. Practical patient-specific cardiac blood flow simulations using SPH. Biomedical Imaging (ISBI), 2013 IEEE 10th International Symposium on; 2013: IEEE.

155. Mao W, Li K, Sun W. Fluid–Structure Interaction Study of Transcatheter Aortic Valve Dynamics Using Smoothed Particle Hydrodynamics. Cardiovascular engineering and technology. 2016;7(4):374-88.

156. Shahriari S, Kadem L, Rogers B, Hassan I. Smoothed particle hydrodynamics method applied to pulsatile flow inside a rigid two-dimensional model of left heart cavity. International journal for numerical methods in biomedical engineering. 2012;28(11):1121-43.

157. Maciá F, Antuono M, González LM, Colagrossi A. Theoretical analysis of the no-slip boundary condition enforcement in SPH methods. Progress of theoretical physics. 2011;125(6):1091-121.

158. Marrone S, Colagrossi A, Antuono M, Colicchio G, Graziani G. An accurate SPH modeling of viscous flows around bodies at low and moderate Reynolds numbers. Journal of Computational Physics. 2013;245:456-75.

159. Violeau D, Issa R. Numerical modelling of complex turbulent free-surface flows with the SPH method: an overview. International Journal for Numerical Methods in Fluids. 2007;53(2):277-304.

160. Monaghan J. A turbulence model for Smoothed Particle Hydrodynamics. European Journal of Mechanics-B/Fluids. 2011;30(4):360-70.

161. Uribe S, Beerbaum P, Sørensen TS, Rasmusson A, Razavi R, Schaeffter T. Four-dimensional (4D) flow of the whole heart and great vessels using real-time respiratory self-gating. Magnetic resonance in medicine. 2009;62(4):984-92.

162. Markl M, Harloff A, Bley TA, Zaitsev M, Jung B, Weigang E, Langer M, Hennig J, Frydrychowicz A. Time-resolved 3D MR velocity mapping at 3T: Improved navigator-gated assessment of vascular anatomy and blood flow. Journal of magnetic resonance imaging. 2007;25(4):824-31.

163. Zheng X, Seo J, Vedula V, Abraham T, Mittal R. Computational modeling and analysis of intracardiac flows in simple models of the left ventricle. European Journal of Mechanics-B/Fluids. 2012;35:31-9.

164. SIMULIA. ABAQUS Analysis user's Manual. Dassault Systemes Simulia Corp, Providence, RI. 2010.

165. Demirdžić I, Perić M. Space conservation law in finite volume calculations of fluid flow. International journal for numerical methods in fluids. 1988;8(9):1037-50.

166. Ferziger JH, Peric M. Computational methods for fluid dynamics: Springer Science & Business Media; 2012.

167. Saber NR, Gosman A, Wood NB, Kilner PJ, Charrier CL, Firmin DN. Computational flow modeling of the left ventricle based on in vivo MRI data: initial experience. Annals of biomedical engineering. 2001;29(4):275-83.

168. Le TB, Sotiropoulos F. Fluid–structure interaction of an aortic heart valve prosthesis driven by an animated anatomic left ventricle. Journal of computational physics. 2013;244:41-62.

169. Seo JH, Vedula V, Abraham T, Mittal R. Multiphysics computational models for cardiac flow and virtual cardiography. International journal for numerical methods in biomedical engineering. 2013;29(8):850-69.

170. Seo JH, Mittal R. Effect of diastolic flow patterns on the function of the left ventricle. Physics of Fluids (1994-present). 2013;25(11):110801.

171. Chnafa C, Mendez S, Nicoud F. Image-based large-eddy simulation in a realistic left heart. Computers & Fluids. 2014;94:173-87.

172. Moosavi M-H, Fatouraee N, Katoozian H, Pashaei A, Camara O, Frangi AF. Numerical simulation of blood flow in the left ventricle and aortic sinus using magnetic resonance imaging and computational fluid dynamics. Computer methods in biomechanics and biomedical engineering. 2014;17(7):740-9.

173. Doost SN, Zhong L, Su B, Morsi YS. The numerical analysis of non-Newtonian blood flow in human patient-specific left ventricle. Computer methods and programs in biomedicine. 2016;127:232-47.

174. Khalafvand S, Zhong L, Ng E. Three-dimensional CFD/MRI modeling reveals that ventricular surgical restoration improves ventricular function by modifying intraventricular blood flow. International journal for numerical methods in biomedical engineering. 2014;30(10):1044-56.

175. Lorenz CH, Walker ES, Morgan VL, Klein SS, Graham TP. Normal human right and left ventricular mass, systolic function, and gender differences by cine magnetic resonance imaging. Journal of Cardiovascular Magnetic Resonance. 1999;1(1):7-21.

176. Kheradvar A, Pedrizzetti G. Vortex formation in the cardiovascular system: Springer Science & Business Media; 2012.

177. Lantz J, Henriksson L, Persson A, Karlsson M, Ebbers T. Patient-Specific Simulation of Cardiac Blood Flow From High-Resolution Computed Tomography. Journal of Biomechanical Engineering. 2016;138(12):121004.

178. Vedula V, George R, Younes L, Mittal R. Hemodynamics in the left atrium and its effect on ventricular flow patterns. Journal of biomechanical engineering. 2015;137(11):111003.

179. Elbaz MS, Calkoen EE, Westenberg JJ, Lelieveldt BP, Roest AA, van der Geest RJ. Vortex flow during early and late left ventricular filling in normal subjects: quantitative characterization using retrospectively-gated 4D flow cardiovascular magnetic resonance and three-dimensional vortex core analysis. Journal of Cardiovascular Magnetic Resonance. 2014;16(1):78.

180. Kim WY, Walker PG, Pedersen EM, Poulsen JK, Oyre S, Houlind K, Yoganathan AP. Left ventricular blood flow patterns in normal subjects: a quantitative analysis by three-dimensional magnetic resonance velocity mapping. Journal of the American College of Cardiology. 1995;26(1):224-38.

181. Fujimoto S, Mohiaddin RH, Parker KH, Gibson DG. Magnetic resonance velocity mapping of normal human transmitral velocity profiles. Heart and vessels. 1995;10(5):236-40.

182. Otto CM. Textbook of clinical echocardiography: Elsevier Health Sciences; 2013.

183. Imanparast A, Fatouraee N, Sharif F. The impact of valve simplifications on left ventricular hemodynamics in a three dimensional simulation based on in vivo MRI data. Journal of biomechanics. 2016;49(9):1482-9.

184. Mihalef V, Ionasec RI, Sharma P, Georgescu B, Voigt I, Suehling M, Comaniciu D. Patient-specific modelling of whole heart anatomy, dynamics and haemodynamics from four-dimensional cardiac CT images. Interface Focus. 2011;1(3):286-96.

185. Frayne R, Steinman DA, Rutt BK, Ethier CR. Accuracy of MR phase contrast velocity measurements for unsteady flow. Journal of Magnetic Resonance Imaging. 1995;5(4):428-31.

186. Lee VS, Spritzer CE, Carroll BA, Pool LG, Bernstein MA, Heinle SK, MacFall JR. Flow quantification using fast cine phase-contrast MR imaging, conventional cine phase-contrast MR imaging, and Doppler sonography: in vitro and in vivo validation. AJR American journal of roentgenology. 1997;169(4):1125-31.

187. Christiansen JP, Karamitsos TD, Myerson SG. Assessment of valvular heart disease by cardiovascular magnetic resonance imaging: a review. Heart, Lung and Circulation. 2011;20(2):73-82.

188. Kilner PJ, Gatehouse PD, Firmin DN. Flow measurement by magnetic resonance: a unique asset worth optimising. Journal of Cardiovascular Magnetic Resonance. 2007;9(4):723-8.

189. Kitajima HD, Sundareswaran KS, Teisseyre TZ, Astary GW, Parks WJ, Skrinjar O, Oshinski JN, Yoganathan AP. Comparison of particle image velocimetry and phase contrast MRI in a patient-specific extracardiac total cavopulmonary connection. Journal of biomechanical engineering. 2008;130(4):041004.

190. Stankovic Z, Allen BD, Garcia J, Jarvis KB, Markl M. 4D flow imaging with MRI. Cardiovascular Diagnosis and Therapy. 2014;4(2):173-92.

191. Guide AB. Version 2016. Dassault Systémes Simulia Corp, Providence, RI. 2016.

192. Colagrossi A, Landrini M. Numerical simulation of interfacial flows by smoothed particle hydrodynamics. Journal of Computational Physics. 2003;191(2):448-75.

193. Adami S. Modeling and Simulation of Multiphase Phenomena with Smoothed Particle Hydrodynamics: Technische Universität München; 2014.

194. Domenichini F, Querzoli G, Cenedese A, Pedrizzetti G. Combined experimental and numerical analysis of the flow structure into the left ventricle. Journal of biomechanics. 2007;40(9):1988-94.

195. Saber NR, Wood NB, Gosman A, Merrifield RD, Yang G-Z, Charrier CL, Gatehouse PD, Firmin DN. Progress towards patient-specific computational flow modeling of the left heart via combination of magnetic resonance imaging with computational fluid dynamics. Annals of biomedical engineering. 2003;31(1):42-52.

196. Marom G. Numerical methods for fluid–structure interaction models of aortic valves. Archives of Computational Methods in Engineering. 2015;22(4):595-620.

197. Vedula V, Seo J-H, Lardo AC, Mittal R. Effect of trabeculae and papillary muscles on the hemodynamics of the left ventricle. Theor Comput Fluid Dyn. 2015;30(1-2):3-21.

198. Charonko JJ, Kumar R, Stewart K, Little WC, Vlachos PP. Vortices formed on the mitral valve tips aid normal left ventricular filling. Annals of biomedical engineering. 2013;41(5):1049-61.

199. Seo JH, Vedula V, Abraham T, Lardo AC, Dawoud F, Luo H, Mittal R. Effect of the mitral valve on diastolic flow patterns. Physics of Fluids. 2014;26(12):121901.

200. Nakamura M, Wada S, Yamaguchi T. Computational analysis of blood flow in an integrated model of the left ventricle and the aorta. Journal of Biomechanical Engineering. 2006;128(6):837-43.

201. Carmody C, Burriesci G, Howard I, Patterson E. An approach to the simulation of fluid–structure interaction in the aortic valve. Journal of biomechanics. 2006;39(1):158-69.

202. Marom G. Numerical methods for fluid–structure interaction models of aortic valves. Archives of Computational Methods in Engineering. 2014:1-26.

203. Monaghan J. Smoothed particle hydrodynamics and its diverse applications. Annual Review of Fluid Mechanics. 2012;44:323-46.

204. Shahriari S. Computational modeling of cardiovascular flows using smoothed particle hydrodynamics: Citeseer; 2011.

205. Ma C, Oka M, Iijima K, editors. A numerical simulation for coupling behavior between smoothed particle hydrodynamics and structural finite element method. 6th International Conference On Marine Structures (Marstruct 2017); 2017; Lisbon, Portugal: CRC Press/Balkema.

206. Hermange C, et al., editor. Development of a coupling strategy between Smoothed Particle Hydrodynamics and Finite Element Method for violent fluid-structure interaction problems. Proceedings of 3rd International Conference on Violent Flows; 2016; Osaka, Japan.

207. Caballero A, Mao W, Liang L, Oshinski J, Primiano C, McKay R, Kodali S, Sun W. Modeling Left Ventricular Blood Flow Using Smoothed Particle Hydrodynamics. Cardiovasc Eng Techn. 2017;8(4):465-79. Epub 2017/07/27. doi: 10.1007/s13239-017-0324-z. PubMed PMID: 28744784; PMCID: PMC5709227.

208. Mao W, Caballero A, McKay R, Primiano C, Sun W. Fully-coupled fluid-structure interaction simulation of the aortic and mitral valves in a realistic 3D left ventricle model. PloS one. 2017;12(9):e0184729.

209. Gasser TC, Ogden RW, Holzapfel GA. Hyperelastic modelling of arterial layers with distributed collagen fibre orientations. Journal of The Royal Society Interface. 2006;3(6):15-35. doi: 10.1098/rsif.2005.0073.

210. Ogden R, editor. Large deformation isotropic elasticity-on the correlation of theory and experiment for incompressible rubberlike solids. Proceedings of the Royal Society of London A: Mathematical, Physical and Engineering Sciences; 1972: The Royal Society.

211. Pham T, Sun W. Material properties of aged human mitral valve leaflets. Journal of Biomedical Materials Research - Part A. 2013. doi: 10.1002/jbm.a.34939.

212. Sun W, Martin C, Pham T. Computational modeling of cardiac valve function and intervention. Annual review of biomedical engineering. 2014;16:53-76.

213. Saikrishnan N, Kumar G, Sawaya FJ, Lerakis S, Yoganathan AP. Accurate Assessment of Aortic Stenosis. Circulation. 2014;129(2):244-53.

214. Chandran KB, Rittgers SE, Yoganathan AP. Biofluid mechanics: the human circulation: CRC press; 2012.

215. Sturla F, Votta E, Stevanella M, Conti CA, Redaelli A. Impact of modeling fluid–structure interaction in the computational analysis of aortic root biomechanics. Medical engineering & physics. 2013;35(12):1721-30.

216. Leyh RG, Schmidtke C, Sievers H-H, Yacoub MH. Opening and closing characteristics of the aortic valve after different types of valve-preserving surgery. Circulation. 1999;100(21):2153-60.

217. He Z, Ritchie J, Grashow JS, Sacks MS, Yoganathan AP. In vitro dynamic strain behavior of the mitral valve posterior leaflet. Journal of biomechanical engineering. 2005;127(3):504-11.

218. He Z, Sacks M, Baijens L, Wanant S, Shah P, Yoganathan A. Effects of papillary muscle position on in-vitro dynamic strain on the porcine mitral valve. The Journal of heart valve disease. 2003;12(4):488-94.

219. Jimenez JH, Soerensen DD, He Z, Ritchie J, Yoganathan AP. Mitral valve function and chordal force distribution using a flexible annulus model: an in vitro study. Annals of biomedical engineering. 2005;33(5):557-66.

220. Chnafa C, Mendez S, Nicoud F. Image-Based Simulations Show Important Flow Fluctuations in a Normal Left Ventricle: What Could be the Implications? Annals of biomedical engineering. 2016;44(11):3346-58.

221. Bavo A, Pouch A, Degroote J, Vierendeels J, Gorman J, Gorman R, Segers P. Patient-specific CFD models for intraventricular flow analysis from 3D ultrasound imaging: Comparison of three clinical cases. Journal of Biomechanics. 2017;50:144-50.

222. Zamorano JL. The ESC textbook of cardiovascular imaging: Dordrecht: Springer; 2010.

223. Lee C-H, Rabbah J-P, Yoganathan AP, Gorman RC, Gorman JH, Sacks MS. On the effects of leaflet microstructure and constitutive model on the closing behavior of the mitral valve. Biomechanics and modeling in mechanobiology. 2015;14(6):1281-302.

224. Rausch MK, Bothe W, Kvitting J-PE, Göktepe S, Miller DC, Kuhl E. In vivo dynamic strains of the ovine anterior mitral valve leaflet. Journal of biomechanics. 2011;44(6):1149-57.

225. Sacks MS, Enomoto Y, Graybill JR, Merryman WD, Zeeshan A, Yoganathan AP, Levy RJ, Gorman RC, Gorman JH. In-vivo dynamic deformation of the mitral valve anterior leaflet. The Annals of thoracic surgery. 2006;82(4):1369-77.

226. Amini R, Eckert CE, Koomalsingh K, McGarvey J, Minakawa M, Gorman JH, Gorman RC, Sacks MS. On the in vivo deformation of the mitral valve anterior leaflet: effects of annular geometry and referential configuration. Annals of biomedical engineering. 2012;40(7):1455-67.

227. Sacks MS, He Z, Baijens L, Wanant S, Shah P, Sugimoto H, Yoganathan A. Surface strains in the anterior leaflet of the functioning mitral valve. Annals of biomedical engineering. 2002;30(10):1281-90.

228. Jimenez JH, Liou SW, Padala M, He Z, Sacks M, Gorman RC, Gorman JH, Yoganathan AP. A saddle-shaped annulus reduces systolic strain on the central region of the mitral valve anterior leaflet. The Journal of thoracic and cardiovascular surgery. 2007;134(6):1562-8.

229. Padala M, Hutchison RA, Croft LR, Jimenez JH, Gorman RC, Gorman JH, Sacks MS, Yoganathan AP. Saddle shape of the mitral annulus reduces systolic strains on the P2

segment of the posterior mitral leaflet. The Annals of thoracic surgery. 2009;88(5):1499-504.

230. Dahl SK, Thomassen E, Hellevik LR, Skallerud B. Impact of pulmonary venous locations on the intra-atrial flow and the mitral valve plane velocity profile. Cardiovascular Engineering and Technology. 2012;3(3):269-81.

231. Schenkel T, Malve M, Reik M, Markl M, Jung B, Oertel H. MRI-based CFD analysis of flow in a human left ventricle: methodology and application to a healthy heart. Annals of biomedical engineering. 2009;37(3):503-15.

232. Gabbay U, Yosefy C. The underlying causes of chordae tendinae rupture: a systematic review. International journal of cardiology. 2010;143(2):113-8.

233. Grande-Allen KJ, Ratliff NB, Griffin B, Cosgrove 3rd D, Vesely I. Case report: outer sheath rupture may precede complete chordal rupture in fibrotic mitral valve disease. The Journal of heart valve disease. 2001;10(1):90-3.

234. Khodaei S, Fatouraee N, Nabaei M. Numerical simulation of mitral valve prolapse considering the effect of left ventricle. Mathematical biosciences. 2017;285:75-80.

235. Castillo JG, Anyanwu AC, El-Eshmawi A, Adams DH. All anterior and bileaflet mitral valve prolapses are repairable in the modern era of reconstructive surgery. European Journal of Cardio-Thoracic Surgery. 2013;45(1):139-45.

236. Hayek E, Gring CN, Griffin BP. Mitral valve prolapse. The Lancet. 2005;365(9458):507-18.

237. Geis N, Raake P, Mereles D, Chorianopoulos E, Szabo G, Katus HA, Bekeredjian R, Pleger ST. Percutaneous repair of severe mitral valve regurgitation secondary to chordae rupture in octogenarians using MitraClip. Journal of interventional cardiology. 2017.

238. Mokadam NA, Stout KK, Verrier ED. Management of acute regurgitation in left-sided cardiac valves. Texas Heart Institute Journal. 2011;38(1):9.

239. Patel H, Desai M, Tuzcu EM, Griffin B, Kapadia S. Pulmonary hypertension in mitral regurgitation. Journal of the American Heart Association. 2014;3(4):e000748.

240. Rodriguez D. Left Ventricular Pressure-Volume Analysis: an example of function assessment on a sheep: Université Paris Sud; 2015.

241. Rimehaug AE, Lyng O, Nordhaug DO, Løvstakken L, Aadahl P, Kirkeby-Garstad I. Cardiac power integral: a new method for monitoring cardiovascular performance. Physiological reports. 2013;1(6):e00159.

242. Kameyama T, Asanoi H, Ishizaka S, Yamanishi K, Fujita M, Sasayama S. Energy conversion efficiency in human left ventricle. Circulation. 1992;85(3):988-96.

243. Nishimura RA, Otto CM, Bonow RO, Carabello BA, Erwin JP, Fleisher LA, Jneid H, Mack MJ, McLeod CJ, O'gara PT. 2017 AHA/ACC focused update of the 2014 AHA/ACC guideline for the management of patients with valvular heart disease: a report of the American College of Cardiology/American Heart Association Task Force on Clinical Practice Guidelines. Circulation. 2017;135(25):e1159-e95.

244. Torigoe T, Sakaguchi H, Kitano M, Kurosaki K-i, Shiraishi I, Kagizaki K, Ichikawa H, Yagihara T. Clinical characteristics of acute mitral regurgitation due to ruptured chordae tendineae in infancy—experience at a single institution. European journal of pediatrics. 2012;171(2):259-65.

245. Kunzelman K, Cochran K. Mechanical properties of basal and marginal mitral valve chordae tendineae. ASAIO Journal. 1990;36(3):M405-7.

246. Zuo K, Pham T, Li K, Martin C, He Z, Sun W. Characterization of biomechanical properties of aged human and ovine mitral valve chordae tendineae. Journal of the mechanical behavior of biomedical materials. 2016;62:607-18.

247. Sedransk KL, Grande-Allen KJ, Vesely I. Failure mechanics of mitral valve chordae tendineae. The Journal of heart valve disease. 2002;11(5):644-50.

248. Jimenez JH, Soerensen DD, He Z, Ritchie J, Yoganathan AP. Effects of papillary muscle position on chordal force distribution: an in-vitro study. J Heart Valve Dis. 2005;14(3):295-302.

249. Wei L, Jiang L, Li Y. The use of artificial chordae in mitral valve repair. Journal of cardiac surgery. 2017.

250. Wunderlich NC, Beigel R, Ho SY, Nietlispach F, Cheng R, Siegel RJ. Imaging for Mitral Interventions: Methods and Efficacy. JACC: Cardiovascular Imaging. 2018;11(6):872-901.

251. Reimink MS, Kunzelman KS, Verrier ED, Cochran RP. The Effect of Anterior Chordal Replacement on Mitral Valve Function and Stresses: A Finite Element Study. Asaio Journal. 1995;41(3):M754-M62.

252. Choi A, McPherson DD, Kim H. Biomechanical evaluation of the pathophysiologic developmental mechanisms of mitral valve prolapse: effect of valvular morphologic alteration. Medical & biological engineering & computing. 2016;54(5):799-809.

253. Rausch MK, Tibayan FA, Miller DC, Kuhl E. Evidence of adaptive mitral leaflet growth. journal of the mechanical behavior of biomedical materials. 2012;15:208-17.

254. Stephens EH, Nguyen TC, Itoh A, Ingels Jr NB, Miller DC, Grande-Allen KJ. The effects of mitral regurgitation alone are sufficient for leaflet remodeling. Circulation. 2008;118(14 0):S243.

255. Gosain AK, Song L-S, Santoro T, Weihrauch D, Bosi BO, Corrao MA, Chilian WM. Effects of transforming growth factor-beta and mechanical strain on osteoblast cell counts: an in vitro model for distraction osteogenesis. Plastic and reconstructive surgery. 2000;105(1):130-6; discussion 7-9.

256. De Filippo RE, Atala A. Stretch and growth: the molecular and physiologic influences of tissue expansion. Plastic and reconstructive surgery. 2002;109(7):2450-62.

257. Davis NP, Han H-C, Wayman B, Vito R. Sustained axial loading lengthens arteries in organ culture. Annals of biomedical engineering. 2005;33(7):867-77.

258. Little SH. Quantifying mitral valve regurgitation: new solutions from the 3rd dimension. Journal of the American Society of Echocardiography. 2010;23(1):9-12.

259. Ginghina C. The Coandă effect in cardiology. Journal of Cardiovascular Medicine. 2007;8(6):411-3.

260. Le Tourneau T, Messika-Zeitoun D, Russo A, Detaint D, Topilsky Y, Mahoney DW, Suri R, Enriquez-Sarano M. Impact of left atrial volume on clinical outcome in

organic mitral regurgitation. Journal of the American College of Cardiology. 2010;56(7):570-8.

261. Imasaka K-i, Tomita Y, Tanoue Y, Tominaga R, Tayama E, Onitsuka H, Ueda T. Early mitral valve surgery for chronic severe mitral regurgitation optimizes left ventricular performance and left ventricular mass regression. The Journal of thoracic and cardiovascular surgery. 2013;146(1):61-6.

262. Bavo AM, Rocatello G, Iannaccone F, Degroote J, Vierendeels J, Segers P. Fluid-structure interaction simulation of prosthetic aortic valves: comparison between immersed boundary and arbitrary Lagrangian-Eulerian techniques for the mesh representation. PloS one. 2016;11(4):e0154517.

263. Shahriari S, Kadem L. Smoothed Particle Hydrodynamics Method and Its Applications to Cardiovascular Flow Modeling. Numerical Methods and Advanced Simulation in Biomechanics and Biological Processes: Elsevier; 2018. p. 203-19.

264. Toma M. The Emerging Use of SPH In Biomedical Applications.

265. Liang L, Kong F, Martin C, Pham T, Wang Q, Duncan J, Sun W. Machine learning–based 3-D geometry reconstruction and modeling of aortic valve deformation using 3-D computed tomography images. International journal for numerical methods in biomedical engineering. 2017;33(5):e2827.

266. Icardo JM, Colvee E, Revuelta JM. Structural analysis of chordae tendineae in degenerative disease of the mitral valve. International journal of cardiology. 2013;167(4):1603-9.

267. Goliasch G, Bartko PE, Pavo N, Neuhold S, Wurm R, Mascherbauer J, Lang IM, Strunk G, Hülsmann M. Refining the prognostic impact of functional mitral regurgitation in chronic heart failure. European heart journal. 2017;39(1):39-46.

268. Rossi A, Dini FL, Faggiano P, Cicoira M, Frattini S, Simioniuc A, Gullace M, Ghio S, Enriquez-Sarano M, Temporelli PL. Independent prognostic value of functional mitral regurgitation in patients with heart failure. A quantitative analysis of 1256 patients with ischaemic and non-ischaemic dilated cardiomyopathy. Heart. 2011;97(20):1675-80.

269. Iung B. Management of ischaemic mitral regurgitation. Heart. 2003;89(4):459-64. PubMed PMID: PMC1769268.

270. Piérard LA, Carabello BA. Ischaemic mitral regurgitation: pathophysiology, outcomes and the conundrum of treatment2010 2010-12-01 14:02:53.

271. Acker MA, Parides MK, Perrault LP, Moskowitz AJ, Gelijns AC, Voisine P, Smith PK, Hung JW, Blackstone EH, Puskas JD, Argenziano M, Gammie JS, Mack M, Ascheim DD, Bagiella E, Moquete EG, Ferguson TB, Horvath KA, Geller NL, Miller MA, Woo YJ, D'Alessandro DA, Ailawadi G, Dagenais F, Gardner TJ, O'Gara PT, Michler RE, Kron IL. Mitral-Valve Repair versus Replacement for Severe Ischemic Mitral Regurgitation. New England Journal of Medicine. 2014;370(1):23-32. doi: 10.1056/NEJMoa1312808. PubMed PMID: 24245543.

272. Goldstein D, Moskowitz AJ, Gelijns AC, Ailawadi G, Parides MK, Perrault LP, Hung JW, Voisine P, Dagenais F, Gillinov AM, Thourani V, Argenziano M, Gammie JS, Mack M, Demers P, Atluri P, Rose EA, O'Sullivan K, Williams DL, Bagiella E, Michler RE, Weisel RD, Miller MA, Geller NL, Taddei-Peters WC, Smith PK, Moquete E, Overbey JR, Kron IL, O'Gara PT, Acker MA. Two-Year Outcomes of Surgical Treatment of Severe Ischemic Mitral Regurgitation. New England Journal of Medicine. 2016;374(4):344-53. doi: 10.1056/NEJMoa1512913. PubMed PMID: 26550689.

273. McGee EC, Gillinov AM, Blackstone EH, Rajeswaran J, Cohen G, Najam F, Shiota T, Sabik JF, Lytle BW, McCarthy PM, Cosgrove DM. Recurrent mitral regurgitation after annuloplasty for functional ischemic mitral regurgitation. J Thorac Cardiovasc Surg. 2004;128(6):916-24. Epub 2004/12/02. doi: 10.1016/j.jtcvs.2004.07.037. PubMed PMID: 15573077.

274. Chatzistergiou KT, Papanastasiou CA, Kokkinidis DG, Ziakas A, Karvounis H, Karamitsos TD. MitraClip device for patients with functional mitral valve regurgitation: a systematic review. Hellenic Journal of Cardiology. 2019.

275. Glower DD. Surgical Approaches to Mitral Regurgitation. Journal of the American College of Cardiology. 2012;60(15):1315-22. doi: http://dx.doi.org/10.1016/j.jacc.2011.11.081.

276. Acker MA, Parides MK, Perrault LP, Moskowitz AJ, Gelijns AC, Voisine P, Smith PK, Hung JW, Blackstone EH, Puskas JD, Argenziano M, Gammie JS, Mack M, Ascheim DD, Bagiella E, Moquete EG, Ferguson TB, Horvath KA, Geller NL, Miller MA, Woo YJ, D'Alessandro DA, Ailawadi G, Dagenais F, Gardner TJ, O'Gara PT, Michler RE, Kron IL. Mitral-Valve Repair versus Replacement for Severe Ischemic Mitral Regurgitation. New England Journal of Medicine. 2014;370(1):23-32. doi: doi:10.1056/NEJMoa1312808. PubMed PMID: 24245543.

277. Nicolini F, Agostinelli A, Vezzani A, Molardi A, Benassi F, Gallingani A, Romano G, Gherli T. Surgical treatment for functional ischemic mitral regurgitation: current options and future trends. Acta bio-medica : Atenei Parmensis. 2015;86(1):17-26. Epub 2015/05/08. PubMed PMID: 25948023.

278. de Oliveira JMF, Antunes MJ. Mitral valve repair: better than replacement. Heart. 2006;92(2):275-81. doi: 10.1136/hrt.2005.076208. PubMed PMID: PMC1860778.

279. Bothe W, Kvitting JP, Swanson JC, Goktepe S, Vo KN, Ingels NB, Miller DC. How do annuloplasty rings affect mitral leaflet dynamic motion? European journal of cardio-thoracic surgery : official journal of the European Association for Cardio-thoracic Surgery. 2010;38(3):340-9. Epub 2010/03/26. doi: 10.1016/j.ejcts.2010.02.011. PubMed PMID: 20335042; PMCID: Pmc2913157.

280. Jensen MO, Jensen H, Smerup M, Levine RA, Yoganathan AP, Nygaard H, Hasenkam JM, Nielsen SL. Saddle-shaped mitral valve annuloplasty rings experience lower forces compared with flat rings. Circulation. 2008;118(14 Suppl):S250-5. Epub 2008/10/10. doi: 10.1161/circulationaha.107.746776. PubMed PMID: 18824763.

281. Laing G, Dupont PE. Beating-heart Mitral Valve Chordal Replacement. Conference Proceedings. 2011;2011:2476-9. doi: 10.1109/IEMBS.2011.6090687. PubMed PMID: PMC3294288.

282. Choi A, Rim Y, Mun JS, Kim H. A novel finite element-based patient-specific mitral valve repair: virtual ring annuloplasty. Bio-medical materials and engineering. 2014;24(1):341-7. Epub 2013/11/12. doi: 10.3233/bme-130816. PubMed PMID: 24211915; PMCID: Pmc4044101.

283. Stevanella M, Maffessanti F, Conti C, Votta E, Arnoldi A, Lombardi M, Parodi O, Caiani E, Redaelli A. Mitral Valve Patient-Specific Finite Element Modeling from Cardiac MRI: Application to an Annuloplasty Procedure. Cardiovasc Eng Tech. 2011;2(2):66-76. doi: 10.1007/s13239-010-0032-4.

284. Mansi T, Voigt I, Georgescu B, Zheng X, Mengue EA, Hackl M, Ionasec RI, Noack T, Seeburger J, Comaniciu D. An integrated framework for finite-element modeling of mitral valve biomechanics from medical images: application to MitralClip intervention planning. Medical image analysis. 2012;16(7):1330-46. Epub 2012/07/07. doi: 10.1016/j.media.2012.05.009. PubMed PMID: 22766456.

285. Wang Q, Sun W. Finite element modeling of mitral valve dynamic deformation using patient-specific multi-slices computed tomography scans. Ann Biomed Eng. 2013;41(1):142-53. doi: 10.1007/s10439-012-0620-6. PubMed PMID: 22805982.

286. Lee C-H, Oomen PJA, Rabbah JP, Yoganathan A, Gorman RC, Gorman JH, Amini R, Sacks MS. A High-Fidelity and Micro-anatomically Accurate 3D Finite Element Model for Simulations of Functional Mitral Valve. In: Ourselin S, Rueckert D, Smith N, editors. Functional Imaging and Modeling of the Heart: 7th International Conference, FIMH 2013, London, UK, June 20-22, 2013 Proceedings. Berlin, Heidelberg: Springer Berlin Heidelberg; 2013. p. 416-24.

287. Pham T, Kong F, Martin C, Wang Q, Primiano C, McKay R, Elefteriades J, Sun W. Finite Element Analysis of Patient-Specific Mitral Valve with Mitral Regurgitation. Cardiovascular engineering and technology. 2017;8(1):3-16.

288. Holzapfel GA, Gasser TC, Ogden RW. A New Constitutive Framework for Arterial Wall Mechanics and a Comparative Study of Material Models. Journal of elasticity and the physical science of solids. 2000;61(1):1-48. doi: 10.1023/a:1010835316564.

289. Ogden RW. Large Deformation Isotropic Elasticity - On the Correlation of Theory and Experiment for Incompressible Rubberlike Solids. Proceedings of the Royal Society of London A Mathematical and Physical Sciences. 1972;326(1567):565-84. doi: 10.1098/rspa.1972.0026.

290. Liang L, Kong F, Martin C, Pham T, Wang Q, Duncan J, Sun W. Machine learning–based 3-D geometry reconstruction and modeling of aortic valve deformation using 3-D computed tomography images. International journal for numerical methods in biomedical engineering. 2017;33(5).

291. Rushmer RF, Finlayson BL, Nash AA. Movements of the mitral valve. Circulation research. 1956;4(3):337-42. Epub 1956/05/01. PubMed PMID: 13317029.

292. Yellin EL, Peskin C, Yoran C, Koenigsberg M, Matsumoto M, Laniado S, McQueen D, Shore D, Frater RW. Mechanisms of mitral valve motion during diastole. American Journal of Physiology - Heart and Circulatory Physiology. 1981;241(3):H389.

293. Wang Q, Primiano C, Sun W. Can isolated annular dilatation cause significant ischemic mitral regurgitation? Another look at the causative mechanisms. Journal of biomechanics. 2014;47(8):1792-9.

294. Jimenez JH, Soerensen DD, He Z, He S, Yoganathan AP. Effects of a saddle shaped annulus on mitral valve function and chordal force distribution: an in vitro study. Ann Biomed Eng. 2003;31(10):1171-81. Epub 2003/12/03. PubMed PMID: 14649491.

295. Jimenez JH, Soerensen DD, He Z, Ritchie J, Yoganathan AP. Mitral valve function and chordal force distribution using a flexible annulus model: an in vitro study. Ann Biomed Eng. 2005;33(5):557-66. Epub 2005/06/29. PubMed PMID: 15981857.

296. Mansi T, Voigt I, Assoumou Mengue E, Ionasec R, Georgescu B, Noack T, Seeburger J, Comaniciu D. Towards patient-specific finite-element simulation of MitralClip procedure. Medical image computing and computer-assisted intervention : MICCAI International Conference on Medical Image Computing and Computer-Assisted Intervention. 2011;14(Pt 1):452-9. Epub 2011/10/19. PubMed PMID: 22003649.

297. Little SH. Is it Really Getting Easier to Assess Mitral Regurgitation Using the Proximal Isovelocity Surface Area? Journal of the American Society of Echocardiography. 2012;25(8):824-6. doi: 10.1016/j.echo.2012.06.019.

298. Krieger EV, Lee J, Branch KR, Hamilton-Craig C. Quantitation of mitral regurgitation with cardiac magnetic resonance imaging: a systematic review. Heart. 2016;102(23):1864-70.

299. Krog ØE, Elster AC, editors. Fast gpu-based fluid simulations using sph. International Workshop on Applied Parallel Computing; 2010: Springer.

300. Horton A, Wittek A, Joldes GR, Miller K. A meshless Total Lagrangian explicit dynamics algorithm for surgical simulation. International Journal for Numerical Methods in Biomedical Engineering. 2010;26(8):977-98.

301. Savic V, Pozzoli A, Gülmez G, Demir H, Batinkov N, Kuwata S, Weber A, Vogel R, Tanner F, Zuber M. Transcatheter mitral valve chord repair. Annals of cardiothoracic surgery. 2018;7(6):731.

302. Colli A, Manzan E, Aidietis A, Rucinskas K, Bizzotto E, Besola L, Pradegan N, Pittarello D, Janusauskas V, Zakarkaite D. An early European experience with transapical off-pump mitral valve repair with NeoChord implantation. European Journal of Cardio-Thoracic Surgery. 2018.

303. Jensen H, Jensen MO, Waziri F, Honge JL, Sloth E, Fenger-Gron M, Nielsen SL. Transapical neochord implantation: Is tension of artificial chordae tendineae dependent on

the insertion site? The Journal of thoracic and cardiovascular surgery. 2014;148(1):138-43.

304. Gaidulis G, Votta E, Selmi M, Aidietiene S, Aidietis A, Kacianauskas R. Numerical simulation of transapical off-pump mitral valve repair with neochordae implantation. Technol Health Care. 2018;26(S2):635-45. Epub 2018/05/31. doi: 10.3233/THC-182510. PubMed PMID: 29843286.

305. Colli A, Zucchetta F, Torregrossa G, Manzan E, Bizzotto E, Besola L, Bellu R, Sarais C, Pittarello D, Gerosa G. Transapical off-pump mitral valve repair with Neochord Implantation (TOP-MINI): step-by-step guide. Annals of cardiothoracic surgery. 2015;4(3):295.

306. Caimmi PP, Sabbatini M, Fusaro L, Borrone A, Cannas M. A study of the mechanical properties of ePTFE suture used as artificial mitral chordae. Journal of cardiac surgery. 2016;31(8):498-502.

307. NeoChord I. Instructions for use: NeoChord DS1000 System 2018. Available from: https://neochord.com/wp-content/uploads/2019/02/700010-002_Rev_5_IFU_pc_eng.pdf.

308. Gammie JS, Bartus K, Gackowski A, D'Ambra MN, Szymanski P, Bilewska A, Kusmierczyk M, Kapelak B, Rzucidlo-Resil J, Moat N. Beating-heart mitral valve repair using a novel ePTFE cordal implantation device: a prospective trial. Journal of the American College of Cardiology. 2018;71(1):25-36.

309. Gammie JS, Wilson P, Bartus K, Gackowski A, Hung J, D'Ambra MN, Kolsut P, Bittle GJ, Szymanski P, Sadowski J. Transapical beating-heart mitral valve repair with an expanded polytetrafluoroethylene cordal implantation device: initial clinical experience. Circulation. 2016;134(3):189-97.

310. Colli A, Adams D, Fiocco A, Pradegan N, Longinotti L, Nadali M, Pandis D, Gerosa G. Transapical NeoChord mitral valve repair. Annals of cardiothoracic surgery. 2018;7(6):812.

311. Guy TS, Hill AC. Mitral valve prolapse. Annual review of medicine. 2012;63:277-92.

312. Sturla F, Onorati F, Votta E, Stevanella M, Milano AD, Pechlivanidis K, Puppini G, Redaelli A, Faggian G. Repair of mitral valve prolapse through ePTFE neochordae: a finite element approach from CMR. Biomedical Technology: Springer; 2015. p. 117-28.

313. Quick DW, Kunzelman KS, Kneebone JM, Cochran RP. Collagen synthesis is upregulated in mitral valves subjected to altered stress. ASAIO journal (American Society for Artificial Internal Organs: 1992). 1997;43(3):181-6.

314. Stephens EH, Nguyen TC, Itoh A, Ingels Jr NB, Miller DC, Grande-Allen KJ. The effects of mitral regurgitation alone are sufficient for leaflet remodeling. Circulation. 2008;118(14_suppl_1):S243-S9.

315. Weber A, Hurni S, Vandenberghe S, Wahl A, Aymard T, Vogel R, Carrel T. Ideal site for ventricular anchoring of artificial chordae in mitral regurgitation. Elsevier; 2012.

316. Colli A, Bizzotto E, Manzan E, Besola L, Pradegan N, Bellu R, Pittarello D, Gerosa G. Patient-specific ventricular access site selection for the NeoChord mitral valve repair procedure. The Annals of thoracic surgery. 2017;104(2):e199-e202.

317. Seeburger J, Rinaldi M, Nielsen SL, Salizzoni S, Lange R, Schoenburg M, Alfieri O, Borger MA, Mohr FW, Aidietis A. Off-pump transapical implantation of artificial neo-chordae to correct mitral regurgitation: the TACT Trial (Transapical Artificial Chordae Tendinae) proof of concept. Journal of the American College of Cardiology. 2014;63(9):914-9.

318. Colli A, Gerosa G. Letter by Colli and Gerosa Regarding Article,"Transapical Beating-Heart Mitral Valve Repair With an Expanded Polytetrafluoroethylene Cordal Implantation Device: Initial Clinical Experience". Circulation. 2017;135(3):e16-e7.

319. Grinberg D, Cottinet PJ, Thivolet S, Audigier D, Capsal JF, Le MQ, Obadia JF. Measuring chordae tension during transapical neochordae implantation: Toward understanding objective consequences of mitral valve repair. J Thorac Cardiovasc Surg. 2019;158(3):746-55. Epub 2018/11/21. doi: 10.1016/j.jtcvs.2018.10.029. PubMed PMID: 30454983.

320. Askov JB, Honge J, Nygaard H, Hasenkam JM, Nielsen SL, Jensen M. Papillary muscle force transducer for measurement in vivo. Cardiovascular Engineering and Technology. 2011;2(3):196-202.

321. Askov JB, Honge JL, Jensen MO, Nygaard H, Hasenkam JM, Nielsen SL. Significance of force transfer in mitral valve–left ventricular interaction: In vivo assessment. The Journal of thoracic and cardiovascular surgery. 2013;145(6):1635-41. e1.

322. Heuts S, Kawczynski M, Olsthoorn JR, Sardari NP. Late rupture of transapically beating heart implanted neochords. The Journal of thoracic and cardiovascular surgery. 2018.

323. David TE, Armstrong S, Ivanov J. Chordal replacement with polytetrafluoroethylene sutures for mitral valve repair: a 25-year experience. The Journal of thoracic and cardiovascular surgery. 2013;145(6):1563-9.

324. Grinberg D, Adamou NK, Pozzi M, Obadia J-F. Artificial mitral chordae: When length matters. The Journal of thoracic and cardiovascular surgery. 2019;157(2):e23.

325. Kassem S, Ricciardi G, Salvi L, Alimento M. Late left ventricular rupture as a complication of NeoChord implantation for mitral valve repair. The Journal of thoracic and cardiovascular surgery. 2018;156(1):e1.

326. Castillo JG, Anyanwu AC, El-Eshmawi A, Gordon RE, Adams DH. Early rupture of an expanded polytetrafluoroethylene neochord after complex mitral valve repair: an electron microscopic analysis. The Journal of thoracic and cardiovascular surgery. 2013;145(3):e29-e31.

327. Instructions for Use for GORE-TEX Suture [2/1/2019]. Available from: https://www.goremedical.com/products/suture---ifu/instructions.

328. Komeda M, Glasson JR, Bolger AF, Daughters II GT, Ingels Jr NB, Miller DC. Papillary muscle–left ventricular wall "complex". The Journal of thoracic and cardiovascular surgery. 1997;113(2):292-301.

329. Colli A, Manzan E, Rucinskas K, Janusauskas V, Zucchetta F, Zakarkaitė D, Aidietis A, Gerosa G. Acute safety and efficacy of the NeoChord procedure. Interactive cardiovascular and thoracic surgery. 2015;20(5):575-81.

330. Lansac E, Lim KH, Shomura Y, Goetz WA, Lim HS, Rice NT, Saber H, Duran CM. Dynamic balance of the aortomitral junction. The Journal of thoracic and cardiovascular surgery. 2002;123(5):911-8.

331. Nombela-Franco L, Ribeiro HB, Urena M, Allende R, Amat-Santos I, DeLarochellière R, Dumont E, Doyle D, DeLarochellière H, Laflamme J. Significant mitral regurgitation left untreated at the time of aortic valve replacement: a comprehensive review of a frequent entity in the transcatheter aortic valve replacement era. Journal of the American College of Cardiology. 2014;63(24):2643-58.

332. Barreiro CJ, Patel ND, Fitton TP, Williams JA, Bonde PN, Chan V, Alejo DE, Gott VL, Baumgartner WA. Aortic valve replacement and concomitant mitral valve regurgitation in the elderly: impact on survival and functional outcome. Circulation. 2005;112(9_supplement):I-443-I-7.

333. Sannino A, Losi MA, Schiattarella GG, Gargiulo G, Perrino C, Stabile E, Toscano E, Giugliano G, Brevetti L, Franzone A. Meta-analysis of mortality outcomes and mitral regurgitation evolution in 4,839 patients having transcatheter aortic valve implantation for severe aortic stenosis. The American journal of cardiology. 2014;114(6):875-82.

334. Malaisrie SC, Hodson RW, McAndrew TC, Davidson C, Swanson J, Hahn RT, Pibarot P, Jaber WA, Quader N, Zajarias A, Svensson L, George I, Trento A, Thourani VH, Szeto WY, Dewey T, Smith CR, Leon MB, Webb JG. Outcomes after Transcatheter and Surgical Aortic Valve Replacement in Intermediate Risk Patients with Preoperative Mitral Regurgitation: Analysis of PARTNER II Randomized Cohort. Structural Heart. 2018;2(4):336-43. doi: 10.1080/24748706.2018.1475781.

335. Sannino A, Grayburn PA. Mitral regurgitation in patients with severe aortic stenosis: diagnosis and management. Heart. 2018;104(1):16-22.

336. Egron S, Fujita B, Gullón L, Pott D, Schmitz-Rode T, Ensminger S, Steinseifer U. Radial Force: An Underestimated Parameter in Oversizing Transcatheter Aortic Valve Replacement ProsthesesIn Vitro Analysis with Five Commercialized Valves. Asaio Journal. 2018;64(4):536-43.

337. Nombela-Franco L, Eltchaninoff H, Zahn R, Testa L, Leon MB, Trillo-Nouche R, D´Onofrio A, Smith CR, Webb J, Bleiziffer S, De Chiara B, Gilard M, Tamburino C, Bedogni F, Barbanti M, Salizzoni S, García del Blanco B, Sabaté M, Moreo A, Fernández C, Ribeiro HB, Amat-Santos I, Urena M, Allende R, García E, Macaya C, Dumont E, Pibarot P, Rodés-Cabau J. Clinical impact and evolution of mitral regurgitation following transcatheter aortic valve replacement: a meta-analysis. Heart. 2015;101(17):1395. doi: 10.1136/heartjnl-2014-307120.

338. Unger P, Dedobbeleer C, Eynden FV, Lancellotti P. Mitral regurgitation after transcatheter aortic valve replacement: does the prosthesis matter? International journal of cardiology. 2013;168(2):1706-9.

339. Giordana F, Capriolo M, Frea S, Marra WG, Giorgi M, Bergamasco L, Omedè PL, Sheiban I, D'Amico M, Bovolo V. Impact of TAVI on mitral regurgitation: a prospective echocardiographic study. Echocardiography. 2013;30(3):250-7.

340. Almasood A, Al Ahmari S, El-shurafa H, Alotaibi M, AlAbdallah M, Al-Amri H. The change in mitral regurgitation severity after trans-catheter aortic valve implantation. Journal of the Saudi Heart Association. 2015;27(1):10-7.

341. de Jaegere P, Rocatello G, Prendergast BD, de Backer O, Van Mieghem NM, Rajani R. Patient-specific computer simulation for transcatheter cardiac interventions: what a clinician needs to know. Heart. 2019;105(Suppl 2):s21-s7. doi: 10.1136/heartjnl-2018-313514.

342. Caballero A, Sulejmani F, Martin C, Pham T, Sun W. Evaluation of transcatheter heart valve biomaterials: biomechanical characterization of bovine and porcine pericardium. Journal of the Mechanical Behavior of Biomedical Materials. 2017;75:486-94.

343. Sulejmani F, Caballero A, Martin C, Pham T, Sun W. Evaluation of transcatheter heart valve biomaterials: Computational modeling using bovine and porcine pericardium. Journal of the Mechanical Behavior of Biomedical Materials. 2019;97:159-70. doi: https://doi.org/10.1016/j.jmbbm.2019.05.020.

344. Tzamtzis S, Viquerat J, Yap J, Mullen MJ, Burriesci G. Numerical analysis of the radial force produced by the Medtronic-CoreValve and Edwards-SAPIEN after transcatheter aortic valve implantation (TAVI). Medical Engineering & Physics. 2013;35(1):125-30. doi: https://doi.org/10.1016/j.medengphy.2012.04.009.

345. Dvir D, Lavi I, Eltchaninoff H, Himbert D, Almagor Y, Descoutures F, Vahanian A, Tron C, Cribier A, Kornowski R. Multicenter Evaluation of Edwards SAPIEN Positioning During Transcatheter Aortic Valve Implantation With Correlates for Device Movement During Final Deployment. JACC: Cardiovascular Interventions. 2012;5(5):563-70. doi: 10.1016/j.jcin.2012.03.005.

346. Sun W, Li K, Sirois E. Simulated elliptical bioprosthetic valve deformation: Implications for asymmetric transcatheter valve deployment. Journal of Biomechanics. 2010;43(16):3085-90. doi: https://doi.org/10.1016/j.jbiomech.2010.08.010.

347. LLC MC. Medtronic CoreValve system Instructions for Use 2017. Available from: https://www.accessdata.fda.gov/cdrh_docs/pdf13/P130021S033C.pdf.

348. Auricchio F, Conti M, De Beule M, De Santis G, Verhegghe B. Carotid artery stenting simulation: from patient-specific images to finite element analysis. Medical engineering & physics. 2011;33(3):281-9.

349. Yoon S-H, Lefèvre T, Ahn J-M, Perlman GY, Dvir D, Latib A, Barbanti M, Deuschl F, De Backer O, Blanke P, Modine T, Pache G, Neumann F-J, Ruile P, Arai T, Ohno Y, Kaneko H, Tay E, Schofer N, Holy EW, Luk NHV, Yong G, Lu Q, Kong WKF, Hon J, Kao H-L, Lee M, Yin W-H, Park D-W, Kang S-J, Lee S-W, Kim Y-H, Lee CW, Park S-W, Kim H-S, Butter C, Khalique OK, Schaefer U, Nietlispach F, Kodali SK, Leon MB, Ye J, Chevalier B, Leipsic J, Delgado V, Bax JJ, Tamburino C, Colombo A, Søndergaard L, Webb JG, Park S-J. Transcatheter Aortic Valve Replacement With Early- and New-Generation Devices in Bicuspid Aortic Valve Stenosis. Journal of the American College of Cardiology. 2016;68(11):1195. doi: 10.1016/j.jacc.2016.06.041.

350. Das R, Puri R. Transcatheter Treatment of Bicuspid Aortic Valve Disease: Imaging and Interventional Considerations. Frontiers in cardiovascular medicine. 2018;5:91-. doi: 10.3389/fcvm.2018.00091. PubMed PMID: 30073170.

351. Hopf R, Gessat M, Russ C, Sündermann SH, Falk V, Mazza E. Finite Element Stent Modeling for the Postoperative Analysis of Transcatheter Aortic Valve Implantation. Journal of Medical Devices. 2017;11(2):021002--7. doi: 10.1115/1.4036334.

352. Mylotte D, Lefevre T, Søndergaard L, Watanabe Y, Modine T, Dvir D, Bosmans J, Tchetche D, Kornowski R, Sinning J-M. Transcatheter aortic valve replacement in bicuspid aortic valve disease. Journal of the American College of Cardiology. 2014;64(22):2330-9.

353. Jilaihawi H, Chen M, Webb J, Himbert D, Ruiz CE, Rodés-Cabau J, Pache G, Colombo A, Nickenig G, Lee M, Tamburino C, Sievert H, Abramowitz Y, Tarantini G, Alqoofi F, Chakravarty T, Kashif M, Takahashi N, Kazuno Y, Maeno Y, Kawamori H, Chieffo A, Blanke P, Dvir D, Ribeiro HB, Feng Y, Zhao Z-G, Sinning J-M, Kliger C, Giustino G, Pajerski B, Imme S, Grube E, Leipsic J, Vahanian A, Michev I, Jelnin V, Latib A, Cheng W, Makkar R. A Bicuspid Aortic Valve Imaging Classification for the TAVR Era. JACC: Cardiovascular Imaging. 2016;9(10):1145. doi: 10.1016/j.jcmg.2015.12.022.

354. Szymański P, Hryniewiecki T, Dąbrowski M, Sorysz D, Kochman J, Jastrzębski J, Kukulski T, Zembala M. Mitral and aortic regurgitation following transcatheter aortic valve replacement. Heart. 2016;102(9):701. doi: 10.1136/heartjnl-2015-308842.

355. Shibayama K, Harada K, Berdejo J, Mihara H, Tanaka J, Gurudevan Swaminatha V, Siegel R, Jilaihawi H, Makkar Raj R, Shiota T. Effect of Transcatheter Aortic Valve Replacement on the Mitral Valve Apparatus and Mitral Regurgitation. Circulation: Cardiovascular Imaging. 2014;7(2):344-51. doi: 10.1161/CIRCIMAGING.113.000942.

356. Veronesi F, Corsi C, Sugeng L, Mor-Avi V, Caiani Enrico G, Weinert L, Lamberti C, Lang Roberto M. A Study of Functional Anatomy of Aortic-Mitral Valve Coupling Using 3D Matrix Transesophageal Echocardiography. Circulation: Cardiovascular Imaging. 2009;2(1):24-31. doi: 10.1161/CIRCIMAGING.108.785907.

357. Shah AP, Russo M, Nathan S, Tsang W, Lang RM, Veronesi F, Horlick EM, Osten M, Meineri M, Hahn RT. A three-dimensional echocardiographic study on aortic–mitral coupling in transcatheter aortic valve replacement. European Heart Journal - Cardiovascular Imaging. 2013;14(10):950-6. doi: 10.1093/ehjci/jet058.

358. Vergnat M, Levack MM, Jackson BM, Bavaria JE, Herrmann HC, Cheung AT, Weiss SJ, Gorman JH, Gorman RC. The Effect of Surgical and Transcatheter Aortic Valve Replacement on Mitral Annular Anatomy. The Annals of Thoracic Surgery. 2013;95(2):614-9. doi: https://doi.org/10.1016/j.athoracsur.2012.10.026.

359. Grayburn Paul A, Weissman Neil J, Zamorano Jose L. Quantitation of Mitral Regurgitation. Circulation. 2012;126(16):2005-17. doi: 10.1161/CIRCULATIONAHA.112.121590.

360. Katte F, Franz M, Jung C, Figulla HR, Leistner D, Jakob P, Stähli BE, Kretzschmar D, Lauten A. Impact of concomitant mitral regurgitation on transvalvular gradient and flow in severe aortic stenosis: a systematic ex vivo analysis of a subentity of low-flow low-gradient aortic stenosis. EuroIntervention. 2018;13(14):1635-44.

361. Caballero A, Mao W, McKay R, Sun W. The impact of balloon-expandable transcatheter aortic valve replacement on concomitant mitral regurgitation: a comprehensive computational analysis. J R Soc Interface. 2019;16(157):20190355. Epub 2019/08/15. doi: 10.1098/rsif.2019.0355. PubMed PMID: 31409236; PMCID: PMC6731489.

362. Abdelghani M, Abdel-Wahab M, Hemetsberger R, Landt M, Merten C, Toelg R, Richardt G. Fate and long-term prognostic implications of mitral regurgitation in patients undergoing transcatheter aortic valve replacement. Int J Cardiol. 2019;288:39-43. Epub 2019/04/06. doi: 10.1016/j.ijcard.2019.03.048. PubMed PMID: 30948219.

363. Feldt K, De Palma R, Bjursten H, Petursson P, Nielsen NE, Kellerth T, Jönsson A, Nilsson J, Rück A, Settergren M. Change in mitral regurgitation severity impacts survival after transcatheter aortic valve replacement. International Journal of Cardiology. 2019.

364. De Chiara B, Moreo A, De Marco F, Musca F, Oreglia J, Lobiati E, Bruschi G, Belli O, Mauri F, Klugmann S. Influence of corevalve revalving system implantation on

mitral valve function. Catheterization and Cardiovascular Interventions. 2011;78(4):638-44.

365. Yong Z, Van Dijk K, Koch K, Vis M. Effect of transcatheter aortic valve implantation with the Medtronic-CoreValve bioprosthesis on mitral valve area and pressure gradient. Eur J Echocardiogr. 2010;11(Suppl 2):ii9-ii11.

366. Bedogni F, Latib A, De Marco F, Agnifili M, Oreglia J, Pizzocri S, Latini RA, Lanotte S, Petronio AS, De Carlo M. Interplay between mitral regurgitation and transcatheter aortic valve replacement with the CoreValve Revalving System: a multicenter registry. Circulation. 2013;128(19):2145-53.

367. Tzikas A, Piazza N, van Dalen BM, Schultz C, Geleijnse ML, van Geuns RJ, Galema TW, Nuis RJ, Otten A, Gutierrez-Chico JL. Changes in mitral regurgitation after transcatheter aortic valve implantation. Catheterization and Cardiovascular Interventions. 2010;75(1):43-9.

368. Abdel-Wahab M, Mehilli J, Frerker C, Neumann F-J, Kurz T, Tölg R, Zachow D, Guerra E, Massberg S, Schäfer U. Comparison of balloon-expandable vs self-expandable valves in patients undergoing transcatheter aortic valve replacement: the CHOICE randomized clinical trial. Jama. 2014;311(15):1503-14.

369. Jerez-Valero M, Urena M, Webb J. Clinical impact of the presence of aortic regurgitation following transcatheter aortic valve implantation: insights into the degree and acuteness of presentation. J Am Coll Cardiol Intv. 2014;7:1022-32.

370. Liu M, Liang L, Sun W. A new inverse method for estimation of in vivo mechanical properties of the aortic wall. Journal of the mechanical behavior of biomedical materials. 2017;72:148-58.

371. Hsu M-C, Bazilevs Y. Blood vessel tissue prestress modeling for vascular fluid–structure interaction simulation. Finite Elements in Analysis and Design. 2011;47(6):593-9. doi: https://doi.org/10.1016/j.finel.2010.12.015.

372. Votta E, Presicce M, Della Corte A, Dellegrottaglie S, Bancone C, Sturla F, Redaelli A. A novel approach to the quantification of aortic root in vivo structural mechanics. International journal for numerical methods in biomedical engineering. 2017;33(9):e2849.

373. Liang L, Liu M, Martin C, Sun W. A machine learning approach as a surrogate of finite element analysis–based inverse method to estimate the zero-pressure geometry of human thoracic aorta. International journal for numerical methods in biomedical engineering. 2018;34(8):e3103.

374. Liang L, Liu M, Martin C, Sun W. A deep learning approach to estimate stress distribution: a fast and accurate surrogate of finite-element analysis. Journal of The Royal Society Interface. 2018;15(138):20170844.

375. Mauri L, Foster E, Glower DD, Apruzzese P, Massaro JM, Herrmann HC, Hermiller J, Gray W, Wang A, Pedersen WR. 4-year results of a randomized controlled trial of percutaneous repair versus surgery for mitral regurgitation. Journal of the American College of Cardiology. 2013;62(4):317-28.

376. Stone GW, Lindenfeld J, Abraham WT, Kar S, Lim DS, Mishell JM, Whisenant B, Grayburn PA, Rinaldi M, Kapadia SR. Transcatheter mitral-valve repair in patients with heart failure. New England Journal of Medicine. 2018;379(24):2307-18.

377. Obadia J-F, Messika-Zeitoun D, Leurent G, Iung B, Bonnet G, Piriou N, Lefèvre T, Piot C, Rouleau F, Carrié D. Percutaneous repair or medical treatment for secondary mitral regurgitation. New England Journal of Medicine. 2018;379(24):2297-306.

378. Goldberg SL. Reflections on percutaneous therapies for secondary mitral regurgitation. Cardiovascular revascularization medicine: including molecular interventions. 2019;20(6):528.

379. Grayburn PA, Sannino A, Packer M. Proportionate and disproportionate functional mitral regurgitation: a new conceptual framework that reconciles the results of the MITRA-FR and COAPT trials. JACC: Cardiovascular Imaging. 2019;12(2):353-62.

380. Lim DS, Reynolds MR, Feldman T, Kar S, Herrmann HC, Wang A, Whitlow PL, Gray WA, Grayburn P, Mack MJ. Improved functional status and quality of life in prohibitive surgical risk patients with degenerative mitral regurgitation after transcatheter mitral valve repair. Journal of the American College of Cardiology. 2014;64(2):182-92.

381. Sorajja P, Vemulapalli S, Feldman T, Mack M, Holmes DR, Stebbins A, Kar S, Thourani V, Ailawadi G. Outcomes with transcatheter mitral valve repair in the United States: an STS/ACC TVT registry report. Journal of the American College of Cardiology. 2017;70(19):2315-27.

382. Ailawadi G, Lim DS, Mack MJ, Trento A, Kar S, Grayburn PA, Glower DD, Wang A, Foster E, Qasim A. One-year outcomes after MitraClip for functional mitral regurgitation. Circulation. 2019;139(1):37-47.

383. Sacks M, Drach A, Lee CH, Khalighi A, Rego B, Zhang W, Ayoub S, Yoganathan A, Gorman RC, Gorman Iii JH. On the simulation of mitral valve function in health, disease, and treatment. J Biomech Eng. 2019;141(7):070804. Epub 2019/04/21. doi: 10.1115/1.4043552. PubMed PMID: 31004145.

384. Prescott B, Abunassar C, Baxevanakis KP, Zhao L. Computational evaluation of mitral valve repair with MitraClip2019.

385. Sturla F, Vismara R, Jaworek M, Votta E, Romitelli P, Pappalardo OA, Lucherini F, Antona C, Fiore GB, Redaelli A. In vitro and in silico approaches to quantify the effects of the Mitraclip® system on mitral valve function. Journal of biomechanics. 2017;50:83-92.

386. Sturla F, Redaelli A, Puppini G, Onorati F, Faggian G, Votta E. Functional and biomechanical effects of the edge-to-edge repair in the setting of mitral regurgitation: consolidated knowledge and novel tools to gain insight into its percutaneous implementation. Cardiovascular engineering and technology. 2015;6(2):117-40.

387. Zhong Q, Zeng W, Huang X, Zhao X. Finite Element Analysis for Edge-to-Edge Technique to Treat Post-Mitral Valve Repair Systolic Anterior Motion. Acta of bioengineering and biomechanics. 2014;16(4).

388. Morgan AE, Wozniak CJ, Gulati S, Ge L, Grossi EA, Weinsaft JW, Ratcliffe MB. Uneven MitraClip Application Does Not Increase Leaflet Stress in a Finite Element Model. JAMA surgery. 2017;152(1):111.

389. Borghetti V, Campana M, Scotti C, Domenighini D, Totaro P, Coletti G, Pagani M, Lorusso R. Biological versus prosthetic ring in mitral-valve repair: enhancement of mitral annulus dynamics and left-ventricular function with pericardial annuloplasty at long term. European journal of cardio-thoracic surgery. 2000;17(4):431-9.

390. Kong F, Pham T, Martin C, Elefteriades J, McKay R, Primiano C, Sun W. Finite element analysis of annuloplasty and papillary muscle relocation on a patient-specific mitral regurgitation model. PloS one. 2018;13(6):e0198331.

391. Magruder JT, Crawford TC, Grimm JC, Fredi JL, Shah AS. Managing mitral regurgitation: focus on the MitraClip device. Medical devices (Auckland, NZ). 2016;9:53.

392. Kuwata S, Taramasso M, Czopak A, Luciani M, Pozzoli A, Ho E, Guadagnoli AF, Saccocci M, Gaemperli O, Nietlispach F. Continuous direct left atrial pressure: intraprocedural measurement predicts clinical response following MitraClip therapy. JACC: Cardiovascular Interventions. 2019;12(2):127-36.

393. Turyan Medvedovsky A, Tonchev I, Tahiroglu I, Lotan C, Gilon D, Planer D, Danenberg HD, Beeri R, Shuvy M. MitraClip Therapy in Critically Ill Patients with Severe Functional Mitral Regurgitation and Refractory Heart Failure. Structural Heart. 2019:1-6.

394. Noack T, Kiefer P, Mallon L, Lurz P, Bevilacqua C, Banusch J, Emrich F, Holzhey DM, Vannan M, Thiele H. Changes in dynamic mitral valve geometry during percutaneous edge–edge mitral valve repair with the MitraClip system. Journal of echocardiography. 2019;17(2):84-94.

395. Schmidt FP, von Bardeleben RS, Nikolai P, Jabs A, Wunderlich N, Münzel T, Hink U, Warnholtz A. Immediate effect of the MitraClip® procedure on mitral ring geometry in primary and secondary mitral regurgitation. European Heart Journal–Cardiovascular Imaging. 2013;14(9):851-7.

396. Schueler R, Momcilovic D, Weber M, Welz A, Werner N, Mueller C, Ghanem A, Nickenig G, Hammerstingl C. Acute changes of mitral valve geometry during interventional edge-to-edge repair with the MitraClip system are associated with midterm outcomes in patients with functional valve disease: preliminary results from a prospective single-center study. Circulation: Cardiovascular Interventions. 2014;7(3):390-9.

397. Donmez E, Salcedo EE, Quaife RA, Burke JM, Gill EA, Carroll JD. The acute effects of edge-to-edge percutaneous mitral valve repair on the shape and size of the mitral annulus and its relation to mitral regurgitation. Echocardiography. 2019.

398. Mantegazza V, Pasquini A, Agati L, Fusini L, Muratori M, Gripari P, Ali SG, Vignati C, Bartorelli AL, Ferrari C. Comprehensive Assessment of Mitral Valve Geometry and Cardiac Remodeling With 3-Dimensional Echocardiography After Percutaneous Mitral Valve Repair. The American journal of cardiology. 2018;122(7):1195-203.

399. Schueler R, Kaplan S, Melzer C, Öztürk C, Weber M, Sinning J-M, Welz A, Werner N, Nickenig G, Hammerstingl C. Impact of interventional edge-to-edge repair on mitral valve geometry. International journal of cardiology. 2017;230:468-75.

400. Patzelt J, Zhang Y, Magunia H, Ulrich M, Jorbenadze R, Droppa M, Zhang W, Lausberg H, Walker T, Rosenberger P. Improved mitral valve coaptation and reduced mitral valve annular size after percutaneous mitral valve repair (PMVR) using the MitraClip system. European Heart Journal-Cardiovascular Imaging. 2017;19(7):785-91.

401. McCarthy KP, Ring L, Rana BS. Anatomy of the mitral valve: understanding the mitral valve complex in mitral regurgitation. European Journal of echocardiography. 2010;11(10):i3-i9.

402. Mahmood F, Gorman III JH, Subramaniam B, Gorman RC, Panzica PJ, Hagberg RC, Lerner AB, Hess PE, Maslow A, Khabbaz KR. Changes in mitral valve annular geometry after repair: saddle-shaped versus flat annuloplasty rings. The Annals of thoracic surgery. 2010;90(4):1212-20.

403. Jimenez JH, Forbess J, Croft LR, Small L, He Z, Yoganathan AP. Effects of annular size, transmitral pressure, and mitral flow rate on the edge-to-edge repair: an in vitro study. The Annals of thoracic surgery. 2006;82(4):1362-8.

404. Warraich HJ, Chaudary B, Maslow A, Panzica PJ, Pugsley J, Mahmood F. Mitral annular nonplanarity: correlation between annular height/commissural width ratio and the nonplanarity angle. Journal of cardiothoracic and vascular anesthesia. 2012;26(2):186-90.

405. Baumgartner H, Falk V, Bax JJ, De Bonis M, Hamm C, Holm PJ, Iung B, Lancellotti P, Lansac E, Rodriguez Munoz D. 2017 ESC/EACTS guidelines for the management of valvular heart disease. European heart journal. 2017;38(36):2739-91.

406. Ladich E, Michaels MB, Jones RM, McDermott E, Coleman L, Komtebedde J, Glower D, Argenziano M, Feldman T, Nakano M. Pathological healing response of explanted MitraClip devices. Circulation. 2011;123(13):1418-27.

407. Altiok E, Hamada S, Brehmer K, Kuhr K, Reith S, Becker M, Schröder J, Almalla M, Lehmacher W, Marx N. Analysis of procedural effects of percutaneous edge-to-edge mitral valve repair by 2D and 3D echocardiography. Circulation: Cardiovascular Imaging. 2012;5(6):748-55.

408. Biaggi P, Felix C, Gruner C, Herzog BA, Hohlfeld S, Gaemperli O, Stähli BE, Paul M, Held L, Tanner FC. Assessment of mitral valve area during percutaneous mitral valve repair using the MitraClip system: comparison of different echocardiographic methods. Circulation: Cardiovascular Imaging. 2013;6(6):1032-40.

409. Noack T, Janietz M, Lurz P, Kiefer P, Sieg F, Marin-Cuartas M, Spampinato R, Besler C, Rommel K-P, Holzhey D. Dynamic mitral valve geometry in patients with primary and secondary mitral regurgitation: implications for mitral valve repair. European Journal of Cardio-Thoracic Surgery. 2019.

410. Buzzatti N, De Bonis M, Denti P, Barili F, Schiavi D, Di Giannuario G, La Canna G, Alfieri O. What is a "good" result after transcatheter mitral repair? Impact of 2+ residual mitral regurgitation. The Journal of thoracic and cardiovascular surgery. 2016;151(1):88-96.

411. Cheng R, Dawkins S, Tat E, Makar M, Hussaini A, Makkar RR, Trento A, Siegel RJ, Kar S. Relation of residual mitral regurgitation despite elevated mitral gradients to risk of heart failure hospitalization after MitraClip repair. The American journal of cardiology. 2017;120(9):1595-600.

412. Paranskaya L, D'Ancona G, Bozdag-Turan I, Akin I, Kische S, Turan GR, Rehders T, Ortak J, Nienaber CA, Ince H. Residual mitral valve regurgitation after percutaneous mitral valve repair with the mitraclip® system is a risk factor for adverse one-year outcome. Catheterization and Cardiovascular Interventions. 2013;81(4):609-17.

413. Singh GD, Smith TW, Rogers JH. Multi-M itra C lip therapy for severe degenerative mitral regurgitation:"Anchor" technique for extremely flail segments. Catheterization and Cardiovascular Interventions. 2015;86(2):339-46.

414. Stone GW, Vahanian AS, Adams DH, Abraham WT, Borer JS, Bax JJ, Schofer J, Cutlip DE, Krucoff MW, Blackstone EH. Clinical trial design principles and endpoint definitions for transcatheter mitral valve repair and replacement: part 1: clinical trial design principles: a consensus document from the Mitral Valve Academic Research Consortium. Journal of the American College of Cardiology. 2015;66(3):278-307.

415. Zoghbi WA, Adams D, Bonow RO, Enriquez-Sarano M, Foster E, Grayburn PA, Hahn RT, Han Y, Hung J, Lang RM. Recommendations for noninvasive evaluation of native valvular regurgitation: a report from the American Society of Echocardiography developed in collaboration with the Society for Cardiovascular Magnetic Resonance. Journal of the American Society of Echocardiography. 2017;30(4):303-71.

416. Corrigan III FE, Chen JH, Maini A, Lisko JC, Alvarez L, Kamioka N, Reginauld S, Gleason PT, Condado JF, Wei JW. Pulmonary venous waveforms predict rehospitalization and mortality after percutaneous mitral valve repair. JACC: Cardiovascular Imaging. 2018.

417. Dietl A, Prieschenk C, Eckert F, Birner C, Luchner A, Maier LS, Buchner S. 3D vena contracta area after MitraClip© procedure: precise quantification of residual mitral regurgitation and identification of prognostic information. Cardiovascular ultrasound. 2018;16(1):1.

418. Palmiero G, Ascione L, Briguori C, Carlomagno G, Sordelli C, Ascione R, Pisacane F, Monda V, Severino S, Caso P. The mitral-to-aortic flow-velocity integral ratio in the real world echocardiographic evaluation of functional mitral regurgitation before and after percutaneous repair. Journal of interventional cardiology. 2017;30(4):368-73.

419. Magne J, Sénéchal M, Mathieu P, Dumesnil JG, Dagenais F, Pibarot P. Restrictive annuloplasty for ischemic mitral regurgitation may induce functional mitral stenosis. Journal of the American College of Cardiology. 2008;51(17):1692-701.

420. Chan KL, Chen S-Y, Chan V, Hay K, Mesana T, Lam BK. Functional significance of elevated mitral gradients after repair for degenerative mitral regurgitation. Circulation: Cardiovascular Imaging. 2013;6(6):1041-7.

421. Bertrand PB, Verbrugge FH, Verhaert D, Smeets CJ, Grieten L, Mullens W, Gutermann H, Dion RA, Levine RA, Vandervoort PM. Mitral valve area during exercise after restrictive mitral valve annuloplasty: importance of diastolic anterior leaflet tethering. Journal of the American College of Cardiology. 2015;65(5):452-61.

422. Herrmann HC, Rohatgi S, Wasserman HS, Block P, Gray W, Hamilton A, Zunamon A, Homma S, Di Tullio MR, Kraybill K. Mitral valve hemodynamic effects of percutaneous edge-to-edge repair with the MitraClip™ device for mitral regurgitation. Catheterization and cardiovascular interventions. 2006;68(6):821-8.

423. Boerlage-van Dijk K, Van Riel AC, de Bruin-Bon RH, Wiegerinck EM, Koch KT, Vis MM, Meregalli PG, Bindraban NR, Mulder BJ, Piek JJ. Mitral inflow patterns after MitraClip implantation at rest and during exercise. Journal of the American Society of Echocardiography. 2014;27(1):24-31. e1.

424. Neuss M, Schau T, Isotani A, Pilz M, Schöpp M, Butter C. Elevated mitral valve pressure gradient after MitraClip implantation deteriorates long-term outcome in patients with severe mitral regurgitation and severe heart failure. JACC: Cardiovascular Interventions. 2017;10(9):931-9.

425. Toggweiler S, Zuber M, Sürder D, Biaggi P, Gstrein C, Moccetti T, Pasotti E, Gaemperli O, Faletra F, Petrova-Slater I. Two-year outcomes after percutaneous mitral

valve repair with the MitraClip system: durability of the procedure and predictors of outcome. Open Heart. 2014;1(1):e000056.

426. Bach DS. Echo/Doppler evaluation of hemodynamics after aortic valve replacement: principles of interrogation and evaluation of high gradients. JACC: Cardiovascular Imaging. 2010;3(3):296-304.

427. Zoghbi WA, Chambers JB, Dumesnil JG, Foster E, Gottdiener JS, Grayburn PA, Khandheria BK, Levine RA, Marx GR, Miller FA. Recommendations for evaluation of prosthetic valves with echocardiography and Doppler ultrasound: a report from the American Society of Echocardiography's Guidelines and Standards Committee and the Task Force on Prosthetic Valves, developed in conjunction with the American College of Cardiology Cardiovascular Imaging Committee, Cardiac Imaging Committee of the American Heart Association, the European Association of Echocardiography, a registered branch of the European Society of Cardiology, the Japanese Society of Echocardiography and the Canadian Society of Echocardiography, endorsed by the American College of Cardiology Foundation, American Heart Association, European Association of Echocardiography, a registered branch of the European Society of Cardiology, the Japanese Society of Echocardiography, and Canadian Society of Echocardiography. Journal of the American Society of Echocardiography. 2009;22(9):975-1014.

428. Jeyhani M, Shahriari S, Labrosse M. Experimental Investigation of Left Ventricular Flow Patterns After Percutaneous Edge-to-Edge Mitral Valve Repair. Artificial organs. 2018;42(5):516-24.

429. Maisano F, Redaelli A, Pennati G, Fumero R, Torracca L, Alfieri O. The hemodynamic effects of double-orifice valve repair for mitral regurgitation: a 3D computational model. European journal of cardio-thoracic surgery. 1999;15(4):419-25.

430. Kang W-S, Choi JW, Kang J-E, Chung JW, Kim S-H. Determination of mitral valve area with echocardiography, using intra-operative 3-dimensional versus intra-& post-operative pressure half-time technique in mitral valve repair surgery. Journal of cardiothoracic surgery. 2013;8(1):98.

431. Kar S, Sharma R. Current assessment of mitral regurgitation: not making the grade. Journal of the American College of Cardiology; 2015.

432. Shi L, He Z. Hemodynamics of the mitral valve under edge-to-edge repair: an in vitro steady flow study. Journal of biomechanical engineering. 2009;131(5):051010.

433. Redaelli A, Guadagni G, Fumero R, Maisano F, Alfieri O. A computational study of the hemodynamics after “edge-to-edge” mitral valve repair. Journal of biomechanical engineering. 2001;123(6):565-70.

434. Hu Y, Shi L, Parameswaran S, Smirnov S, He Z. Left ventricular vortex under mitral valve edge-to-edge repair. Cardiovascular engineering and technology. 2010;1(4):235-43.

435. Du D, Jiang S, Wang Z, Hu Y, He Z. Effects of suture position on left ventricular fluid mechanics under mitral valve edge-to-edge repair. Bio-medical materials and engineering. 2014;24(1):155-61.

436. Filomena D, Cimino S, Maestrini V, Cantisani D, Petronilli V, Mancone M, Tonti G, Pedrizzetti G, Agati L. Changes in Intraventricular Flow Patterns after MitraClip Implant in Patients with Functional Severe Mitral Regurgitation. Journal of the American Society of Echocardiography. 2019;32(9):1250-3. e1.

437. Cimino S, Palombizio D, Cicogna F, Cantisani D, Reali M, Filomena D, Petronilli V, Iacoboni C, Agati L. Significant increase of flow kinetic energy in “nonresponders” patients to cardiac resynchronization therapy. Echocardiography. 2017;34(5):709-15.

438. Eleid MF, Sanon S, Reeder GS, Suri RM, Rihal CS. Continuous left atrial pressure monitoring during MitraClip: assessing the immediate hemodynamic response. JACC: Cardiovascular Interventions. 2015;8(7):e117-e9.

439. Horstkotte J, Kloeser C, Beucher H, Schwarzlaender E, von Bardeleben R, Boekstegers P. Intraprocedural assessment of mitral regurgitation during the mitraclip procedure: Impact of continuous left atrial pressure monitoring. Catheterization and Cardiovascular Interventions. 2016;88(7):1134-43.

440. Ikenaga H, Yoshida J, Hayashi A, Nagaura T, Yamaguchi S, Rader F, Siegel RJ, Kar S, Shiota T. Usefulness of intraprocedural pulmonary venous flow for predicting recurrent mitral regurgitation and clinical outcomes after percutaneous mitral valve repair with the MitraClip. JACC: Cardiovascular Interventions. 2019;12(2):140-50.

441. Nordsletten D, Niederer S, Nash M, Hunter P, Smith N. Coupling multi-physics models to cardiac mechanics. Progress in biophysics and molecular biology. 2011;104(1-3):77-88.

442. Wittek A, Karatolios K, Bihari P, Schmitz-Rixen T, Moosdorf R, Vogt S, Blase C. In vivo determination of elastic properties of the human aorta based on 4D ultrasound data. Journal of the mechanical behavior of biomedical materials. 2013;27:167-83.

443. Wittek A, Derwich W, Karatolios K, Fritzen CP, Vogt S, Schmitz-Rixen T, Blase C. A finite element updating approach for identification of the anisotropic hyperelastic properties of normal and diseased aortic walls from 4D ultrasound strain imaging. Journal of the mechanical behavior of biomedical materials. 2016;58:122-38.

444. Liu M, Liang L, Sulejmani F, Lou X, Iannucci G, Chen E, Leshnower B, Sun W. Identification of in vivo nonlinear anisotropic mechanical properties of ascending thoracic aortic aneurysm from patient-specific CT scans. Scientific reports. 2019;9(1):1-13.

445. Liu M, Liang L, Sun W. Estimation of in vivo constitutive parameters of the aortic wall using a machine learning approach. Computer methods in applied mechanics and engineering. 2019;347:201-17.

446. Hong G-R, Kim M, Pedrizzetti G, Vannan MA. Current clinical application of intracardiac flow analysis using echocardiography. Journal of cardiovascular ultrasound. 2013;21(4):155-62.

447. Pedrizzetti G, La Canna G, Alfieri O, Tonti G. The vortex—an early predictor of cardiovascular outcome? Nature Reviews Cardiology. 2014;11(9):545.

448. Bahlmann E, Gerdts E, Cramariuc D, Gohlke-Baerwolf C, Nienaber CA, Wachtell K, Seifert R, Chambers JB, Kuck KH, Ray S. Prognostic value of energy loss index in asymptomatic aortic stenosis. Circulation. 2013;127(10):1149-56.

449. Cimino S, Pedrizzetti G, Tonti G, Canali E, Petronilli V, De Luca L, Iacoboni C, Agati L. In vivo analysis of intraventricular fluid dynamics in healthy hearts. European Journal of Mechanics-B/Fluids. 2012;35:40-6.

450. Vesely I. The evolution of bioprosthetic heart valve design and its impact on durability. Cardiovascular Pathology. 2003;12(5):277-86. doi: http://dx.doi.org/10.1016/S1054-8807(03)00075-9.

451. Aguiari P, Fiorese M, Iop L, Gerosa G, Bagno A. Mechanical testing of pericardium for manufacturing prosthetic heart valves. Interactive CardioVascular and Thoracic Surgery. 2016;22(1):72-84. doi: 10.1093/icvts/ivv282.

452. Trowbridge E, Crofts C. Pericardial heterograft valves: an assessment of leaflet stresses and their implications for heart valve design. Journal of biomedical engineering. 1987;9(4):345-55.

453. Sacks MS, Chuong CJ. Orthotropic Mechanical Properties of Chemically Treated Bovine Pericardium. Annals of Biomedical Engineering. 1998;26(5):892-902. doi: 10.1114/1.135.

454. Sacks MS, Chuong CC, More R. Collagen fiber architecture of bovine pericardium. ASAIO journal. 1994;40(3):M632-M7.

455. Sun W, Sacks MS, Sellaro TL, Slaughter WS, Scott MJ. Biaxial mechanical response of bioprosthetic heart valve biomaterials to high in-plane shear. J Biomech Eng. 2003;125(3):372-80. Epub 2003/08/22. PubMed PMID: 12929242.

456. Langdon SE, Chernecky R, Pereira CA, Abdulla D, Lee JM. Biaxial mechanical/structural effects of equibiaxial strain during crosslinking of bovine pericardial xenograft materials. Biomaterials. 1999;20(2):137-53.

457. Páez JG, Jorge E, Rocha A, Maestro M, Castillo-Olivares J, Millan I, Carrera A, Cordon A, Tellez G, Burgos R. Mechanical effects of increases in the load applied in uniaxial and biaxial tensile testing: Part I. Calf pericardium. Journal of Materials Science: Materials in Medicine. 2002;13(4):381-8.

458. Ohtani O, USHIKI T, TAGUCHI T, KIKUTA A. Collagen fibrillar networks as skeletal frameworks: a demonstration by cell-maceration/scanning electron microscope method. Archives of histology and cytology. 1988;51(3):249-61.

459. Bailey AJ, Paul RG, Knott L. Mechanisms of maturation and ageing of collagen. Mechanisms of Ageing and Development. 1998;106(1–2):1-56. doi: http://dx.doi.org/10.1016/S0047-6374(98)00119-5.

460. LaCroix AS, Duenwald-Kuehl SE, Brickson S, Akins TL, Diffee G, Aiken J, Vanderby R, Lakes RS. Effect of Age and Exercise on the Viscoelastic Properties of Rat Tail Tendon. Annals of Biomedical Engineering. 2013;41(6):1120-8. doi: 10.1007/s10439-013-0796-4.

461. Goh KL, Holmes DF, Lu HY, Richardson S, Kadler KE, Purslow PP, Wess TJ. Ageing Changes in the Tensile Properties of Tendons: Influence of Collagen Fibril Volume

Fraction. Journal of Biomechanical Engineering. 2008;130(2):021011-. doi: 10.1115/1.2898732.

462. Danielsen CC, Andreassen TT. Mechanical properties of rat tail tendon in relation to proximal-distal sampling position and age. Journal of biomechanics. 1988;21(3):207-12.

463. Bailey AJ. Molecular mechanisms of ageing in connective tissues. Mechanisms of Ageing and Development. 2001;122(7):735-55. doi: http://dx.doi.org/10.1016/S0047-6374(01)00225-1.

464. Sizeland KH, Wells HC, Higgins J, Cunanan CM, Kirby N, Hawley A, Mudie ST, Haverkamp RG. Age Dependent Differences in Collagen Alignment of Glutaraldehyde Fixed Bovine Pericardium. BioMed research international. 2014;2014.

465. Ramlawi B, Anaya-Ayala JE, Reardon MJ. Transcatheter aortic valve replacement (TAVR): access planning and strategies. Methodist DeBakey cardiovascular journal. 2012;8(2):22.

466. Taramasso M, Pozzoli A, Latib A, La Canna G, Colombo A, Maisano F, Alfieri O. New devices for TAVI: technologies and initial clinical experiences. Nat Rev Cardiol. 2014;11(3):157-67. doi: 10.1038/nrcardio.2013.221.

467. Bia D, Pessana F, Armentano R, Perez H, Graf S, Zocalo Y, Saldias M, Perez N, Alvarez O, Silva W, Machin D, Sueta P, Ferrin S, Acosta M, Alvarez I. Cryopreservation procedure does not modify human carotid homografts mechanical properties: an isobaric and dynamic analysis. Cell Tissue Bank. 2006;7(3):183-94. Epub 2006/08/26. doi: 10.1007/s10561-005-0655-0. PubMed PMID: 16933040.

468. Gerson CJ, Goldstein S, Heacox AE. Retained structural integrity of collagen and elastin within cryopreserved human heart valve tissue as detected by two-photon laser scanning confocal microscopy. Cryobiology. 2009;59(2):171-9. Epub 2009/07/14. doi: 10.1016/j.cryobiol.2009.06.012. PubMed PMID: 19591817.

469. Sacks MS, Sun W. Multiaxial mechanical behavior of biological materials. Annu Rev Biomed Eng. 2003;5:251-84. Epub 2003/05/06. doi: 10.1146/annurev.bioeng.5.011303.120714. PubMed PMID: 12730082.

470. Garcia-Herrera CM, Atienza JM, Rojo FJ, Claes E, Guinea GV, Celentano DJ, Garcia-Montero C, Burgos RL. Mechanical behaviour and rupture of normal and

pathological human ascending aortic wall. Med Biol Eng Comput. 2012;50(6):559-66. Epub 2012/03/07. doi: 10.1007/s11517-012-0876-x. PubMed PMID: 22391945.

471. Wan W, Dixon J B, Gleason Rudolph L. Constitutive Modeling of Mouse Carotid Arteries Using Experimentally Measured Microstructural Parameters. Biophysical Journal. 2012;102(12):2916-25. doi: 10.1016/j.bpj.2012.04.035. PubMed PMID: PMC3379026.

472. Rezakhaniha R, Agianniotis A, Schrauwen JTC, Griffa A, Sage D, Bouten CVC, Vosse FN, Unser M, Stergiopulos N. Experimental investigation of collagen waviness and orientation in the arterial adventitia using confocal laser scanning microscopy. Biomechanics and Modeling in Mechanobiology. 2011;11(3):461-73. doi: 10.1007/s10237-011-0325-z.

473. Schneider CA, Rasband WS, Eliceiri KW. NIH Image to ImageJ: 25 years of image analysis. Nat Meth. 2012;9(7):671-5.

474. Jähne B. Spatio-temporal image processing: theory and scientific applications: Springer Science & Business Media; 1993.

475. Junqueira LC, Montes GS, Sanchez EM. The influence of tissue section thickness on the study of collagen by the Picrosirius-polarization method. Histochemistry. 1982;74(1):153-6. Epub 1982/01/01. PubMed PMID: 7085347.

476. Rich L, Whittaker P. Collagen and picrosirius red staining: a polarized light assessment of fibrillar hue and spatial distribution. Braz J Morphol Sci. 2005;22(2):97-104.

477. Aikawa E, Whittaker P, Farber M, Mendelson K, Padera RF, Aikawa M, Schoen FJ. Human semilunar cardiac valve remodeling by activated cells from fetus to adult: implications for postnatal adaptation, pathology, and tissue engineering. Circulation. 2006;113(10):1344-52. Epub 2006/03/15. doi: 10.1161/circulationaha.105.591768. PubMed PMID: 16534030.

478. Sun W, Abad A, Sacks MS. Simulated bioprosthetic heart valve deformation under quasi-static loading. J Biomech Eng. 2005;127(6):905-14. PubMed PMID: 16438226.

479. Fung Y-c. Biomechanics: mechanical properties of living tissues: Springer Science & Business Media; 2013.

480. Holzapfel G, Gasser T, Ogden R. A New Constitutive Framework for Arterial Wall Mechanics and a Comparative Study of Material Models. Journal of Elasticity. 2000;61(1-3):1-48. doi: 10.1023/A:1010835316564.

481. Gasser TC, Ogden RW, Holzapfel GA. Hyperelastic modelling of arterial layers with distributed collagen fibre orientations. J R Soc Interface. 2006;3(6):15-35. PubMed PMID: 16849214.

482. Chen X, Nadiarynkh O, Plotnikov S, Campagnola PJ. Second harmonic generation microscopy for quantitative analysis of collagen fibrillar structure. Nat Protocols. 2012;7(4):654-69.

483. Ottani V, Raspanti M, Ruggeri A. Collagen structure and functional implications. Micron. 2001;32(3):251-60. doi: http://dx.doi.org/10.1016/S0968-4328(00)00042-1.

484. Bailey AJ, Paul RG, editors. The mechanisms and consequences of the maturation and ageing of collagen. Proceedings of the Indian Academy of Sciences-Chemical Sciences; 1999: Springer.

485. Charlebois M, McKee MD, Buschmann MD. Nonlinear tensile properties of bovine articular cartilage and their variation with age and depth. Journal of biomechanical engineering. 2004;126(2):129-37.

486. Martin C, Pham T, Sun W. Significant differences in the material properties between aged human and porcine aortic tissues. European Journal of Cardio-Thoracic Surgery. 2011;40(1):28-34.

487. Stephens EH, de Jonge N, McNeill MP, Durst CA, Grande-Allen KJ. Age-related changes in material behavior of porcine mitral and aortic valves and correlation to matrix composition. Tissue Engineering Part A. 2009;16(3):867-78.

488. Curwin SL, Roy RR, Vailas AC. Regional and age variations in growing tendon. Journal of morphology. 1994;221(3):309-20.

489. Woo SL-Y, Buckwalter JA. Injury and repair of the musculoskeletal soft tissues. Savannah, Georgia, June 18–20, 1987. Journal of Orthopaedic Research. 1988;6(6):907-31. doi: 10.1002/jor.1100060615.

490. Shadwick RE. Elastic energy storage in tendons: mechanical differences related to function and age. Journal of Applied Physiology. 1990;68(3):1033-40.

491. Parry DAD. The molecular fibrillar structure of collagen and its relationship to the mechanical properties of connective tissue. Biophysical Chemistry. 1988;29(1–2):195-209. doi: http://dx.doi.org/10.1016/0301-4622(88)87039-X.

492. Gathercole LJ, Keller, A. Light microscopic waveforms in collagenous tissues and their structural implications. In: Atkins EDT, Keller, A., editor. Structure of Fibrous Biopolymers. London1975. p. 153–87.

493. Diamant J, Keller A, Baer E, Litt M, Arridge R. Collagen; ultrastructure and its relation to mechanical properties as a function of ageing. Proceedings of the Royal Society of London B: Biological Sciences. 1972;180(1060):293-315.

494. Christie GW, Barratt-Boyes BG. Age-dependent changes in the radial stretch of human aortic valve leaflets determined by biaxial testing. The Annals of thoracic surgery. 1995;60:S156-S9.

495. Páez JMG, Carrera A, Cordón A, Jorge-Herrero E, Rocha A, Salvador J, Méndez J, Castillo-Olivares JL, Milláan I, Sainz N. Uniaxial and biaxial tensile strength of calf pericardium used in the construction of bioprostheses: biomaterial selection criteria. Journal of biomaterials applications. 2000;15(1):47-64.

496. Gauvin R, Marinov G, Mehri Y, Klein J, Li B, Larouche D, Guzman R, Zhang Z, Germain L, Guidoin R. A comparative study of bovine and porcine pericardium to highlight their potential advantages to manufacture percutaneous cardiovascular implants. Journal of biomaterials applications. 2013;28(4):552-65.

497. Bai M, Zhang T, Ling T, Zhou Z, Xie H, Zhang W, Hu G, Jiang C, Li M, Feng B. Guided bone regeneration using acellular bovine pericardium in a rabbit mandibular model: in-vitro and in-vivo studies. Journal of periodontal research. 2014;49(4):499-507.

498. Hülsmann J, Grün K, El Amouri S, Barth M, Hornung K, Holzfuß C, Lichtenberg A, Akhyari P. Transplantation material bovine pericardium: biomechanical and immunogenic characteristics after decellularization vs. glutaraldehyde-fixing. Xenotransplantation. 2012;19(5):286-97.

499. Oswal D, Korossis S, Mirsadraee S, Wilcox H, Watterson K, Fisher J, Ingham E. Biomechanical characterization of decellularized and cross-linked bovine pericardium. JOURNAL OF HEART VALVE DISEASE. 2007;16(2):165.

500. Crofts C, Trowbridge E. The tensile strength of natural and chemically modified bovine pericardium. Journal of biomedical materials research. 1988;22(2):89-98.

501. Páez JG, Carrera A, Jorge E, Millán I, Cordón A, Rocha A, Maestro M, Castillo-Olivares J. Hysteresis of a biomaterial: Influence of sutures and biological adhesives. Journal of Materials Science: Materials in Medicine. 2007;18(5):715-24.

502. Mendoza-Novelo B, Avila EE, Cauich-Rodríguez JV, Jorge-Herrero E, Rojo FJ, Guinea GV, Mata-Mata JL. Decellularization of pericardial tissue and its impact on tensile viscoelasticity and glycosaminoglycan content. Acta biomaterialia. 2011;7(3):1241-8.

503. Sánchez-Arévalo F, Farfán M, Covarrubias D, Zenit R, Pulos G. The micromechanical behavior of lyophilized glutaraldehyde-treated bovine pericardium under uniaxial tension. Journal of the mechanical behavior of biomedical materials. 2010;3(8):640-6.

504. Hiester ED, Sacks MS. Optimal bovine pericardial tissue selection sites. I. Fiber architecture and tissue thickness measurements. Journal of biomedical materials research. 1998;39(2):207-14.

505. Hiester ED, Sacks MS. Optimal bovine pericardial tissue selection sites. II. Cartographic analysis. Journal of biomedical materials research. 1998;39(2):215-21.

506. Trowbridge E, Roberts KM, Crofts C, Lawford P. Pericardial heterografts. Toward quality control of the mechanical properties of glutaraldehyde-fixed leaflets. The Journal of thoracic and cardiovascular surgery. 1986;92(1):21-8.

507. Hasan A, Ragaert K, Swieszkowski W, Selimović Š, Paul A, Camci-Unal G, Mofrad MR, Khademhosseini A. Biomechanical properties of native and tissue engineered heart valve constructs. Journal of Biomechanics. 2014;47(9):1949-63.

508. Merryman WD, Huang H-YS, Schoen FJ, Sacks MS. The effects of cellular contraction on aortic valve leaflet flexural stiffness. Journal of biomechanics. 2006;39(1):88-96.

509. Venkatasubramanian RT, Grassl ED, Barocas VH, Lafontaine D, Bischof JC. Effects of freezing and cryopreservation on the mechanical properties of arteries. Annals of Biomedical engineering. 2006;34(5):823-32.

510. Sung HW, Chang Y, Chiu CT, Chen CN, Liang HC. Crosslinking characteristics and mechanical properties of a bovine pericardium fixed with a naturally occurring crosslinking agent. Journal of biomedical materials research. 1999;47(2):116-26.

511. Masson I, Fialaire-Legendre A, Godin C, Boutouyrie P, Bierling P, Zidi M. Mechanical properties of arteries cryopreserved at −80 °C and −150 °C. Medical Engineering & Physics. 2009;31(7):825-32. doi: http://dx.doi.org/10.1016/j.medengphy.2009.03.009.

512. Brossollet L, Vito R. The effects of cryopreservation on the biaxial mechanical properties of canine saphenous veins. Journal of biomechanical engineering. 1997;119(1):1-5.

513. Ng BH, Chou SM, Lim BH, Chong A. The changes in the tensile properties of tendons after freeze storage in saline solution. Proceedings of the Institution of Mechanical Engineers, Part H: Journal of Engineering in Medicine. 2005;219(6):387-92.

514. Foutz T, Stone E, Abrams Jr C. Effects of freezing on mechanical properties of rat skin. American journal of veterinary research. 1992;53(5):788-92.

515. Vinci MC, Tessitore G, Castiglioni L, Prandi F, Soncini M, Santoro R, Consolo F, Colazzo F, Micheli B, Sironi L. Mechanical compliance and immunological compatibility of fixative-free decellularized/cryopreserved human pericardium. PloS one. 2013;8(5):e64769.